MODAL AND RADIATION CHARACTERISTICS OF THE CROSSED-SEPTUM DIELECTRIC LOADED WAVEGUIDE FOR WIDEBAND APPLICATIONS

by

Daniel S. Purdy

Dissertation submitted to the Faculty of the
Virginia Polytechnic Institute and State University
in partial fulfillment of the requirements for the degree of

DOCTOR OF PHILOSOPHY

in

Electrical Engineering

APPROVED:

Dr. Warren L. Stutzman (Chairman)

Dr. Timothy Pratt

Dr. William Davis

Dr. Gary Brown

Dr. Yuriko Renardy

Dr. H. Wade Swinford (Dissertation reviewer, China Lake)

March, 1995

MODAL AND RADIATION CHARACTERISTICS OF THE CROSSED-SEPTUM DIELECTRIC LOADED WAVEGUIDE FOR WIDEBAND APPLICATIONS

by

Daniel S. Purdy

Committee Chairman: Dr. Warren L. Stutzman

Electrical Engineering

(ABSTRACT)

Broadband, high power, dual polarized phased arrays constructed from waveguide type elements generally require a 90 degree rotationally symmetric waveguide cross sectional geometry that can support single-mode propagation over the desired bandwidth. This dissertation presents a novel method of obtaining bandwidth enhancement of a square waveguide using both dielectric loading and mode filters that retains the 90 degree rotational symmetry. By placing two orthogonal dielectric slabs transverse to the guide, one obtains what is referred to as the crossed-septum waveguide (CSW). The bandwidth enhancement of the square waveguide is achieved by exploiting the modal symmetry properties of the electric field about a given axis within the guide. The objective is to increase the modal separation between the TE_{10} (or TE_{01}) mode having even/odd (or odd/even) symmetry and TE_{20} mode having odd/odd symmetry in the guide. The TE_{11} and TM_{11} modes having even/even symmetry are forced to attenuate rapidly by the use of mode filters.

An analysis of the CSW is performed using the mode matching technique to determine the electromagnetic fields, phase constants and modal cutoff frequencies. A numerical study of the modal cutoff frequencies as a function of septum thickness and dielectric constant is performed. The TE_{20} mode is found to split into two distinctly different modes upon the introduction of the dielectric septum and are referred to as the

'U'-upper and 'L'-lower modes. The analysis shows that one can obtain increased cutoff frequency separation between the TE_{10} and TE_{20L} modes, however the TM_{12} mode may limit bandwidth performance. A process for designing and experimentally verifying a mode filter for supporting the dual polarization requirement is described. The mode filter consisting of a thin conductive film is demonstrated using the resonant cavity technique, and is experimentally shown to suppress unwanted TM_{11} and TE_{11} higher-order mode resonances.

A general case multi-mode radiation analysis is used to identify dominant mode and higher-order mode far-field radiation characteristics. Co- and cross-polarization measurements are performed and show that energy can be largely confined to dominant mode. Under these conditions, the patterns are reasonably well behaved and degrade gracefully at the high frequencies. The concept is demonstrated over a 2.2:1 bandwidth. A potential application of the CSW is a phased array antenna radiating element that supports dual polarization.

ACKNOWLEDGMENTS

The author would like to express his sincere appreciation to Dr. Warren L. Stutzman for his immeasurable contributions to my personal and professional growth. He has remained a constant source of guidance and inspiration throughout this endeavor. Dr. H. Wade Swinford's keen insight and sound judgment were pivotal in both the Fellowship and the research. Many thanks are also given to Dr. William Davis for his helpful advise and for the use of the measurement equipment in the radio laboratory at Virginia Tech. The author is grateful for the many thoughtful comments and suggestions from all of the graduate committee members including Dr. Tim Pratt, Dr. Gary Brown and Dr. Yuriko Renardy. In their own way, each of the graduate committee members provided the unique and diverse contributions essential to the successful completion this work.

The support and funding of the China Lake Academic Fellowship Office is acknowledged. Mr. Lew Ballanger's support within the Fellowship Committee and the Department at China Lake is also gratefully noted. The author would like to acknowledge Mr. Randall Nealy for his assistance in performing the waveguide and antenna measurements, and also Ms. Katia Estabridis for her help in the acquisition of the waveguide components used in the measurements. Finally, the author wishes to express his appreciation to his family members for their patience and understanding throughout this undertaking.

TABLE OF CONTENTS

APPENDICES:

LIST OF FIGURES

LIST OF TABLES

to my daughter and 'hiking buddy':
April Lynn Purdy

CHAPTER 1

INTRODUCTION

1.1 Overview of the Dissertation

This report describes research in support of the program to develop a broadband, high power, multi-polarization phased array antenna. The development of a *wideband radiating element* for use in a proposed phased array antenna is the focal point of the research. The research is motivated by the need for the Government to develop a broadband multi-functional test 'radar simulator' for use in a generic set of applications. This work was performed during the 1992-1994 time period for the Threat Simulation Department at the Naval Air Warfare Center, Weapons Division, China Lake, California.

1.2 Motivation and Perspective

A 'radar simulator' (also referred to as a 'threat simulator') is a measurement device, used for testing electronic countermeasures (ECM) and electronic counter-countermeasures (ECCM) on a test and evaluation (T&E) range such as that found at the Naval Air Warfare Center, China Lake CA. Figure 1-1 illustrates a radar simulator operating in a typical test environment. A functional description of a radar (threat) simulator can be found in references [1]-[4]. The radar simulator provides an interactive test bed for the ECM/ECCM equipment found on modern military aircraft and simulates a set of conditions from which tactics and the effectiveness of electronic warfare equipment are evaluated.

The phased array antenna is the component of a *radar system* that allows an electronically scanned beam to search a volume of space, locate and track a target, and

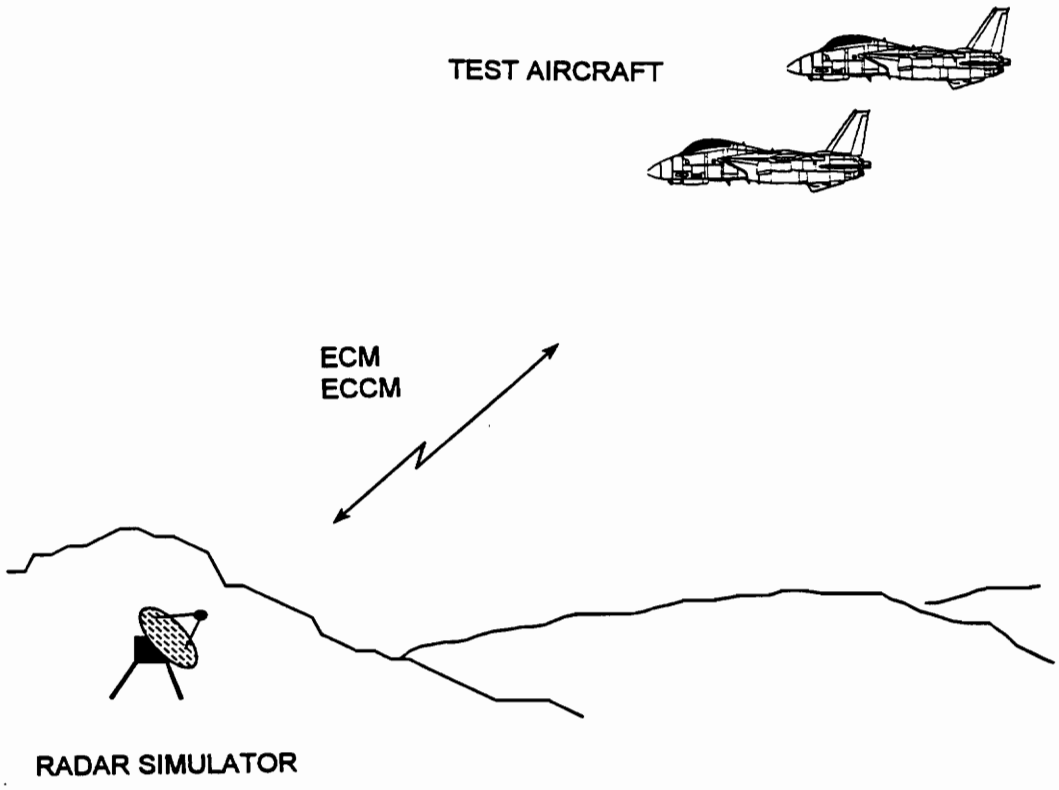

Figure 1-1. Conceptual illustration of a radar 'threat simulator' in a test environment.

guide missiles to engage the target if necessary. A radar simulator is a measurement device that simulates a specific phased array radar system. The radar simulator can therefore be thought of as somewhat of an 'elaborate voltmeter' or measurement device, that is used to measure a set of parameters in a controlled test environment. Therefore, the radar simulator must perform not necessarily as an operational radar, but rather as a test measurement system that simulates important characteristics of a radar system. This provides an additional degree of freedom for the antenna designer for evaluation of the phased array antenna performance tradeoffs.

In past years several specialized phased array radar simulator systems have been built that cost in the tens of millions of dollars. These systems were designed to operate over a relatively narrow frequency band, typically, around 10% or less of the center frequency. A significant portion of the cost incurred in the radar simulator development historically has been due to the fact the systems developed were relatively specialized systems and could only perform a limited set of specialized tasks. Therefore, a cost savings could not be realized by building more than one because a significant part of the cost is due to non recurring engineering (NRE), (e.g., the NRE is not distributed over multiple systems, but applied to only one system).

Approximately 30-50% of the cost in a modern radar simulator development is due to the phased array antenna system. It is believed that if a broadband multi-functional phased array antenna could be developed, it would offer cost savings in two areas. First, manufacturing one antenna that can be reprogrammed and used for several applications or tasks will offer cost savings since reprogramming an existing antenna should be more cost effective than building an entirely new one, including the development, design and manufacture. Secondly, if multiple antennas are manufactured using the same design, it should be possible to distribute the NRE over multiple antennas, thus providing a substantial cost savings.

In order to fully understand the phased array performance drivers which motivate this research, it is useful to provide some illustrative numbers. A set of five basic electrical requirements for a proposed hypothetical phased array is given in Table 1-1. First, the antenna polarization must be programmable, to support various applications which are expected to occur. Circular (right hand or left hand) and linear (vertical or horizontal) are the four basic requirements. Second, the power levels depend on the specific application and could be as high as about 150 kW, and could have up to about 40 % duty cycle.

Third, the goal is to achieve in excess of one octave bandwidth ranging from lower X-band to Ku-band. The frequency of operation is also application dependent and is 'tunable' by reconfiguring the system. The operating frequency is only required to be adjustable over relatively long periods of time (such as hours or days, rather than milliseconds or seconds). The fourth parameter is the beamwidth which is assumed to be adjustable dependent on the specific application. Typical beamwidths range from about 0.75-1.5 degrees adjustable by illumination of the array aperture (see Section 2.2). The fifth desired specification is the need to support electronic scanning angles of up to about 15-30 degrees. Chapter 2 will discuss how each of these parameters defines the radiating element requirements addressed in this study.

Table 1-1.
Proposed Hypothetical Phased Array Performance Specifications and Parameters.

PARAMETER	SPECIFICATION	COMMENTS
polarization	circular or linear	adjustable
power levels	peak up to ~150 kW	up to 40% duty cycle
operational frequency	lower X-band to Ku, more than one octave	narrow instantaneous bandwidth
beamwidth	about 0.75-1.5 degrees	adjustable
scan angles	about ± 30° to ± 15 °	may accept lower scan angles at higher frequencies if necessary

Implicit in each of these requirements is that these are goals and hence not 'written in stone'. The radar simulator is a test measurement device that operates in a controlled environment, and in many cases it could be worthwhile to tradeoff performance for the convenience of having one multi-functional antenna system. Parameters such as efficiency, loss, scan angles and side lobe levels are tradeoff factors, to name a few.

1.3 Summary and Problem Statement

The performance specifications stated in Section 1.2 serve as drivers for the phased array antenna development, and consequently the radiating element development.

For high power ground based phased array radar antenna applications, the waveguide radiating element is the preferred radiator type, due to its good high power capabilities. The waveguide radiating element has the additional advantage of providing a natural transition to a phase shifter, which is also constructed of waveguide for high power applications. The waveguide is used as an interface between a phase shifter and free space, setting up a field distribution at the aperture leading to radiation. The problem addressed in this report is the development and performance assessment of a candidate high power radiating element for a phased-array antenna system that can support the necessary multiple polarization requirements while achieving the bandwidth requirements.

Our approach is to extend the usable single-mode bandwidth of a square waveguide by the use of dielectric slabs strategically placed at locations such that the dual polarization capabilities of the square waveguide are preserved. The dielectric slabs are placed in such a way that certain modal cutoff frequencies can be affected based on the symmetry properties of the modes. Additionally, mode filters are used to attenuate energy in higher-order modes, which could be detrimental to the phased array performance. The problem is viewed in terms of a set of tradeoff considerations, where broadband operation is needed and therefore the objective is to achieve *graceful degradation* at the high frequency end of operation. Each of these considerations is described in more detail in the following chapters, as outlined in Section 1.5.

The novel part of this research is in the theoretical and experimental investigation of a new type of radiating element, referred to as the crossed-septum waveguide (CSW), which contains the dielectric loading (slabs) and mode filters described above. A complete definition of the CSW is provided in Chapter 3, along with a basic discussion on the concept of exploitation of the symmetry properties to enhance the bandwidth and retain dual polarization. The analysis of the CSW is achieved by the use of a mode matching technique to solve for the cutoff frequencies, phase constants, and the electromagnetic fields inside of the waveguide. The mode matching technique is a numerical method useful in solving boundary value problems and is employed because the CSW has a nonseparable geometry, for which a closed form solution is not readily obtainable. The derived models for the CSW are experimentally verified by measurement of the cutoff frequency of the dominant mode and higher-order modes, using the resonant cavity technique. Radiation patterns are computed and compared to those measured for an

experimental CSW radiating element. Implications for the phased array antenna are given based on the measured and computed results.

1.4 Technical Approach

The novel component of this research is the investigation of a new type of radiating element that shows potential as a broadband radiating element candidate. The thrust is to investigate, develop, analyze, characterize and assess the new radiating structure, and determine its usefulness in broadband applications. The flowchart in Figure 1-2 gives a broad overview of the analysis and experimental techniques used to characterize the CSW.

The first step in the research is to consider a hypothetical broadband phased array and relate this into a set of radiating element requirements necessary for the CSW. This is performed in the background discussion portion of this report by reviewing the literature on broadband waveguide type arrays. After defining the CSW and explaining conceptually why it is believed to be a broadband phased array element candidate, a theoretical investigation of a 2-dimensional cross-section of the CSW is performed to determine the modal characteristics.

Following a theoretical investigation, the next step is to experimentally verify the dominant mode and some of the higher-order mode cutoff frequencies for comparison theory. This will demonstrate the validity of the analysis technique, from which the fields and the cutoff frequencies of the higher-order modes are determined. The mode filter investigation is accomplished by experiment to demonstrate the concept and show the bandwidth enhancement can be achieved.

Once the modal characteristics are well understood (by theory and experiment), the radiation properties of an open-ended waveguide consisting of the CSW is investigated. An analysis is performed and experimentally validated by measurements using the Satellite Communications Group's Antenna Lab at Whittemore Hall.

Finally, once the CSW has been characterized both experimentally and theoretically, a discussion of the results is applied to the original phased array problem. Several of the key points including the advantages and disadvantages are given as a practical consideration.

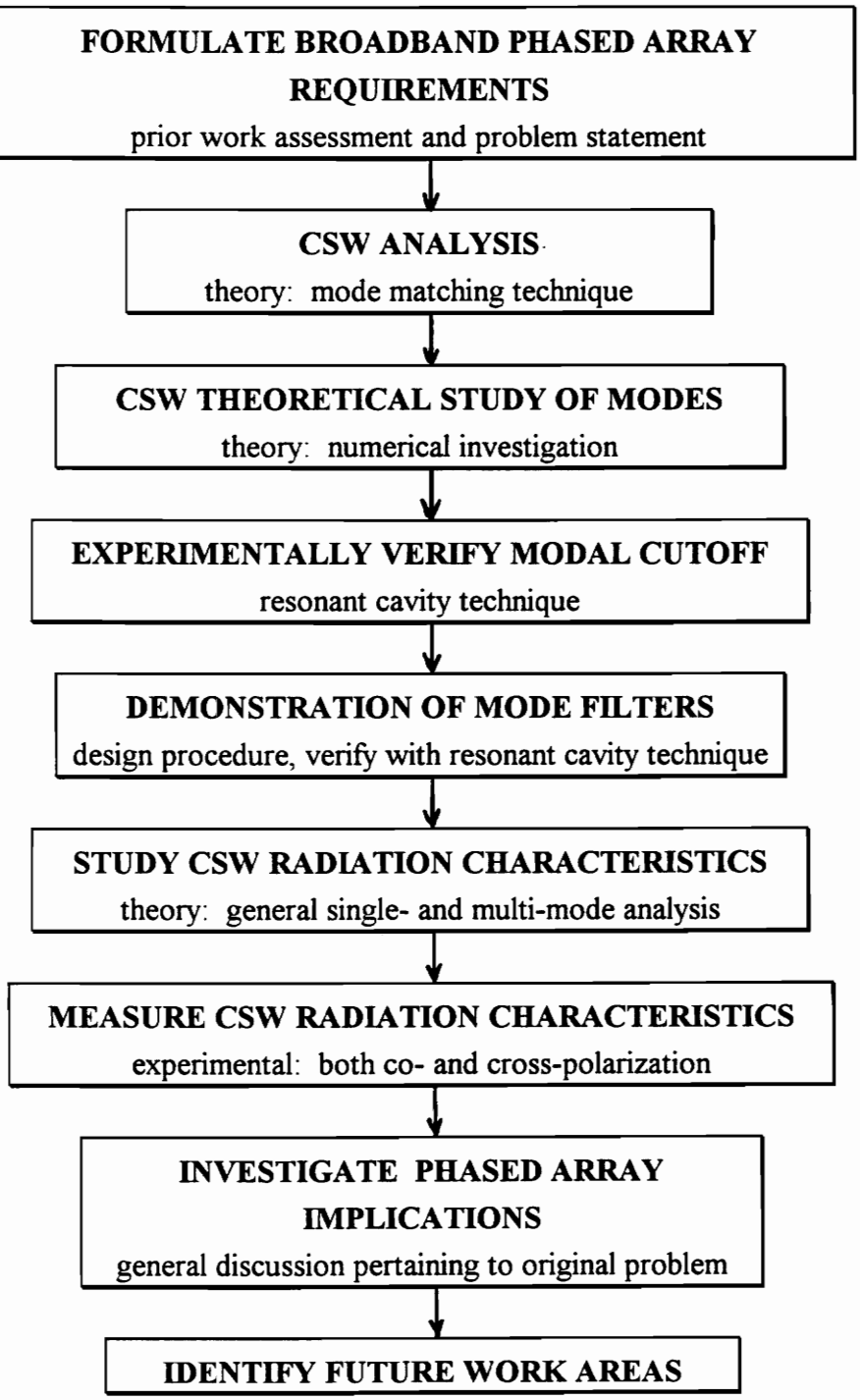

Figure 1-2, CSW assessment technical approach.

1.5 Organization of the Dissertation

Chapter 2 of this dissertation introduces the reader to the topic of phased array antennas and provides a background discussion. A basic space-fed phased array antenna is considered and the basic theory for the system is described. A discussion of array theory and mutual coupling will indicate that the control and containment of energy to the dominant single-mode of propagation is the key driver in a phased array radiating element. From a discussion of background work, the radiating element is one of the key components that must be developed to satisfy the broadband hypothetical phased array requirements. This chapter also provides a discussion of the prior work in the areas of broadband arrays, wideband dielectric loaded waveguide structures, and dielectric loaded antennas.

Chapter 3 defines and discusses the Crossed-Septum Waveguide (CSW), a novel broadband phased array element, which is assessed in this dissertation. A qualitative understanding of how it works is also provided. In Chapter 3, we will define symmetry properties, geometry, and parameters that are varied to obtain bandwidth enhancement. An overview of the field symmetry relationships useful in analyzing the waveguide are also provided.

Chapter 4 continues with the derivation of the system of equations necessary for solving the CSW boundary value problem. The form of solutions in the analysis of the CSW is obtained using the mode matching technique. Chapter 5 applies numerical techniques to solve the system of equations derived in Chapter 4. In Chapter 5 a study of the CSW is performed to investigate the modal characteristics of the CSW. The modal cutoff frequencies, fields and symmetry properties of the fields are investigated, as a function of septum width and dielectric constant.

Results of an experimental investigation with a length of the CSW using the resonant cavity technique is reported in Chapter 6. The experimental investigation used two CSW versions and the results verified the cutoff frequencies of the dominant mode and some of the higher-order modes. The mode filters necessary for the bandwidth extension are described and experimentally demonstrated.

The radiation characteristics of an open-ended CSW are discussed in Chapter 7. The CSW is analyzed using aperture theory techniques, assuming a general multimode

analysis. The multimode analysis is useful in distinguishing the salient features of single-mode and multimode radiation. Both co- and cross-polarization measurements are performed over an octave bandwidth and compared to theory.

Chapter 8 discusses the practical implications of the results derived in this investigation with respect to the phased array application. This report addresses many of the key points necessary to demonstrate the usefulness of the CSW in the phased array application. It does not however answer every conceivable question related to the CSW and the phased array. Several of the key areas identified as future work are given in the Chapter 10. A summary and conclusions are provided in Chapter 9.

1.6 References for Chapter 1

[1] "Electronic Combat Range User's Guide-Volume 1: an Overview," NAWCWPNS TM 7260, Vol. 1, May ,1993.

[2] "Electronic Combat Range User's Guide-Volume 2: ECR Threat Simulator Parameters," NAWCWPNS TM 7260, Vol. 2, May ,1993. (Publication: SECRET-NOFORN)

[3] "Electronic Combat Range User's Guide-Volume 3: Test Data," NAWCWPNS TM 7260, Vol. 3, July ,1993.

[4] D.M.North, "Special Report: China Lake Weapons Center", Aviation Week and Space Technology, pp. 46-87 January 20, 1986.

CHAPTER 2

PROBLEM STATEMENT AND BACKGROUND DISCUSSION

2.1 Overview of Chapter 2

This chapter presents both basic phased array theory and a review of the current state of art in wideband phased array research. Prior to a detailed investigation of the radiating element, it is necessary to discuss some of the important phased array requirements. A hypothetical wideband dual polarized phased array is considered and a basic discussion of the relevant theory is provided. The discussion of phased array theory will enable us to identify key drivers and important aspects from which to launch a theoretical and experimental investigation of the CSW. A review of the pertinent literature and prior work conducted in the area of broadband phased arrays is then provided to assess the current state of art in this area of research. The emphasis is placed on waveguide type radiators and systems, but also included are data on other broadband systems for a relative comparison to the approach addressed in this report.

2.2 Basic Array Descriptions and Definitions

2.2.1 Space-fed Phased Arrays

Consider the hypothetical phased array antenna system shown in Figure 2-1. The antenna system is assumed to be polarization adjustable so that it can be configured to operate in any of the four polarization modes used by radar systems including vertical or horizontal linear, and left- or right-hand circular polarization. Such systems are also referred to as dual polarized or polarization diverse systems. The antenna system

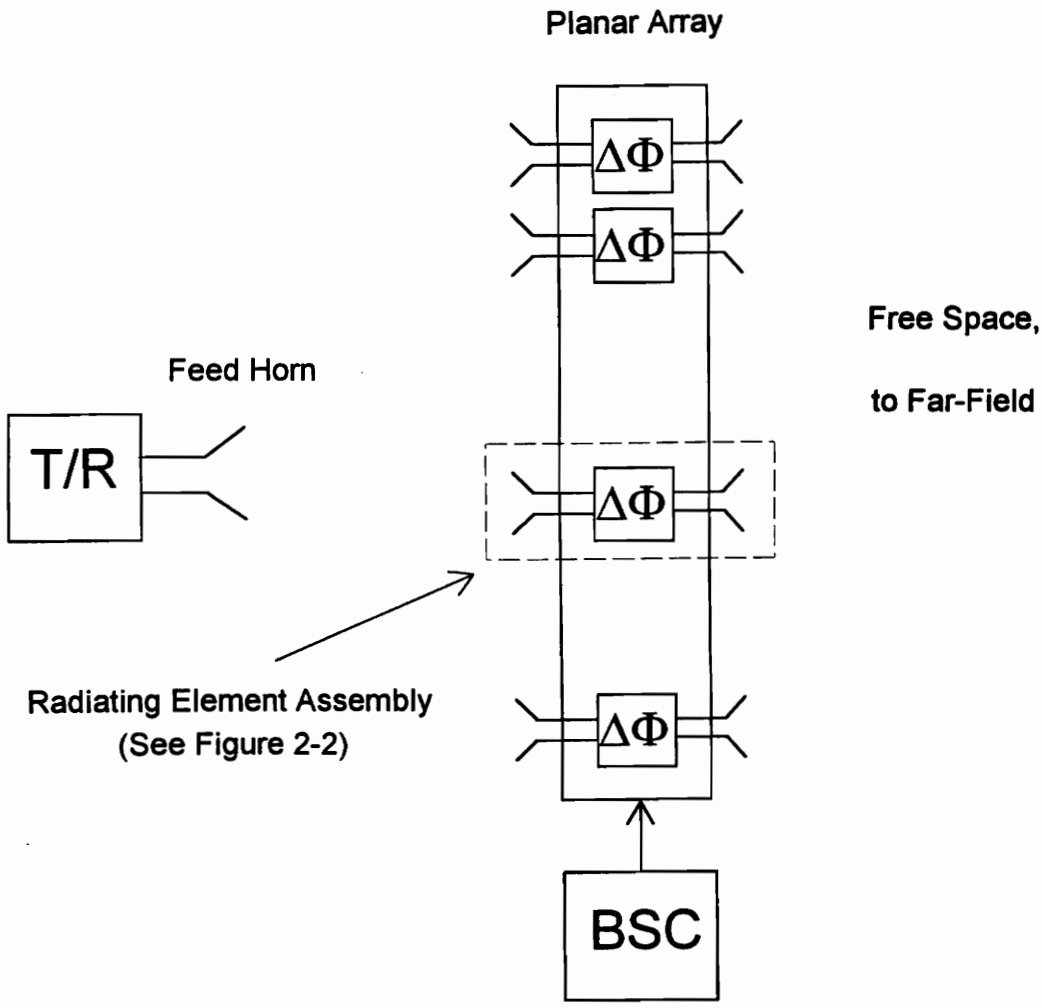

Figure 2-1. Hypothetical space-fed dual-polarized phased array.

consists of a transmitter/receiver (T/R) unit, a feed horn, a beam steering computer (BSC), and a planar array populated with radiating elements. Together, these subsystems comprise what is referred to as a space-fed phased array antenna and radar system [1], [2]. The discussion given below is in terms of the transmit mode, however by reciprocity, a similar discussion also applies to the receive mode.

In the transmit mode the transmitter/receiver unit generates the desired radar signal which is eventually radiated into space. The transmitter as discussed in Chapter 1 is assumed to be capable of generating a relatively high power as would be needed for a radar system. Power levels for the purpose of this discussion can be assumed to be about 150 kW peak power. The practical implications of the assumed power levels are discussed below.

The transmitter is connected to an antenna called the *feed horn*. The feed horn on a search/tracking radar usually consists of a monopulse summing and difference network as described in references [1], [2]. The function of this feed horn is to distribute power to each of the array elements thus forming the space-fed system. The feed horn position is assumed to be movable depending on a particular application. Allowing the feed horn to be longitudinally repositioned permits adjustments in the array amplitude weighting (or illumination taper) which in turn can be used to vary the array's beamwidth for a given phased array application.

The planar array is the main aperture of the antenna and produces the far-field pattern. Since the array receives power (from the left side) and then re-radiates (to the right side), it can be referred to as a *lens array*. Identical radiating elements are assumed to populate the array. Therefore for the array to function over a wide frequency bandwidth, all array elements must also operate over the same range of frequencies. The planar array is populated with what is referred to in Figure 2-1 as multiple phased array radiating element assemblies. A detailed discussion of the radiating element is provided below.

The power handling capacity and the total number of elements needed can be estimated by assuming the hypothetical phased array beamwidth and power requirements given in Chapter 1. The number of elements required for a phased array can be estimated by the simple relationship $HP \approx 60/sN$ where HP is the half power beamwidth in degrees [71], N is the number of array elements in one dimension of the array, and s is the spacing between elements. An illustrative example can be provided by assuming a spacing

of $s = 0.7\lambda_h$, where λ_h is the wavelength at the highest operating frequency for an array operating over one octave bandwidth. At the highest frequency of operation and the largest beamwidth ($HP = 1.5°$) one obtains about 3300 elements illuminated by a maximum peak power of 150 kW, or about 40-50 W per element. Of course, an illumination taper due to the feed horn will distribute more power to the central elements than to the outer elements but we are only concerned with a rough estimate here. At the lowest frequency of operation and the narrowest beamwidth ($HP = 0.75°$) one obtains a total of about 50,000 elements needed in the array[1], and of course the total number of the elements *illuminated* will be determined by the feed horn position. At this time we are less concerned with an exact total number of elements and an exact power handling requirement for the elements, but rather wish to imply the following. The total number of the elements will be in the tens of thousands, and the peak power handling requirements per element is in the tens of Watts.

A detail of the radiating element assembly is shown in Figures 2-2a and 2-2b. As shown, the *radiating element* is the interface between the phase shifter and free space. Conceptually, the radiating element assembly provides a convenient place to view the polarization adjustable characteristics of the proposed array. Obtaining a desired polarization can be achieved by one of at least two methods. The first method is shown in Figure 2-2a and assumes the array lens is transparent, and preserves to some degree, the polarization of the feed horn. Using this approach the feed horn may be used to define or adjust the array system to the desired polarization used in a particular configuration. This implies that both sides of the lens array and the phase shifters must effectively support dual polarization. The second method would employ a switchable polarizer to obtain the desired polarization on the right side of the array as shown in Figure 2-2b. It is believed that one may be able to further develop one of the polarization schemes given in references [3]-[7] to obtain a suitable broadband polarizer; however this effort is left as an area of future work. The advantage of this configuration is that the feed horn, left side of array and phase shifter can all be designed to operate in linear polarization for example. In either case the radiating element discussed in this report provides an interface between the phase shifter (or polarizer) and free space. Due to the power requirements discussed above, the desired approach for a radiating element is the open ended waveguide [2]

[1] It is well known that total number of elements in an array can be reduced using the technique of array thinning. For simplicity array thinning is omitted in this discussion.

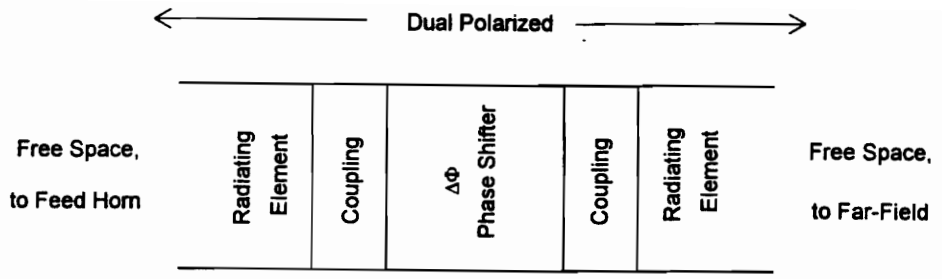

(a)

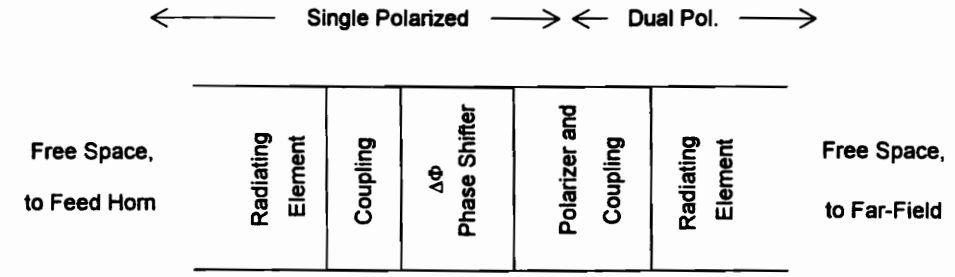

(b)

Figure 2-2. Radiating element assembly. (a) Polarization transparent approach, (b) Polarization switching approach.

since it will support the high power requirements and is relatively easily interfaced to a waveguide-based ferrite phase shifter.

Also shown in Figure 2-2 is the phase shifter and an associated coupling network. The phase shifter is an electronically controllable device that adjusts the desired phase weighting of the radiating elements, in order to rapidly steer the far-field beam to the desired angle. The phase shifter is assumed to be broadband in nature and must operate over the whole frequency range of the array. The power requirements of the phase shifter are dependent on array geometry and transmitter power output and hence are essentially the same as that of the radiating element i.e., tens of Watts. A high power phase shifter that can perform satisfactorily over a frequency range of more than an octave bandwidth is well within the current state of art. Examples of linear polarized ferrite phase shifters satisfying this requirement are provided in references [2], [7], [8], [9]. A detailed analysis of the phase shifter, coupling network, and polarizer is not part of this investigation.

A computer is normally used to compute the differential phase shift for each of the phase shifters to achieve rapid electronic scanning for radar applications. This computer is usually referred to as the Beam Steering Computer (BSC). The BSC must perform calculations and communicate this information rapidly to the phase shifters, to facilitate forming a beam in space at the desired angle. It is further assumed that the BSC is capable of storing and/or computing the necessary phase information (i.e., phase and frequency correction data) as would be needed for the phased array antenna to operate at the desired frequency.

2.2.2 Bandwidth Considerations

2.2.2.1 Bandwidth Definitions

In the literature, one finds two definitions for expressing bandwidth including bandwidth ratio and bandwidth percentage. The bandwidth ratio is defined as the ratio of highest operating frequency, f_H to that of the lowest operating frequency, f_L

$$BW(\text{ratio}) = \frac{f_H}{f_L}:1 \tag{2.1}$$

The other common definition is percentage bandwidth and is given by

$$BW(\%) = 200\% \left[\frac{f_H - f_L}{f_H + f_L} \right] \tag{2.2}$$

where f_H and f_L are the highest and lowest operating frequencies respectively. For convenience, the conversion from percentage bandwidth to ratio is given by

$$BW(\text{ratio}) = \frac{200\% + BW(\%)}{200\% - BW(\%)} \tag{2.3}$$

Unless otherwise specified, this report will refer to the definition given by (2.1) however the reader may use (2.3) to obtain ratio from percentage if so desired. Unless otherwise specified, the bandwidth referred to in this report is tunable bandwidth, and is not necessarily the same as instantaneous bandwidth. Tunable bandwidth is defined as the range of operational frequencies in which the array (and hence radiating elements) must satisfactorily perform, subject to being adjusted or re-configured for another application.

2.2.2.2 Practical Vs. Theoretical Bandwidth

In practice, the entire theoretical bandwidth of waveguide cannot be used. The low frequency limitation of the waveguide radiating element occurs due to the attenuation of the finite conductivity waveguide walls. The reader may refer to [10, p.379] or numerous other texts on waveguide theory for a plot of waveguide loss vs. frequency. As the frequency of operation approaches cutoff, attenuation increases without bound. The commonly accepted values for the lowest frequency of operation are about 5-10% above the cutoff frequency of the dominant or lowest order mode of propagation as a result of the high attenuation. When the radiating element is placed in an array environment, the highest frequency of operation can be limited by a higher-order mode cutoff frequency and lattice spacing as discussed below. Near the cutoff frequency of a higher-order mode the array may experience blindness--a resonance phenomena in which no real power is radiated. The blindness phenomena is discussed in further detail in Section 2.3. In this report, we distinguish between theoretical and practical bandwidth based on these guidelines when necessary.

2.3 Basic Array Theory

2.3.1 Array Factor and Element Spacing

Since the goal of this report is to investigate a potential waveguide type radiating element, emphasis is placed on array theory as it pertains to waveguide type elements. Consider a planar phased array as shown in Figure 2-3, having element spacing d_x and d_y in the x- and y-directions respectively. The periodic element arrangement forms a rectangular lattice. Each of the elements is assumed to have a linearly progressive phase at the m,n^{th} element given by $e^{-jk_o(md_x u_o + nd_y v_o)}$ and an amplitude weighting $|a_{mn}|$. The magnitude of the electric field at a fixed radial distance in the far zone is given by [1]

$$E(\theta,\phi) = K\sum_n \sum_m f_{nm}(\theta,\phi)|a_{nm}|\exp\left\{jk_o\left[md_x(u-u_o)+nd_y(v-v_o)\right]\right\} \tag{2.4}$$

where:

$a_{mn} = |a_{mn}|e^{-jk_o(md_x u_o + nd_y v_o)}$

$u = \sin\theta\cos\phi$

$v = \sin\theta\sin\phi$

$u_o = \sin\theta_o\cos\phi_o$

$v_o = \sin\theta_o\sin\phi_o$

$k_o = 2\pi/\lambda_o$

λ_o = wavelength in free space

K = complex constant

$f_{mn}(\theta,\phi)$= the m,n^{th} element field pattern

θ_o,ϕ_o = beam steer angles.

The element pattern is usually assumed to have a broad beamwidth with a radiation pattern that is relatively constant over the desired scan range. In (2.4) there are an infinite number of maxima generally located at

$$u - u_o = \pm\frac{\lambda_o}{d_x}\cdot p \tag{2.5}$$

and

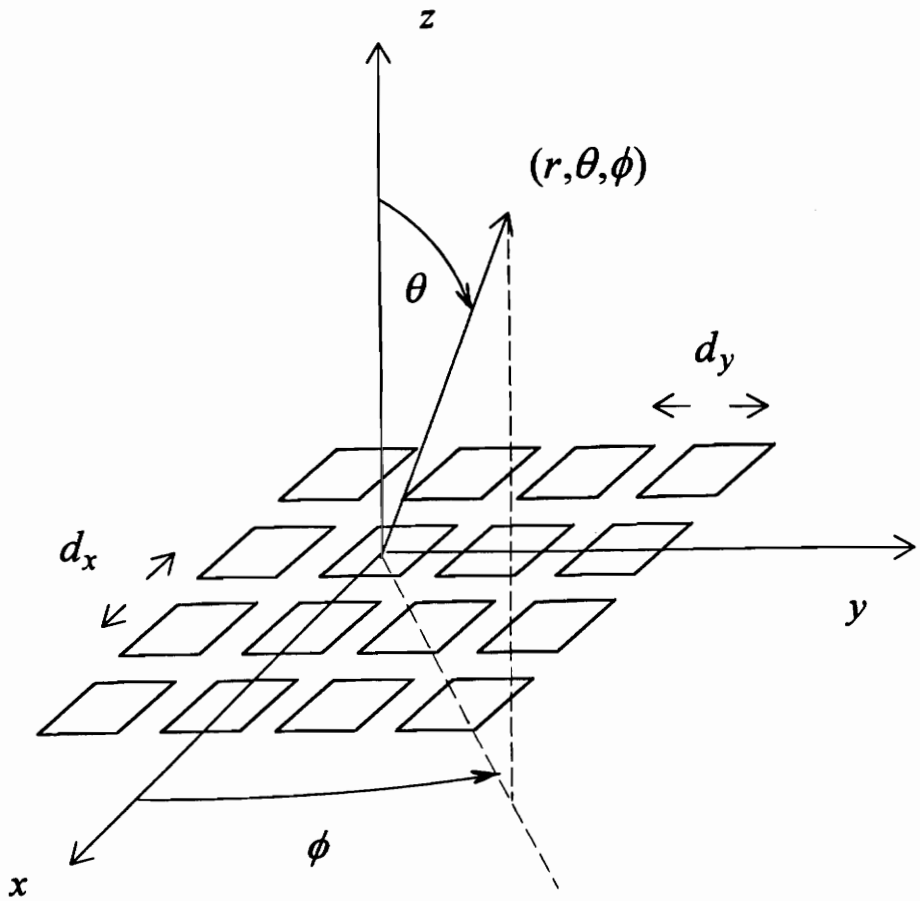

Figure 2-3. Rectangular array lattice of waveguide elements.

$$v - v_o = \pm \frac{\lambda_o}{d_y} \cdot q \tag{2.6}$$

where $p,q = 0,1,2,\ldots$ The maxima in (2.4) are referred to as grating lobes and form an infinite lattice as shown in Figure 2-4. The area inside the unit circle given by $u^2 + v^2 \leq 1$ represents physically radiated energy and is referred to as *real* or *visible space*. The area outside the unit circle is referred to as *imaginary* or *invisible space* since it is not associated with physically radiated energy.

The grating lobe inside the unit circle is referred to as the *main beam*. As shown in Figure 2-4 the main beam (and all grating lobes) and can be moved within the lattice by varying the linear phase progression in a_{mn}. In practice, this is accomplished by electronically adjusting the phase shifters for a given beam steer angle (θ_o, ϕ_o). Since one normally desires to scan a single beam in real space, the objective in designing the phased array is to space the elements sufficiently close so that the only one grating lobe exists within the unit circle for a given scan range. For a phased array radiating element to operate over a wide range of frequencies, the element's physical dimensions must be sufficiently small so that it can fit within the array lattice, at the highest frequency of operation, while placing the grating lobes outside real space[2]. Therefore, for no grating lobes in real space, at the highest frequency of operation one has a maximum element spacing given by [1]

$$\frac{d_{\max}}{\lambda_h} < \frac{1}{1 + \sin\left|\theta_{\max}\right|} \tag{2.7}$$

where λ_h is the wavelength at the highest frequency of operation, and $d_{\max}$ is the element spacing d_x or d_y, corresponding to the maximum scan angle $\theta_{\max}$ in the *x-z* or *y-z* planes respectively. The above discussion is relevant only for a simplified array analysis where interaction among elements is neglected. To accurately describe a phased array element performance, one must treat the array surface as a boundary value problem as discussed in the next section. The minimum dimensions for array element spacing given in (2.7) are

[2] For this illustrative discussion, we are assuming no grating lobes in real space, and a rectangular array lattice. A triangular array lattice is well known to allow increased element spacing and hence reduce the total number of elements needed.

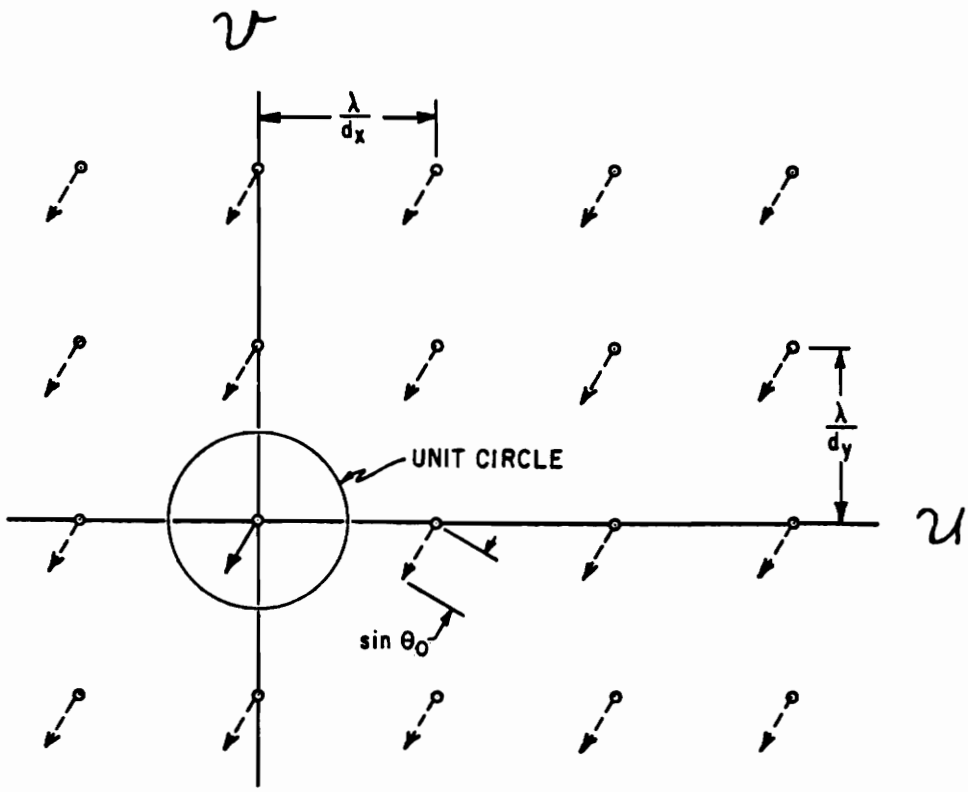

Figure 2-4. Grating lobe lattice for a rectangular array element lattice. The dots indicate grating lobe position for zero scan angle. The arrows indicate grating lobe movement as the array is scanned. Reprinted from [2].

necessary but in some cases are not sufficient conditions for minimal element spacing and size as will be discussed in the following section.

2.3.2 Mutual Coupling Considerations

A well known phenomena between two or more radiating elements in an array is the electromagnetic coupling of energy from one element to another. This phenomena is referred to as *mutual coupling* and imposes requirements on a phased array radiating element that are in some cases more stringent than that of an isolated radiator. Mutual coupling can alter the input impedance of a radiating element when placed in an array lattice compared to the impedance of the same element in an isolated environment. Generally speaking, the closer the elements are placed to each other, the greater the coupling. Therefore, in the rigorous design of an array one must treat the array as a boundary value problem.

A condition referred to as *scan blindness* can occur due to mutual coupling. In the literature blindness has also been referred to as the surface wave effect, surface wave resonance, element pattern nulls and blind spots. Blindness in a phased array antenna occurs when the array main beam is scanned to some angle, and the reflection coefficient seen by each of the array elements approaches unity. Array blindness causes two severe problems. First, when scanned to the blind spot no energy is radiated into the far-field and hence a radar system cannot "see" a target at that angle. Second, during the transmit mode all power incident the elements from a transmitter source will be reflected back into the source, possibly causing damage to the transmitter. The blindness phenomena has been reported extensively in the literature for large arrays with various element types including waveguides [11], printed dipole arrays [12], flared notches [13] and slot arrays [14]. The discussion here is primarily concerning waveguide type arrays, however blindness is a consideration generally for scanning arrays of most element types. Figure 2-5 shows experimental results of a planar array with sizes of 7×7, 13×13 and 19×19 elements. In the pattern measurements shown, the arrays are configured with the center element connected to a source and all other elements terminated to a matching resistance. The patterns show that as the number of elements is increased, a null in the pattern appears at about $\pm 26°$, just inside the grating lobe angle of $29.1°$. If all elements were connected to a transmitter source and appropriately phased (instead of terminated); then

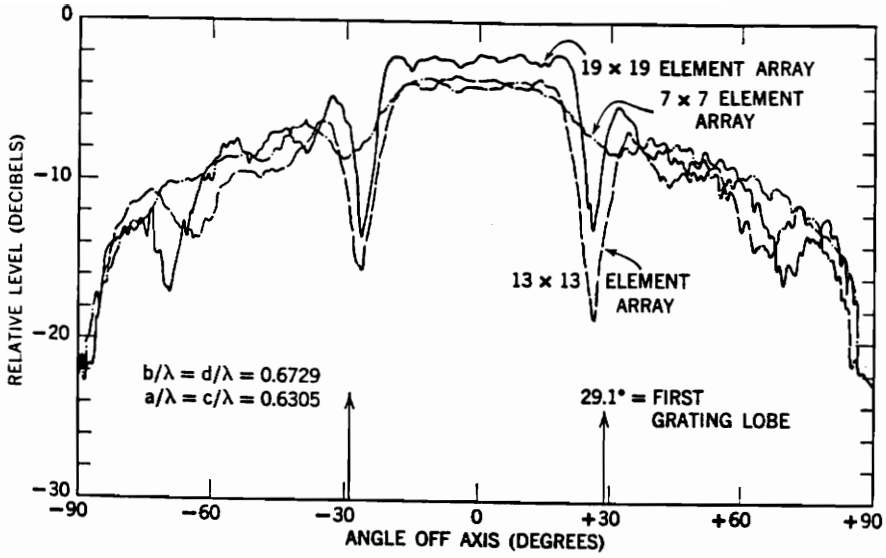

Figure 2-5. E-plane patterns of various sized arrays with the central element excited and all others terminated. Reprinted from [11].

by superposition the phased array would experience blindness when scanned to the nulls indicated by the single element excitation patterns [15].

For large arrays (about 1000 or more elements) one may assume an infinitely large array where all elements have identical coupling effects, and the edge effects of the finite array are neglected. For the infinite array model, one assumes that all elements are identical and have a uniform amplitude excitation with a linear phase progression across the array aperture. Edelberg and Oliner [16] in 1960 presented an early approach to model the effect of mutual coupling of a phased array during scanning. Their approach was to assume an infinitely large array and divide the region above the array surface into spatial periods referred to as unit cells as shown in Figure 2-6. The unit cell is assumed to support a TEM wave in the direction of the scan angle of the main beam, plus an infinite series of TE and TM modes. Each unit cell is assumed to be fed by a slot supporting only the TE_{10} mode. Scanning of the main beam is modeled by introducing a phase shift between successive unit cells. Using this approach, an expression is obtained for the admittance seen by the slot feeding the array in the form of an infinite series. This series is referred to as the grating lobe series [17], [18]. Since the grating lobe series is obtained assuming that only the TE_{10} mode is present in the slot, it is referred to as single-mode mutual coupling theory. In the examples of scanned arrays in the literature, as will be shown below for comparison, the grating lobe series can provide a good approximation of element admittance. However, singularities (and a reflection coefficient of unity) in the grating lobe series can occur as grating lobes enter real space therefore erroneously indicating a blind spot. This prediction of a blindness was found to be incomplete due to the formulation lacking inclusion of higher-order modes in the waveguide element. This point is discussed further below.

The work of Farrell and Kuhn [19] was the first rigorous analytical work that was able to accurately predict and explain blindness for arrays of waveguide elements. The mode matching technique was employed to analyze an infinite array of rectangular waveguide array elements. In their approach, the fields in the external region (above the $z>0$ plane) are expanded in a Floquet series [20] and the fields in the internal region (below the $z<0$ plane) are also expanded in a series of waveguide solutions including both the dominant (propagating) and higher-order evanescent (non-propagating) modes. They showed that the inclusion of higher-order modes to the solution of the boundary value problem was in certain cases essential to the accurate prediction of the blindness

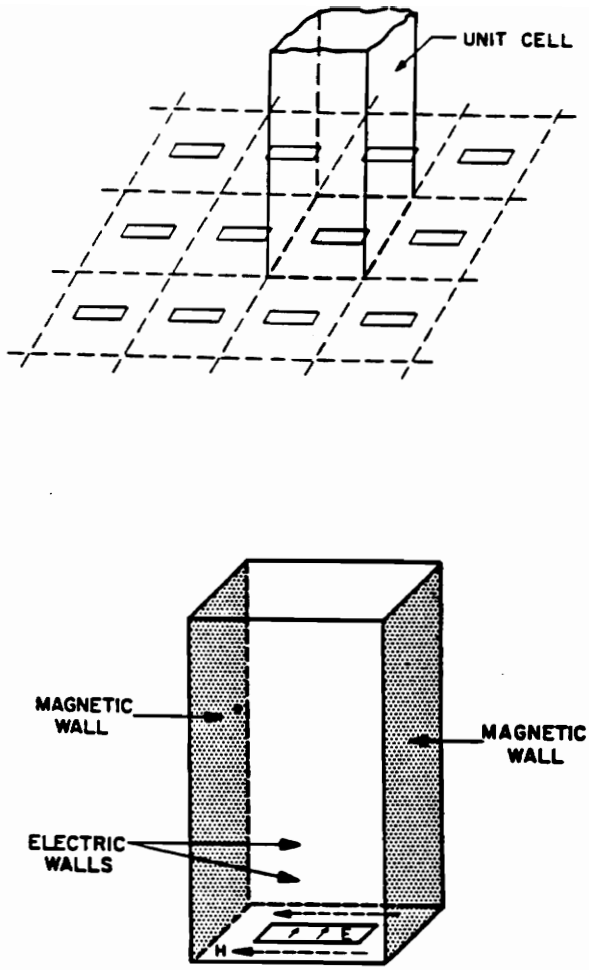

Figure 2-6. Unit cell for an array of slots with a rectangular element lattice. Reprinted from [16].

phenomena. Shown in Figure 2-7 is an element pattern for a 95-element array, for comparison to modal theory and the grating lobe series. As shown, there is excellent agreement between theory and experiment. Also, the singularity obtained from the grating lobe series fails to predict the blind spot whereas the modal theory indicates a null in the vicinity of the experimental null. Using this multiple mode analysis technique, the null is actually found to be caused by a zero in the conductance of the waveguide admittance, rather than the admittance singularity obtained using the grating lobe series.

Other researchers [21], [22], [23], [14] have also performed rigorous analysis on infinite waveguide phased arrays in which the effects of higher-order waveguide modes are included. The method used by Diamond [21] is based on the principle that the electric field and the aperture are related and can be obtained from each other and expressed in a series of coefficients. The formulation using this method, one equates the complex power radiated by an element to the complex power present in the waveguide opening to solve for the coefficients. In this manner the driving point admittance of the waveguide in the array are determined also showing pattern nulls dependent on higher-order modes. The approach taken by Borgiotti [22] also includes the expansion of the half space above the array into a Floquet series and the region below into a series of waveguide modes. Galerkin's method is employed in this approach to solve the array boundary value problem. The results for a rectangular waveguide covered with a dielectric sheet are shown in Figures 2-8 indicate the inclusion of the higher-order waveguide modes are in some cases necessary to accurate predict the blind spots. Amitay and Galindo [23] have analyzed an infinite array of circular waveguide elements. The analysis was performed to allow both orthogonal linear polarizations and the results indicate a strong dependence on higher-order mode excitation, scan angle and polarization. In Stark's review paper [14] he has also included original work on solving the array boundary value problem and investigating mutual coupling. He considers an infinite array of slot type waveguide elements, and employs Galerkin's method in obtaining results that confirm the relationship between blindness and higher-order modes in waveguide type elements.

A graphical method of determining bounds for blind spots is given by Knittel [24] that provides insight to the blindness problem in terms of higher-order mode cutoff frequency relationships. The method uses a set of normalized curves on the $k-\beta$ diagram as shown in Figure 2-9, which also includes the array geometry. The vertical axis represents varying frequency, with $k_o = 2\pi/\lambda_o$ where λ_o is the free space wavelength.

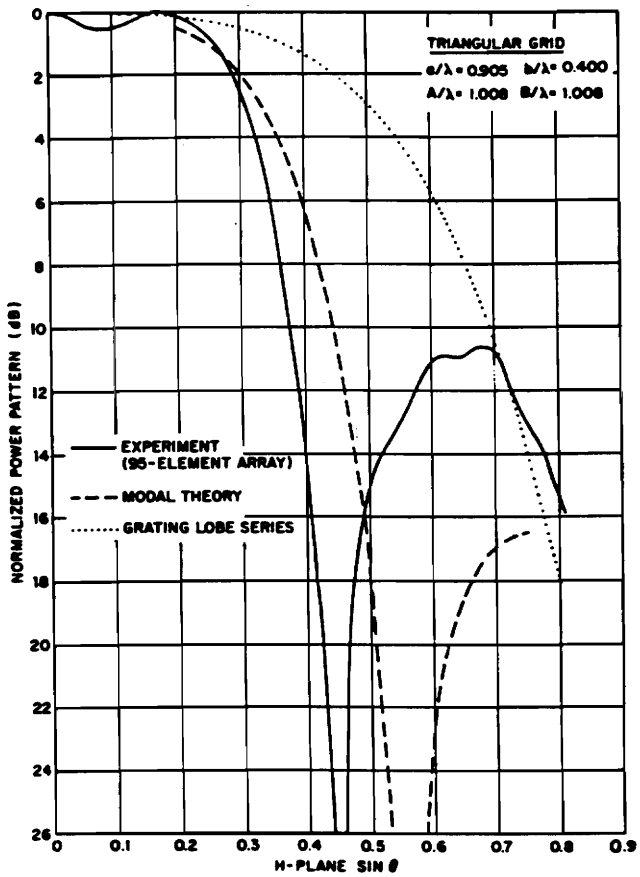

Figure 2-7. Comparison of theory and experiment, using both single-mode (grating lobe series) and multi-mode analysis. Reprinted from [19].

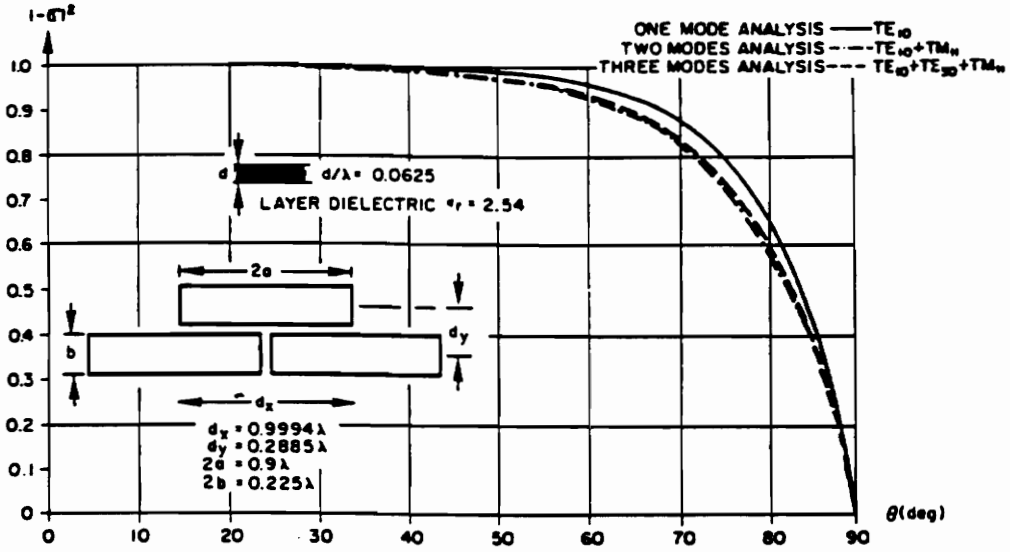

(a)

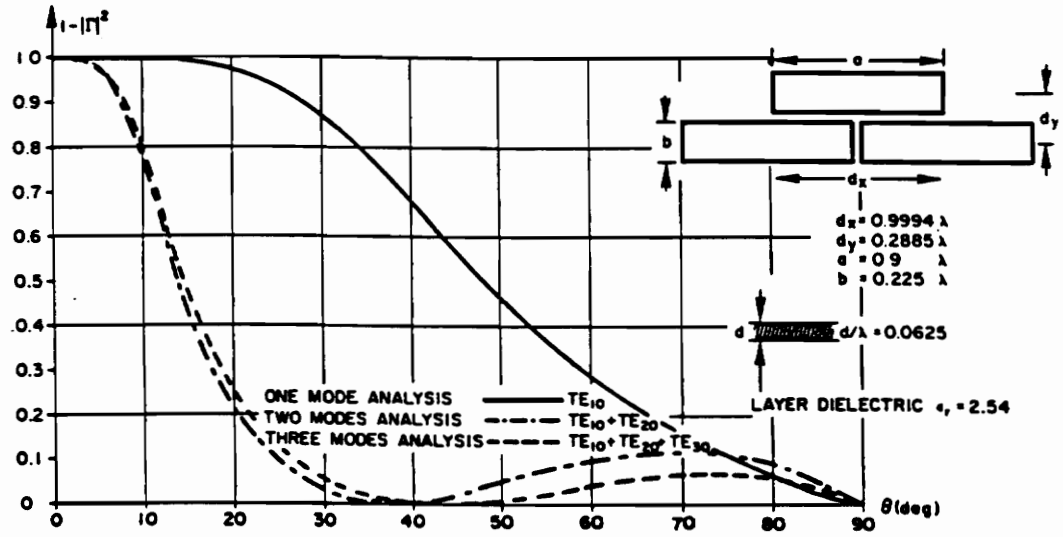

(b)

Figure 2-8. Mutual coupling effects of higher-order modes. Shown is an infinite array of rectangular elements with dielectric layer over the array.
(a) E-plane scan. (b) H-plane scan. Reprinted from [22].

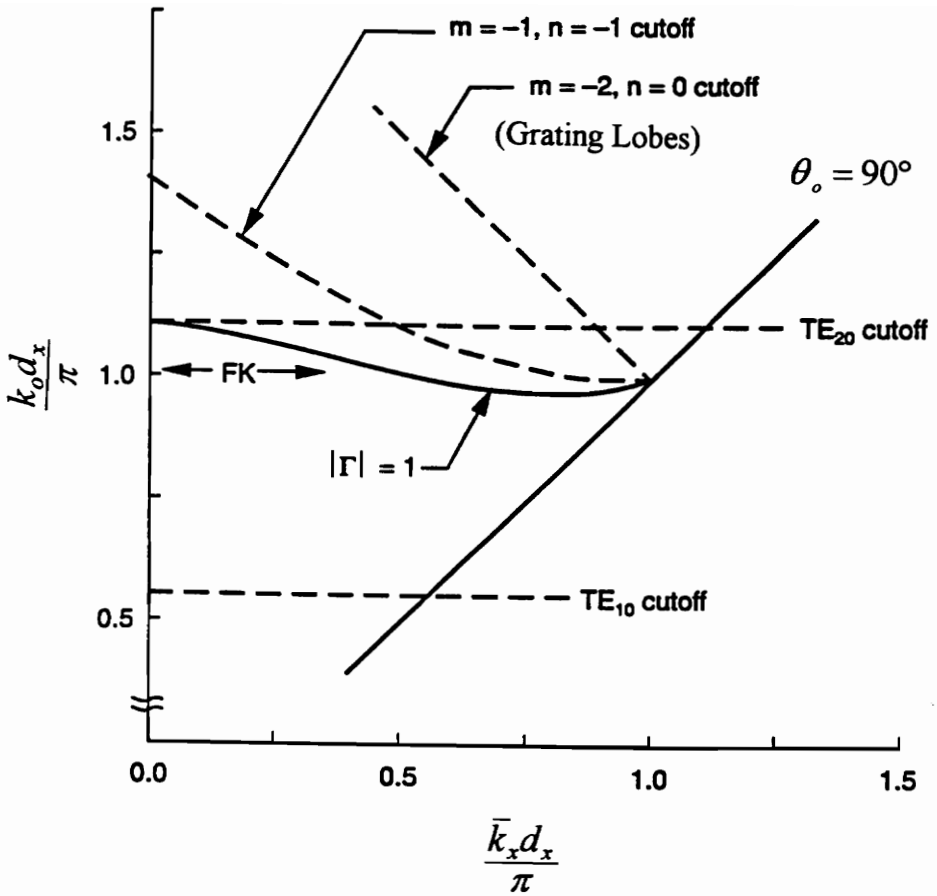

$$\bar{k}_x = k_o \sin\theta_o$$

Figure 2-9. Knittel's graphical method for bounding array blindness, based on higher order modes and grating lobe loci. The curve labeled $|\Gamma| = 1$ shows array blindness and is bounded by the higher order mode and the grating lobe. Reprinted from [70].

The horizontal axis and corresponding horizontal lines represent constant frequency with varying scan angle, where $\bar{k}_x = k_o \sin\theta_o$ in these figures. The diagonal line on the plot indicates a constant scan angle and the region above the $\theta_o = 90°$ represents visible space. The dashed horizontal lines on the figure represent the cutoff frequency of the given modes in the waveguide. Dashed diagonal line and curve indicates the loci of the grating lobe series singularities (i.e., scan angles for appearance of grating lobes in real space) for a given array geometry. The solid curve labeled "FK" indicates the loci of the blind spots, which have been computed using the dimensions, geometry and analysis technique for the Farrell and Kuhn method [19] discussed above. The figure illustrates that blindness is a high frequency limitation and that it is bounded by the higher mode cutoff frequency and the grating lobe singularity loci. Therefore, one has a graphical technique for providing bounds on the blindness phenomena based on the presence of higher-order modes in the waveguide and the array lattice.

There have also been several studies conducted on the mutual coupling in waveguide array elements that support multiple higher-order modes [25], [26], [27], [28]. Tang and Wong [26] and Wong *et al.* [25], have discussed the use of intentionally excited higher-order modes in a waveguide phased array elements. In [26] it was demonstated that excitation of the dominant mode and the next higher-order mode can be used to improve the match for wide scan angles. In [25] H-plane scan nulls were observed for an array of rectangular elements without appropriate matching. However, using the multimode technique the waveguide was dielectrically loaded and excited using the TE_{10}, TE_{20} and the TE_{30} modes and it was observed that the null was eliminated and matching improved considerably. Another multimode study was conducted by Constantini and Knittel [28] in which they considered excitation of the TE_{10} and TE_{30} modes to improve matching in a rectangular waveguide. They showed that one could improve the match over a scan range however nulls may also be observed if the higher-order modes are excited properly. Yet another approach is described by Mailloux and Steyskal [27] on a multimode method performing at two frequency bands separated by an octave. The radiating element consists of a rectangular waveguide with multiple dielectric slab inserts. At the low frequency band of operation only the TE_{10} mode propagates and the next higher-order mode that can contribute to blindness is the TE_{20} mode. However at the high frequency band, both the TE_{10} and the TE_{20} contain propagating energy and the next higher-order mode that can contribute to blindness is the TE_{30} mode. The multimode

examples given above demonstrate that as one extends beyond the first higher-order mode and associated blind spot, a suitable match can be obtained over an extended frequency that is bounded by the next higher mode.

A conceptual understanding of the mutual coupling phenomena and the associated array scan blindness can be formed from the body of previous work in the area of phased array antennas. The blindness phenomena can be conceptually viewed as shown in Figure 2-10, [29]. If an appreciable amount of energy is permitted to couple into a higher-order mode, even if the frequency is below the cutoff of the corresponding mode, then there may exist a scan angle for which the dominant mode and the higher-order mode can cancel, and the array radiates no energy. This, as stated before, is equivalent to the reflection coefficient being unity and the blindness occurs at this angle. This blindness is the result of the boundary conditions on the surface of the array and occurs due to a higher-order mode resonance, as a function of scan angle.

In summary, the most important aspects of blindness as it pertains to the problem at hand are:

- Blindness is an upper frequency limitation due to a higher-order mode resonance.
- A graphical technique presented in Figure 2-9 bounds blindness by the next higher-order cutoff frequency and the grating lobe loci.
- Prior work [25]-[28] has demonstrated that a phased array can also be matched over some set of scan angles above the first higher-order mode of operation. Under this condition the next blindness can be bounded by the next higher-order mode cutoff.

2.4 Summary of Radiating Element Requirements

In Chapter 1, a set of goals necessary for a hypothetical wideband phased array were discussed. Considering these array requirements and the cumulative discussion of the theory in Sections 2.2 and 2.3, one can outline a set of goals necessary for a broadband phased array radiating element. These element performance goals therefore represent a perspective from which the CSW will be evaluated both theoretically and experimentally in the following Chapters.

- The radiating element must operate over the desired frequency range. The energy must be confined mostly to a single-mode of propagation, i.e., the dominant mode. The

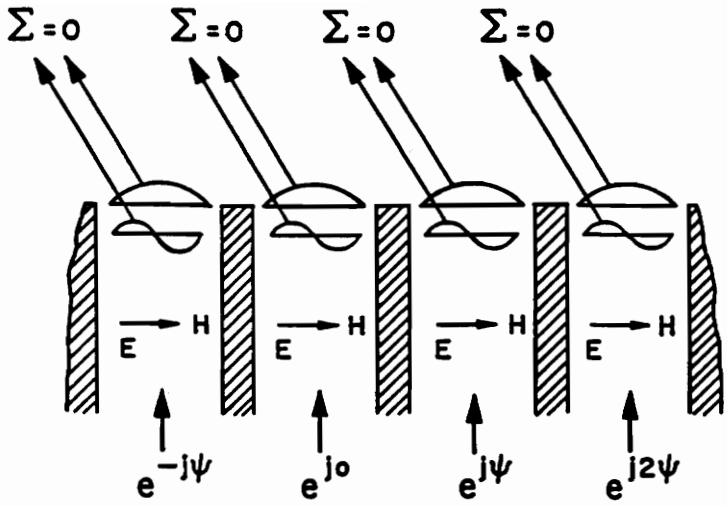

Figure 2-10. Conceptual illustration of array blindness. The radiation from a dominant and higher-order mode sum to zero creating a blind spot at some scan angle in the far-field. Reprinted from [29].

usable bandwidth is defined in terms of the single-mode bandwidth of the waveguide. The single-mode bandwidth is a factor in determining the usable bandwidth in which the array can be scanned while avoiding blindness in the far-field pattern due to mutual coupling, as was discussed in Section 2.2.

- An element that can support both vertical and horizontal (linear) polarization is necessary since it will support dual polarization. To facilitate dual polarization, the element must possess 90 degree rotational symmetry. Cross sectional geometries such as a circle and square are examples of elements with 90 degree rotational symmetry. The CSW as defined in Chapter 3 is a square waveguide loaded with a dielectric insert such that is preserves the 90 degree rotational symmetry. The mode filtering scheme discussed in Chapters 3 and 6 must also preserve the 90 degree rotational symmetry.
- An alternative approach mentioned in Section 2.5 to achieve the arbitrary polarization is by use of two linear polarized orthogonal elements placed in the array. This however is not desirable since it requires doubling the number of elements when compared to the single radiating element approach. We approach this problem under the premise that a single element is a requirement.
- The radiating element must meet certain physical size restrictions in order to fit in the array lattice. The size restrictions are governed by the scan and frequency characteristics of the array. The mutual coupling and blindness phenomena may necessitate further size reduction in excess of that required by the grating lobe lattice requirements.
- A typical phased array radar system may have transmitter powers up to about 150 kW peak power. This translates to a 'typical' requirement of up to approximately 40-50 W peak power per radiating element for this application. A waveguide type radiating element is ideally suited for this application at X and Ku band frequencies and therefore the subject of this investigation. The CSW investigated in this report is constructed from a waveguide and hence a suitable candidate.

2.5 Discussion of Prior Work

In this section we discuss prior work as it pertains to the research conducted in Chapters 4 through 7 of this report. In order to demonstrate the originality of the work presented, we must consider several key aspects of the prior work in the literature. A discussion of previously investigated waveguide cross-section geometries is given, followed by discussion of bandwidth enhancement of waveguides using dielectric loading. A discussion of other phased array methods which are of interest for comparative reasons is also provided. These other methods include wideband solid state distributive arrays and other alternative beam scanning methods. Finally, a review of dielectric loaded waveguide apertures is given for comparison to the novel approach given in this report.

2.5.1 Waveguide Cross-Sectional Geometries

A summary of each of the waveguide element cross sections for which there has been bandwidth related research is shown in Figure 2-11. Each of these support dual polarization and have been investigated in various forms as is discussed below.

One of the most obvious waveguide cross-sectional geometric shapes that has 90 degree rotational symmetry is the square waveguide shown in Figure 2-11a. The single-mode bandwidth of a square waveguide is 1.414:1(34.3%) and is determined by the TE_{10} and TE_{11} / TM_{11} mode cutoff frequencies. Tsandouglas and Knittel [30] investigated a dual-polarized array of square waveguide elements. The square waveguides were matched by introducing multiple transverse dielectric layers within the waveguide, and also by adding dielectric slabs layers external to the waveguide on the array surface. Studies were performed on two designs with bandwidths of 20% and 25%. A 267-element array was constructed to demonstrate performance for multiple polarizations.

Another waveguide type element that uses a square geometry is described by Bryant [31], who employs an electrically short ($\approx \lambda / 10$) piece of square waveguide operating below the dominant mode cutoff frequency and an aperture loaded with a thin dielectric plug shown in Figure 2-12. The waveguide is excited by a pair of orthogonal coaxial fed probes which can provide the desired polarization by proper phase and amplitude adjustments of the applied signal. The concept of using a short section of cutoff waveguide was developed by Wheeler [32], [33] and is reported to improve the

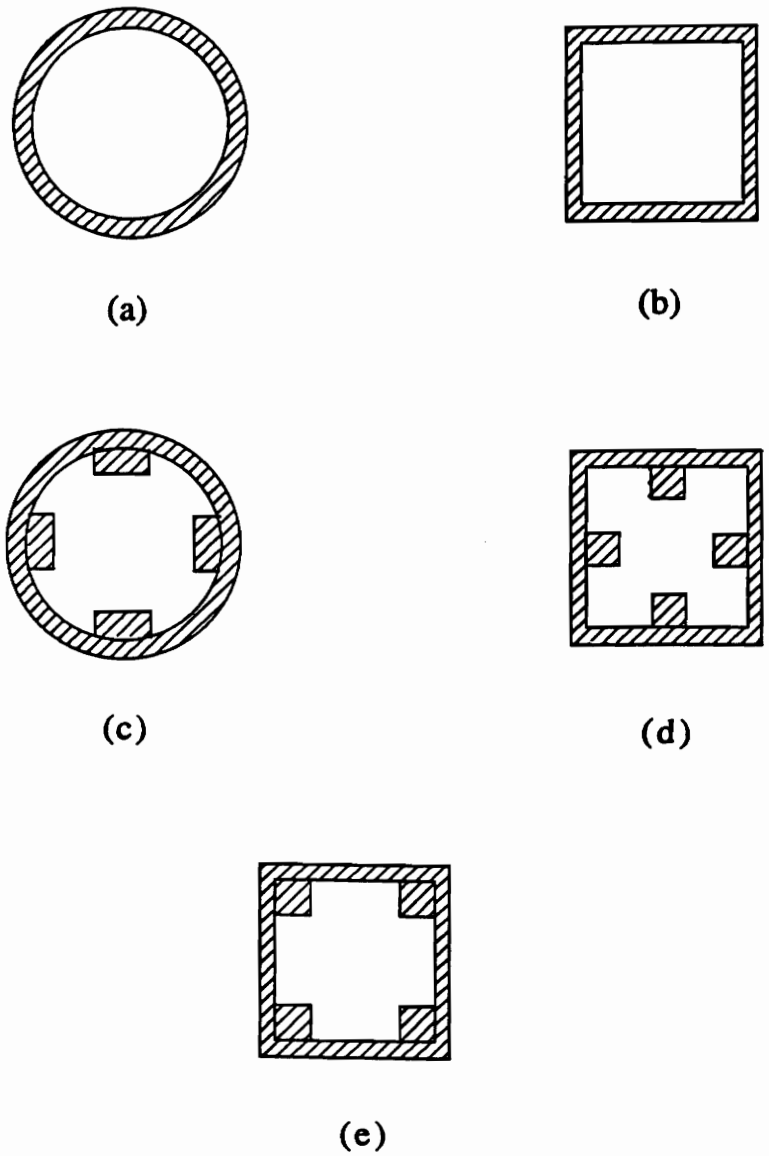

Figure 2-11. Cross-sectional views of waveguide elements that support dual polarization. (a) Circular. (b) Square. (c) Ridge loaded circular. (d) Ridge loaded square. (e) Crossed.

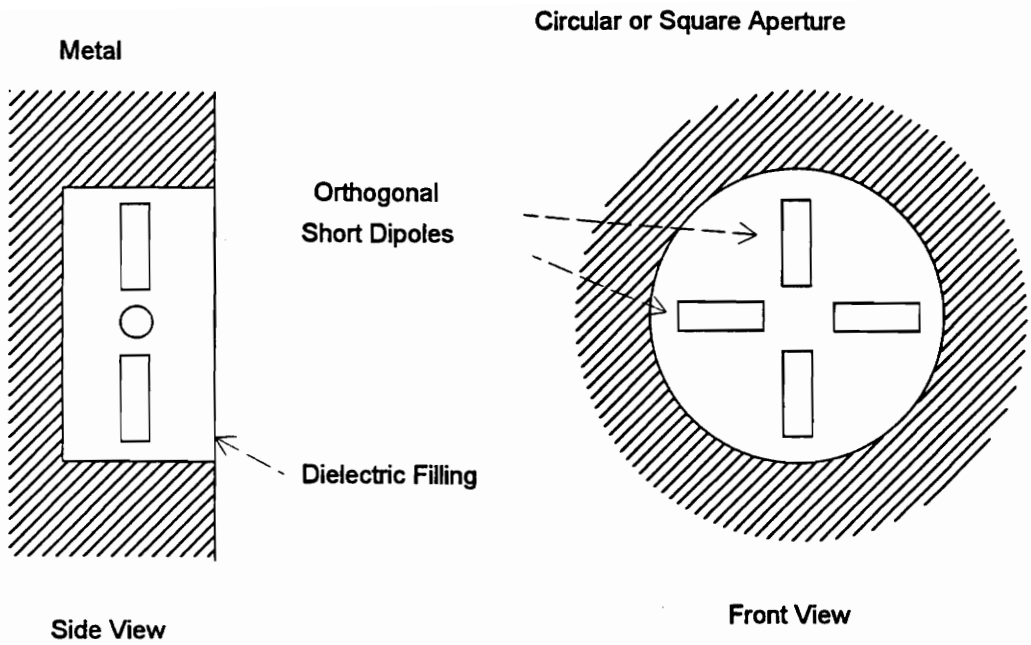

Figure 2-12. Conceptual illustration of the Wheeler element. The aperture consists of a short piece of waveguide ($\sim \lambda / 10$) operated below cutoff frequency. After [32],[33].

impedance match. The reported array bandwidth using this element was found to be 20% for which a suitable match was achieved. A similar approach also employing a short section of cutoff square waveguide was used by Foti and Shelley [34], who demonstrated a 2.08:1 (71%) bandwidth in an array scanning to $\pm 60°$. This is an impressive array element performance in terms of bandwidth. It is uncertain to the author as to how one would interface Foti's element to a waveguide for high power use.

The circular waveguide shown in Figure 2-11b is also candidate for dual polarized arrays since it also satisfies the symmetry requirements for dual polarization. The bandwidth of an unloaded circular waveguide is the determined by the TE_{11} and TM_{10} mode cutoff frequencies and is found to be 1.3062:1(26.5%). Therefore, an unloaded circular waveguide offers less bandwidth than the square waveguide discussed above. An analysis of an infinite array of circular waveguides is found in [11] and [23] in which they reported obtaining bandwidths of 15% with well matched performance. Chen [35] discusses a design approach for an array of circular waveguide elements loaded with dielectric plugs and covered with a dielectric sheet. He reports obtaining 16% bandwidth and discusses obtaining a suitable impedance match over a $\pm 60°$ scan. Schmier and Buckley [36] reported obtaining a 30% bandwidth over a 30° scan cone using the element geometry shown in Figure 2-13. Their element is referred to as the 'artificial puck wideband element' and uses a coaxial-fed circular waveguide loaded with metallic ridges, discs and a dielectric such that the dual polarization characteristics are maintained. Another variation of the circular waveguide element was developed by Wheeler [32], [33] (see Figure 2-12) and is analogous square element discussed above which uses a short piece of cutoff waveguide. The element was successfully matched in an array with VSWR of less than 2.0 over a bandwidth of 13% for a scan cone of 30°.

The bandwidth enhancement properties achieved by the introduction of one or two metallic ridges normal to the broad wall of a rectangular waveguide are well known [10]. Since single- and dual-ridged waveguides are known to provide multi-octave bandwidth for rectangular waveguides, a logical extension of this work would be to investigate bandwidth enhancement of a square or circular waveguide using ridge loading. In ridge loading a square or circular waveguide, four symmetric ridges must be added to maintain the desired dual polarization characteristics. The first published work on quadruple-ridge loading was reported by Shimizu [37] who experimentally investigated an octave bandwidth circular waveguide feed horn for a reflector antenna. Later work performed by

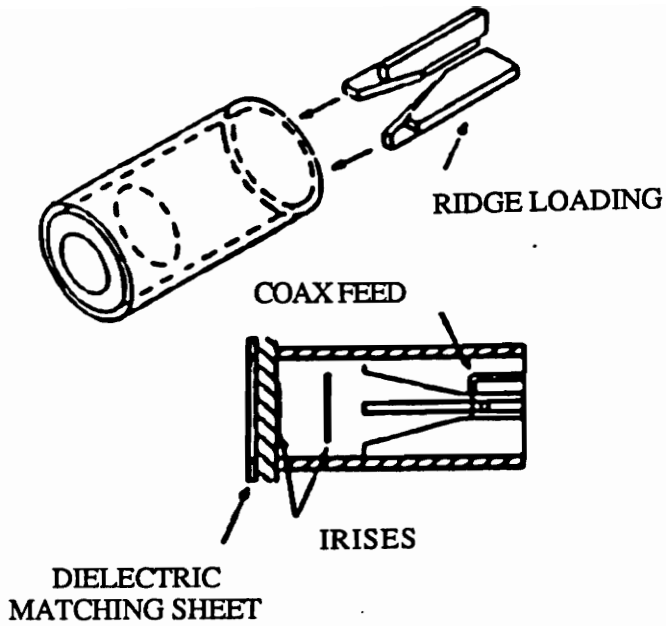

Figure 2-13. Artificial puck wideband radiating element. Reprinted from [36].

M.H. Chen *et al.* [38] focused on a theoretical and experimental investigation of both circular and square quadruple-ridged waveguide shown in Figures 2-11c and 2-11d receptively. Detailed studies were conducted on the modal characteristics and the results showed that as the depth of the ridge inside the square waveguide increases, bandwidth *decreases* which is in contrast to dual-ridge loading of a rectangular waveguide. For the case of quadruple-ridged circular waveguide, bandwidth was found to increase somewhat, but only to about 38%. Therefore, ridge loading of circular waveguides does increase bandwidth, however only to an amount slightly more than that of an unloaded square waveguide.

Several array studies using quadruple-ridged waveguide have been conducted. C.C. Chen [39] has demonstrated array performance of a quadruple-ridged circular waveguide phased array over a bandwidth of 16% and a scan half cone scan angle of 60°. Researchers Robinson *et al.* [40] reported an experimental array that uses the element described by Sokora [41]. This element [41] is quadruple-ridge loaded variant of a square waveguide, in which ridges are extended beyond the waveguide at the radiating end of the guide. The Robinson shows a single element pattern at the low, mid and high frequency over a 3:1 bandwidth. Array pattern measurements are given at the middle frequency; however, no pattern data are given for the array at the high and low operating frequencies. It is not possible to determine from reference [40] whether the array will function without blindness at the highest frequency of operation since these data are not presented.

The cross-shaped waveguide cross-sectional geometry shown in Figure 2-11e was investigated by Stalzer *et al.* [42] as a possible candidate for a broadband element. The finite element solution technique was used to solve for the fields and the cutoff frequencies for the first several modes. Stalzer obtains a maximum theoretical single-mode bandwidth (as a function of dimensions of the guide) of about 38%, which is just slightly larger than the bandwidth of an unloaded square waveguide. It is believed that the quadruple-ridged circular waveguide and the cross-shaped waveguide represent the maximum obtained single-mode bandwidth of about 38% for waveguide cross-sections in the literature that support dual polarization.

A summary of single-mode bandwidths for waveguide cross-sections discussed in this section is provided in Table 2-1. The single-mode bandwidths given in Table 2-1 are the *theoretical* bandwidths, defined by (2.2) and should not be confused with the practical

bandwidth discussed in Section 2.2.2.2. The bandwidths of the dielectric loaded circular and square waveguides also given in the table are discussed in the following section.

Table 2-1.
Theoretical Single-Mode Bandwidth for Various Waveguide Cross-Sectional Geometries.
(The geometries shown support dual polarization.)

Cross-Section	Bandwidth (%)
square	34.3
circular	26.5
quad-ridged circular	38 maximum
quad-ridged square	< 34.3
cross-shaped	38 maximum
dielectric loaded circular	31.8 maximum
dielectric loaded square	< 34.3

2.5.2 Bandwidth Extension: Dielectric Loaded Waveguides

There has been a considerable effort to increase the bandwidth of waveguides through the use of dielectric loading. This section outlines prior work and states the relevance to the overall problem of obtaining a dual polarized broadband phased array element. A summary of the more relevant waveguide cross-sectional geometries is provided in Figure 2-14 and includes both single and dual polarized methods.

Dielectric loading of a rectangular waveguide using E-plane slabs has been investigated by Gardiol [43], Findakly [44], and Halevy *et al.* [45]. The problem was treated for a general number of slabs with arbitrary spacing, however of particular interest is the rectangular waveguide with one centrally located slab in a reduced height waveguide as shown in Figure 2-14a. Bandwidth in excess of two octaves is obtainable by choosing a sufficiently large dielectric constant and a thin slab. This technique of increasing the bandwidth of a rectangular waveguide is analogous to ridge loaded rectangular waveguide as discussed in Section 2.5.1. The example of a dielectrically loaded rectangular waveguide illustrates that bandwidth extension can be achieved, however, unfortunately a

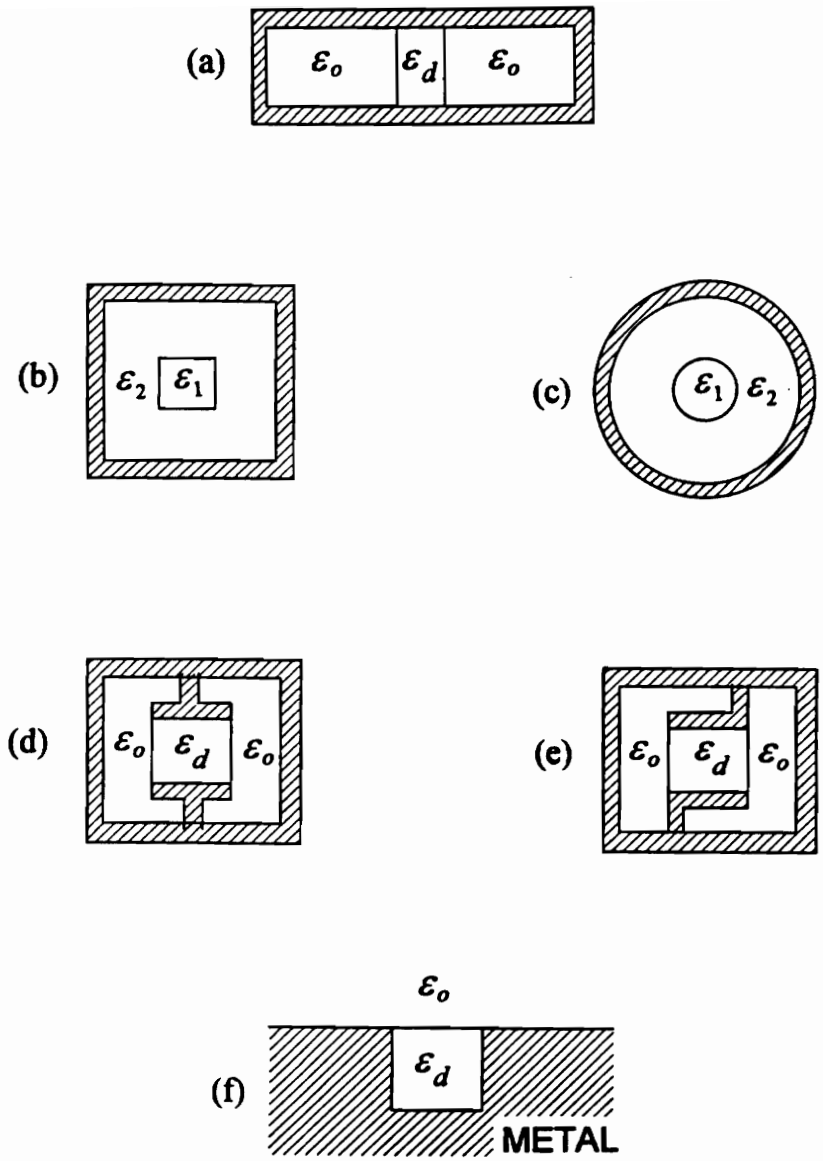

Figure 2-14. Dielectric loaded bandwidth enhancement schemes.
Shown are the waveguide cross-sections views. (a) E-plane slab loading. (b) Dielectric loaded square. (c) Dielectric loaded circular. (d) Double T-septum. (e) Double L-septum. (f) Insert dielectric guide.

price paid in terms of performance. Obviously, the rectangular waveguide does not support dual polarization and furthermore the power handling capabilities of the waveguide are reduced because of the reduction in height needed to obtain the bandwidth. For the special case of a square waveguide loaded with a single vertical slab, bandwidth is actually reduced.

Dielectric loading of both square and circular waveguide was investigated by Tsandouglas [47], [46]. In an effort to increase the bandwidth of a square waveguide, Tsandouglas [46] studied the effects of dielectric loading the waveguide shown in Figure 2-14b. The dielectric loading consisted of a transverse square section of the guide located in the center of the square waveguide. In all the computed test cases the dielectric was found to reduce the single-mode bandwidth. A similar study was conducted for circular waveguides with dielectric lining [47] shown in Figure 2-14c. By varying parameters, it was shown that one can increase single-mode bandwidth of a circular waveguide to 31.8% which is slightly less than an unloaded square waveguide.

Other researchers have investigated bandwidth characteristics of dielectric loaded waveguide using various geometries and schemes. Mazumder and Saha [48] investigated a novel waveguide referred to as the double T-septum waveguide. The double T-Septum shown in Figure 2-14d consists of two metallic T-shaped posts placed in the broad walls of rectangular guide. A dielectric loaded double T-septum waveguide and a version referred to as the single T-septum have also been investigated by Mansour and Macphie [49]. Bandwidths of three octaves (8:1 or ~150 %) have been reported. The inhomogeneously filled double L-Septa waveguide (see Figure 2-14e) studied by Saha and Guha [50] is obtained by placing two L-shaped metallic posts on the broad walls of a rectangular waveguide. A bandwidth ratio of 12:1 (or ~170 %) was reported for the double L-septum waveguide with proper dielectric loading. Pennock *et al.* [51] discuss the multiple layer inset dielectric guide which is formed by cutting a longitudinal groove in a ground plane and filling it with dielectric material as shown in Figure 2-14f. The inset dielectric guide is reported to have a single-mode bandwidth of 66% which is comparable to similar dual-ridged waveguide. Each of these methods demonstrate that bandwidth enhancement can be obtained by dielectric loading waveguides; however, these schemes are not likely to be suitable candidates for broadband array radiator elements because of symmetry requirements needed for dual polarization. There appears to be no additional

work in the literature on extending these principles to a dual polarized version that meets the 90 degree rotational symmetry requirement.

A summary of waveguide cross-sectional goemetries that employ dielectric loading to obtain bandwidth extension is shown in Table 2-2. The table gives theoretical single-mode bandwidth for waveguide cross-sections that do not support dual polarization (see Table 2-1 for cross-sections that do support dual polarization).

Table 2-2.
Summary of Bandwidth for Dielectric-loaded Waveguides that do not Support Dual Polarization

Waveguide cross-section	Bandwidth (%)
E-plane slab loading	more than 66 %
double T-septum	~ 150 %
double L-septum	~ 170 %
inset dielectric guide	66 %

2.5.3 Wideband Solid State Phased Array Methods

A considerable development effort for the last 10-12 years has been underway to increase the reliability, reduce the cost and weight, and increase the flexibility of phased array radar systems, through the use of monolithic microwave integrated circuits (MMIC) technology [52], [53], [54]. MMIC devices are high density solid state GaAs circuits that are constructed on a substrate, often for miniaturized applications. Using MMIC technology, the functions of the centralized transmitter and receiver can be distributed to each of the array element locations in what is referred to as a transmit/receive (T/R) module. In the literature, this approach is referred to as the distributed or the active (compared to passive) array approach. A particularly desirable feature for the 'radar simulator' requirement discussed in Chapter 1 is that one obtains a high power transmitter using the multiple distributed low power signal amplifiers. Generally, dual polarization is accomplished by switching and appropriately phasing two linear or circular orthogonally

polarized elements. There may also be other advantages inherent in moving the receiver systems closer to the receiving antenna, in terms of reducing the noise figure.

Povinelli and Grove [55] have investigated a 6-18 GHz active array for the shared aperture array program. They used both microstrip fed log periodic antennas and flare notch type radiators mounted orthogonally to obtain the desired polarization agility. Priolo *et al.* [56], also investigated a 6-18 GHz active phased array composed of a T/R module and tapered notches radiators. The array investigated consisted of four elements and could also achieve polarization agility. In each of these examples the T/R modules could supply on the order of 1 Watt to each of the radiators.

Although the distributed element approach offers attractive features, it does not meet all of the hypothetical phased array requirements given in Table 1-1. The power levels are considerably lower than is needed for a high power application of this type. Furthermore, the cost per module of $200-500 [54], [55] indicates that such an approach may be cost prohibitive for large high power scanned arrays.

2.5.4 Other Electronic Scanning Methods

Other wideband electronic scanning methods include various lens type approaches. The Rotman-Turner lens [57] is a wideband array capable of multi-octave performance, realized by feeding a transmit signal at various points along a locus described by transcendental equations. The distance between the feed point locus and the array elements is such that a linear phase tilt can be obtained simply by moving the feed point along the locus thus achieving scan in one plane. A scheme of extending the Rotman-Turner lens to two dimensions is given in reference [58]. Although this offers wideband performance, it would be difficult to realize at high power levels due to the required switching network, and further would be problematic (if possible) to implement in a monopulse configuration which is a requirement for a tracking radar system.

A 96-element wideband linear polarized array constructed from rectangular waveguide elements has been demonstrated by Laughlin *et al.* [59]. The array elements used were rectangular waveguides with an aspect ratio[3] of about 2; therefore the single-mode bandwidth is determined by the cutoff frequencies of the TE_{10} and the TE_{20} modes providing about one octave of bandwidth. The array was well matched over a 60° cone of

[3] The aspect ratio of a waveguide is defined by the width of the broad wall divided by the width of the narrow wall.

scan from 3.5 to 6.5 GHz which is 63 % bandwidth. The mutual coupling and the impedance matching considerations for double-ridged waveguide elements have been investigated by Montgomery [60] where he was able to obtain a 4:1 VSWR match over a 60° scan cone. The bandwidth with which this was achieved was 43%. A dual ridged waveguide like the rectangular waveguide is of course limited to linear polarization.

An approach to obtaining wideband performance could be to substitute in place of each dual polarized radiating element two linear orthogonal polarized radiating elements [61]. This technique has been demonstrated by Huang [62] using microstrip patch elements, and could conceivably be extended to waveguide elements. To obtain a desired polarization, the phase and amplitude of the two elements would be adjusted. The approach would then entail using a rectangular waveguide [59], an E-plane slab dielectrically loaded waveguide [43], or ridged waveguide elements [60] as the linearly polarized elements. However, there are several immediately obvious problems and disadvantages with this method. First, it doubles the number of radiating elements, phase shifters, and associated control hardware need to steer the beam. Secondly, it doubles the density of elements needed on the array aperture such that it is questionable whether or not the elements could physically fit within the array lattice needed for a wideband application. In addition, one would question whether or not there are underlying mutual coupling effects and associated impedance matching unknown difficulties resulting from the dense orthogonal element lattice. It is believed that this approach is less desirable when compared to the dual polarization single element pursued in this report.

2.5.5 Dielectric Loaded Horns

Various schemes of dielectric loading horn antennas have been employed to reduce cross-polarization and sidelobe level, increase bandwidth and efficiency, lower noise figure and improve phase errors across aperture [63],[64]. This has been accomplished by several approaches for rectangular, circular, and other aperture shapes including both smooth-walled and corrugated surfaces. Of importance in this review are rectangular shaped apertures where the emphasis of the approach has been to characterize or enhance bandwidth performance, and also geometric shapes that may have some relevance to the approach in this report. Circular waveguides and conical shaped horns are omitted from this discussion.

Tsandouglas and Fitzerald [65] studied the effect of dielectrically loading the E-plane of a rectangular horn antenna. Wedges were placed on the edges (side walls) and tapered such that the wide end extended to the mouth of the horn and the end tapered extends to the throat of the horn. The emphasis of the study was to increase the aperture efficiency by changing the amplitude distribution of the TE_{10} mode. Nair [66] investigated the loading of both E- and H-plane walls of a rectangular horn and showed that the technique can be used for pattern shaping. A flange loaded horn with a dielectric wedge inserted into the H-plane has been investigated by Tourneur [67] and demonstrated at 12-17 GHz.

A square hard horn is formed by filling both the E- and H-plane side wall corrugations with dielectric slabs. The square hard horn has been studied by Kildal and Zienuitycz [68], [69] in terms of cross-polarization, gain, bandwidth and sidelobe level. This study is interesting because the geometry will support dual polarization. Cross-polarization levels of less than -30 dB and bandwidths of 10% have been demonstrated.

2.6 Summary of Chapter 2

This chapter has presented the problem statement and thoroughly discussed the background germane to the problem at hand. The discussion focused on arrays of waveguide elements. Section 2.2 provided basic definitions of phased array components, polarization, and bandwidth. Section 2.3 reviewed basic array theory in terms of array scanning principles and mutual coupling. Mutual coupling is one of the major factors that must be considered when designing an array element due to a phenomena referred to as array blindness. A review of mutual coupling shows that one must avoid operating near higher-order mode cutoff frequencies to avoid blindness. Therefore, for a wideband phased array, one will need a corresponding bandwidth that supports single-mode propagation within the waveguide. Based on prior work discussed in Section 2.3, a detailed description of phased array element requirements needed for the hypothetical array (see Table 1-1) are given in Section 2.4. The key requirements include 90° rotational symmetry, high power handing capability, and single-mode bandwidth of more than an octave.

A discussion of prior work on wideband dual polarized arrays was given in Section 2.5. Although the focus was on waveguide type elements, several alternative methods that do not use a dual polarized waveguide element were also given for comparative purposes. Chapter 3 will define and outline an approach to obtaining bandwidth enhancement of a radiating element that supports dual polarization that is clearly novel, when compared the prior work.

2.7 References for Chapter 2

[1] R. Tang and R.W. Burns, "Chapter 20 - Phased arrays", *Antenna Engineering Handbook*, Second Edition, edited by R.C. Johnson and H. Jasik, New York: McGraw-Hill, 1984.

[2] T.C. Cheston and J. Frank, "Chapter 7 - Phased array radar antennas", *Radar Handbook*, Second Edition, edited by M.I. Skolnik, New York: McGraw-Hill, 1990.

[3] M.H. Chen and G.N. Tsandouglas, "A wide-band square waveguide array polarizer", *IEEE Trans. Antennas Propagat.*, vol. AP-21, NO.5, pp. 389-391, May 1973.

[4] E. Lier and T. Schag-Pettersen, "An extremely broadband waveguide polarizer", *IEEE International Symposium on Antennas and Propagation Digest*, pp. 1286-1289, 1988.

[5] E. Lier and T. Schag-Pettersen, "A novel type of waveguide polarizer with large cross-polar bandwidth", *IEEE Trans. on Microwave Theory Tech.*, vol. MTT-36, NO.11, pp. 1531-1534, November, 1988.

[6] L.V. Skrypnik, V.N. Pochernyaev and S.V. Mirnyi, "Designing a square waveguide polarizer", Radio electronics and Communications Systems (translated from Izvestiya Vuz Radioelektronika), Vol. 32, No.2, pp.91-92, 1989.

[7] S. Koul and B. Bhat, *Microwave and Millimeter Wave Phase Shifters-Volume I.-Dielectric and Ferrite Phase Shifters*, Boston: Artec House, 1991.

[8] E.B. El-Sharaway, "Double ridged waveguide phase shifters for broadband applications", *IEEE Trans. on Microwave Theory Tech.*, vol. MTT-41, No. 12, pp. 2161-2165, December 1993. {gives 6-16 GHz design }

[9] Ferrite phase shifter performance data sheet, Electro Magnetic Sciences (EMS), Norcross GA, May, 1992.

[10] C.A. Balanis, *Advanced Engineering Electromagnetics*, New York: John Wiley and Sons, 1989.

[11] N. Amitay, V. Galindo, and C.P. Wu, *Theory and Analysis of Phased Arrays*, John Wiley and Sons: New York, 1972.

[12] D.M. Pozar and D.H. Schaubert, "Scan blindness in infinite arrays of printed dipoles," *IEEE Trans. Antennas Propagat.*, vol. AP-32, NO.6, pp. 602-610, June 1984.

[13] D.H. Schaubert, J.A. Anders, M.E. Cooley, and N.E. Buris, "Moment method analysis of infinite stripline-fed tapered slot antenna arrays with a ground plane," *IEEE Trans. Antennas Propagat.*, vol. AP-42, NO.8, pp. 1161-1166, August 1994.

[14] L.Stark "Microwave theory of phased-array antennas", *Proc of IEEE*, vol. 62, NO. 12, pp.1661-1701, December 1974.

[15] V. Galindo and C.P. Wu, " The relation between the far-zone pattern of the singly excited element and the transmission coefficient of the principal lobe in an infinite array", *IEEE Trans. Antennas Propagat.*, vol. AP-14, NO.3, pp. 397-398, May 1966.

[16] S. Edelberg, A.A. Oliner, "Mutual coupling effects in large antenna arrays: Part I-slot arrays", *IRE Trans. Antennas Propagat.*, vol. AP-8, pp. 286-297, May 1960.

[17] H.A. Wheeler," The grating lobe series for the impedance variation in a planar phased array antenna", ", *IEEE Trans. Antennas Propagat.*, vol. AP-14, NO.6, pp. 707-714, November 1966.

[18] R.J. Mailloux, "Phased array theory and review", *Proc. IEEE.*, vol. 70, no. 3, pp.246-291, March 1982.

[19] G.F. Farrell and D.H. Kuhn, "Mutual coupling in infinite planar array of rectangular waveguide horns", *IEEE Trans. Antennas Propagat.*, vol. AP-16, no. 4, pp. 405-414, July 1968.

[20] R.E. Collin, *Field Theory of Guided Waves*, New York: IEEE Press, 1991, Chapter 9.

[21] B.L. Diamond, "A generalized approach to the analysis of infinite planar array antennas", *Proc. IEEE*, vol. 56, NO.11, pp. 1837-1851, November 1968.

[22] G.V. Borgiotti, "Modal analysis of periodic planar phased arrays of apertures", *Proc. IEEE*, vol. 56, NO.11, pp. 1881-1892, November 1968.

[23] N. Amitay and V. Galindo, "The analysis of circular waveguide phased arrays," *Bell Sys. Tech. J.*, vol. 47, pp.1903-1932, November 1968.

[24] G.H. Knittel, "The relation of blindness to higher-order mode cutoff conditions," *IEEE G-AP Int. Symp. Digest*, pp. 69-72, September, 1971.

[25] N.S. Wong, R. Tang, S.W. Lee, W.R. Jones, "Multimode phased array element for wide angle impedance matching", Phased Array Antennas, MA: Artech House, Ed. G.H. Knittel and A. Oliner, pp.178-186, 1972.

[26] R.Tang and H.A. Wong, "Multimode phased array element for wide scan angle impedance matching", *PROC IEEE*, vol. 56, NO. 11, pp. 1951-1959, November 1968.

[27] R.J. Mailloux, H. Steyskal, "Analysis of a dual-frequency array technique" *IEEE Trans. Antennas Propagat.*, vol. AP-27, NO.2, pp. 130-136, March 1978.

[28] R.J. Costantini and G.H. Knittel, "A theoretical study of a simple multimode phased-array element for wide-angle impedance matching", *IEEE International Symposium on Antennas and Propagation Digest*, pp. 85-88, 1971.

[29] A.A. Oliner, "Surface-wave effects and blindness in phased-array antennas," *Phased Array Antennas*, Editors A. Oliner and G. Knittel, MA: Artech House, pp.107-112, 1972.

[30] G.N. Tsandouglas and G.H. Knittel, "The analysis and design of dual-polarization square-waveguide phased arrays", *IEEE Trans Antennas Propagat.*, vol. AP-21, pp. 796-808, November 1973.

[31] G.H. Bryant, R.W. Wills and I.S. Altaf, "Waveguide Element design for a phased array," *IEE International Conference on Antennas and Propagation (ICAP 85)*, Part I. pp.31-34, 1985.

[32] H.A. Wheeler, "A systematic approach to the design of a radiator element for a phased array antenna", *Proc IEEE*, vol. 56, no. 11, pp. 1940-1951, November 1968.

[33] L. Stark, "A comparison of array element types", *Phased Array Antennas*, Editors A. Oliner and G. Knittel, MA: Artech House, pp.51-67, 1972.

[34] S.J. Foti and M.W. Shelley,"An experimental wideband polarisation diverse phased array", Military Microwaves '90 Conference Proceedings, July 1990, pp.263-271.

[35] C.C. Chen, "Wideband wide-angle impedance matching and polarization characteristics of circular waveguide phased arrays," *IEEE Trans. Antennas Propagat.*, vol. AP-22, no. 3, pp. 414-418, May 1974.

[36] R.G. Schmier and M.J. Buckey, "Broadband circular waveguide radiating element for use in phased array antennas", *IEEE International Symposium on Antennas and Propagation Digest*, pp. 1236-1239, 1994.

[37] J.K. Shimizu, "Octave-bandwidth feed horn for paraboloid", *IRE Trans. Antennas Propagat.*, vol. AP-9, pp. 223-224, March 1961., See also *Electromagnetic Horn Antennas*, ed. A.W. Love, New York: IEEE Press, 1976.

[38] M.H. Chen, "Modal characteristics of quadruple-ridged circular and square waveguide," *IEEE Trans. on Microwave Theory Tech.*, vol. MTT-22, no. 8, pp. 801-804, August 1974.

[39] C.C. Chen, "Quadruple ridged-loaded circular waveguide phased arrays", *IEEE Trans Antennas Propagat.*, vol. AP-22, pp. 481-483, May 1974.

[40] F.W. Robinson, S.J. Woodhouse and M.A. Eidem, "Towards a 3:1 band phased array", *IEE International Conference on Antennas and Propagation, (ICAP 89)*, Part I. pp.178-181., 1989

[41] S.A. Soroka, "A physically compact quad ridged horn design", *IEEE International Symposium on Antennas and Propagation*, pp. 903-906, 1986.

[42] H.J. Stalzer, M.D. Greenman and F.G. Wellworth, "Modes of crossed rectangular waveguide", *IEEE Trans. Antennas and Propagat.*, vol. AP-24, no. 3 pp. 220-223, March 1976.

[43] F.E. Gardiol, "Higher-order modes in dielectrically loaded rectangular waveguides," *IEEE Trans. on Microwave Theory Tech.*, vol. MTT-16, no. 11, pp. 919-924, November 1968.

[44] T.K. Findakly and H. M. Haskal, "On the Design of dielectric loaded waveguides," *IEEE Trans. on Microwave Theory Tech.*, vol. MTT-24, no. 1, pp. 39-43, January 1976.

[45] S. Halevy, S. Raz and H. Cory, "Bandwidth optimization by a dielectric loading", *IEEE Trans. on Microwave Theory Tech.*, vol. MTT-26, no.6, pp. 407-412, June 1978.

[46] G.N. Tsandouglas, "Propagation in dielectric-lined square waveguides," *IEEE Trans. on Microwave Theory Tech.*, vol. MTT-23, no.5, pp. 406-410, May 1975.

[47] G.N. Tsandouglas, "Bandwidth enhancement in dielectric-lined circular waveguides", *IEEE Trans. on Microwave Theory Tech.*, vol. MTT-21, no. 10, pp. 651-654, October 1973.

[48] G.G. Mazumder and P.K. Saha, "A novel rectangular waveguide with double T-septums," *IEEE Trans. on Microwave Theory Tech.*, vol. MTT-33, no.11, pp. 1235-1238, November 1985.

[49] R.R. Mansour and R. H. Macphie "Properties of the dielectrically loaded T-septum waveguide", *IEEE Trans. on Microwave Theory Tech.*, vol. MTT-37, no.10, pp. 1654-1657, October 1989.

[50] P.K. Saha and D. Guha, "Characteristics of inhomogeneously filled double L-septa waveguides," *IEEE Trans. on Microwave Theory Tech.*, vol. MTT-40, no.11, pp. 2050-2053, November 1992.

[51] S.R. Pennock, N. Izzat and T. Rozzi, "Very wideband operation of a twin-layer inset dielectric guide", *IEEE Trans. on Microwave Theory Tech.*, vol. MTT-40, no. 10, pp. 1910-1917, October 1992.

[52] E. Brookner, "Array radars: an update," *Microwave Journal*, pp. 117-138, February 1987.

[53] R. Douville and M.G. Stubbs, "MIC Technology for phased arrays," *Microwave Journal*, pp. 143-163, March 1988.

[54] R. Tang and R.W. Burns, "Array technology", *Proc. IEEE*, vol. 80, no. 1, January 1992.

[55] M.J. Povinelli and C.E. Grove, "Wideband apertures for active planar multi-function phased arrays," *IEEE National Radar Conference*, 1989, pp.125-128.

[56] M. Priolo, G.St. Onge, W. Coughlin III, J. Bugeau, and D. Meharry, "Transmit/receive modules for 6 to 18 GHz multifunction arrays", *IEEE Microwave Theory and Technique-Symposium Digest*, 1990, pp. vol.3, 1227-1230.

[57] W. Rotman and R.F. Turner, "Wide-angle microwave lens for line source applications," *IEEE Trans. Antennas Propagat.*, vol. AP-11, pp. 623-632, November 1963.

[58] G.C. Sole and M.S. Smith, "Multiple beam forming for planar antenna arrays using a three-dimensional rotman lens", *IEE Proceedings*, vol. 134, pt-H, no. 4, August 1987.

[59] G.J. Laughlin, E.V. Byron and T.C. Cheston, "Very wide band phased-array antenna", *IEEE Trans. Antennas Propagat.*, vol. AP-20, No. 6, pp. 699-704, November 1972.

[60] J.P. Montgomery, "Ridged waveguide phased array elements", *IEEE Trans. Antennas Propagat.*, vol. AP-24, NO.1, pp. 46-53, November 1976.

[61] J.C. Nolen, "Phased array polarization agility", *IEEE Trans. Antennas Propagat.*, vol. AP-13, pp. 820-821, July 1965.

[62] J. Huang, "A technique for an array to generate circular polarization with linear polarized elements," *IEEE Trans. Antennas Propagat.*, vol. AP-34, NO.9, pp. 1113-1124, September 1986.

[63] A.W. Love, *Electromagnetic Horn Antennas*, New York, IEEE Press, pp. 353, 1974.

[64] R. Chatterjee, *Dielectric and Dielectric-Loaded Antennas*, New York: John Wiley and Sons, 1985.

[65] G.N. Tsandouglas and W.D. Fitzgerald, "Aperture efficiency in dielectrically loaded horns," *IEEE Trans. Antennas and Propagat.*, vol. AP-21, no. 1 pp. 69-74, January 1972.

[66] R.A. Nair, "Symmetric dielectric loading on E- and H-plane walls of a rectangular horn for pattern shaping," *Int. J. Electronics*, vol. 63, no. 4, pp. 479-488, 1987.

[67] C. J. Tourneur, " Calculation of E-Plane radiation pattern of a flange loaded H-plane quasi sectoral horns," International Conference on Antennas and Propagation (ICAP 83), pp. 132-135, 1983.

[68] W. Zieniutycz and P.S. Kildal, "Study of wall region and dielectric losses in a square hard horn," *IEE Proceedings-H*, Vol. 139, No. 2, April 1992.

[69] P.S. Kildal, "Bandwidth of a square hard horn," *IEE Proceedings-H*, Vol. 135, No. 4, August 1988.

[70] R.J. Mailloux, Phased Array Antenna Handbook, Boston: Artech House, 1994.

[71] W.L. Stutzman and G.A. Thiele, *Antenna Theory and Design*, New York: John Wiley and Sons, 1981, Chapter 1.

CHAPTER 3

DEFINING THE CROSSED-SEPTUM WAVEGUIDE (CSW)

3.1 Overview of the Crossed-Septum Waveguide (CSW)

Section 2.4 outlined the requirements of a radiating element needed for the hypothetical phased array antenna. The desired element is a waveguide type element with an aperture that supports dual polarization and offers broadband performance in terms of single-mode propagation. This chapter introduces the crossed-septum waveguide (CSW), which is a novel dielectrically loaded square waveguide. A discussion of the bandwidth enhancement concept is best accomplished by first considering a square waveguide and then expanding the discussion to the inhomogeneous dielectric loaded waveguide, which is the CSW.

The cutoff frequencies for the TE_{mn} and TM_{mn}, modes of an unloaded (or filled with a homogeneous dielectric) square metallic waveguide are given by [1]

$$f_c(m,n) = \frac{1}{2a\sqrt{\mu\varepsilon}}\sqrt{m^2+n^2} \tag{3.1}$$

where for TM modes

$$m, n = 1, 2 \ldots$$

and for TE modes

$$m, n = 0, 1, 2 \ldots \text{ and } m = n \neq 0$$

and a is the width of the guide, ε is the permittivity, and μ is the permeability of the material inside the waveguide.

The cutoff frequencies of the first several modes of the unloaded waveguide are given in Table 3-1. In the table the cutoff frequencies f_C are normalized to that of the

TE_{10} mode. The TE_{10} mode is the dominant mode of propagation within the waveguide. For a square waveguide, the TE_{01} mode is of course identical to the TE_{10} except that it is rotated by 90 degrees and hence is also a dominant mode but is referred to as the orthogonal dominant mode. Table 3-1 provides comments on each of the modes that are important to this analysis, and will be referred to later in this discussion. The single-mode bandwidth of the square waveguide is 1.414:1. The next higher-order modes above the dominant mode are the TE_{11} and TM_{11} modes.

Table 3-1.

Cutoff Frequencies of the First Several Modes for an Unloaded Waveguide.

mode type	normalized f_c	comments
TE_{10}, TE_{01}	1.000	dominant mode of propagation
TE_{11}	1.414	higher-order mode, to be 'removed' by mode filters
TM_{11}	1.414	higher-order mode, to be 'removed' by mode filters
TE_{20}, TE_{02}	2.000	higher-order mode, increased separation relative to the TE_{10} mode
TE_{21}, TM_{21}	2.236	higher-order modes
TE_{22}, TM_{22}	2.828	higher-order modes

The research described in this report involves the use of an inhomogeneous, dielectric loading technique to alter certain modal cutoff frequencies and extend the usable bandwidth of the square waveguide. A cross-sectional view of the waveguide element under consideration is shown in Figure 3-1 and was originally suggested by Swinford [12] as a possible broadband radiator for use in a phased array. The waveguide shown is a square waveguide, loaded with a thin dielectric slab or 'septum'. We will refer to this dielectrically loaded waveguide as the cross-septum waveguide (CSW).

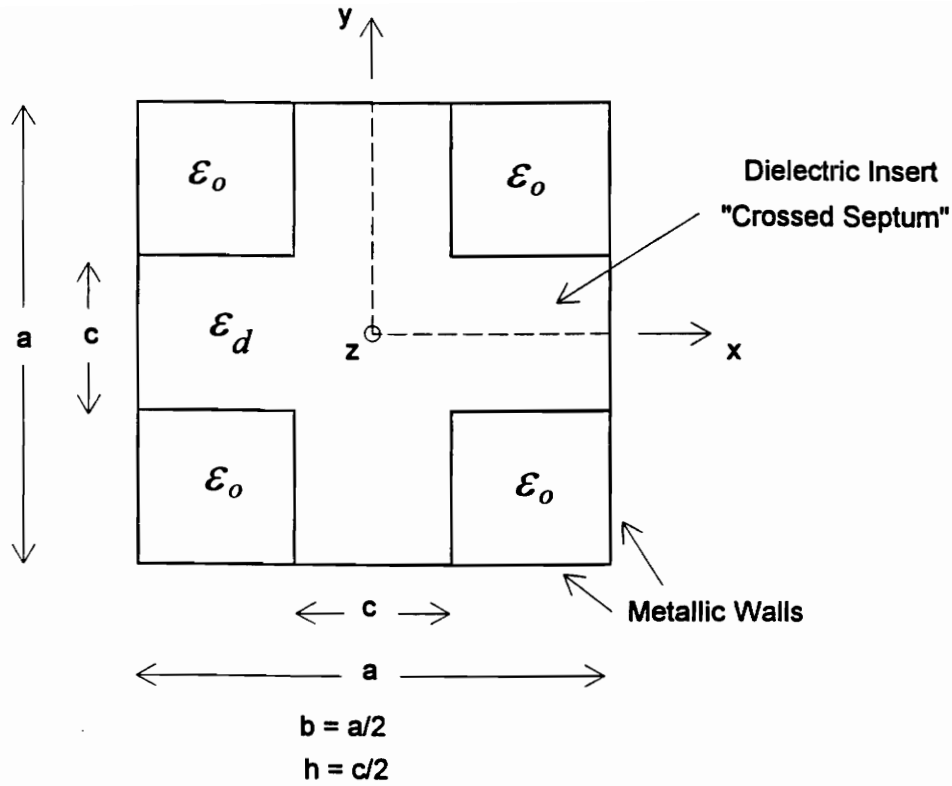

Figure 3-1. Cross-sectional view of the crossed-septum waveguide (CSW). The mode filters are omitted.

The bandwidth enhancement concept is shown in Figure 3-2. The TE_{10} mode[1], which has a maximum electric field in the center, will be significantly affected by the presence of the vertical septum such that the cutoff frequency, $f_c(TE_{10})$ can be lowered. Conversely, the TE_{20} mode which has a near zero electric field in the center of the waveguide will be less affected by the dielectric septum, and the cutoff frequency $f_c(TE_{20})$ will be lowered less. Therefore, the desired goal is to obtain increased mode separation between the TE_{10} and TE_{20} modes by exploiting the symmetry differences in the electric field patterns. However, the slab loaded waveguide in Figure 3-2 does not have the desired symmetry properties and must be modified. By combining a horizontal and vertical dielectric septum, a cross shaped dielectric slab is obtained, with the desired 90 degree rotational symmetry necessary for dual polarization as shown in Figure 3-1.

In obtaining bandwidth enhancement we must also consider the TE_{11} and TM_{11} modes. Once again our conceptual discussion will focus on the symmetry properties of the electric fields in the guide. The goal is to use mode filters (suppressors) to attenuate the TE_{11} and TM_{11} modes, which possess significantly different symmetry and field structures (compared to the dominant mode). A further discussion and detailed description is provided in the following section, and also in Chapter 6.

In the context of the above discussion, the goal of this report is to show that one can enhance the single-mode bandwidth of a square waveguide using the dielectric loading and mode filtering scheme. The objective is to obtain single-mode bandwidth, defined as

$$BW_{CSW} = \frac{f_c(TE_{20})}{f_c(TE_{10})} \quad . \tag{3.2}$$

Conceptually this approach is reasonable if one accepts certain practical limitations from the onset of the problem. If one uses proper coupling into the desired mode and mode filtering techniques to suppress the TE_{11} and TM_{11} modes, it is thought that this technique can be used to provide a design that exhibits *graceful degradation* over the wide frequency range of operation. For the desired application, the CSW will have a relatively short length in terms of wavelength and will not have any bends or discontinuities, which

[1] The introduction of a dielectric results in hybrid modes. We are here referring to hybrid modes that resemble the corresponding TE and TM modes for the case of the unloaded waveguide. A thorough discussion of the hybrid modes is provided in Chapter 5, however the TE and TM mode designations are retained for simplicity to avoid confusion during the discussion of this report.

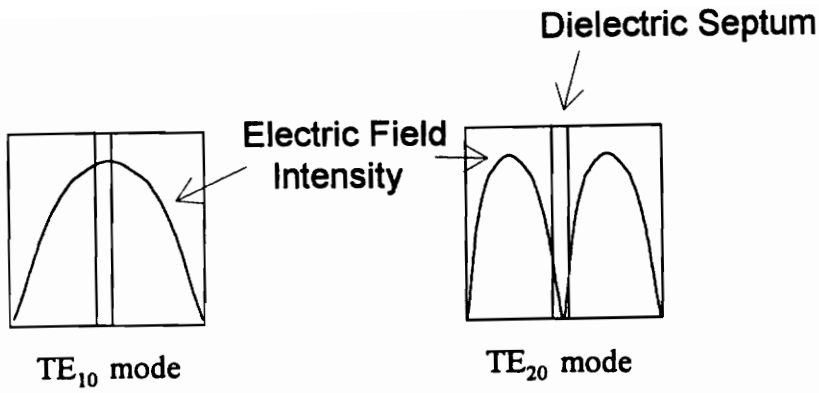

Figure 3-2. Concept of bandwidth enhancement using a dielectric septum. Note the electric field is a maximum in the center of the guide for the TE_{10} mode compared to a minimum field intensity for the TE_{20} mode. Combining both the vertical and horizontal septum provides 90 degree rotational symmetry as shown in Figure 3-1.

could excite or couple energy into these undesired modes. In terms of the definition of single-mode bandwidth, a more appropriate description might be "quasi" single-mode bandwidth. By "quasi" single-mode bandwidth, what is meant is that some portion of the useful bandwidth will exist above the higher-order mode cutoff frequencies, however energy coupled into a higher-order mode will be made to decay rapidly by the use of mode filters rather than by the cutoff condition. Therefore, the objective is to avoid coupling into the undesired TE_{11} and TM_{11} higher-order modes and to aggressively attenuate energy which is coupled into these modes.

3.2 Symmetry Properties of the CSW

The symmetry properties of the fields in a square waveguide such as the CSW can be used to simplify the analysis by reducing the complicated geometry of the CSW into a set of equivalent simpler geometries. McIsaac [2,3] derives a generalized procedure for classifying the mode types and symmetry properties of certain classes of waveguides. Also given is a procedure for determining the minimum sector angle (i.e., minimal cross section area) and associated boundary conditions of a waveguide necessary and sufficient to completely determine all modal eigenvalues and electromagnetic fields for a given symmetry type waveguide. This method allows one to determine a set of equivalent boundary values problems (BVP) from the original waveguide boundaries subject to the appropriate symmetry properties. Suppose that the coordinate system of the guide is as shown in Figure 3-1 and further assume that the medium is linear and isotropic. Then all modal solutions and fields can be derived from an equivalent set of boundary value problems as shown in Figure 3-3. In the figures the dielectric is not shown but is assumed to be present. The boundaries of the equivalent problems consist of either perfect electric conductors (PEC) or perfect magnetic conductors (PMC) satisfying boundary conditions of zero tangential electric field and zero tangential magnetic field, respectively.

In Figure 3-3 there are two square shaped equivalent boundary value problems and four triangular shapeD BVPs. From an analysis point of view, it would be convenient to analyze the same geometric shaped structure for all symmetry cases. Therefore using image theory we will choose to reduce the four BVPs in Figures 3-3c-f to two square shaped BVPs. Figures 3-3c and 3-3d will combine to form Figure 3-4c, and Figures 3-3e

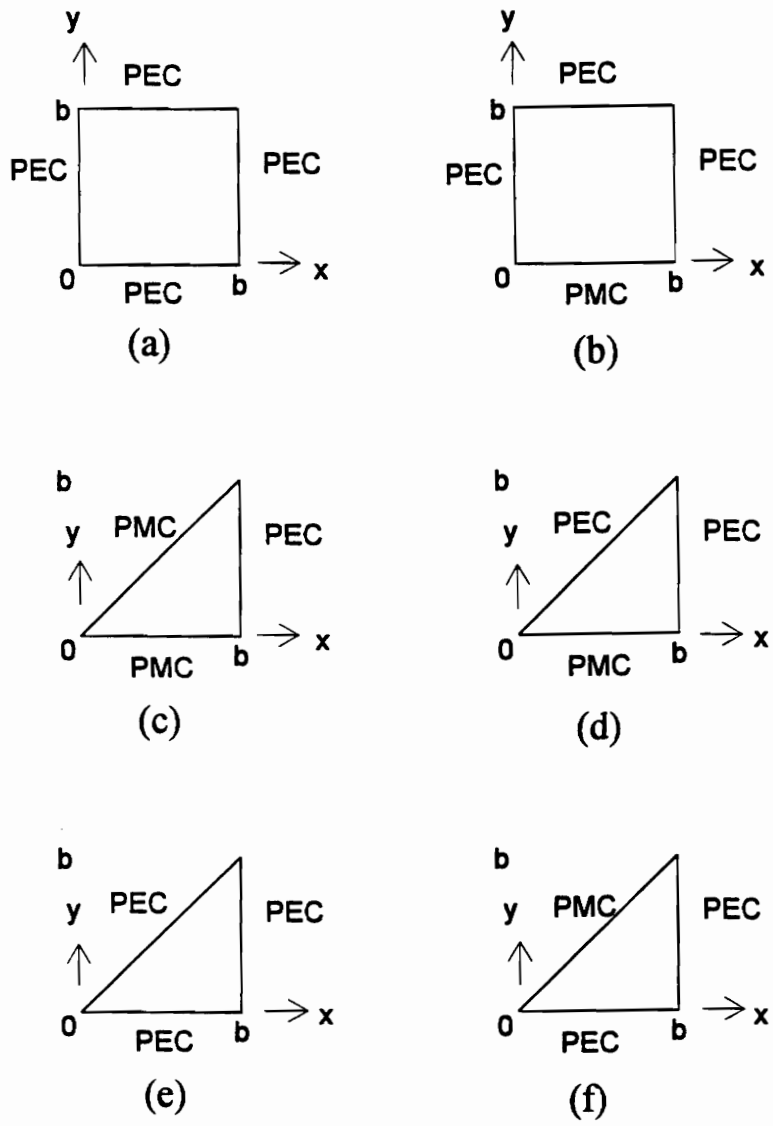

Figure 3-3. Minimal equivalent sectors of the CSW based on symmetry reduction procedure of McIsaac [2],[3].

and 3-3f will combine to form Figure 3-4d. The result is a set of four unique BVPs with identical size and shape, but different boundary conditions as shown in Figure 3-4. This procedure has hence reduced the original CSW problem with dimensions of $a \times a$ to an equivalent set of four problems, each with dimensions of $a/2 \times a/2$. Once solutions for each of the equivalent systems are obtained, the fields of the equivalent systems can be used to reconstruct the fields in the entire waveguide based on symmetry properties. This represents a significant simplification of the problem in terms of solving the BVP. The purpose for doing this will be made more clear in the discussion provided in Chapter 4.

One can describe the behavior of an electric field about the center of the waveguide such as the CSW in Figure 3-1 based on the boundary conditions on the axes. Where the boundary on an axis is a PMC, the electric field is a maximum and has *even* symmetry about that boundary. Conversely, where the boundary on an axis is a PEC, the electric field is zero and hence has *odd* symmetry about that boundary. Therefore, in this report symmetry of properties of the electric-field will be used to define symmetry cases as discussed below. For all valid TE_{mn} and TM_{mn} modes given in equation (3.1), we define the term *symmetry cases* as follows:

- For even/odd symmetry cases (see Figure 3-4a)
  TE_{mn} , TM_{mn} where $m = 1,3,\cdots$ and $n = 0,2,\cdots$

- For odd/even symmetry cases (see Figure 3-4b)
  TE_{mn} , TM_{mn} where $m = 0,2,\cdots$ and $n = 1,3,\cdots$

- For even/even symmetry cases (see Figure 3-4c)
  TE_{mn} , TM_{mn} where $m = 1,3,\cdots$ and $n = 1,3,\cdots$

- For odd/odd symmetry cases (see Figure 3-4d)
  TE_{mn} , TM_{mn} where $m = 0,2,\cdots$ and $n = 0,2,\cdots$

For example, an even/odd symmetry mode such as the TE_{10} mode has a maximum/minimum electric field on the *y/x* axis and has even/odd symmetry in the *x/y* directions. For convenience Table 3-2 lists the dominant mode and several of the important higher-order modes in an unloaded square waveguide. The analysis and results

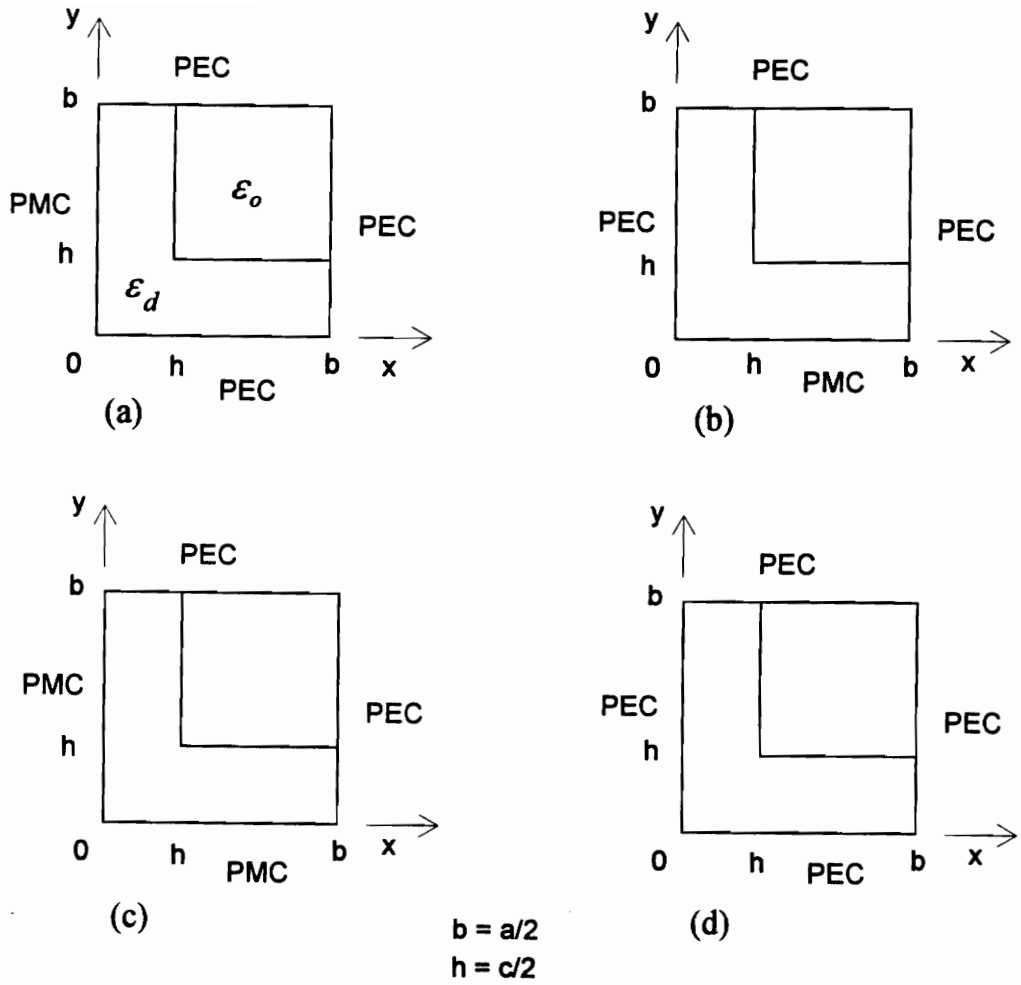

Figure 3-4. Definitions of 'symmetry cases' showing boundary conditions used in the analysis of the CSW. (a) even/odd, (b) odd/even, (c) even/even, (d) odd/odd.

in Chapters 4 and 5 will show that the modes in the CSW are hybrid modes. It will further be shown that the characteristics of a given mode as a function of waveguide parameters will depend on symmetry properties of the mode. Hence these symmetry definitions will be referred to frequently in the following sections.

Table 3.2.
Mode Symmetry Definitions of the Square Waveguide.
Given are the modes for an unloaded waveguide based on properties of the electric fields about the center of the guide.

DEFINED SYMMETRY	MODES
even/odd	$TE_{10}, TE_{12}, TM_{12}, \cdots$
odd/even	$TE_{01}, TE_{21}, TM_{21}, \cdots$
even/even	$TE_{11}, TM_{11}, TE_{31}, TE_{13}, TM_{31}, \cdots$
odd/odd	$TE_{20}, TE_{22}, TM_{22}, \cdots$

3.3 Discussion of Mode Filters

The bandwidth extension concept of Section 3.1 is predicated on the use of: 1) dielectric loading for increased mode separation between the TE_{10} and TE_{20} modes, and 2) a mode filter to confine the propagating energy to the desired dominant (TE_{10} or TE_{01}) mode above the cutoff frequency of undesired modes (i.e., TE_{11}, TM_{11}). This section discusses the relevance of the mode filter to the bandwidth extension concept.

A mode filter is a discontinuity, obstacle or alteration in a waveguide that interferes with the transport of energy in an undesired mode, while leaving the desired mode characteristics relatively unchanged. In the literature [4-11] one finds various schemes that can be employed to suppress unwanted modes in a waveguide system. For example Ren [4] discusses the use of thin metallic plates to suppress unwanted spurious modes in a dielectric resonator filter. In the design of a nonradiative dielectric circulator, Yoshinaga [5] develops a novel mode suppressor based the on the $\lambda/4$ choke principle,

also constructed from a thin metallic plates. The use of metallic wires and rings is described by Ishii [7] and Tan [11] to implement mode filters. A mode filter can also be constructed using an obstacle such as a screw placed transversely within a stripline as demonstrated by Das [6]. Thin resistive films have been used to realize mode filters as reported in references [8], [9], [10]. A thin resistive film can be formed by coating a thin sheet of mylar with a conductive material such as aquadag or graphite.

Each of these methods has advantages and disadvantages particularly to the geometry of the waveguide and the task at hand. However one common principle in each of these mode filtering implementations is that the obstacle introduces a conductive body into the waveguide system. The conducting body is placed such that the conductive surface is parallel to the electric field of the undesired mode, and perpendicular to the electric field of the desired mode. In this respect the objective of the design of the mode filter is to significantly alter the boundary conditions of the undesired mode leave the boundary conditions of the desire mode relatively unaffected. Appendix D provides a discussion of a canonical case ideal mode filter.

One can explain the mode filter requirements of the CSW in terms of symmetry properties of the modes in the waveguide. It was stated in Section 3.2 that the dominant mode will have even/odd (or equivalently odd/even) symmetry. The undesired modes have even/even symmetry, which is different from the dominant mode symmetry. Therefore the task of designing a mode filter is that of designing a scheme to exploit the difference in these two types of symmetry. It is conceptually reasonable to expect that this can be achieved by recalling that the even symmetry modes have a maximum electric field in the center of the guide, compared to odd symmetry modes which have a minimal electric field in the center of the guide.

Since the introduction of a mode filter implies some sort of modification to the internal structure of the guide, it is not reasonable to expect that this can be done without affecting the dominant (desired) mode also to some degree. The design goal also becomes that of holding the dominant mode attenuation to a minimum. The implementation of a mode filter is ultimately a tradeoff consideration between retaining energy in the desired modes and limiting energy in the undesired modes. A detailed discussion of the filter implementation for the CSW is given in Chapter 6. It will be shown that a thin resistive film can be strategically placed in the CSW such that it attenuates the even/even symmetry modes while having a lesser effect on the dominant mode.

3.4 References for Chapter 3

[1] C.A. Balanis, *Advanced Engineering Electromagnetics*, New York: John Wiley and Sons, 1989.

[2] P.R. McIsaac, " Symmetry-induced modal characteristics of uniform waveguides-I: summary and results," *IEEE Trans. on Microwave Theory Tech.*, vol. MTT-23, NO.5, pp. 421-429, May 1975.

[3] P.R. McIsaac, " Symmetry-induced modal characteristics of uniform waveguides-II: Theory," *IEEE Trans. on Microwave Theory Tech.*, vol. MTT-23, NO.5, pp. 429-433, May 1975.

[4] C.L. Ren, "Mode suppressor for dielectric resonator filters," *IEEE Microwave Theory and Tech. Symposium Digest*, vol. 1, pp. 389-391, 1982. {thin metal plate inserted to alter BCs of the undesired mode and not the desire mode}

[5] H.Yoshinaga and T. Yoneyama, "Design and fabrication of a nonradiative dielectric waveguide circulator", *IEEE Trans. on Microwave Theory Tech.*, vol. MTT-36, no. 11 pp. 1526-1528, November 1988. {thin metal strip and includes a $\lambda/4$ choke shaped to also attenuate a TEM mode that could be excited}

[6] B.N. Das and K.V.S.V.R. Prasad, "Impedance of a transverse slot in the ground plane of an offset stripline", *IEEE Trans. Antennas Propagat.*, vol. AP-32, no.11, pp. 1245-1248, November 1984. {metal transverse screws inside the guide}

[7] T.K. Ishii, *Microwave Engineering*, New York: Ronald Press, 1966. {metallic rings}

[8] G.N. Tsandouglas, D.H. Temme, and F.G. Willwerth, "Longitudinal Section Mode Analysis of Dielectrically loaded waveguides with application to phase shifter design", *IEEE Trans. on Microwave Theory and Techniques*, vol. MTT-18, no. 2. Feb. 1970. {thin resistive film}

[9] L. Stark, C.V. Bell, R.A. Notvest, R.E. Griswold, D.A. Charlton and R.W. Howard, "Microwave components for wide-band phased arrays", *Proc. IEEE*, vol. 56, no.11, pp.1908-1923, November 1968. {thin resistive films using aquadag coating}

[10] K. Hashimto, "Circular TE_{0n} mode filters for guided millimeter-wave transmission," *IEEE Trans. on Microwave Theory and Techniques*, vol. MTT-24, no. 1. pp. 25-31 January 1976. {resistive sheet in a circular waveguide}

[11] F.C.F. Tan and J. Helszajn, "Suppression of higher-order modes in waveguide-junction circulators using coupled open dielectric resonators," *IEEE Trans. on Microwave Theory and Techniques*, vol. MTT-24, no. 1. pp. 271-273 January 1976. {thin metallic wires parallel to the undesired mode electric field}

[12] H.W. Swinford, private communication, Naval Air Warfare Center, China Lake, CA., May, 1992.

CHAPTER 4

FORM OF SOLUTIONS FOR THE CSW

4.1 Overview of the Modal Analysis Applied to the CSW

The first goal in the investigation of the CSW is to perform a rigorous analysis to obtain expressions for the phase constants and electromagnetic fields for all waveguide modes of interest. Both the fields and the modal cutoff frequencies must be accurately determined in order to predict the usable bandwidth and to calculate the far-field patterns, which are studied in further chapters. In this chapter a discussion of the available analysis methods which were considered for this task will be given, along with a justification for the analysis method chosen--the mode matching technique. Following this is a detailed derivation of the form of solutions for each of the symmetry cases used throughout the remainder of this report.

4.2 Analysis Methods Considered

In obtaining solutions for the CSW (i.e., electromagnetic fields, phase constants and modal cutoff frequencies) one must solve Maxwell's equations subject to boundary conditions. By inspection of the CSW geometry defined in Figure 3-1 one finds that the permittivity within the waveguide is transversely inhomogeneous and of the form $\varepsilon = \varepsilon(x,y) \neq g(x)h(y)$. This in turn implies that the form of solutions for the waveguide are also nonseparable. For a nonseparable waveguide cross-section, one must turn to numerical methods to obtain solutions because closed form solutions usually are not possible. In this section a brief outline of the methods considered for the CSW analysis is now given. This discussion is by no means an exhaustive study or treatment of all the possible methods of solving boundary value problems. Rather, the purpose of this

discussion is to identify important features of several relevant methods for solving the CSW boundary value problem. There appears to be considerable flexibility in choosing a suitable analysis technique. The choice of analysis methods is by no means unique; however there are several salient features of each of the methods that can allow one to select a suitable technique.

The mode matching method [1], [3], [4] is a rigorous numerical method that can be applied to transversely inhomogeneous cross-sectional geometries such as the CSW. The method is based on a Fourier series expansion of the fields (or potentials) in various "regions" within the waveguide. For the CSW the cross-sectional geometry is divided into suitable regions that can be readily expressed in series form. In the formulation of the problem one then applies one of a number of techniques to solve for the coefficients of the series. One of these techniques could be the use of orthogonality relationships to obtain the series coefficients. The resulting solution is exact in the limit, when an infinite number of terms are included. An advantage of the mode matching solution technique is that it does not suffer from spurious solutions inherent in the finite elements technique (discussed below). Another advantage of the mode matching method is that cross-sectional geometries that can be divided into piecewise separable regions are conveniently expressed in series form, thus are well suited to this technique. This point will be discussed further below. The most serious limitation of the mode matching technique is that once formulated, it is relatively inflexible in terms of changes to the waveguide cross-sectional geometry--a problem not inherent to the finite element technique.

Finite element techniques [1], [2], [5], [6] for solving electromagnetic boundary value problems appear to be well suited for solving dielectric loaded waveguide problems such as the CSW. In the formulation, the problem is cast in terms of variational integral equations referred to as a functional. These integral equations are a functional which is stationary about a solution. In the numerical implementation of the functional, a cross-sectional portion of the waveguide is reduced or discretized into a set of smaller segments comprising a mesh. The elements of the mesh are assigned boundary conditions including continuity of tangential electric and magnetic fields resulting in a system of equations. Solution to the system of equations yields the desired results in terms of phase constants and electromagnetic fields. The major advantage of the finite element technique is that the method can be applied to a wide range of arbitrary cross-sectional waveguide geometries, provided that it can be expressed in a mesh with suitable element sizes. Although very

powerful and flexible, the finite element method has the disadvantage of yielding spurious solutions. The spurious solutions have no physical meaning and therefore finite element method solutions must be checked for validity. Often this can be done by examining the field quantities of the solutions to determine if certain physical parameters are satisfied. There are methods outlined in the literature [5] to eliminate spurious solutions however there appears to be a price paid in numerical efficiency.

The perturbation method [7] is a well known method for computing modal cutoff frequencies of an "unknown" waveguide given that one has a solution to a similar "known" system. The perturbation can be, for example, in the form of an inward change in the wall of the waveguide, or also a small change in the material inside the waveguide system. In its practical implementation it is often in the form of an approximation. In the case of the CSW one easily has a "known" system, being that of the square waveguide, and then the perturbation consists of the dielectric septum introduced to the guide. The perturbation method has the advantage of relative ease of formulation however to implement it in its practical form it has two disadvantages. First, the perturbation method does not provide a rigorous expression for the electromagnetic fields. Second, it is an approximate technique that usually results in a reduction of accuracy as the perturbation is increased.

As stated there are several appropriate methods for analyzing the CSW. Both the mode matching and finite element techniques are preferred over the perturbation technique due to the greater accuracy and also since the fields components are more directly obtained in the formulation. The mode matching technique does not suffer from the problem of spurious solutions inherent in the finite element technique. The mode matching analysis was chosen since an arbitrary shaped cross-section was not required, and that the technique has desirable analytical features.

4.3 CSW Modal Solution Technique Using Mode Matching

The mode matching technique is described in the literature [1], [3], [4] and is the technique employed for determining the modal characteristics of the CSW. The mode matching technique is especially well suited for solving the waveguide geometries that are nonseparable but can be treated as piecewise separable. The solution technique for an

inhomogeneously loaded waveguide is based on superposition, and involves the combining of both TE and TM modes to express the results, which are found to be hybrid modes. Hybrid modes are modes that are in general neither purely TE or TM, but contain field components that can only be solved by a combination of both mode sets. A further discussion of hybrid modes is provided in Chapter 5.

Recalling from Chapter 3, the form of solutions for a square waveguide with symmetrical dielectric loading can be obtained using symmetry properties of the fields in the waveguide. The original problem shown in Figure 3-1 is therefore divided into a set of simplified sub problems, referred to as symmetry cases and defined in Figure 3-4. Each of the four symmetry cases imposes a different set of different boundary conditions, bounded by the metallic walls with perfect electric conductors (PEC) and by the axes with PECs and perfect magnetic conductors (PMC), resulting in a set of unique solutions. Figure 4-1 shows the equivalent CSW symmetry cases however further sub-divided into three homogeneous regions. Since each of the three regions are homogeneous, they are piecewise separable and therefore the fields can be expanded into an infinite series for each region. The infinite series is essentially a Fourier series with coefficients that are solved both term-by-term and by using the orthogonality relationships.

In solving for the fields, the concept of magnetic and electric vector potentials are used. The magnetic vector potential $\vec{A}$, and electric vector potential $\vec{F}$ defined by [8] are used to express the magnetic field $\vec{H}$,and electric field $\vec{E}$, as

$$\vec{H} = \vec{H}_A + \vec{H}_F \tag{4.1}$$

and

$$\vec{E} = \vec{E}_A + \vec{E}_F \tag{4.2}$$

respectively, where the fields due to $\vec{A}$ and $\vec{F}$ are given by[1]

$$\vec{H}_A = \frac{1}{\mu}\nabla \times \vec{A} \tag{4.3}$$

$$\vec{H}_F = -j\omega\vec{F} - \frac{j}{\omega\mu\varepsilon}\nabla\left(\nabla \bullet \vec{F}\right) \tag{4.4}$$

[1] A Lorentz gauge is assumed. Also assumed are an $\exp(j\omega t)$ time variation and a source free region for the waveguide analysis.

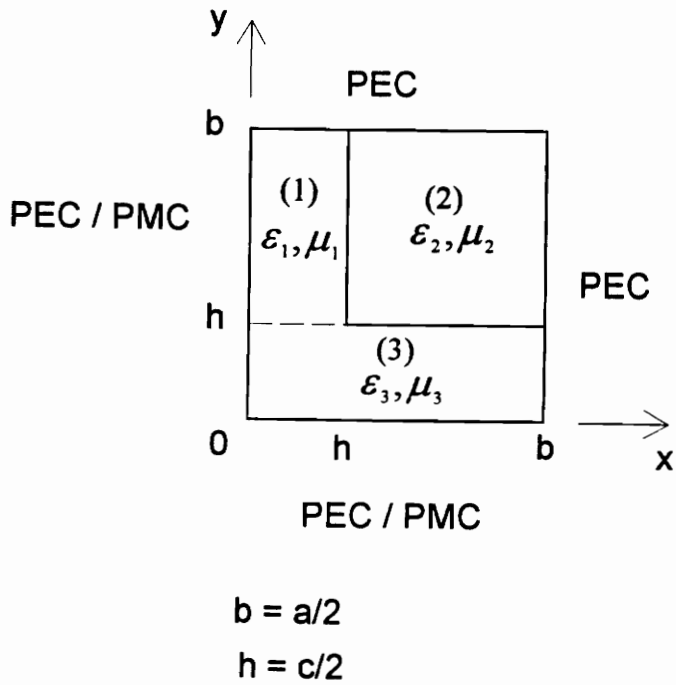

Figure 4-1. Defined regions of the CSW for the symmetry cases.

$$\vec{E}_F = -\frac{1}{\varepsilon}\nabla \times \vec{F} \tag{4.5}$$

$$\vec{E}_A = -j\omega\vec{A} - \frac{j}{\omega\mu\varepsilon}\nabla\left(\nabla \bullet \vec{A}\right). \tag{4.6}$$

The magnetic and electric vector potentials in a source free region must satisfy the vector wave equations

$$\left(\nabla^2 + k^2\right)\vec{A} = 0 \tag{4.7}$$

$$\left(\nabla^2 + k^2\right)\vec{F} = 0 \tag{4.8}$$

respectively, and k is the wave number defined below.

An infinitely long 2-dimensional cross-section of the waveguide is used in the analyses of the waveguide portion of the CSW. Solution of the CSW is accomplished using the mode matching technique which is based on a series expansion of the fields. The electric and magnetic fields are of the form

$$\vec{E}^{(i)} = \sum_{n=1}^{N}\left\{E_{xn}^{(i)}\hat{x} + E_{yn}^{(i)}\hat{y} + E_{zn}^{(i)}\hat{z}\right\}e^{-jk_z z} \tag{4.9}$$

$$\vec{H}^{(i)} = \sum_{n=1}^{N}\left\{H_{xn}^{(i)}\hat{x} + H_{yn}^{(i)}\hat{y} + H_{zn}^{(i)}\hat{z}\right\}e^{-jk_z z} \tag{4.10}$$

where i = 1,2,3 for each region of the waveguide as defined in Figure 4-1. In equations (4.9) and (4.10), $E_{xn}^{(i)}$, $H_{xn}^{(i)}$ and so on will be referred to a *field coefficients* and are defined below. The subscript xn will be used to denote the nth term of the x-directed component (and similarly for y- and z-directed components). The harmonic function $e^{-jk_z z}$ is assumed for waves traveling in the z-direction, where k_z is the axial or longitudinal phase constant (also referred to as the propagation constant or wave number). By superposition, the fields are solved in each region in terms of $TE^{(x)}$ and $TM^{(x)}$ modes and later combined.

- For $TE^{(x)}$ solutions a series expansion of the following form is used:

$$\vec{F} = \sum_{n=1}^{N} F_{xn}^{(i)} \hat{x} \tag{4.11}$$

$$\vec{A} = 0 \tag{4.12}$$

where F_{xn} is a scalar function and each term in the series expansion must satisfy the scalar wave equation

$$\left(\nabla^2 + k^2\right) F_{xn} = 0. \tag{4.13}$$

The proper form of solution of (4.13) is given by

$$F_{xn}^{(i)} = F_n^{(i)} \varphi(\tilde{k}_{xn}^{(i)} x) \varphi(\tilde{k}_{yn}^{(i)} y) e^{-jk_z z} \tag{4.14}$$

where $\varphi(\xi)$ are the harmonic functions $\cos(\xi)$ and $\sin(\xi)$ with the appropriate arguments. For $TE^{(x)}$ modes in each of the regions, we define transverse phase constants (propagation constants or wave numbers) $\tilde{k}_{xn}^{(i)}$ and $\tilde{k}_{yn}^{(i)}$ corresponding to the x- and y-directions respectively, which are complex in general. In equation (4.14), $F_n^{(i)}$ will be referred to as *amplitude constants*, which is also complex in general. It is assumed that the waves are traveling in the z-direction, hence $e^{-jk_z z}$ is used, where k_z is the phase constant in the z-direction. For a wave propagating in the axial direction, a necessary condition for matching of the z-components of the fields is that k_z must be the same in all three regions.

Given that each of the regions of the CSW are piecewise separable, the propagation constants satisfy the separability condition

$$k_i^2 = \tilde{k}_{xn}^{(i)2} + \tilde{k}_{yn}^{(i)2} + k_z^2 \tag{4.15}$$

The propagation constant in an unbounded medium is given by $k_i = \omega\sqrt{\mu_i \varepsilon_i}$, where μ_i is the permeability and ε_i is the permittivity of the medium, and (i) is the region. For the CSW, $k_1 = k_3$ since these two regions consist of the same medium.

- For $TM^{(x)}$ solutions a series expansion of the following form is used:

$$\vec{A} = \sum_{n=1}^{N} A_{xn}^{(i)} \hat{x} \tag{4.16}$$

$$\vec{F} = 0 \tag{4.17}$$

where A_{xn} is a scalar function and each term in the series expansion must also satisfy the scalar wave equation

$$\left(\nabla^2 + k^2\right) A_{xn} = 0. \tag{4.18}$$

The proper form of solutions is given by

$$A_{xn}^{(i)} = A_n^{(i)} \varphi(k_{xn}^{(i)} x) \varphi(k_{yn}^{(i)} y) e^{-jk_z z} \tag{4.19}$$

and $\varphi(\xi)$ are the harmonic functions $\cos(\xi)$ and $\sin(\xi)$with the appropriate arguments. For $TM^{(x)}$ modes in each of the regions, we define phase constants $k_{xn}^{(i)}$ and $k_{yn}^{(i)}$ corresponding to the x- and y-directions respectively, which are complex in general. In equation (4.19), $A_n^{(i)}$ will be referred to as *amplitude constants*. It is assumed that the waves are traveling in the z-direction, hence $e^{-jk_z z}$ is also used here.

Given that each of the regions of the CSW as defined are piecewise separable system, the phase constants will satisfy the separability condition

$$k_i^2 = k_{xn}^{(i)2} + k_{yn}^{(i)2} + k_z^2 \tag{4.20}$$

where i =1,2,3 for each of the regions.

Solving the CSW problem requires imposing boundary conditions at each of the interfaces within the waveguide regions. The tangential components of the fields at the $(x = h)$ interface of regions (1) and (2) are matched if

$$\begin{Bmatrix} H_{xn,zn}^{(1)}(x = h) \\ E_{xn,zn}^{(1)}(x = h) \end{Bmatrix} = \begin{Bmatrix} H_{xn,zn}^{(2)}(x = h) \\ E_{xn,zn}^{(2)}(x = h) \end{Bmatrix} \tag{4.21}$$

and

$$\tilde{k}_{yn}^{(1)} = \tilde{k}_{yn}^{(2)} \tag{4.22}$$

$$k_{yn}^{(1)} = k_{yn}^{(2)}. \tag{4.23}$$

The conditions given by (4.22) and (4.23) are necessary to match transverse y-directed components of the fields, which are equated term-by-term. From (4.15) and (4.20) where i =1,2 and noting that k_z is the same in all regions of the guide, one obtains

$$\tilde{k}_{xn}^{(1)2} - \tilde{k}_{xn}^{(2)2} = k_1^2 - k_2^2 \tag{4.24}$$

$$k_{xn}^{(1)2} - k_{xn}^{(2)2} = k_1^2 - k_2^2 \tag{4.25}$$

Boundary conditions must next be satisfied by equating the tangential components of the electric and magnetic fields on the boundaries between regions: (1 and 3); and regions (2 and 3). The coefficients are solved by multiplying each of the four tangential field components evaluated at (y = h) by an appropriate orthogonal function and integrating over x on the interval from 0 to b, expressed as

$$\int_0^b \sum_{n=1}^{N} \begin{Bmatrix} H_{xn,zn}^{(1),(2)}(y=h) \\ E_{xn,zn}^{(1),(2)}(y=h) \end{Bmatrix} \varphi(k_{xp}^{(3)}x)\, dx = \int_0^b \sum_{n=1}^{N} \begin{Bmatrix} H_{xn,zn}^{(3)}(y=h) \\ E_{xn,zn}^{(3)}(y=h) \end{Bmatrix} \varphi(k_{xp}^{(3)}x)\, dx \tag{4.26}$$

To simplify the right side of (4.26), the following orthogonallity relationships are used:

$$\int_0^b \varphi(k_n x)\varphi(k_p x)\, dx = \begin{cases} b/2, n = p \neq 1 \\ 0, \quad n \neq p \end{cases} \tag{4.27}$$

The four boundary conditions given in equations (4.26) result in a set of four equations of the following form. For simplicity, we define these four equations using the following notation:

$$a_1(p)A_p^{(3)} - \sum_{n=1}^{N} A_n^{(1)} b_1(p,n) = 0 \tag{4.28}$$

$$f_1(p)F_p^{(3)} - \sum_{n=1}^{N} F_n^{(1)} g_1(p,n) = 0 \tag{4.29}$$

$$a_2(p)A_p^{(3)} - \sum_{n=1}^{N}\left\{A_n^{(1)} b_2(p,n)\right\} + f_2(p)F_p^{(3)} - \sum_{n=1}^{N}\left\{F_n^{(1)} g_2(p,n)\right\} = 0 \tag{4.30}$$

$$a_3(p)A_p^{(3)} - \sum_{n=1}^{N}\left\{A_n^{(1)} b_3(p,n)\right\} + f_3(p)F_p^{(3)} - \sum_{n=1}^{N}\left\{F_n^{(1)} g_3(p,n)\right\} = 0 \tag{4.31}$$

As defined in equations (4.28) through (4.31), $a_{1,2,3}(p)$, $b_{1,2,3}(p,n)$, $f_{1,2,3}(p)$ and $g_{1,2,3}(p,n)$ will be referred to as *series coefficients* and $A_n^{(i)}$ and $F_n^{(i)}$ will be referred to as *amplitude constants*.

When evaluated, the left side of (4.26) will contain a summation and integrals which cannot be simplified by the use of the orthogonal properties used in simplifying the right side. Therefore, the following integrals are defined for later use, with the appropriate arguments (the appropriate phase constants will be substituted in place of s and t):

$$\mathrm{I}_1(s,t) = \int_0^h \sin sx \, \sin tx \, dx \tag{4.32}$$

$$\mathrm{I}_2(s,t) = \int_0^h \cos sx \, \cos tx \, dx \tag{4.33}$$

$$\mathrm{I}_3(s,t) = \int_0^h \sin sx \, \cos tx \, dx \tag{4.34}$$

$$\mathrm{I}_4(s,t) = \int_h^b \sin s(x-b) \, \sin tx \, dx \tag{4.35}$$

$$\mathrm{I}_5(s,t) = \int_h^b \cos s(x-b) \, \cos tx \, dx \tag{4.36}$$

$$\mathrm{I}_6(s,t) = \int_h^b \sin s(x-b) \, \cos tx \, dx \tag{4.37}$$

$$\mathrm{I}_7(s,t) = \int_h^b \cos s(x-b) \, \sin tx \, dx \tag{4.38}$$

The above solution technique is used to obtain a system of equations for each of the symmetry cases, as described in the following sections.

4.4 Form of Solutions

4.4.1 Even / Odd Symmetry Solutions

By referring to the even/odd symmetry case defined in Figure 3-4 and by enforcing the appropriate boundary conditions defined for each of the three regions in Figure 4-1, one obtains the electric vector potentials for the $TE^{(x)}$ modes given by

$$F_{xn}^{(1)} = F_n^{(1)} \cos(\tilde{k}_{xn}^{(1)} x) \cos\left[\tilde{k}_{yn}^{(1)}(y-b)\right] e^{-jk_z z} \tag{4.39}$$

$$F_{xn}^{(2)} = F_n^{(2)} \sin\left[\tilde{k}_{xn}^{(2)}(x-b)\right] \cos\left[\tilde{k}_{yn}^{(2)}(y-b)\right] e^{-jk_z z} \tag{4.40}$$

$$F_{xn}^{(3)} = F_n^{(3)} \cos(\tilde{k}_{xn}^{(3)} x) \cos(\tilde{k}_{yn}^{(3)} y) e^{-jk_z z} \tag{4.41}$$

For the $TM^{(x)}$ modes the magnetic vector potentials for each of the three regions are given by

$$A_{xn}^{(1)} = A_n^{(1)} \sin(k_{xn}^{(1)} x) \sin\left[k_{yn}^{(1)}(y-b)\right] e^{-jk_z z} \tag{4.42}$$

$$A_{xn}^{(2)} = A_n^{(2)} \cos\left[k_{xn}^{(2)}(x-b)\right] \sin\left[k_{yn}^{(2)}(y-b)\right] e^{-jk_z z} \tag{4.43}$$

$$A_{xn}^{(3)} = A_n^{(3)} \sin(k_{xn}^{(3)} x) \sin(k_{yn}^{(3)} y) e^{-jk_z z} \tag{4.44}$$

where:

$$k_{xn}^{(3)} = \tilde{k}_{xn}^{(3)} = \frac{(2n-1)\pi}{2b} \tag{4.45}$$

The electric and magnetic field series expansion coefficients are computed using the vector potentials substituted into equations (4.1) through (4.6). The field coefficients are omitted from this section however are provided in Appendix A, for this symmetry case (and each of the other symmetry cases). Using the tangential field coefficients and from equations (4.21) through (4.25) , one obtains:

$$\frac{F_n^{(1)}}{\varepsilon_1} \cos \tilde{k}_{xn}^{(1)} h = \frac{F_n^{(2)}}{\varepsilon_2} \sin \tilde{k}_{xn}^{(2)} (h-b) \tag{4.46}$$

$$\frac{F_n^{(1)}}{\mu_1\varepsilon_1}\tilde{k}_{xn}^{(1)}\sin\tilde{k}_{xn}^{(1)}h=-\frac{F_n^{(2)}}{\mu_2\varepsilon_2}\tilde{k}_{xn}^{(2)}\cos\tilde{k}_{xn}^{(2)}(h-b) \tag{4.47}$$

$$\frac{A_n^{(1)}}{\mu_1}\sin k_{xn}^{(1)}h=\frac{A_n^{(2)}}{\mu_2}\cos k_{xn}^{(2)}(h-b) \tag{4.48}$$

$$\frac{A_n^{(1)}}{\mu_1\varepsilon_1}k_{xn}^{(1)}\sin k_{xn}^{(1)}h=-\frac{A_n^{(2)}}{\mu_2\varepsilon_2}k_{xn}^{(2)}\cos k_{xn}^{(2)}(h-b) \tag{4.49}$$

The three equations (4.24), (4.46) and (4.47) are used to determine $\tilde{k}_{xn}^{(1)}$, $\tilde{k}_{xn}^{(2)}$ and $F_n^{(2)}$ in terms of $F_n^{(1)}$. Similarly, equations (4.25), (4.48) and (4.49) are used to determine , $k_{xn}^{(1)}$, $k_{xn}^{(2)}$ and $A_n^{(2)}$ and in terms of $A_n^{(1)}$.

Using the tangential field series expansions, and the equations and definitions given in (4.26) through (4.38), the series coefficients are obtained as:

$$a_1(p)=\frac{b}{2\mu_1\varepsilon_1}\left(k_1^2-k_{xp}^{(3)2}\right)\sin k_{yp}^{(3)}h \tag{4.50}$$

$$\begin{aligned} b_1(p,n)=&\frac{1}{\mu_1\varepsilon_1}\left(k_1^2-k_{xn}^{(1)2}\right)\sin k_{yn}^{(1)}(h-b)\mathrm{I}_1(k_{xn}^{(1)},k_{xp}^{(3)})+\\ &\frac{1}{\mu_2\varepsilon_2}\frac{A_n^{(2)}}{A_n^{(1)}}\left(k_2^2-k_{xn}^{(2)2}\right)\sin k_{yn}^{(2)}(h-b)\mathrm{I}_7(k_{xn}^{(2)},k_{xp}^{(3)}) \end{aligned} \tag{4.51}$$

$$f_1(p)=\frac{b}{2\mu_1\varepsilon_1}\left(k_1^2-\tilde{k}_{xp}^{(3)2}\right)\cos\tilde{k}_{yp}^{(3)}h \tag{4.52}$$

$$\begin{aligned} g_1(p,n)=&\frac{1}{\mu_1\varepsilon_1}\left(k_1^2-\tilde{k}_{xn}^{(1)2}\right)\cos\tilde{k}_{yn}^{(1)}(h-b)\mathrm{I}_2(\tilde{k}_{xn}^{(1)},\tilde{k}_{xp}^{(3)})+\\ &\frac{1}{\mu_2\varepsilon_2}\frac{F_n^{(2)}}{F_n^{(1)}}\left(k_2^2-\tilde{k}_{xn}^{(2)2}\right)\cos\tilde{k}_{yn}^{(2)}(h-b)\mathrm{I}_6(\tilde{k}_{xn}^{(2)},\tilde{k}_{xp}^{(3)}) \end{aligned} \tag{4.53}$$

$$a_2(p)=\frac{-bk_z}{2\omega\mu_1\varepsilon_1}k_{xp}^{(3)}\sin k_{yp}^{(3)}h \tag{4.54}$$

$$b_2(p,n) = -\frac{k_z k_{xn}^{(1)}}{\omega\mu_1\varepsilon_1}\sin k_{yn}^{(1)}(h-b)\,\mathrm{I}_2(k_{xn}^{(1)},k_{xp}^{(3)}) + \frac{k_z k_{xn}^{(2)}}{\omega\mu_2\varepsilon_2}\frac{A_n^{(2)}}{A_n^{(1)}}\sin k_{yn}^{(2)}(h-b)\,\mathrm{I}_6(k_{xn}^{(2)},k_{xp}^{(3)}) \tag{4.55}$$

$$f_2(p) = \frac{-b}{2\varepsilon_1}\tilde{k}_{yp}^{(3)}\sin\tilde{k}_{yp}^{(3)}h \tag{4.56}$$

$$g_2(p,n) = \frac{-1}{\varepsilon_1}\tilde{k}_{yn}^{(1)}\sin\tilde{k}_{yn}^{(1)}(h-b)\,\mathrm{I}_2(\tilde{k}_{xn}^{(1)},\tilde{k}_{xp}^{(3)}) - \frac{1}{\varepsilon_2}\tilde{k}_{yn}^{(2)}\sin\tilde{k}_{yn}^{(2)}(h-b)\,\mathrm{I}_6(\tilde{k}_{xn}^{(2)},\tilde{k}_{xp}^{(3)}) \tag{4.57}$$

$$a_3(p) = \frac{-b}{2\mu_1}k_{yp}^{(3)}\cos k_{yp}^{(3)}h \tag{4.58}$$

$$b_3(p,n) = \frac{-1}{\mu_1}k_{yn}^{(1)}\cos k_{yn}^{(1)}(h-b)\,\mathrm{I}_1(k_{xn}^{(1)},k_{xp}^{(3)}) - \frac{1}{\mu_2}\frac{A_n^{(2)}}{A_n^{(1)}}k_{yn}^{(2)}\cos k_{yn}^{(2)}(h-b)\,\mathrm{I}_7(k_{xn}^{(2)},k_{xp}^{(3)}) \tag{4.59}$$

$$f_3(p) = \frac{bk_z}{2\omega\mu_1\varepsilon_1}\tilde{k}_{xp}^{(3)}\cos\tilde{k}_{yp}^{(3)}h \tag{4.60}$$

$$g_3(p,n) = \frac{k_z\tilde{k}_{xn}^{(1)}}{\omega\mu_1\varepsilon_1}\cos\tilde{k}_{yn}^{(1)}(h-b)\,\mathrm{I}_1(\tilde{k}_{xn}^{(1)},\tilde{k}_{xp}^{(3)}) - \frac{k_z\tilde{k}_{xn}^{(2)}}{\omega\mu_2\varepsilon_2}\frac{F_n^{(2)}}{F_n^{(1)}}\cos\tilde{k}_{yn}^{(2)}(h-b)\,\mathrm{I}_7(\tilde{k}_{xn}^{(2)},\tilde{k}_{xp}^{(3)}) \tag{4.61}$$

A discussion of how the results of this section are used to obtain cutoff frequencies, bandwidth and electric and magnetic fields is provided in the Chapter 5.

4.4.2 Odd / Even Symmetry Solutions

By referring to the odd/even symmetry case defined in Figure 3-4 and by enforcing the appropriate boundary conditions defined for each of the three regions in Figure 4-1, one obtains the electric vector potentials for the $TE^{(x)}$ modes given by

$$F_{xn}^{(1)} = F_n^{(1)} \sin(\tilde{k}_{xn}^{(1)} x) \cos\left[\tilde{k}_{yn}^{(1)}(y-b)\right] e^{-jk_z z} \tag{4.62}$$

$$F_{xn}^{(2)} = F_n^{(2)} \sin\left[\tilde{k}_{xn}^{(2)}(x-b)\right] \cos\left[\tilde{k}_{yn}^{(2)}(y-b)\right] e^{-jk_z z} \tag{4.63}$$

$$F_{xn}^{(3)} = F_n^{(3)} \sin(\tilde{k}_{xn}^{(3)} x) \sin(\tilde{k}_{yn}^{(3)} y) e^{-jk_z z} \tag{4.64}$$

For the $TM^{(x)}$ modes the magnetic vector potentials for each of the three regions are given by

$$A_{xn}^{(1)} = A_n^{(1)} \cos(k_{xn}^{(1)} x) \sin\left[k_{yn}^{(1)}(y-b)\right] e^{-jk_z z} \tag{4.65}$$

$$A_{xn}^{(2)} = A_n^{(2)} \cos\left[k_{xn}^{(2)}(x-b)\right] \sin\left[k_{yn}^{(2)}(y-b)\right] e^{-jk_z z} \tag{4.66}$$

$$A_{xn}^{(3)} = A_n^{(3)} \cos(k_{xn}^{(3)} x) \cos(k_{yn}^{(3)} y) e^{-jk_z z} \tag{4.67}$$

where:

$$k_{xn}^{(3)} = \tilde{k}_{xn}^{(3)} = \frac{(n-1)\pi}{b} \tag{4.68}$$

The electric and magnetic field expansion coefficients are computed using the vector potentials substituted into equations (4.1) through (4.6) and are provided in Appendix A. Using the using the tangential field coefficients and from equations (4.21) through (4.25), one obtains:

$$\frac{F_n^{(1)}}{\varepsilon_1} \sin \tilde{k}_{xn}^{(1)} h = \frac{F_n^{(2)}}{\varepsilon_2} \sin \tilde{k}_{xn}^{(2)} (h-b) \tag{4.69}$$

$$\frac{F_n^{(1)}}{\mu_1 \varepsilon_1} \tilde{k}_{xn}^{(1)} \cos \tilde{k}_{xn}^{(1)} h = \frac{F_n^{(2)}}{\mu_2 \varepsilon_2} \tilde{k}_{xn}^{(2)} \cos \tilde{k}_{xn}^{(2)} (h-b) \tag{4.70}$$

$$\frac{A_n^{(1)}}{\mu_1}\cos k_{xn}^{(1)}h = \frac{A_n^{(2)}}{\mu_2}\cos k_{xn}^{(2)}(h-b) \tag{4.71}$$

$$\frac{A_n^{(1)}}{\mu_1\varepsilon_1}k_{xn}^{(1)}\sin k_{xn}^{(1)}h = \frac{A_n^{(2)}}{\mu_2\varepsilon_2}k_{xn}^{(2)}\sin k_{xn}^{(2)}(h-b) \tag{4.72}$$

Equations (4.24), (4.69) and (4.70) are used to determine $\tilde{k}_{xn}^{(1)}$, $\tilde{k}_{xn}^{(2)}$ and $F_n^{(2)}$ in terms of $F_n^{(1)}$. Similarly, equations (4.25), (4.71) and (4.72) are used to determine $k_{xn}^{(1)}$, $k_{xn}^{(2)}$ and $A_n^{(2)}$ in terms of $A_n^{(1)}$.

Using the equations and definitions given in (4.26) through (4.38), the series coefficients for the odd/even symmetry case are given by:

$$a_1(p) = \frac{b}{2\mu_1\varepsilon_1}\left(k_1^2 - k_{xp}^{(3)2}\right)\cos k_{yp}^{(3)}h\,(1+\delta_p) \tag{4.73}$$

$$\begin{aligned} b_1(p,n) = {} & \frac{1}{\mu_1\varepsilon_1}\left(k_1^2 - k_{xn}^{(1)2}\right)\sin k_{yn}^{(1)}(h-b)\,\mathrm{I}_2(k_{xn}^{(1)}, k_{xp}^{(3)}) + \\ & \frac{1}{\mu_2\varepsilon_2}\frac{A_n^{(2)}}{A_n^{(1)}}\left(k_2^2 - k_{xn}^{(2)2}\right)\sin k_{yn}^{(2)}(h-b)\,\mathrm{I}_5(k_{xn}^{(2)}, k_{xp}^{(3)}) \end{aligned} \tag{4.74}$$

$$f_1(p) = \frac{b}{2\mu_1\varepsilon_1}\left(k_1^2 - \tilde{k}_{xp}^{(3)2}\right)\sin \tilde{k}_{yp}^{(3)}h\,u(p-2) \tag{4.75}$$

$$\begin{aligned} g_1(p,n) = {} & \frac{u(p-2)}{\mu_1\varepsilon_1}\left(k_1^2 - \tilde{k}_{xn}^{(1)2}\right)\cos \tilde{k}_{yn}^{(1)}(h-b)\,\mathrm{I}_1(\tilde{k}_{xn}^{(1)}, \tilde{k}_{xp}^{(3)}) + \\ & \frac{u(p-2)}{\mu_2\varepsilon_2}\frac{F_n^{(2)}}{F_n^{(1)}}\left(k_2^2 - \tilde{k}_{xn}^{(2)2}\right)\cos \tilde{k}_{yn}^{(2)}(h-b)\,\mathrm{I}_4(\tilde{k}_{xn}^{(2)}, \tilde{k}_{xp}^{(3)}) \end{aligned} \tag{4.76}$$

$$a_2(p) = \frac{bk_z}{2\omega\mu_1\varepsilon_1}k_{xp}^{(3)}\cos k_{yp}^{(3)}h \tag{4.77}$$

$$b_2(p,n) = \frac{k_z k_{xn}^{(1)}}{\omega\mu_1\varepsilon_1} \sin k_{yn}^{(1)}(h-b)\,\mathrm{I}_1(k_{xn}^{(1)}, k_{xp}^{(3)}) + \frac{k_z k_{xn}^{(2)}}{\omega\mu_2\varepsilon_2} \frac{A_n^{(2)}}{A_n^{(1)}} \sin k_{yn}^{(2)}(h-b)\,\mathrm{I}_4(k_{xn}^{(2)}, k_{xp}^{(3)}) \tag{4.78}$$

$$f_2(p) = \frac{b}{2\varepsilon_1} \tilde{k}_{yp}^{(3)} \cos \tilde{k}_{yp}^{(3)} h\; u(p-2) \tag{4.79}$$

$$g_2(p,n) = \frac{-1}{\varepsilon_1} \tilde{k}_{yp}^{(1)} \sin \tilde{k}_{yn}^{(1)}(h-b)\,\mathrm{I}_1(\tilde{k}_{xn}^{(1)}, \tilde{k}_{xp}^{(3)})\; u(p-2) - \frac{1}{\varepsilon_2} \tilde{k}_{yn}^{(2)} \frac{F_n^{(2)}}{F_n^{(1)}} \sin \tilde{k}_{yn}^{(2)}(h-b)\,\mathrm{I}_4(\tilde{k}_{xn}^{(2)}, \tilde{k}_{xp}^{(3)})\; u(p-2) \tag{4.80}$$

$$a_3(p) = \frac{b}{2\mu_1} k_{yp}^{(3)} \sin k_{yp}^{(3)} h\; (1+\delta_p) \tag{4.81}$$

$$b_3(p,n) = \frac{-1}{\mu_1} k_{yn}^{(1)} \cos k_{yn}^{(1)}(h-b)\,\mathrm{I}_2(k_{xn}^{(1)}, k_{xp}^{(3)}) - \frac{1}{\mu_2} \frac{A_n^{(2)}}{A_n^{(1)}} k_{yn}^{(2)} \cos k_{yn}^{(2)}(h-b)\,\mathrm{I}_5(k_{xn}^{(2)}, k_{xp}^{(3)}) \tag{4.82}$$

$$f_3(p) = \frac{-bk_z}{2\omega\mu_1\varepsilon_1} \tilde{k}_{xp}^{(3)} \sin \tilde{k}_{yp}^{(3)} h\; u(p-2) \tag{4.83}$$

$$g_3(p,n) = \frac{-k_z \tilde{k}_{xn}^{(1)}}{\omega\mu_1\varepsilon_1} \cos \tilde{k}_{yn}^{(1)}(h-b)\,\mathrm{I}_2(\tilde{k}_{xn}^{(1)}, \tilde{k}_{xp}^{(3)})\; u(p-2) - \frac{k_z \tilde{k}_{xn}^{(2)}}{\omega\mu_2\varepsilon_2} \frac{F_n^{(2)}}{F_n^{(1)}} \cos \tilde{k}_{yn}^{(2)}(h-b)\,\mathrm{I}_5(\tilde{k}_{xn}^{(2)}, \tilde{k}_{xp}^{(3)})\; u(p-2) \tag{4.84}$$

In equations (4.73) through (4.84) we define

$$\delta_p = \begin{cases} 1, & p = 1 \\ 0, & p \neq 1 \end{cases} \tag{4.85}$$

and

$$u(p-2)=\begin{cases}1, & p\geq 2\\ 0, & p=1\end{cases}. \tag{4.86}$$

Equations (4.85) and (4.86) occur as the result of degenerate cases, when $\sin\tilde{k}_{x1}^{(3)}x=0$ and $\cos\tilde{k}_{x1}^{(3)}x=1$ are substituted into (4.27). A discussion of how the results of this section are used to obtain cutoff frequencies and fields is provided in the Chapter 5.

4.4.3 Even / Even Symmetry Solutions

The even/even symmetry case is similar to that of the even/odd symmetry case except that the lower boundary on the x-axis is a PMC instead of a PEC, as shown in Figures 3-4 and 4-1. The boundary conditions and electric vector potentials are the same as those given in the even/odd symmetry case in regions (1) and (2), and therefore $F_{xn}^{(1)}$ and $F_{xn}^{(2)}$ are given by equations (4.39) and (4.40) respectively. Likewise, the magnetic vector potentials $A_{xn}^{(1)}$ and $A_{xn}^{(2)}$ given by (4.42) and (4.43), respectively. However, the boundary conditions in region 3 are unique to this symmetry case and the vector potentials are given by

$$F_{xn}^{(3)}=F_n^{(3)}\cos(\tilde{k}_{xn}^{(3)}x)\sin(\tilde{k}_{yn}^{(3)}y)e^{-jk_z z} \tag{4.87}$$

$$A_{xn}^{(3)}=A_n^{(3)}\sin(k_{xn}^{(3)}x)\cos(k_{yn}^{(3)}y)e^{-jk_z z} \tag{4.88}$$

Since the vector potentials (and also the field series expansion coefficients) in regions 1 and 2 are the same as for the even/odd symmetry case, it follows that equations (4.46) through (4.49) are used to determine $\tilde{k}_{xn}^{(1,2)}$, $k_{xn}^{(1,2)}$, $A_n^{(2)}$ and $F_n^{(2)}$ in terms of $A_n^{(1)}$ and $F_n^{(1)}$. In region 3, the transverse phase constant is given by

$$k_{xn}^{(3)}=\tilde{k}_{xn}^{(3)}=\frac{(2n-1)\pi}{2b} \tag{4.89}$$

The matrix coefficients are also for the even/even symmetry case are very similar to those obtained in the even/odd case, since the fields are the same in regions (1) and (2). Therefore, using symmetry properties; $b_1(p,n)$ is given by (4.51), $g_1(p,n)$ is given by (4.53), $b_2(p,n)$ is given by (4.55), $g_2(p,n)$ is given by (4.57), $b_3(p,n)$ is given by (4.59),

and $g_3(p,n)$ is given by (4.61). Since the vector potentials and field coefficients in region 3 are unique to this symmetry case, we obtain results given as follows:

$$a_1(p) = \frac{b}{2\mu_1\varepsilon_1}\left(k_1^2 - k_{xp}^{(3)2}\right)\cos k_{yp}^{(3)}h \tag{4.90}$$

$$f_1(p) = \frac{b}{2\mu_1\varepsilon_1}\left(k_1^2 - \tilde{k}_{xp}^{(3)2}\right)\sin \tilde{k}_{yp}^{(3)}h \tag{4.91}$$

$$a_2(p) = \frac{-bk_z}{2\omega\mu_1\varepsilon_1}k_{xp}^{(3)}\cos k_{yp}^{(3)}h \tag{4.92}$$

$$f_2(p) = \frac{b}{2\varepsilon_1}\tilde{k}_{yp}^{(3)}\cos \tilde{k}_{yp}^{(3)}h \tag{4.93}$$

$$a_3(p) = \frac{b}{2\mu_1}k_{yp}^{(3)}\sin k_{yp}^{(3)}h \tag{4.94}$$

$$f_3(p) = \frac{bk_z}{2\omega\mu_1\varepsilon_1}\tilde{k}_{xp}^{(3)}\sin \tilde{k}_{yp}^{(3)}h \ . \tag{4.95}$$

Chapter 5 provides a discussion of how the results of this section are used to obtain cutoff frequencies and fields.

4.4.4 Odd / Odd Symmetry Solutions

The odd/odd symmetry case is similar to that of the odd/even symmetry case except that the lower boundary on the x-axis is a PEC instead of a PMC, as shown in Figures 3-4 and 4-1. Therefore, the electric vector potentials are the same as those given in the odd/even symmetry case in regions 1 and 2, and hence $F_{xn}^{(1)}$ and $F_{xn}^{(2)}$ are given by equations (4.62) and (4.63) respectively. Likewise, the magnetic vector potentials $A_{xn}^{(1)}$ and $A_{xn}^{(2)}$ given by (4.65) and (4.66), respectively. However, the boundary conditions in region 3 are unique to the symmetry case and the vector potentials are given by

$$F_{xn}^{(3)} = F_n^{(3)} \sin(\tilde{k}_{xn}^{(3)} x) \cos(\tilde{k}_{yn}^{(3)} y) e^{-jk_z z} \tag{4.96}$$

$$A_{xn}^{(3)} = A_n^{(3)} \cos(k_{xn}^{(3)} x) \sin(k_{yn}^{(3)} y) e^{-jk_z z} \tag{4.97}$$

Since the vector potentials in regions 1 and 2 are the same as for the odd/even symmetry case, it follows that equations (4.69) through (4.72) are used to determine $\tilde{k}_{xn}^{(1,2)}$, $k_{xn}^{(1,2)}$, $A_n^{(2)}$ and $F_n^{(2)}$ in terms of $A_n^{(1)}$ and $F_n^{(1)}$. In region 3 the transverse phase constant is given by

$$k_{xn}^{(3)} = \tilde{k}_{xn}^{(3)} = \frac{(n-1)\pi}{b} \tag{4.98}$$

The series coefficients are also for the odd/odd symmetry case are very similar to those obtained in the odd/even case, since the fields are the same in regions 1 and 2. Therefore, using symmetry properties; $b_1(p,n)$ is given by (4.73), $g_1(p,n)$ is given by (4.76), $b_2(p,n)$ is given by (4.78), $g_2(p,n)$ is given by (4.80), $b_3(p,n)$ is given by (4.82), and $g_3(p,n)$ is given by (4.84). Since the vector potentials and field coefficients in region 3 are unique to this symmetry case, we obtain results given as follows

$$a_1(p) = \frac{b}{2\mu_1\varepsilon_1}\left(k_1^2 - k_{xp}^{(3)2}\right) \sin k_{yp}^{(3)} h \, (1+\delta_p) \tag{4.99}$$

$$f_1(p) = \frac{b}{2\mu_1\varepsilon_1}\left(k_1^2 - \tilde{k}_{xp}^{(3)2}\right) \cos \tilde{k}_{yp}^{(3)} h \, u(p-2) \tag{4.100}$$

$$a_2(p) = \frac{-bk_z}{2\omega\mu_1\varepsilon_1} k_{xp}^{(3)} \sin k_{yp}^{(3)} h \tag{4.101}$$

$$f_2(p) = \frac{-b}{2\varepsilon_1} \tilde{k}_{yp}^{(3)} \sin \tilde{k}_{yp}^{(3)} h \, u(p-2) \tag{4.102}$$

$$a_3(p) = \frac{-b}{2\mu_1} k_{yp}^{(3)} \cos k_{yp}^{(3)} h \, (1+\delta_p) \tag{4.103}$$

$$f_3(p) = \frac{-bk_z}{2\omega\mu_1\varepsilon_1} \tilde{k}_{xp}^{(3)} \cos \tilde{k}_{yp}^{(3)} h \, u(p-2) \tag{4.104}$$

Chapter 5 provides a discussion of how the results of this section are used to obtain cutoff frequencies and fields.

4.5 References for Chapter 4

[1] T. Itoh, *Numerical Techniques for Microwave and Millimeter-Wave Passive Structures*, New York: John Wiley and Sons, 1989.

[2] S.M. Saad, "A review of numerical methods for the analysis of arbitrary-shaped microwave and optical dielectric waveguides," *IEEE Trans. on Microwave Theory Tech.*, vol. MTT-33, no. 10, pp. 894-899, October 1985.

[3] K. Solbach and I. Wolff, "Electromagnetic fields and the phase constants of dielectric image lines," *IEEE Trans. on Microwave Theory Tech.*, vol. MTT-26, no. 4, pp. 266-274, February 1978.

[4] W. Schlosser and H.G. Unger, "Partially filled waveguides and surface waveguides of rectangular cross-section," *Advances in Microwaves*, Edited by L.Young, New York: Academic Press, 1966.

[5] Editors: P. Silvester and G. Pelosi, *Finite Elements for Wave Electromagnetics*, New York: IEEE Press, 1994.

[6] Z.J. Csendes and P. Silvester, " Numerical Solution of dielectric loaded waveguide: I-finite element analysis", *IEEE Trans. on Microwave Theory Tech.*, vol. MTT-18, NO.12, pp. 1124-1131, February 1970. {finite elements}

[7] R.F. Harrington, *Time Harmonic Electromagnetic Fields*, New York: McGraw Hill, Chapter 7, 1961. {perturbation method}

[8] C.A. Balanis, *Advanced Engineering Electromagnetics*, New York: John Wiley and Sons, 1989.

CHAPTER 5

CSW NUMERICAL RESULTS

5.1 Overview of Numerical Study

In this chapter the results of a numerical study of the modal characteristics of the CSW are presented. The investigation of the CSW is in terms of modal features, cutoff frequencies, and field plots using the equations derived in the previous chapter. A study is performed with relative permittivity ε_r and septum thickness c/a as parameters of variation. Also explained in this chapter are convergence considerations and a phenomena observed as mode splitting. The relationship of the modal cutoff frequencies as a function of symmetry and mode type is described. Key elements necessary to the bandwidth extension of the square waveguide are shown.

5.2 Numerical Computational Procedure

5.2.1 General Case Hybrid Modes

A system of equations was derived in Chapter 4 using the mode matching technique. In deriving the system of equations, a series expansion and superposition of $TE^{(x)}$ and $TM^{(x)}$ modes in piecewise separable regions of the waveguide resulted in a system of equations of the form

$$a_1(p)A_p^{(3)} - \sum_{n=1}^{N} A_n^{(1)} b_1(p,n) = 0 \tag{5.1}$$

$$f_1(p)F_p^{(3)} - \sum_{n=1}^{N} F_n^{(1)} g_1(p,n) = 0 \tag{5.2}$$

$$a_2(p)A_p^{(3)} - \sum_{n=1}^{N}\left\{A_n^{(1)}b_2(p,n)\right\} + f_2(p)F_p^{(3)} - \sum_{n=1}^{N}\left\{F_n^{(1)}g_2(p,n)\right\} = 0 \tag{5.3}$$

$$a_3(p)A_p^{(3)} - \sum_{n=1}^{N}\left\{A_n^{(1)}b_3(p,n)\right\} + f_3(p)F_p^{(3)} - \sum_{n=1}^{N}\left\{F_n^{(1)}g_3(p,n)\right\} = 0 \tag{5.4}$$

where the series coefficients are also given in Chapter 4. The series coefficients are given according to the four symmetry properties of the equivalent CSW system as defined in Chapter 3. Given that the system of equations has been obtained, the task is then to solve for the cutoff frequencies, phase constants, and fields for use in further chapters when investigating the bandwidth, propagation and radiation characteristics of the CSW. For the three region system in Chapter 4, it is assumed that $\mu_1 = \mu_2 = \mu_3 = \mu_o$, $\varepsilon_1 = \varepsilon_3 = \varepsilon_d$ and $\varepsilon_2 = \varepsilon_o$. Therefore the three region system in Figure 4-1 has the same constitutive relations as the system shown in Figure 3-1.

The system of equations given by (5.1) through (5.4) is exact as $N \to \infty$, however as a practical matter must be truncated for numerical evaluation on a digital computer. The process of truncating the series results in an approximation to the exact series. To simplify the notation, we define sub-matrices for use in the following discussion on solving the system of equations. The coefficients given in equations (5.1) through (5.4) with single arguments p, include $a_1(p)$, $a_2(p)$, $a_3(p)$, $f_1(p)$, $f_2(p)$ and $f_3(p)$. Considering $a_1(p)$, we define a diagonal matrix with $p = 1 \cdots N$ given by

$$\bar{a}_1 \equiv \begin{bmatrix} a_1(1) & 0 & \cdots & 0 \\ 0 & a_1(2) & \cdots & 0 \\ \vdots & \vdots & \ddots & \vdots \\ 0 & 0 & \cdots & a_1(N) \end{bmatrix} \tag{5.5}$$

Similarly, we define $\bar{a}_2$, $\bar{a}_3$, $\bar{f}_1$, $\bar{f}_2$ and $\bar{f}_3$ as diagonal matrices having the form given by (5.5).

The coefficients given in equations (5.1) through (5.4) with two arguments p and n, include $b_1(p,n)$, $b_2(p,n)$, $b_3(p,n)$, $g_1(p,n)$, $g_2(p,n)$ and $g_3(p,n)$. Considering $b_1(p,n)$, we define a $N \times N$ matrix with $p = 1 \cdots N$ and $n = 1 \cdots N$ given by

$$\bar{b}_1 \equiv \begin{bmatrix} b_1(1,1) & b_1(1,2) & \cdots & b_1(1,N) \\ b_1(2,1) & b_1(2,2) & \cdots & b_1(2,N) \\ \vdots & \vdots & \ddots & \vdots \\ b_1(N,1) & b_1(N,2) & \cdots & b_1(N,N) \end{bmatrix} \tag{5.6}$$

Similarly, we define $\bar{b}_2$, $\bar{b}_3$, $\bar{g}_1$, $\bar{g}_2$, and $\bar{g}_3$ as $N \times N$ matrices having the form given by (5.6).

The amplitude coefficients in equations (5.1) through (5.4) include $A_n^{(1)}$, $A_p^{(3)}$, $F_n^{(1)}$ and $F_p^{(3)}$. Considering $A_n^{(1)}$ we define a $1 \times N$ matrix as follows

$$\bar{A}^{(1)} \equiv \begin{bmatrix} A_1^{(1)} \\ A_2^{(1)} \\ \vdots \\ A_N^{(1)} \end{bmatrix}. \tag{5.7}$$

We also define $1 \times N$ matrices $\bar{A}_p^{(3)}$, $\bar{F}_n^{(1)}$ and $\bar{F}_p^{(3)}$ by the form given in equation (5.7).

Using this notation, the system of equations can be written compactly as

$$\left[\begin{array}{c|c|c|c} \bar{a}_1 & \bar{b}_1 & 0 & 0 \\ \hline 0 & 0 & \bar{f}_1 & \bar{g}_1 \\ \hline \bar{a}_2 & \bar{b}_2 & \bar{f}_2 & \bar{g}_2 \\ \hline \bar{a}_3 & \bar{b}_3 & \bar{f}_3 & \bar{g}_3 \end{array}\right] \left[\begin{array}{c} \bar{A}^{(3)} \\ \hline \bar{A}^{(1)} \\ \hline \bar{F}^{(3)} \\ \hline \bar{F}^{(1)} \end{array}\right] = \left[\begin{array}{c} 0 \\ \hline 0 \\ \hline 0 \\ \hline 0 \end{array}\right] \tag{5.8}$$

where the left side of (5.8) is a $4N \times 4N$ square matrix. In obtaining non-trivial solutions of (5.8) it is required that

$$\det \left[\begin{array}{c|c|c|c} \bar{a}_1 & \bar{b}_1 & 0 & 0 \\ \hline 0 & 0 & \bar{f}_1 & \bar{g}_1 \\ \hline \bar{a}_2 & \bar{b}_2 & \bar{f}_2 & \bar{g}_2 \\ \hline \bar{a}_3 & \bar{b}_3 & \bar{f}_3 & \bar{g}_3 \end{array}\right] = 0 \tag{5.9}$$

where det[ ] is the determinant of the matrix argument. The left side of equation (5.9) will be referred to as the *characteristic equation*. The non-trivial solutions of the

characteristic equation are found as a function of one of the two possible parameters. The characteristic equation is a function of the phase constant in the z-direction k_z and frequency ω. Solutions are obtained by either holding frequency ω constant and varying k_z, or by holding k_z constant and varying ω, and then determining the zero crossings. The characteristic equation is found to be either real or imaginary and can be positive or negative. There are an infinite number of solutions of the characteristic equation, each occurring at a different k_z and ω. The solutions are obtainable by use of a root finding algorithm, such as the bisection method [1]. The bisection method which guarantees convergence was found to be significantly more reliable than other derivative based root finding algorithms such as Newton's method.

Once a nontrivial solution to the characteristic equation is found, then both k_z and ω are held constant and one is interested in solving for the amplitude constants so that fields can be obtained. Under these conditions linear algebra techniques [7] are then used to solve the system given by (5.8) with the series coefficients held constant. It was found that the non-trivial solutions for all modes investigated, equation (5.8) has the following characteristic:

$$\operatorname{rank}\begin{bmatrix} \bar{a}_1 & \bar{b}_1 & 0 & 0 \\ 0 & 0 & \bar{f}_1 & \bar{g}_1 \\ \bar{a}_2 & \bar{b}_2 & \bar{f}_2 & \bar{g}_2 \\ \bar{a}_3 & \bar{b}_3 & \bar{f}_3 & \bar{g}_3 \end{bmatrix} = 4N-1 \tag{5.10}$$

where rank[ ] is the rank of the matrix argument. Equation (5.10) is an observation that was found to be valid for all modal solutions discussed in this chapter and further investigated during the research. The physical implications of (5.10) are that given a solution has been found, there is only one set of amplitude constants and field patterns that are found to exist for a given k_z and ω. The amplitude constants of a system with rank $4N-1$ are found to be a $1 \times 4N$ vector given by

$$\begin{bmatrix} \bar{A}^{(3)} \\ \bar{A}^{(1)} \\ \bar{F}^{(3)} \\ \bar{F}^{(1)} \end{bmatrix} = \eta \begin{bmatrix} \bar{a}_1 & \bar{b}_1 & 0 & 0 \\ 0 & 0 & \bar{f}_1 & \bar{g}_1 \\ \bar{a}_2 & \bar{b}_2 & \bar{f}_2 & \bar{g}_2 \\ \bar{a}_3 & \bar{b}_3 & \bar{f}_3 & \bar{g}_3 \end{bmatrix} \tag{5.11}$$

where $\eta[\ ]$ is the nullspace of the matrix argument.

Once the propagation constants and the amplitude coefficients are found, the fields are computed using the field coefficients given in Appendix A. The characteristic equation given by (5.8) assumes both $TE^{(x)}$ and $TM^{(x)}$ modes present to obtain solutions. This consequently is the most general form of solutions and the results are in general found to be hybrid modes. Hybrid modes are modes that are neither purely $TE^{(z)}$ or $TM^{(z)}$ but are combinations of both modes types, as is obtained by the use of superposition of both mode types. In the Sections 5.2.2 and 5.2.3, we will discuss special cases for the solving the system of equations in which the hybrid modes degenerate to pure $TE^{(z)}$ or $TM^{(z)}$ modes at cutoff frequency. Hybrid modes are classified and discussed in more detail in Section 5.3.

5.2.2 Cutoff Frequencies of TE Modes.

By inspection of the system of equations (5.1) through (5.4) and the corresponding series coefficients it is found that the system can be reduced to a simpler form at cutoff frequency, i.e., when $k_z = 0$. From Chapter 4, one can assume the solutions are constructed from only $TM^{(x)}$ series expansions; that is, $\vec{F} = 0$ and $\vec{A} = A_x\hat{x}$ at the cutoff frequency. Then the system of equations reduces to

$$a_1(p)A_p^{(3)} - \sum_{n=1}^{N} A_n^{(1)} b_1(p,n) = 0 \tag{5.12}$$

$$a_3(p)A_p^{(3)} - \sum_{n=1}^{N} \left\{ A_n^{(1)} b_3(p,n) \right\} = 0 \tag{5.13}$$

By using the notation and definitions given by equations (5.5) through (5.7), one can write

$$\left[\begin{array}{c|c} \bar{a}_1 & \bar{b}_1 \\ \hline \bar{a}_3 & \bar{b}_3 \end{array}\right] \left[\begin{array}{c} \bar{A}^{(3)} \\ \hline \bar{A}^{(1)} \end{array}\right] = \left[\begin{array}{c} 0 \\ \hline 0 \end{array}\right] \tag{5.14}$$

Equation (5.14) reduces the $4N \times 4N$ system to a $2N \times 2N$ system resulting in a simplification and 1/4 reduction in computer time. By analogy to Section 5.2.1, the system of equations and the characteristic equation is obtained using

$$\det\left[\begin{array}{c|c}\bar{a}_1 & \bar{b}_1 \\ \hline \bar{a}_3 & \bar{b}_3\end{array}\right] = 0. \tag{5.15}$$

During the numerical investigations, non-trivial solutions of the characteristic equation, the condition

$$\operatorname{rank}\left[\begin{array}{c|c}\bar{a}_1 & \bar{b}_1 \\ \hline \bar{a}_3 & \bar{b}_3\end{array}\right] = 2N - 1 \tag{5.16}$$

was observed for all modes investigated. By analogy to the discussion in Section 5.2.1, the amplitude coefficients are found to be a $1 \times 2N$ vector given by

$$\left[\begin{array}{c}\bar{A}^{(3)} \\ \hline \bar{A}^{(1)}\end{array}\right] = \eta\left[\begin{array}{c|c}\bar{a}_1 & \bar{b}_1 \\ \hline \bar{a}_3 & \bar{b}_3\end{array}\right]. \tag{5.17}$$

The modes having solutions of this form have a zero axial or z-directed electric field and hence are purely $\mathrm{TE}^{(z)}$. This condition is found to only occur at the cutoff frequency of a given mode.

5.2.3 Cutoff Frequencies of TM Modes

By analogy to Section 5.2.2, the system of equations (5.1) through (5.4) can be reduced to a simpler form at cutoff frequency, i.e., when $k_z = 0$ to obtain modes that are purely $\mathrm{TM}^{(z)}$. One can assume the solutions are constructed from only $\mathrm{TE}^{(x)}$ series expansions; that is, $\vec{F} = F_x\hat{x}$ and $\vec{A} = 0$ at the cutoff frequency. Then the system of equations reduces to

$$f_1(p)F_p^{(3)} - \sum_{n=1}^{N} F_n^{(1)} g_1(p,n) = 0 \tag{5.18}$$

$$f_2(p)F_p^{(3)} - \sum_{n=1}^{N} \left\{F_n^{(1)} g_2(p,n)\right\} = 0 \tag{5.19}$$

By using the notation and definitions given by equations (5.5) through (5.7), one can write the characteristic equation in terms of a $2N \times 2N$ matrix as.

$$\left[\begin{array}{c|c} \bar{f}_1 & \bar{g}_1 \\ \hline \bar{f}_2 & \bar{g}_2 \end{array}\right]\left[\begin{array}{c} \bar{F}^{(3)} \\ \hline \bar{F}^{(1)} \end{array}\right] = \left[\begin{array}{c} 0 \\ \hline 0 \end{array}\right] \tag{5.20}$$

By analogy to Section 5.2.2, the system of equations and the characteristic equation solutions are obtained using the same procedure given in equations (5.15) through (5.17). The modes computed for this case are found to be $TM^{(z)}$ at cutoff, meaning the axial magnetic field is zero.

5.3 Classifying the Modes in the CSW

The modal characteristics of the CSW are found by solving for the nontrivial zeros of the characteristic equations, as given in Sections 5.2. To perform the numerical studies on the CSW, software programs were developed using Matlab on an IBM DOS compatible DX2-486-66MHz machine. Once the nontrivial solutions are obtained, the phase constants, amplitude constants and electromagnetic fields are readily computed. The characteristics of the dominant mode and several of the important higher-order modes are now discussed.

In this description of the CSW modal characteristics, we will first describe and classify the resulting hybrid modes observed within the guide. The CSW modes can be classified according to the field structure and symmetry in the guide and to the relationship of the unloaded waveguide degeneracies. For a dielectric loaded waveguide, this can be somewhat confusing because the results are hybrid modes, e.g., neither purely $TE^{(z)}$ nor $TM^{(z)}$, but containing a linear combination of both. Therefore, strictly speaking the notation of using simply $TE^{(z)}$ or $TM^{(z)}$ is no longer accurate except at cutoff frequency.

In classifying the modes one can use notation consistent with that found in the literature [2]. Table 5-1 provides a general summary of notation useful in defining waveguide modes. In an unloaded (or homogeneously filled) square waveguide the $TE^{(z)}$ contains an axial magnetic field component H_z, however the axial electric field E_z is zero. These modes are referred to as H modes. Likewise, in an unloaded square waveguide, the

$TM^{(z)}$ modes contain an axial electric field, however the axial magnetic field is zero. Therefore these modes are referred to as E modes.

Table 5-1.
Classification of Modes for Unloaded and Loaded Waveguides.

Mode type ($\varepsilon_r = 1$)	Axial Fields ($\varepsilon_r = 1$)	Notation of Collin [2] ($\varepsilon_r = 1$)	Hybrid mode type when $\varepsilon_r > 1$
$TE^{(z)}$	$H_z \neq 0, E_z = 0$	H-type	HE_{mn}
$TM^{(z)}$	$H_z \neq 0, E_z = 0$	E-type	EH_{mn}

The usefulness of this notation becomes apparent when considering hybrid modes. A hybrid mode is classified according the whether the mode is dominated by E- or H-modes. For the HE_{mn}-modes the dominant axial component is the magnetic field, and for the EH_{mn} the dominant axial field component is the electric field. In the investigation of the CSW, it is found that the $TE^{(z)}$ become HE_{mn} when the dielectric insert is placed in the waveguide. Conversely, the $TM^{(z)}$-modes are found to be EH_{mn}-modes when the dielectric insert is placed in the waveguide. A list of the modes for an unloaded square waveguide and the similar CSW hybrid mode counterparts is provided in Table 5-2. The modes hybrid modes shown are classified and named according to the symmetry and similarities of the field components, when compared to the unloaded guide. Shown are the unloaded degenerate waveguide modes, the hybrid names according to Collin [2], and the mode designations referred to in the remainder of this report. As indicated, for simplicity the mode designations used through the remainder of this report will be the unloaded waveguide names with a subscript where appropriate, however it is implied that hybrid modes are referred to in general.

Figures 5-1 through 5-5 illustrate the modal characteristics of the CSW electric and magnetic field plots. Shown are the dominant mode and several of the important higher-order modes. Electromagnetic field plots of additional higher-order modes are provided in Appendix C. The field diagrams of Figures 5-1 through 5-5 are computed using the "Test Case #2" parameters which are defined and referred to in Chapters 6 and 7. The arrows in the field plots indicate the magnitude and direction of the transverse

Table 5-2.

Unloaded Square Waveguide Mode and Similar Hybrid Modes for the CSW.

Unloaded square waveguide mode	Hybrid mode for the CSW per Collin [2]	Mode designations used for the remainder of this report	Symmetry case
TE_{10} or TE_{01}	HE_{10} or HE_{01}	TE_{10} or TE_{01}	even/odd or odd/even
TM_{11}	EH_{11}	TM_{11}	even/even
TE_{11}	HE_{11}	TE_{11}	even/even
TE_{20}	HE_{20L}	TE_{20L}	odd/odd
TE_{20}	HE_{20U}	TE_{20U}	odd/odd
TM_{12}	EH_{12}	TM_{12}	even/odd
TE_{12}	HE_{12}	TE_{12}	even/odd
TM_{13}	EH_{13L}	TM_{13L}	even/even
TM_{13}	EH_{13U}	TM_{13U}	even/even

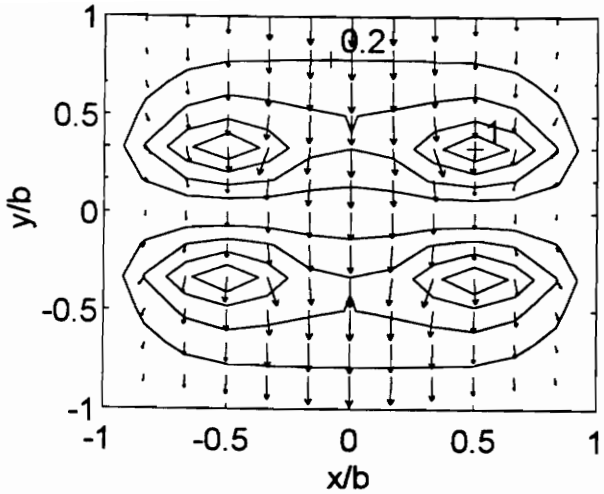

(a)

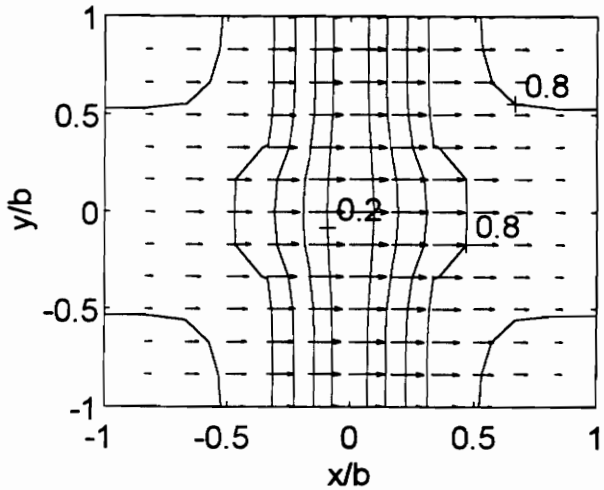

(b)

Figure 5-1. Field distributions of the TE_{10} hybrid mode. (a) Electric field. (b) Magnetic field. Parameters are $\varepsilon_r = 2.56$, c/a = 0.319, frequency = 11.0 GHz, k_z = 260.65rad/s (Test Case # 2). The arrows indicate the magnitude and direction of the transverse field component. Contours indicate the magnitude of the axial (or z-directed) field component in 0.2 increments, normalized to the maximum axial component.

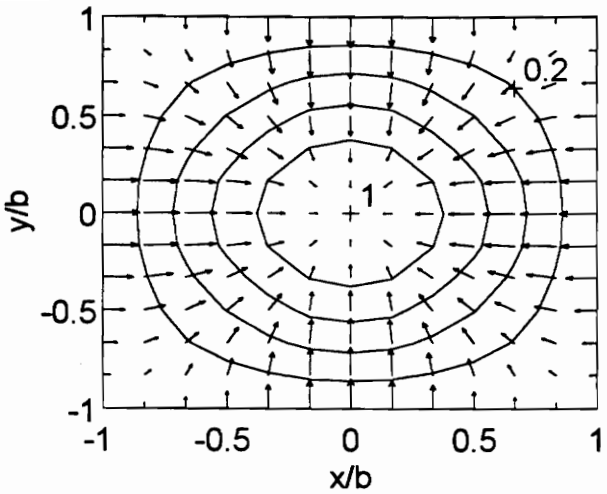

(a)

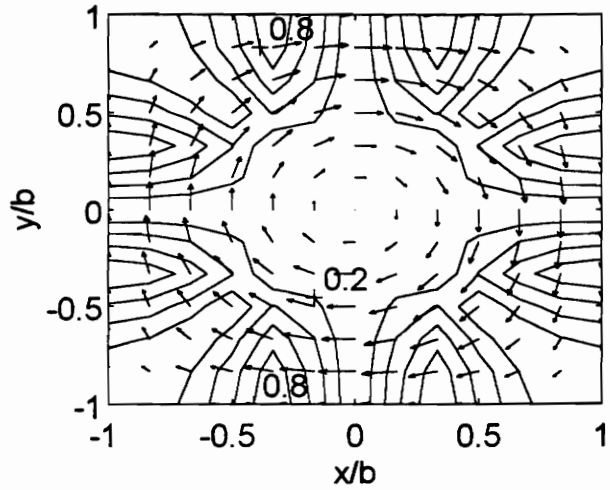

(b)

Figure 5-2. Field distributions of the TM_{11} hybrid mode. (a) Electric field. (b) Magnetic field. Parameters are $\varepsilon_r = 2.56$, c/a = 0.319, frequency = 11.0 GHz, k_z = 174.64 rad/s (Test Case # 2). The arrows indicate the magnitude and direction of the transverse field component. Contours indicate the magnitude of the axial (or z-directed) field component in 0.2 increments, normalized to the maximum axial component.

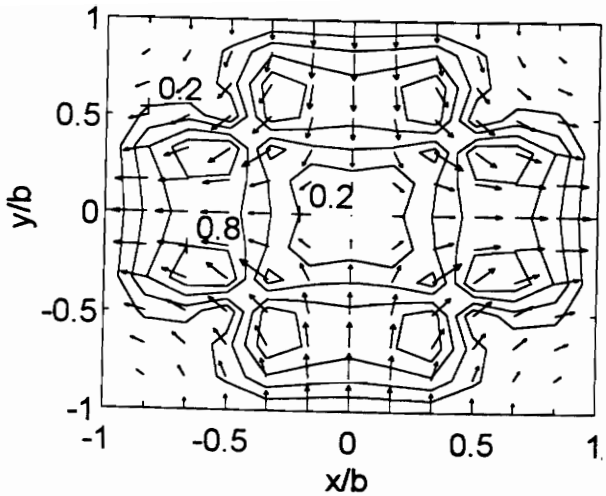

(a)

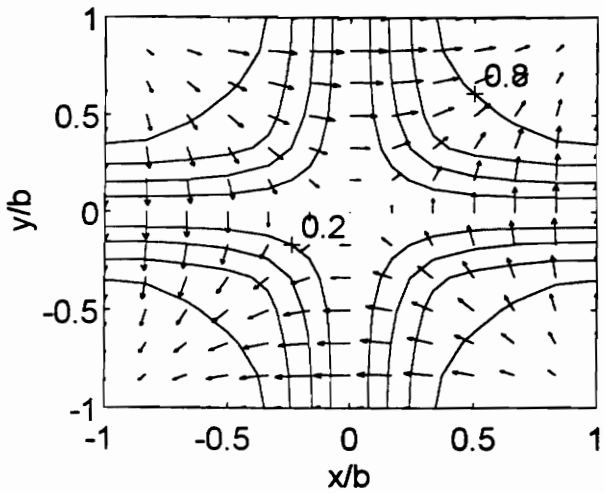

(b)

Figure 5-3. Field distributions of the TE_{11} hybrid mode. (a) Electric field. (b) Magnetic field. Parameters are $\varepsilon_r = 2.56$, $c/a = 0.319$, frequency = 11.0 GHz, $k_z = 130.26$ rad/s (Test Case # 2). The arrows indicate the magnitude and direction of the transverse field component. Contours indicate the magnitude of the axial (or z-directed) field component in 0.2 increments, normalized to the maximum axial component.

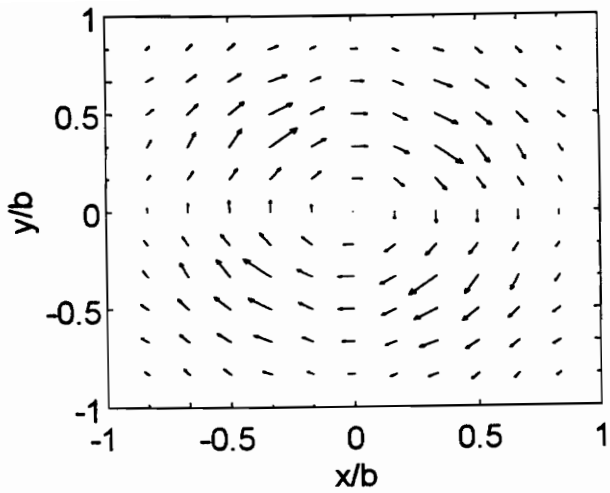

(a)

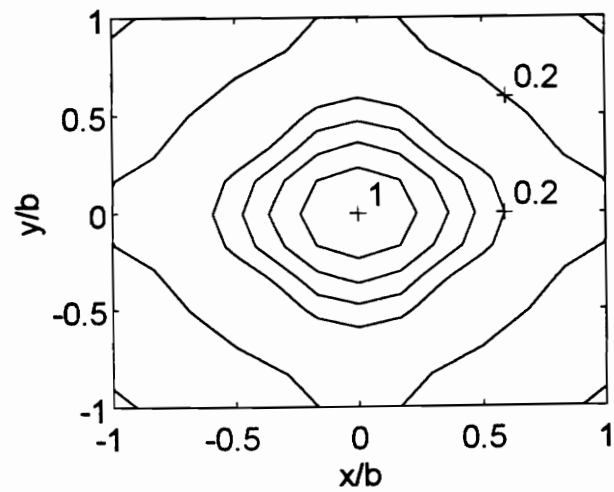

(b)

Figure 5-4. Field distributions of the TE_{20L} hybrid mode. (a) Electric field. (b) Magnetic field. Parameters are $\varepsilon_r = 2.56$, $c/a = 0.319$, cutoff frequency = 15.30 GHz, $k_z = 0$ (Test Case # 2). The arrows indicate the magnitude and direction of the transverse field component. Contours indicate the amplitude of the axial (or z-directed) field component in 0.2 increments, normalized to the maximum axial component.

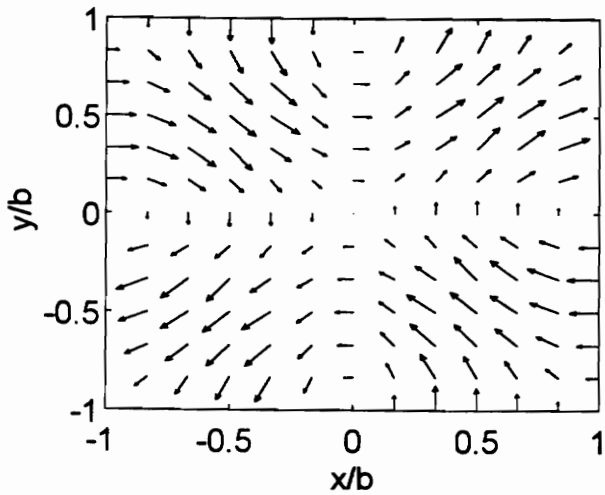

(a)

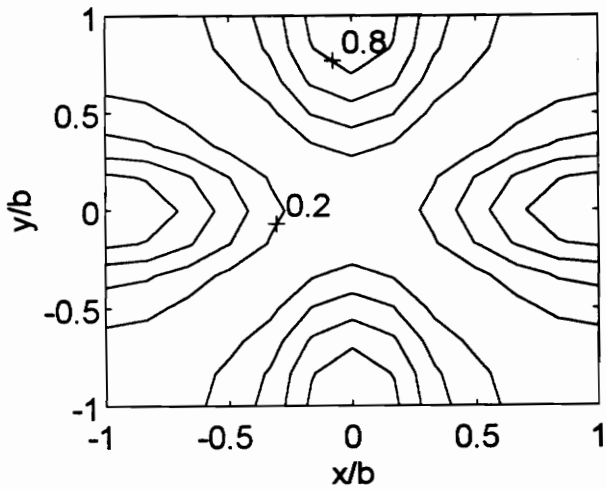

(b)

Figure 5-5. Field distributions of the TE_{20U} hybrid mode. (a) Electric field. (b) Magnetic field. Parameters are $\varepsilon_r = 2.56$, $c/a = 0.319$, cutoff frequency = 16.03 GHz, $k_z = 0$ (Test Case # 2). The arrows indicate the magnitude and direction of the transverse field component. Contours indicate the amplitude of the axial (or z-directed) field component in 0.2 increments, normalized to the maximum axial component.

fields. The solid lines are contour lines showing the magnitude of the axial component of the corresponding field, at contours of 0.2 relative to the maximum axial component. Each of the field plots shown can be compared to the extensive literature (see for example [6]) for which unloaded waveguide field plots are given. One can observe in Figures 5-1 through 5-3 that for the CSW, the TE_{10}, TM_{11} and TE_{11} modes resemble the unloaded waveguide cases, however with some exceptions. Along the axis the dielectric has the affect of redistributing energy in order to satisfy the boundary conditions. This redistribution of energy was observed to depend significantly on permittivity, septum thickness and frequency.

One of the interesting phenomena observed upon introduction of the dielectric insert is the mode splitting phenomena. The TE_{20} mode is found to split into two distinctly different hybrid modes each having different cutoff frequencies. The field plots of the two split modes at cutoff frequency can be found in Figures 5-4 and 5-5, which show significantly different field structures compared to the unloaded waveguide case in the literature [6]. The corresponding mode with the higher or 'upper' cutoff frequency is given the subscript 'U' and referred to as the TE_{20U} mode. The other mode with the 'lower' cutoff frequency is given the subscript 'L' and is referred to as the TE_{20L} mode. The mode splitting phenomena is not unique to the TE_{20} mode. Mode splitting is also found to occur for some higher-order modes with the odd/odd symmetry and certain higher-order modes for even/even symmetry, such as the TM_{13} mode. Mode splitting of the TM_{13} mode results in TM_{13L} and TM_{13U} for the lower and upper hybrid modes respectively. A further discussion of the mode splitting phenomena is provided in Section 5.6.

5.4 Convergence Tests

The mode-matching method is an exact series expansion technique as $N \to \infty$ provided that the series converges. In solving the system and evaluating it on a digital computer one must truncate the series to facilitate computer constraints. A question may then arise as to how many terms of the series are needed and how well the series converges. To test convergence one normally increases the number of terms retained in the series and inspects some quantity (e.g., frequency, k_z , fields etc.) to see if in fact the

series is converging. For the case of this analysis, we are particularly concerned with cutoff frequency since this is a study of bandwidth. Therefore a study of convergence was conducted to ascertain the number terms needed to obtain accurate solutions of frequency given k_z.

Figure 5-6 shows cutoff frequency plotted as a function of number of terms N in the series for various waveguide parameters. Figures 5-6a and 5-6b show convergence tests computed using the same septum thickness $c = a/5$ however with two dielectric constants of ε_r = 2.56 and ε_r = 9.00. Only 2 and 8 terms were needed to obtain convergence to within 1% and .01% respectively of the final computed values. Therefore convergence is not strongly dependent of the relative permittivity for the values computed. Figure 5-6b and 5-6c indicate the effect of decreasing the septum thickness while holding ε_r constant. When c = a/20 the convergence is less rapid and one needs 2 and 14 terms to obtain converge to within 1% and .01% of the final values, respectively.

5.5 Modal Cutoff Frequency Dependence

In Section 5.3 the modes for the CSW were defined and described. In this section the dependence of cutoff frequency on various waveguide parameters is investigated and quantified. The results give insight to which parameter values are suitable for the investigation of bandwidth enhancement using mode filter techniques described in the next chapter. Figure 5-7 shows the cutoff frequencies of the dominant mode and several of the important higher-order modes as a function of the relative permittivity ε_r. In this figure the thickness of the dielectric is held constant at $c = a/6$. As ε_r approaches unity, the modal cutoff frequencies approach the unloaded waveguide values as given in Chapter 3. As shown, the rate of change in cutoff frequency is different among various modes. Figure 5-8 is generate using the same data as in Figure 5-7 except that the cutoff frequencies are plotted as a ratio of cutoff frequencies defined by $f_c(\text{mode}) / f_c(\text{TE}_{10})$ where f_c is the cutoff frequency. Figure 5-8 indicates that relative to the dominant mode, the TM_{11} (even/even symmetry) mode cutoff decreases rapidly as ε_r is increased. The TE_{11} mode (even/even symmetry) remains roughly the same relative to the dominant mode. The TE_{20L} and TE_{20U} (odd/odd symmetry) modes show increased modal cutoff frequency separation relative to the dominant mode and therefore demonstrate one of the

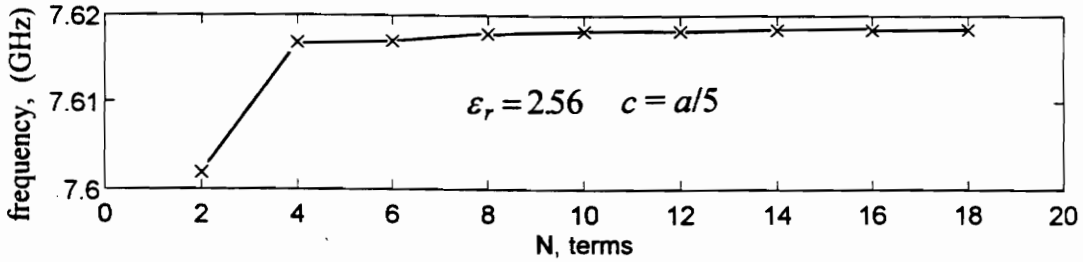

(a)

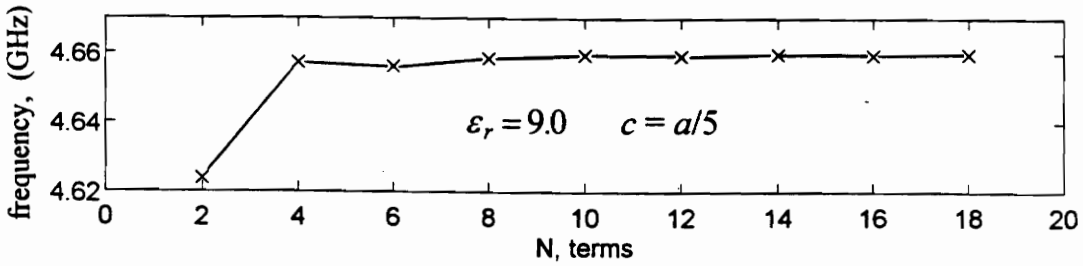

(b)

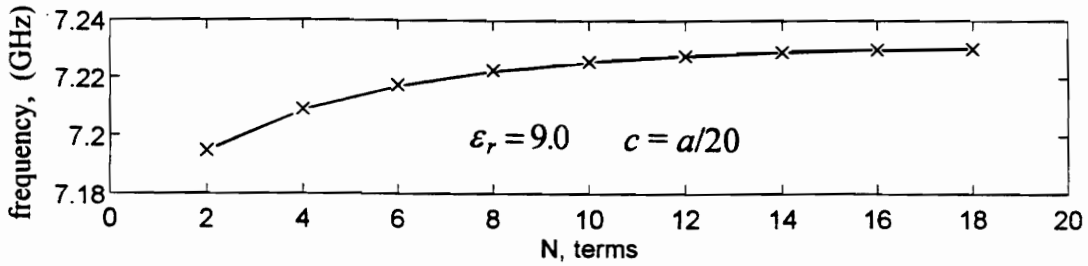

(c)

Figure 5-6. Convergence tests of mode matching technique.

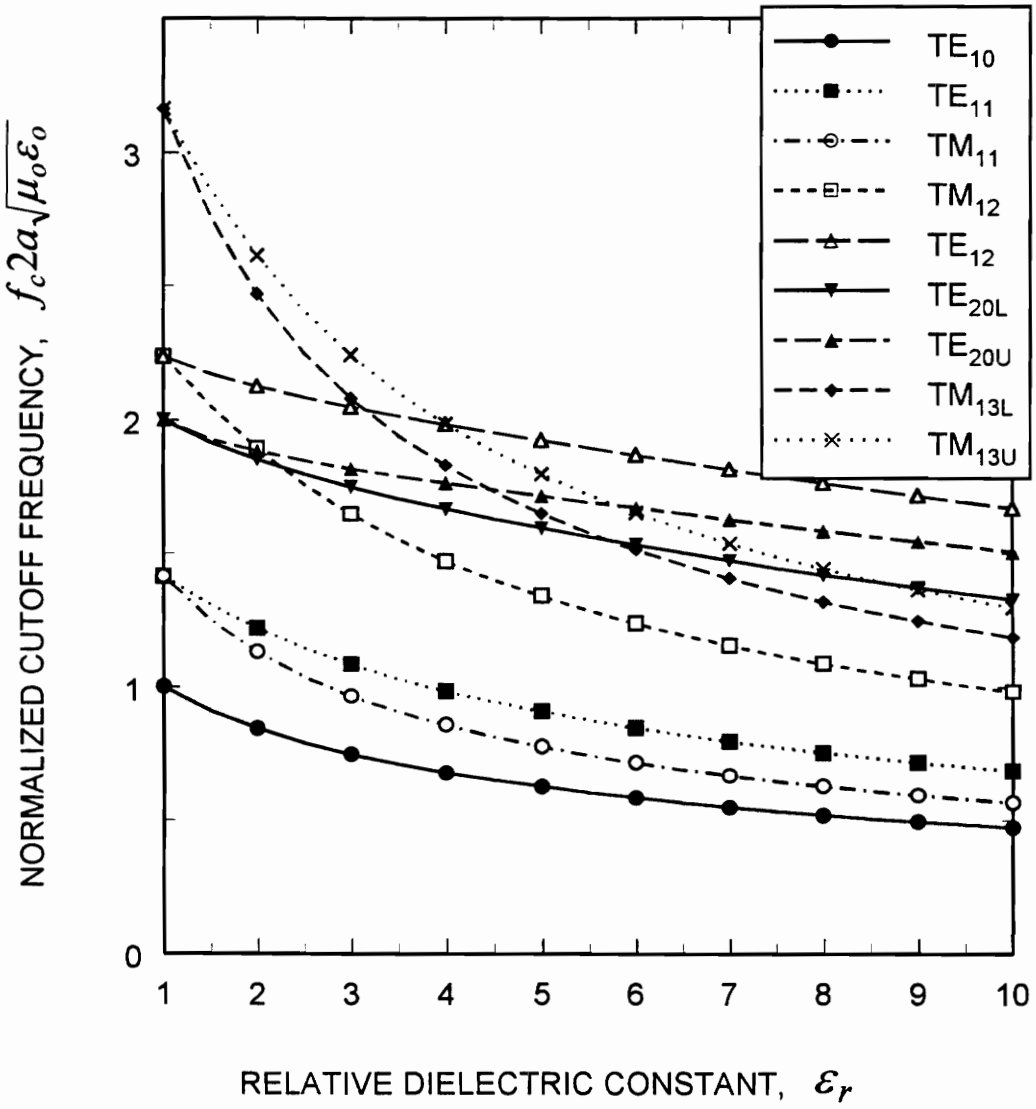

Figure 5-7. Normalized cutoff frequencies vs. ε_r for $c = a/6$. The cutoff frequencies are normalized to the cutoff frequency of the dominant TE_{10} mode in an unloaded square waveguide. Shown are the dominant mode and several relevant higher-order modes.

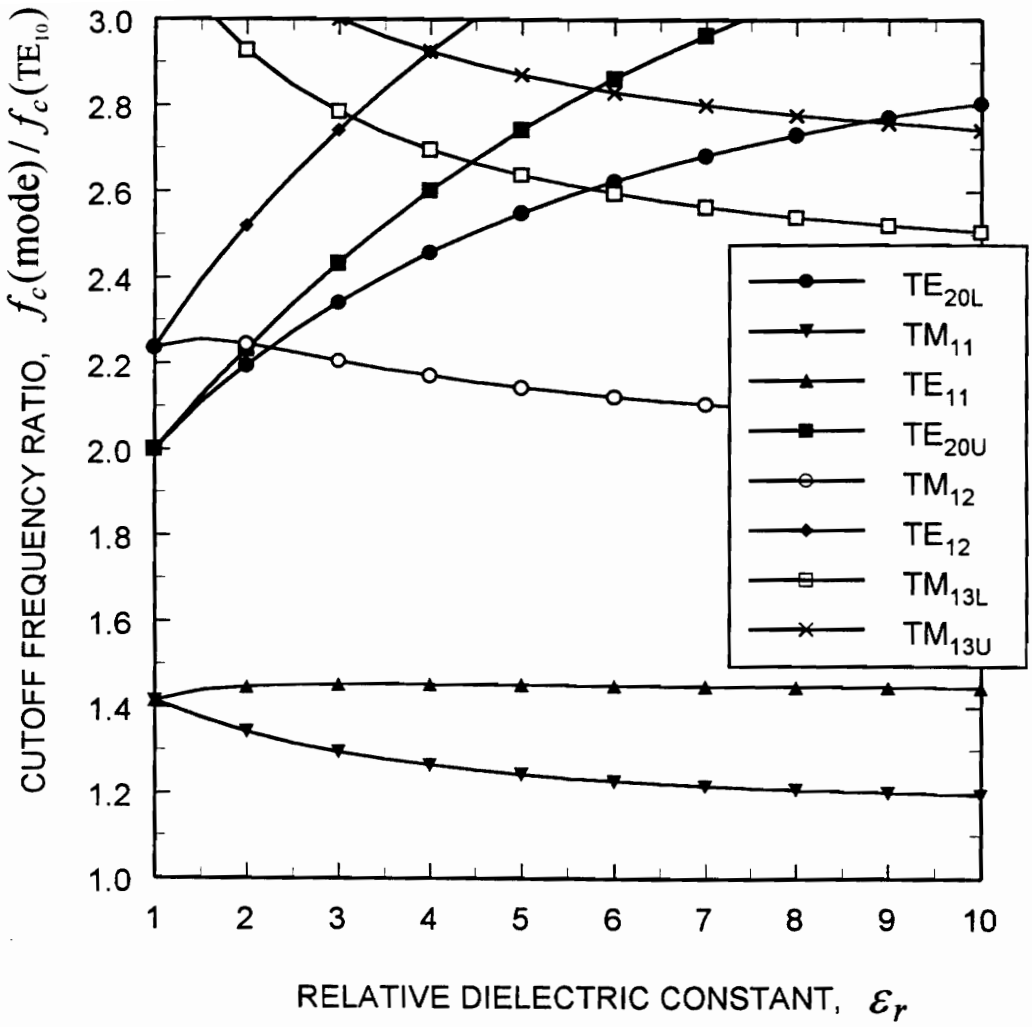

Figure 5-8. Cutoff frequency ratio vs. ε_r for $c = a/6$. The frequencies are normalized to the dominant TE_{10} mode cutoff frequency. Shown are the dominant mode and several relevant higher-order modes.

key characteristics of this study needed for obtaining bandwidth enhancement. Several of the higher-order modes including the TM_{12} (even/odd), the TM_{13L} and TM_{13U} (even/even) modes show a decrease in the cutoff frequency relative to the dominant mode and in fact decrease to below the TE_{20L} mode.

Also of interest is the effect of holding ε_r constant, and varying the relative thickness of the septum on the interval, $0 \le c/a \le 1$ as shown in Figures 5-9 and 5-10 for $\varepsilon_r = 2.56$ and $\varepsilon_r = 9.0$ respectively. Shown are the cutoff frequencies for a given mode relative to the dominant mode cutoff (e.g. $f_c(\text{mode})/f_c(\text{TE}_{10})$). Two key points are made regarding these figures. First, in all cases shown the dielectric loading has the effect of increasing the cutoff frequency separation between the TE_{20L} and the dominant modes. This observation is especially prevalent for dielectric thicknesses of $0 < c/a < 0.5$. Second, for all cases shown, the effect of the dielectric loading is to decrease the ratio of $f_c(\text{TM}_{11})/f_c(\text{TE}_{10})$ and hence the bandwidth of the waveguide. The implications of this are discussed below in further detail.

In Figures 5-8 through 5-10 for dielectric thickness of $0 < c/a < 0.5$, a general trend begins to emerge for the dominant and the first few higher-order modes. The relative of cutoff frequency $f_c(\text{mode})/f_c(\text{TE}_{10})$ of a given mode depends heavily on the symmetry properties of the particular mode. This relationship is summarized in Table 5-3 (however with one additional caveat discussed below). Even/even symmetry modes have a maximum electric field on both axes of the guide and therefore are loaded more heavily than the odd/odd modes which have a minimum in the center of the guide. Even/odd and odd/even modes have a maximum along only one of the axes and therefore change more moderately as a function of the dielectric loading. The caveat to Table 5-3 is that for a given symmetry case, TM modes generally tend to decrease more rapidly than the TE modes of the same symmetry. This can be explained in terms of the relative field strengths for each of the modes. The TM modes generally have a strong axial component of the electric field that is not present in the TE modes, and for modes where this axial component exists in the dielectric region, the result is increased loading relative to the TE modes.

Now that the modal characteristics of the CSW have been analyzed and described, a discussion of the implications on bandwidth is appropriate. In Chapter 3 it was stated

Table 5-3.

Relative Change in Frequency for Each of the Symmetry Cases.

Mode Symmetry Type	Relative Change in Cutoff Frequency as a Function of Mode Symmetry Type
even/even	changes rapidly
even/odd	changes moderately
odd/even	changes moderately
odd/odd	changes slowly

that from the onset of the investigation of the CSW, the concept of the bandwidth extension is based on: a) increased mode separation between the dominant mode and the TE_{20} mode and, b) the use of mode filters to force the TE_{11} and TM_{11} modes to essentially become non-propagating. Assuming successful mode filter demonstration, from Figures 5-9 and 5-10 the bandwidth is limited by either the TM_{12} or TE_{20L} modes[1]. For the case of $\varepsilon_r = 2.56$ from Figure 5-9 the maximum bandwidth under these constraints is about 2.23:1 and occurs at about occurs at c/a of about 0.1 and remains relatively constants to within about 2.20:1 for c/a of 0.3. For the case of $\varepsilon_r = 9.0$ as shown in Figure 5-10 a maximum bandwidth about 2.20:1 occurs at about c/a = 0.02 and c/a = 0.43.

[1] The validity of this assumption is considered further in Chapter 6, when mode filters are investigated. A discussion on filtering of other additional modes is discussed in Chapter 10 under future work.

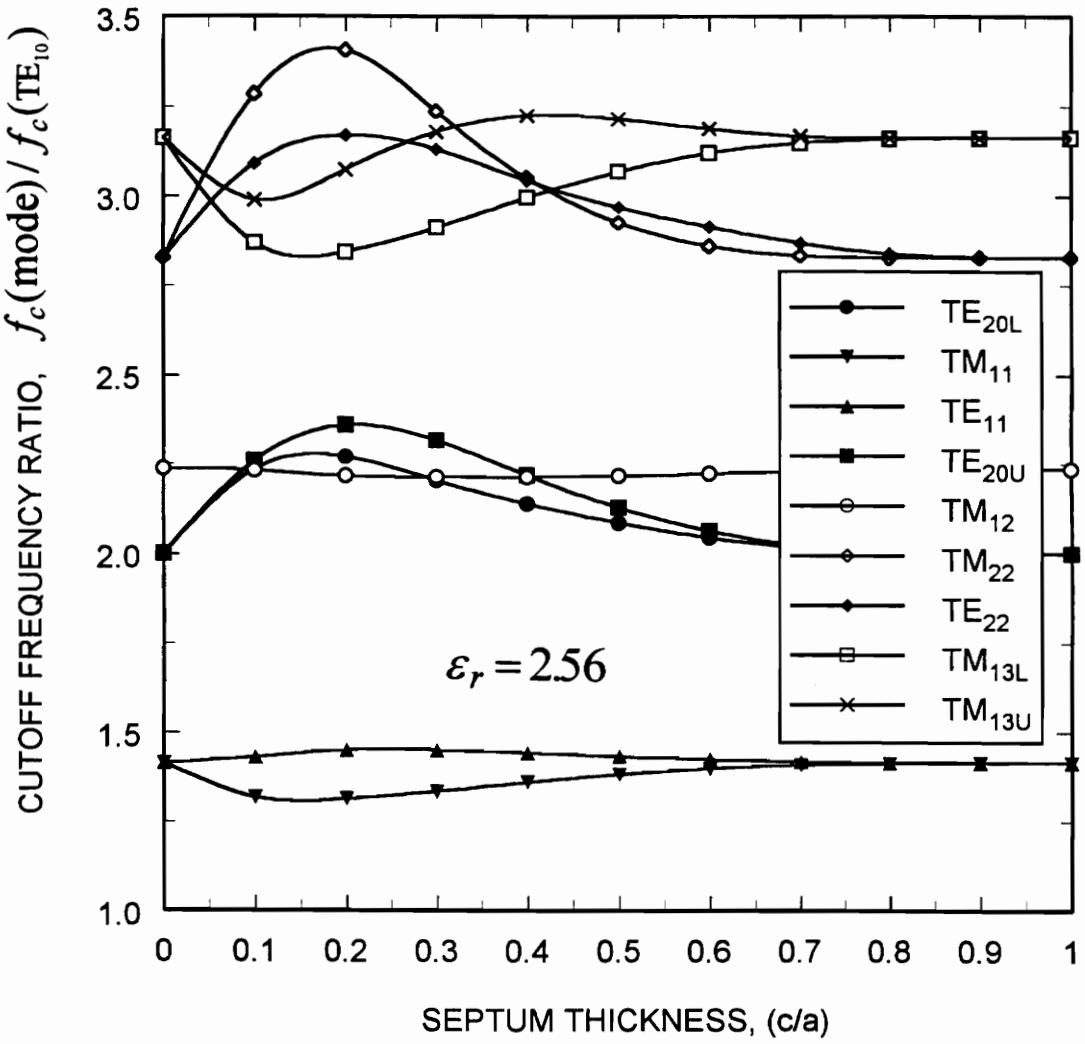

Figure 5-9. Ratio of modal cutoff frequency to dominate mode cutoff as a function of septum thickness *c/a*, with relative dielectric constant $\varepsilon_r = 2.56$.

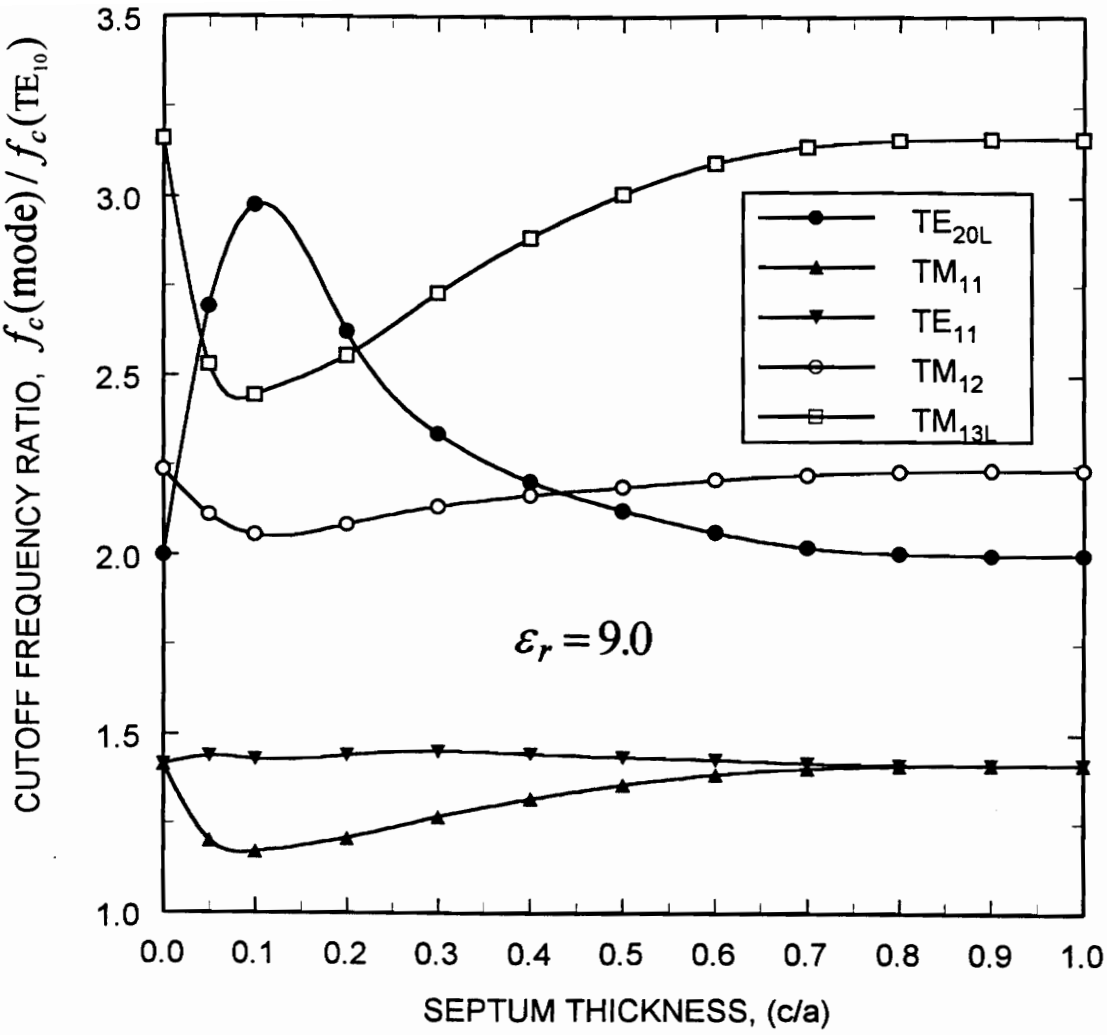

Figure 5-10. Ratio of modal cutoff frequency to dominate mode cutoff as a function of septum thickness *c/a*, with relative dielectric constant $\varepsilon_r = 9.0$.

5.6 Discussion of Mode Splitting Phenomena

In Section 5.3 it was discovered that the introduction of the cross-septum dielectric insert into the square waveguide results in splitting of the TE_{20} mode into two distinct modes referred to as upper and lower modes. Since the TE_{20L} and TE_{20U} modes will play a role in determining the usable bandwidth of the CSW, a further discussion and verification of the results are warranted. In this context, we intend to argue that the existence of the mode splitting is both reasonable and physical. There are at least three observations that verify the mode splitting phenomena. First, during the numerical investigations, the boundaries were thoroughly investigated and it was observed that there are no unusual discontinuities between regions of the guide that would indicate any numerical or nonphysical anomalies. Second, one may refer back to Chapter 3 on the discussion of symmetry properties, where the original CSW boundary value problem was reduced to an intermediate set of 6 equivalent boundary value problems shown in Figure 3-3. The TE_{20L} mode shown in Figure 5-4 can be satisfied by the boundary conditions given in Figure 3-3e consisting of a 45° section of the guide. Likewise, the TE_{20U} mode shown in Figure 5-5 can be satisfied by the boundary conditions shown in Figure 3-3f also consisting of a 45° section of the guide. A similar argument also applies to the TM_{13} mode which also splits into two modes (Figures C-3 and C-4) satisfying the boundary conditions in Figures 3-3c and 3-3d. One can conclude that there are no violations in any of the boundary conditions and regions that could indicate a numerical procedural error or nonphysical solution.

The third comment on the mode splitting phenomena is with respect to the observations of prior work on similar investigations of square waveguides presented in Chapter 2. It is interesting to point out that for ridge loading [3] and crossed waveguide [4] a similar mode splitting phenomena was also observed. However, in the investigation of dielectric loading of the square waveguide [5] mode splitting was not observed. The CSW in contrast to the dielectric loaded waveguide investigated by Tsandouglas [5] does exhibit the mode splitting phenomena.

5.7 References for Chapter 5

[1] W.H. Press, S. A. Teukolsky, W. T. Vetterling and B. P. Flannery, *Numerical Recipes in FORTRAN*, New York: Cambridge University Press, 1992.

[2] R.E. Collin, *Field Theory of Guided Waves*, second edition New York: IEEE Press, 1991.

[3] M.H. Chen, "Modal characteristics of quadruple-ridged circular and square waveguide," *IEEE Trans. on Microwave Theory Tech.*, vol. MTT-22, no. 8, pp. 801-804, August 1974.

[4] H.J. Stalzer, M.D. Greenman and F.G. Wellworth, "Modes of crossed rectangular waveguide", *IEEE Trans. Antennas and Propagat.*, vol. AP-24, no. 3 pp. 220-223, March 1976.

[5] G.N. Tsandouglas, "Propagation in dielectric-lined square waveguides," *IEEE Trans. on Microwave Theory Tech.*, vol. MTT-23, no.5, pp. 406-410, May 1975.

[6] C.A. Balanis, *Advanced Engineering Electromagnetics*, New York: John Wiley and Sons, 1989.

[7] G. Strang, *Linear Algebra and its Applications*, third edition, San Diego: Harcourt Brace Jovanovich, 1988.

CHAPTER 6

EXPERIMENTAL VERIFICATION OF CSW MODAL CHARACTERISTICS

6.1 Overview of CSW Modal Verification

This chapter describes the experimental measurements performed on a length of the CSW for comparison to the calculated results. An explanation of the theory on the measurement technique used in experimentally characterizing the CSW with respect to propagation constants and cutoff frequencies is presented. The resonant cavity measurement technique is described. The measured results demonstrate the bandwidth enhancement and provide an experimental verification of the mode filters. Both loop and probe coupling are investigated. Experimental data are given as a result of measurements of S_{11}.

The process of characterizing the CSW requires multiple tests and cross checks to ensure single-mode propagation and to show that the dominant mode is propagating. Only one set of measurements (i.e., only S_{11} or far-field data) is insufficient. Two independent sets of measurements are required to show dominant mode propagation in the CSW. First, one must show that there is only one mode propagating in the waveguide. This is accomplished by the resonant cavity measurements which are described in this chapter, and involves the measurement of S_{11} of the CSW cavity, both with and without the mode filters present. Second, one must show that the propagating mode is indeed the desired dominant mode, referred to here as the TE_{10} (or TE_{01}) modes. To show this, far-field patterns are observed and compared with analytical results derived from the computed dominant mode patterns. Chapter 7 will discuss analytical and experimental radiation characteristics of the CSW, and hence will further verify the results provided in this chapter.

6.2 Theory on Waveguide/Cavity Measurement Technique [1-3]

The electric and magnetic fields in the CSW for an infinitely long guide are solved in Chapters 4 and 5 using the mode matching technique, and expressed in a series of the form:

$$\vec{E}_n = \sum_{v=1}^{N} \left\{ E_{xv}\hat{x} + E_{yv}\hat{y} + E_{zv}\hat{z} \right\} e^{-jk_{zn}z} \tag{6.1}$$

$$\vec{H}_n = \sum_{v=1}^{N} \left\{ H_{xv}\hat{x} + H_{yv}\hat{y} + H_{zv}\hat{z} \right\} e^{-jk_{zn}z} \ . \tag{6.2}$$

The exponential term in (6.1) and (6.2) is a harmonic function expressing the phase of a wave traveling in the z-direction of an infinitely long waveguide. The fields stated here refer in general to solutions for the nth mode. As described in Section 5.3, the modes propagating within the CSW are classified as hybrid modes, (i.e., HE_{10}, HE_{11}, EH_{11} etc.) however the non-hybrid mode names will be retained for simplicity. In this discussion, modes will be referred to as the dominant mode TE_{10} (and TE_{01}) as well as the higher-order modes, TM_{11}, TE_{11} and so on.

To experimentally verify the CSW modal and propagation characteristics, a method is needed that can verify the cutoff frequencies of various modes, and the longitudinal (z-directed) phase constants, k_z. In the experimental verification of the propagation and modal characteristics of the CSW, several practical problems occur due to the 'non-standard' waveguide size and inhomogeneous dielectric filling. The measurement of electrical properties of a length of a terminated waveguide (e.g., CSW) requires components such as adapters, waveguide interfaces, terminations, slotted lines, coupling mechanisms, etc., each of which must also perform well over the intended broad range of frequencies for the 'non-standard' waveguide size. These problems can be largely avoided by the use of a measurement technique involving a resonant cavity, instead of, for example, a terminated section of waveguide. By placing a metallic wall on the two ends of

a length L, of waveguide, a resonant cavity is formed. The metallic walls enforce the boundary conditions

$$\hat{n} \times \vec{E}(z = 0, L) = 0 \tag{6.3}$$

$$\hat{n} \bullet \vec{H}(z = 0, L) = 0 \tag{6.4}$$

where $\hat{n}$ is a unit normal vector on the inside walls of the cavity. Therefore, in satisfying the boundary conditions, the exponential functions in (6.1) and (6.2) are replaced with the appropriate sine or cosine harmonic functions representing standing waves. The resulting electric and magnetic fields for the resonant cavity therefore have the form

$$\vec{E}_n = \sum_{v=1}^{N} \left\{ E_{xv}\hat{x} + E_{yv}\hat{y} + E_{zv}\hat{z} \right\} \begin{Bmatrix} \sin k_{zn} z \\ \cos k_{zn} z \end{Bmatrix} \tag{6.5}$$

$$\vec{H}_n = \sum_{v=1}^{N} \left\{ H_{xv}\hat{x} + H_{yv}\hat{y} + H_{zv}\hat{z} \right\} \begin{Bmatrix} \sin k_{zn} z \\ \cos k_{zn} z \end{Bmatrix} \tag{6.6}$$

where:

$$k_{zn} = m\pi / L \tag{6.7}$$

and m is an integer that permits the nth mode to satisfy boundary conditions. One therefore obtains resonant cavity modes designated as $TE_{101}, TE_{102}, \ldots, TM_{110}, TM_{111}, \ldots$ and etc. The advantage of this measurement technique is that it provides precise control of the longitudinal phase constant, as specified by the length of the guide. Additionally, measurements can be performed using one port (S_{11}) of a network analyzer without the necessity of additional specially constructed components. Considerable information, as shown below, can be determined from the measurement of S_{11}.

The resonant cavity shown in Figure 6-1 forms a one port energy storage device with an input impedance given by

$$Z_{in} = \frac{P_l + 2j\omega(W_m - W_e)}{\frac{1}{2} I I^*} \tag{6.8}$$

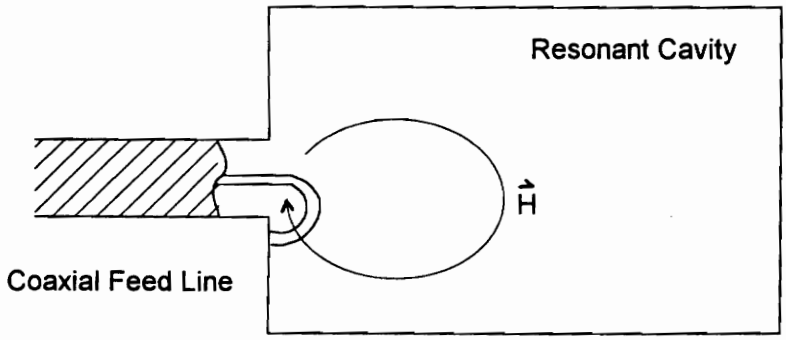

Figure 6-1. Loop coupled cavity system.

where W_m and W_e refer to the energy stored in the magnetic and electric fields, respectively, and P_l is the power dissipated by the cavity, and current I is flowing into the cavity. We will develop the relationship between a resonant cavity system and an RLC equivalent circuit. It will then be shown how information about the modal characteristics of the CSW can be inferred through the use of input impedance (or S_{11}) measurements.

Consider the loop coupled resonant cavity system shown in Figure 6-1. The cavity is excited by a small loop with current I, and generates a magnetic flux ψ. If the flux of the nth mode, ψ_n, is common to ψ, energy will be coupled to the mode from the input current loop. This coupling mechanism is essentially a transformer with mutual coupling M_n. Considering that there are an infinite number of modes, one obtains an equivalent circuit for a cavity coupled loop as shown in Figure 6-2. The input impedance is then found using network analysis to be

$$Z_{in}(\omega) = j\omega L_o + j\sum_{n=1}^{\infty} \frac{\omega^3 M_n^2 C_n}{1-\omega^2 L_n C_n + j\omega C_n R_n} \tag{6.9}$$

where L_o is the inductance of the transformer primary, and L_n, C_n and R_n are the equivalent lumped elements of the nth resonant cavity mode. Each of the nth modes has a resonant frequency given by ω_n, where

$$\omega_n^2 L_n C_n = 1. \tag{6.10}$$

The quality factor, Q, of a resonant circuit is a measure of the frequency selectivity and general performance of the circuit. Q is defined by the ratio of time-average energy stored by the resonant circuit to the energy loss per second of the circuit. For the nth mode, the quality factor is given by

$$Q_n = \frac{\omega_n L_n}{R_n} \tag{6.11}$$

For this discussion and for measurement purposes, it is assumed that Q is relatively large such as on the order of 10 or larger. The assumption of large Q is reasonable since the

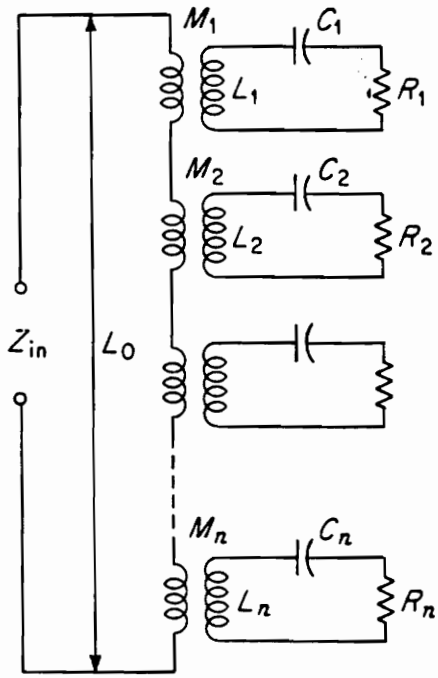

Figure 6-2. Equivalent circuit of a loop coupled cavity. Reprinted from [2].

cavity system has metallic walls and a low loss dielectric insert. Using equation (6.11) the input impedance can be written as

$$Z_{in}(\omega) = j\omega L_o + j\sum_{n=1}^{\infty} \frac{\omega^3 M_n^{\ 2}}{L_n\left(\omega_n^{\ 2} - \omega^2 + j\omega_n\omega/Q_n\right)}. \tag{6.12}$$

Equation (6.12) can be approximated at frequencies near the resonant frequency. At frequencies in the vicinity of ω_n assuming that Q is large, one obtains the following approximation for the input impedance

$$Z_{in}(\omega) = j\omega L_o + j\frac{\omega^3 M_n^{\ 2}}{L_n\left(\omega_n^{\ 2} - \omega^2 + j\omega_n\omega/Q_n\right)} \tag{6.13}$$

This simplification can also be conceptually obtained by inspection of the original equivalent circuit in Figure 6-2. Near the nth resonance, the equivalent circuit is dominated only by the nth resonant circuit, and all other circuits (resonant modes) in the secondary are essentially open circuited. Therefore, the original circuit reduces to a single series resonant circuit fed by a transformer.

By elimination of the transformer secondary, the circuit can be further simplified. Collecting the real and imaginary parts, the input impedance given in (6.13) can be expressed as an equivalent series resistance, R_{eq}, and reactance, X_{eq}, of the form

$$Z_{in}(\omega) = R_{eq}(\omega) + jX_{eq}(\omega) \tag{6.14}$$

where:

$$R_{eq}(\omega) = \frac{\omega^4 \omega_n M_n^{\ 2}}{L_n Q_n\left[\left(\omega_n^{\ 2} - \omega^2\right)^2 + \left(\omega_n\omega/Q_n\right)^2\right]} \tag{6.15}$$

$$X_{eq}(\omega) = \omega L_o + \frac{\omega^3 M_n^{\ 2}\left(\omega_n^{\ 2} - \omega^2\right)}{L_n\left[\left(\omega_n^{\ 2} - \omega^2\right)^2 + \left(\omega_n\omega/Q_n\right)^2\right]} \tag{6.16}$$

The resistive term in (6.14) represents the waveguide losses, due to the imperfectly conducting walls and the imperfect (lossy) dielectric material inside the cavity. The reactive part consists of the magnetic W_m and electric W_e energy as given by (6.8), and therefore represent a series inductor and capacitor, respectively. Therefore the resonant cavity in the vicinity of a modal resonance can be simplified to a series resistance $R_{eq}(\omega)$, an inductance $L_{eq}(\omega)$, and a capacitance $C_{eq}(\omega)$. In the vicinity of the nth mode, the resonant frequency given by $\omega'_n \approx \omega_n$, where $\omega'^2_n L_{eq} C_{eq} = 1$.

To investigate the behavior of a resonant cavity in the vicinity of the nth modal resonance, consider $Z_{in}(\omega)$ given by (6.14) at frequencies of $\omega = \omega_n \pm \Delta\omega$ as shown in Figure 6-3a. In the figure, values of $L_n = M_n = L_o = 1H$, $C_n = 1F$, $\omega_n = 1\ rad/s$ and $R_n = .05\ \Omega$ are conveniently chosen for illustrative purposes. The figure shows the resistive and reactive components of $Z_{in}(\omega)$. It is assumed that the quantity $\Delta\omega$ can vary and become large, but not so large that it is in the vicinity of the next higher or lower modal resonance. At $\omega >> \omega_n$, Z_{in} becomes capacitive since the reactance is negative. Conversely, at $\omega << \omega_n$, Z_{in} becomes inductive since the reactance is positive. At some $\omega \approx \omega_n$, the reactance is zero and Z_{in} becomes purely resistive.

In an experimental investigation of a resonant cavity, one would connect the cavity to a measurement device such as a network analyzer, having a transmission line with characteristic impedance of Z_o. Then the resonant cavity under measurement is equivalently a series RLC circuit connected to the characteristic impedance Z_o. The resonant cavity measurements described in this report were performed using a Hewlett Packard 8409 network analyzer and S-parameter test set. This allows one to sweep the frequency of the applied signal and measure the return loss, $-20\log[|S_{11}(\omega)|]$ of the CSW resonant cavity. For a one port network, $S_{11}(\omega)$ is equal to the reflection coefficient of the port and is given by

$$S_{11}(\omega) = \frac{Z_{in}(\omega) - Z_o}{Z_{in}(\omega) + Z_o} \tag{6.17}$$

where $Z_o = 50\Omega$, the characteristic impedance of the transmission line used for the measurement interface. Therefore, in consideration of equations (6.14), (6.17) and the corresponding discussion above, a measurement of $|S_{11}(\omega)|$ near the resonant frequency

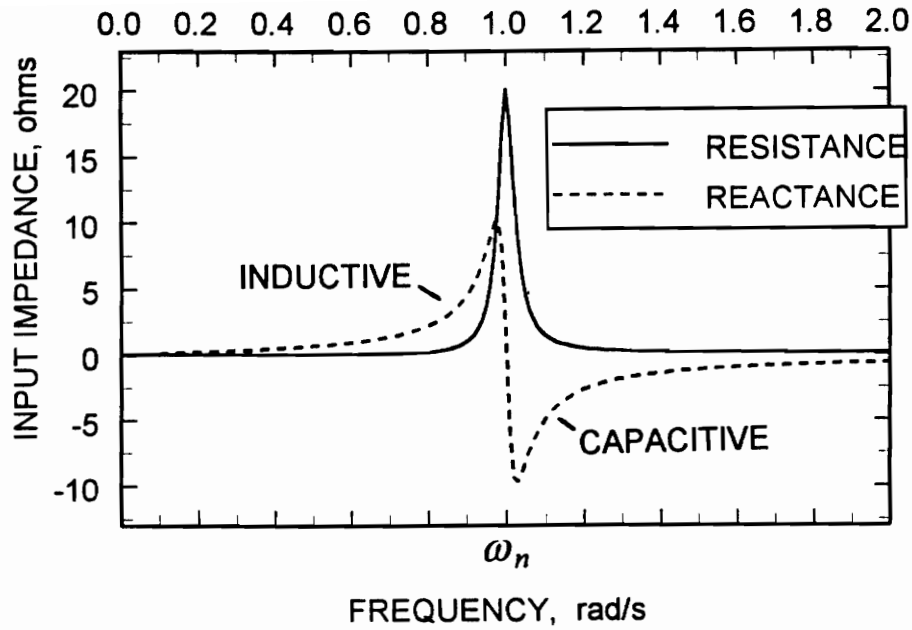

Figure 6-3a. Plot of the input impedance of a resonant cavity in the vicinity of resonance. The data are computed using (6.14) with parameters given by $L_n = M_n = L_o = 1H$, $C_n = 1F$, $\omega_n = 1\ rad/s$ and $R_n = .05\ \Omega$.

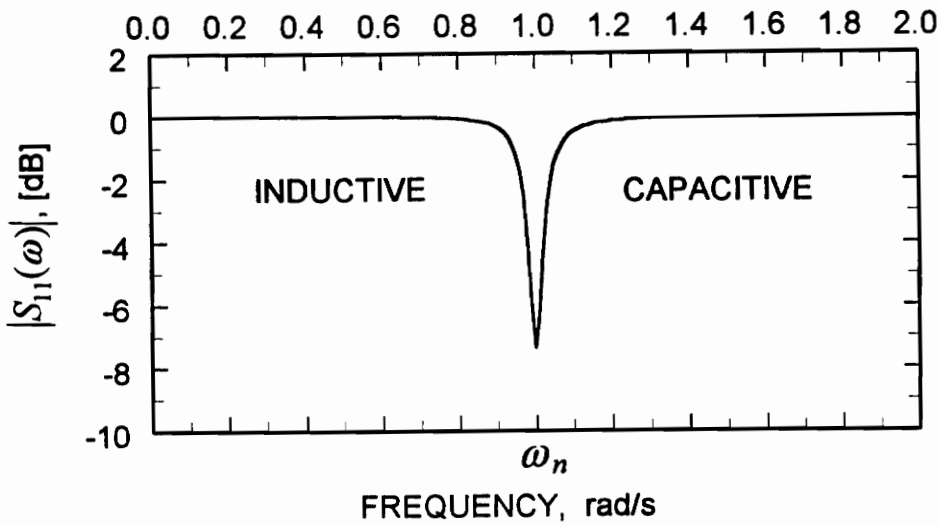

Figure 6-3b. Typical plot of $|S_{11}(\omega)|$ for a resonant cavity in the vicinity of resonance. The resonant cavity has an input impedance given in Figure 6-3a and is connected to transmission line with characteristic impedance given by $Z_o = 50\Omega$.

of the cavity will result in a plot having the form given by that shown in Figure 6-3b. When Z_{in} is purely resistive, the cavity system is most closely matched. Conversely, when Z_{in} is capacitive or inductive, the cavity system becomes less matched. The null represents the purely resistive Z_{in}, and it occurs approximately at the resonant frequency of the cavity. The frequencies where $|S_{11}(\omega)|$ is a maximum represent the capacitive or inductive frequencies, where the cavity system is not resonant.

In the experimental program the waveguide cavity is characterized by measuring the cutoff frequency and phase constants. Since the resonant frequency of the cavity can be measured for various values of k_z, the cutoff frequency can be determined from the asymptotic behavior of the resonant frequency as k_z approaches zero, in a stepwise fashion.

6.3 Coupling Methods

A few comments on the type of coupling used for the CSW measurements are now appropriate. To obtain coupling to a specific mode, one generally places a loop (or probe) in a location where the specific mode also has a strong magnetic (or electric) field in the desired direction. In this report, the use of a small loop to couple to the x-component of the magnetic field will be referred to H_x-loop coupling, as shown in Figure 6-4a. A small loop acts as a magnetic dipole and couples to the magnetic field in the direction normal to the face of the loop.

Although only the analysis of loop coupling is included in this report, coupling to a waveguide or resonant cavity can also be achieved with a probe. The analysis of probe coupling into a resonant cavity can also be done using equivalent circuits. The simplified probe coupled circuit also reduces to a series RLC circuit in the vicinity of the nth resonance. We will refer to E_y-probe coupling and E_z-probe coupling as defined in Figures 6-4b and 6-4c respectively. The electric field excited using probe coupling is in the direction of the probe in the cavity. The subscript will denote the electric field to which the probe couples.

Several different coupling types were considered, and the experimental results are given below. Considering the CSW application for a high powered phased array, a waveguide interface is needed as a transition between a phase shifter (also constructed

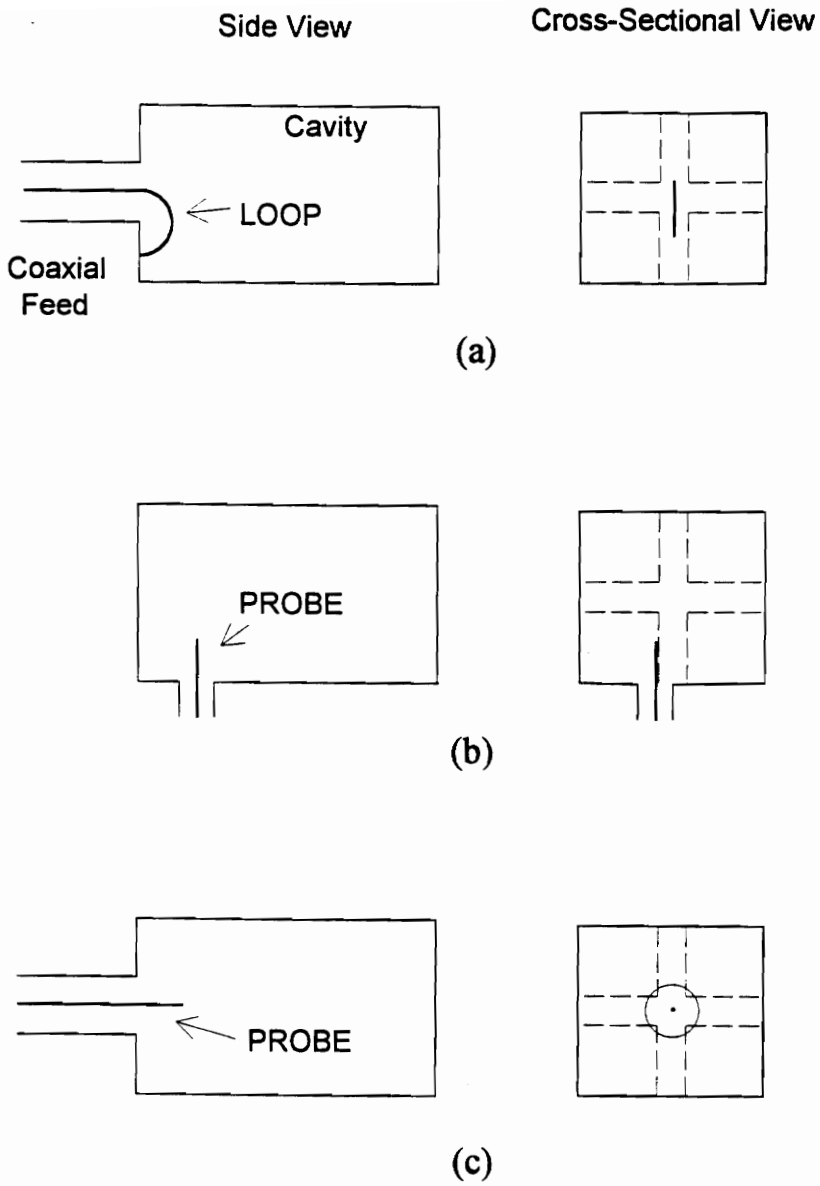

Figure 6-4. Coupling method definitions. (a) H_x-loop coupling. (b) E_y-probe coupling. (c) E_z-probe coupling

from a waveguide) and the CSW. The design and analysis of this component is left as an area of future work (see Chapter 10).

6.4 Description of the Measured Components

6.4.1 Waveguide Components

Several CSW waveguide elements were constructed at China Lake to facilitate experimental measurements. A set of square waveguide components were formed by machining brass into 'L' shaped brackets that could be bolted together forming a hollow square tube (or waveguide). The inside walls of the waveguide had very slight longitudinal grooves that facilitate holding the septum rigidly in place, so it would not move during the measurements, once bolted together. On each end of the waveguide, the ends were drilled and threaded so that a metallic plate could be used to cover the ends forming a resonant cavity. Of course, omitting one endplate forms an open-ended waveguide from which radiation patterns are measured.

Since both probe and loop coupling were considered, at least two waveguide elements had to be constructed. The first using either E_y- probe or H_z-loop coupling was drilled and threaded so that an SMA connector could be placed on the side, with the probe sitting just on the edge of the dielectric septum. The second, using either H_x- loop or E_z-probe was drilled and threaded on the end plate, so that an SMA connector would face the longitudinal direction. Both were measured to have a width $a = 14.93\,mm$ and were square to within $0.15\,mm$. The length of the CSW was $L = 100\ mm$. An unloaded square waveguide of width, $a = 14.93\,mm$ will support a dominant mode cutoff frequency of 10.04 GHz.

6.4.2 Mode Filter Descriptions and Definitions

A mode filter is an obstacle or alteration within a waveguide that 'interferes' with the propagation of a undesired mode, while leaving the desired mode relatively unaffected. As described in Sections 3.1 and 5.5, a mode filter is needed in conjunction with the dielectric septum to increase the usable bandwidth of the square waveguide under consideration. Section 3.3 discussed several of the methods employed in the literature to realize mode filters for various applications. A mode filter that supports linear

polarization can be found in references [4,5] and consists of a thin resistive film placed within the guide in the plane of the electric field of the undesired modes. The approach given here will outline the design of a resistive film mode filter that meets the performance requirements necessary to demonstrate the bandwidth enhancement concept while supporting dual polarization. The resistive film approach was chosen for its relative flexibility to design parameters and ease of fabrication. The mode filter consists of a 0.003 inch thick mylar film, with graphite (#1 pencil lead) deposited on the film, forming a conductive surface less than one skin depth. The conductive surface is strategically placed within the waveguide so that most of the energy is confined to the desired mode. In designing and determining the mode filter location, the following criteria were used:

- For the *desired* mode we wish to position conductive film in order that the E-field is *normal* to the film. This should:
  - not significantly attenuate the desired mode, relative to the undesired mode.
  - minimally alter the boundary conditions.
  - minimally affect or introduce any impedance mismatches.

- For the *undesired* mode we wish to position the conductive film in order that E-field is *tangential* to the film in order to:
  - highly attenuate this undesired mode, relative to the desired mode.
  - maximally alter the boundary conditions.
  - result in an impedance mismatch for the undesired mode, thus favoring coupling of energy into the desired mode.

Therefore, the correct positioning of the mode filters depends on the electric field lines of the desired and undesired modes. To 'remove' the TE_{11} mode, the film can be placed such that the surface area of the conductive surface lies approximately tangential to the electric field lines given in the plots of Chapter 5. The filter is designed so that there is no axial variation in the film over the extent of the CSW length. Therefore once the TE_{11} mode is satisfied, one finds that the film also lies in the electric field plane of the TM_{11} mode which has a strong axial component near the center of the guide. In 'removing' the TM_{11} mode it is desirable to place the mode filter near the center of the guide where the axial field component greatest, however this must be traded with the TE_{11} mode which

becomes weaker near the center of the guide. Another consideration is the dominant TE_{10} (and TE_{01}) mode which has a maximum electric field resembling the TE_{11} mode close to the edges of the guide, along the axes. So the film location must also satisfy the additional constraint of not attenuating the dominant mode and still maintain the 90 degree rotational symmetry necessary for dual polarization. Finally, the mode filter must also perform well over the entire frequency range so it must be positioned in such a way that it is not seriously affected by any changes in the electric field distribution which occur as a function of frequency.

Obtaining a suitable performance is ultimately a tradeoff between suppressing the undesired mode sufficiently, while leaving the desired (dominant) mode unsuppressed. Since the fields in the CSW are known from (6.1) and (6.2), one can consider a given resistive film surface area and compute possible locations for the mode filters by inspection of the tangential and normal electric field components. This gives one a general idea of which shapes and positions are capable of performing well. It was determined that the most practical way to design the mode filter was to compute the relative strength of the normal and tangential electric field for a given mode filter test case. Then an experimental measurement was performed and the thickness of the applied conductive material and position of film were adjusted to find a suitable performance. The mode filter performance is discussed further below.

Several mode filter geometries were experimentally investigated at various positions in the CSW. The mode filter positions were restricted to locations that would fit within the square corner space of the CSW, between the dielectric slabs and the metallic walls. A resistive film that could be embedded into the dielectric was considered but not used, since it would have required considerable additional machining and construction to implement. Figure 6-5 shows three of the geometries or 'types' investigated. The Type-1 mode filter (Figure 6-5a) is constructed with a mylar sheet that is just wide enough to fit between the corners as shown. The amount of surface area of the mylar that is coated with graphite, and the density of the graphite allows one to easily adjust parameters to obtain the desired result. Type-2 mode filters (Figure 6-5b) are constructed out of mylar sheet that is larger than the diagonal between the corners as shown. Therefore, when inserted into the CSW corners, the mylar sheet can be bent inward. The advantage of the Type-2 over Type-1 is that is the conductive are can be place so that is more closely tangential to the undesirable TE_{11} mode. Both Type-1 and Type-2 are designs that

CSW Cross-Sectional View

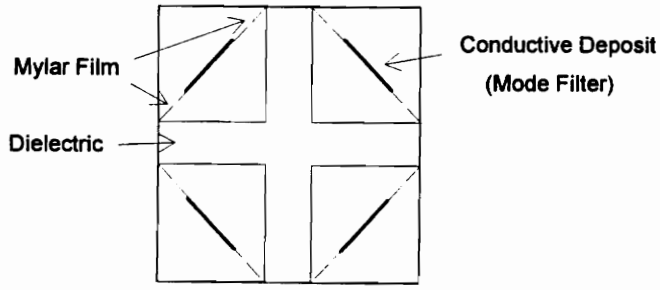

(a) Type 1

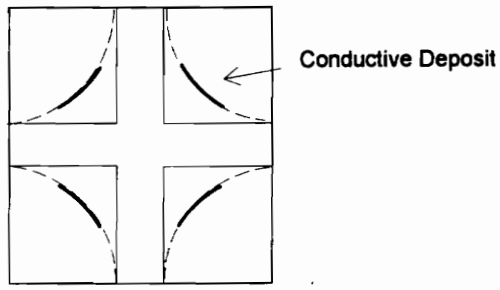

(a) Type 2

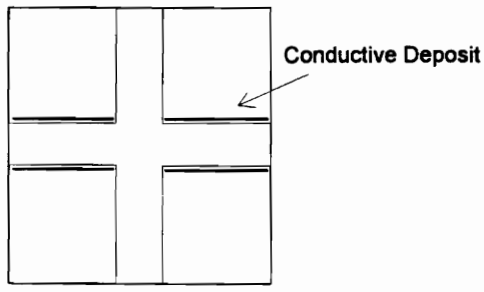

(a) Type 3

Figure 6-5. Mode filter definitions.

possess the desired 90 degree rotational symmetry necessary to support the required dual polarization.

A third mode filter was also constructed and is designated Type-3 (Figure 6-5c). This filter was constructed for test purposes only, and resembles in principle the linear polarized case given in references [4] and [5]. Due to the symmetry properties of the Type-3 mode filter, it will highly attenuate the TE_{01}, TM_{11}, and TE_{11} modes, however have almost no effect on the TE_{10} mode. Although the Type-3 mode filter does not support dual polarization, it is a useful test case and is used to help identify the dominant mode from other higher-order modes. The reason for using the Type-3 mode filter will become clear in the following sections.

6.5. Measured Results

6.5.1 Overview of Resonant Cavity Measurements

The CSW was experimentally investigated using several test cases. Initially, the unloaded square waveguide (CSW housing) was measured, as a canonical test case from which the measurement methodology can be verified. A CSW was constructed using a dielectric insert with $\varepsilon_r = 9.0$, designated 'Test Case # 1' from which the first set of measurements were performed. A second set of measurements were performed using a CSW with a dielectric insert having $\varepsilon_r = 2.56$, designated 'Test Case #2'. A summary of the parameters, dimensions and modal cutoff frequencies for each of the test cases are provided in Table 6-1. Various mode filter and coupling configurations were investigated for each of the test cases as discussed in the remainder of this report.

6.5.2 Unloaded Waveguide Test Case

An unloaded square waveguide provides a simple canonical test case from which the test methodology and can easily be verified and compared to theory. Numerous texts give detailed derivations of the fields and modal resonances, such as [2],[6], and therefore are omitted from here. Measurements were performed on an unloaded square waveguide using the resonant cavity methods described above. The unloaded waveguide which was characterized was the same as that used for constructing CSW, therefore the coupling methods could also be measured and evaluated, both with and without the dielectric

Table 6-1a.
Test Case Parameters.

TEST CASE	Septum thickness (c/a)	Dielectric constant (ε_r)
unloaded waveguide	0	1
Test Case #1	0.1283	9.0 (ceramic)
Test Case #2	0.319	2.56 (polystyrene)

Table 6-1b.
Modal Cutoff Frequencies for Test Models.
Frequencies are Calculated Using the Procedure in Sections 5.2.2 and 5.2.3.

MODE	Test Case # 1 cutoff frequency (GHz)	Test Case # 2 cutoff frequency (GHz)
TE_{10}, TE_{01}	5.443	6.964
TM_{11}	6.451	9.335
TE_{11}	7.864	10.099
TE_{20L}	15.954	15.297
TE_{20U}	17.254	16.033
TM_{12}	11.276	15.428
TE_{12}	19.033	18.350
TM_{13L}	13.493	20.397
TM_{13U}	15.455	22.245

septum present. Both E_y-probe coupling and H_x-loop coupling were investigated to facilitate the experimental adjustments of the coupling mechanism size and location. Investigation of the two coupling mechanisms allows one to compare measured resonance frequencies using each method. A summary of the results is provided in Table 6-2.

The experimental data from the two coupling methods demonstrate two points. First, the measured resonances occur at frequencies that are approximately equal to those predicted by theory. One can note the frequency spacing between the resonances also occurs as predicted by the theory. Second, both methods of coupling yield similar results, as expected. One may at least partially attribute any difference between theoretically predicted and observed resonances for the two different coupling methods to the coupling mechanism being either slightly capacitive or inductive, as was explained in Section 6.2. The measurements using the unloaded waveguide therefore verify the measurement technique to within a reasonable level of certainty, provided care is exercised in interpreting the measured results and correctly identifying the modes.

6.5.3 Test Case #1 Measurements Results

A series of measurements and experiments were conducted on the Test Case #1 CSW (see Table 6-1), using E_y-probe coupling as in Figure 6-4b. A measurement of S_{11} was performed *without* the mode filters to identify the cavity modal resonances; the resulting S_{11} vs. frequency data are shown in Figure 6-6. The first resonance is the dominant TE_{10} mode, and occurs at 5.78 GHz. The first higher-order mode is the TM_{11} mode and occurs at about 6.92 GHz. It becomes difficult to identify the modes beyond about 8 or 9 GHz due to the density of the resonances with respect to frequency. Table 6-3 gives the measured resonances from Figure 6-6 and theoretically predicted values using the mode matching technique described in Chapters 4 and 5, subject to the phase constant of the nth modal resonance given by (6.7). The cutoff frequencies can be obtained from the measured data by observing the asymptotic nature of the resonances as the longitudinal phase constant approaches zero (e.g., $k_z \rightarrow 0$) in a stepwise fashion. Considering the TE_{10} mode, the measured cutoff frequency of about 5.7 GHz compares to within about 5% of the theoretical value of 5.443 GHz given in Table 6-1b. The measured cutoff frequency of 6.92 GHz for the TM_{11} compares to within about 6.8% of the theoretical cutoff frequency of 6.451 GHz.

Table 6-2.
Unloaded Resonant Cavity Measured Data.

Propagating mode	Resonant frequency (theory) GHz	Resonant frequency using E_y- probe coupling (measured) GHz	Resonant frequency using H_x- loop coupling (measured) GHz
TE_{101}	10.040	10.087	10.090
TE_{102}	10.484	10.406	10.375
TE_{103}	11.015	10.986	10.900
TE_{104}	11.717	10.587	11.590
TE_{105}	12.561	12.300	12.415
TE_{106}	13.523	13.293	13.330
TE_{107}	14.578	*	14.410
higher-order modes below here			
TM_{110}	14.199	*	14.050
TM_{111}, TE_{111}	14.279	*	14.230
TM_{112}, TE_{112}	14.516	*	14.590
TM_{113}, TE_{113}	14.904	15.019	15.100
TM_{114}, TE_{114}	15.430	15.712	15.730

NOTE: * indicates that the modal resonance could not be clearly discerned from the data.

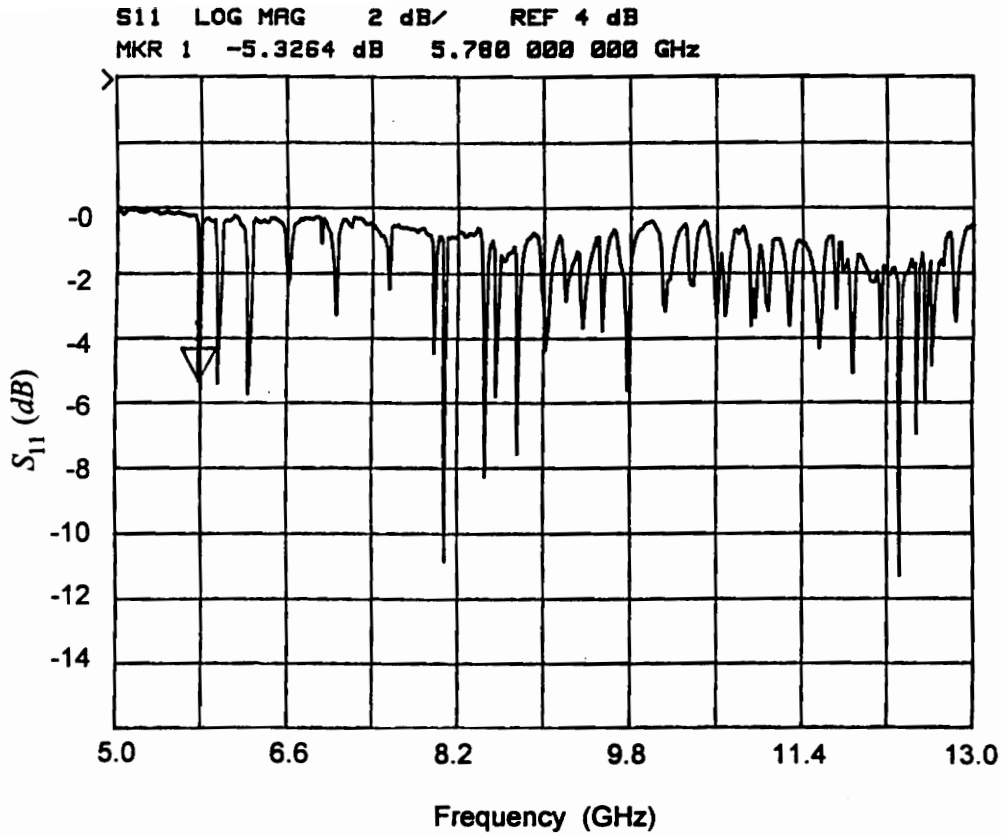

Figure 6-6. Measured $|S_{11}|$ vs. frequency for Test Case #1 without mode filters, using E_y-probe coupling.

Table 6-3.
Resonant Cavity Measurements, for the Test Case # 1 Dielectric Septum Insert.

Propagating mode	Resonant frequency in GHz, predicted from equations (5.9) and (6.7)	Measured resonant frequency in GHz without mode filter installed, (from Fig.6-6)	Measured resonant frequency in GHz with mode filter installed, (from Fig.6-7)
TE_{101}	5.489	5.780	5.730
TE_{102}	5.657	5.950	5.880
TE_{103}	5.923	6.240	6.140
TE_{104}	6.272	6.610	6.500
TE_{105}	6.689	*	6.970
TE_{106}	7.149	*	7.420
TE_{107}	7.648	*	7.940
TE_{108}	8.170	*	8.480
TE_{109}	8.707	*	9.060
$TE_{10\text{-}10}$	9.250	*	9.660
$TE_{10\text{-}11}$	9.804	*	10.260
higher-order modes given below here:			
TM_{110}	6.451	6.920	suppressed
TE_{111}	7.895	8.105	suppressed

NOTE: * indicates that the modal resonance could not be clearly discerned from the data.

Once the resonances were identified for the dominant mode, measurements were then conducted with mode filter Type-1 inserted into the guide. The measured S_{11} data in Figure 6-7, and gives the mode filter performance. The absence of the additional resonances indicates that the higher-order modes are suppressed. As shown the filter results in the confinement of energy to the dominant TE_{10} mode over a frequency bandwidth from about 5.7 to about 9.6 GHz. At the frequencies higher than about 9.6 GHz higher-order modes begin to propagate, as indicated by the additional resonances. The addition resonances observed at higher frequencies are likely due to both coupling and

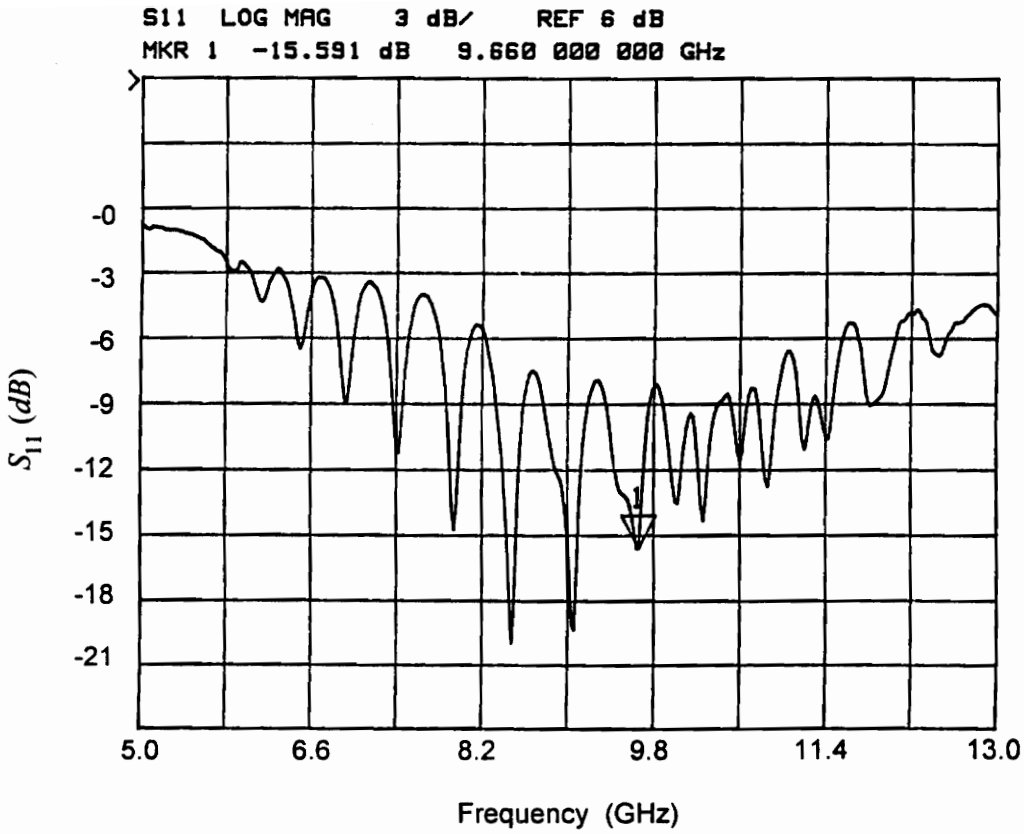

Figure 6-7. Measured $|S_{11}|$ vs. frequency for Test Case #1 with Type 1 mode filters, using E_y-probe coupling.

the frequency dependence of the mode filters. These two points are discussed further below.

Additional experiments were performed using the Type-2 mode filter, however only a slight improvement to about 10 GHz was obtained. At frequencies greater than about 10 GHz, propagation of higher-order modes were observed, and the energy is no longer confined to a single-mode. The maximum frequency of about 10 GHz represents the highest operating frequency obtained (and the largest bandwidth ratio) for the Test Case #1 CSW, for which experimental measurements were performed. Some experimental work was done to obtain increased bandwidth performance over that obtained above. Several modifications in the mode filters were tried experimentally, and did not yield further improvement.

The two likely reasons that further bandwidth could not be achieved are degradation of mode filter performance and dominant mode coupling. First, mode filter performance will depend on frequency. A close inspection of the transverse and axial electric field components for the dominant and the higher order modes can explain the decreased performance at the high frequency end of the CSW. An explanation of the mode filter performance, and high frequency roll off is apparent by close inspection of the hybrid nature of the modes. Recall that in the dominant TE_{10} mode (or more generally all TE modes) of an *unloaded* square waveguide, the electric field is purely transverse and contains no z-directed electric field E_z. However with the insertion of the dielectric septum, hybrid modes are obtained. Only at the cutoff frequency are the electric fields in the loaded waveguide purely transverse. As the frequency increases, the E_z component of the TE_{10} mode increases relative to the transverse field component. This tends to be detrimental to the mode filter performance at higher frequencies in terms of dominant mode propagation since the mode filter lies in the plane of the E_z component and thus the dominant mode energy is more rapidly attenuated.

Similarly, for the TM_{11} mode, close inspection of the electric field components indicates a reduced attenuation level at the higher frequencies of operation. At cutoff frequency the transverse electric field of the TM_{11} mode (or more generally all TM modes) is zero and the electric field is purely axial. As the frequency is increased the strength of the transverse electric field increases relative to the E_z field component. However the mode filter is designed to heavily attenuate the E_z component for the TM_{11}

mode. Then by analogy to the TE mode discussion above, a reduction in mode filter performance for TM modes will occur at higher frequencies.

The second source of degradation at the high frequencies can likely be attributed to the coupling considerations. The TE_{11} and TM_{11} modes each contain a strong transverse component that is heavily excited when using the E_y-probe coupling method. In particular, the transverse electric field component of the TM_{11} mode becomes stronger at the higher frequencies and therefore under this condition coupling into the dominant mode over the undesired modes at the higher frequencies is no longer favorable.

The solution to this problem is to improve the coupling method and to position the mode filters so that performance is less sensitive to changes in field distributions over the intended operating frequency range. Using insight obtained from Test Case #1, another CSW dielectric insert was constructed and is defined as Test Case #2. The measured and computed results are provided in the following section.

6.5.4 Test Case #2 Measurements Results

The Test Case #2 dielectric insert (see Table 6-1) was constructed and experimentally characterized using insight and experience gained from the Test Case #1 data. The two problems encountered in Test Case #1 identified in the previous section were the coupling and mode filter performance at the high frequency end of operation. By inspection of the transverse and axial electric field components of both the dominant and higher-order modes, it was found that increasing the width of the septum to c/a = 0.319, and reducing the dielectric constant to $\varepsilon_r = 2.56$ would produce more desirable performance in terms of achieving improved mode filter performance over the entire bandwidth. As for the coupling method, another cavity back-plate was constructed to facilitate H_x-loop coupling. By inspection of the field plots presented in Chapter 5, one finds that H_x-loop coupling will favor excitation of the dominant mode and not the higher-order modes. The theoretical cutoff frequencies for modes of interest of Test Case #2 are shown in Table 6-1 and the computed modal resonances are given in Table 6-4.

Figure 6-8 shows $|S_{11}|$ measured data performed using H_x-loop coupling for Test Case #2 *without* the mode filters present. As shown in the figure, the first resonance of the dominant TE_{10} mode occurs at about 7.025 GHz and compares well to the first theoretical resonance of 7.041 GHz shown in Table 6-4a. Higher-order modes begin to propagate at about 9.3 GHz for the TM_{11} mode. It is believed that a resonance just above

Table 6-4a.
Dominant Mode Resonances for Test Case #2.

Propagating mode	Resonant frequency in GHz, predicted from equations (5.9) and (6.7)	Measured resonant frequency in GHz, with Type-3 mode filter installed, (from Fig.6-11)	Measured resonant frequency in GHz, with Type-2 mode filter installed, (from Fig.6-10)
TE_{101}	7.041	6.925	6.950
TE_{102}	7.268	7.150	7.150
TE_{103}	7.631	7.500	7.550
TE_{104}	8.110	7.975	8.025
TE_{105}	8.686	8.550	8.575
TE_{106}	9.338	9.175	9.225
TE_{107}	10.051	9.875	9.900
TE_{108}	10.811	10.625	10.650
TE_{109}	11.608	11.400	11.425
TE_{10-10}	12.432	12.200	12.225
TE_{10-11}	13.279	13.050	13.075
TE_{10-12}	14.141	13.900	13.925
TE_{10-13}	15.017	14.775	14.800
TE_{10-14}	15.902	15.625	15.650

Table 6-4b.
Higher-order Modes, E_z- Probe Coupling, Without Mode Filter.

Propagating mode	Resonant frequency in GHz, predicted from equations (5.9) and (6.7)	Measured resonant frequency in GHz, without mode filter, (from Fig.6-9)
TM_{111}	9.396	9.250
TM_{112}	9.577	9.450
TM_{113}	9.871	9.725
TM_{114}	10.267	10.125
TM_{115}	10.752	10.625
TM_{116}	11.315	11.200
TM_{117}	11.942	11.850
TM_{118}	12.622	12.575
TM_{119}	13.346	13.300
TM_{11-10}	14.106	14.075
TM_{11-11}	14.894	14.875
TM_{11-12}	15.705	15.675
TM_{121}	15.459	15.325
TM_{122}	15.553	15.400
TM_{123}	15.707	15.550
TM_{124}	15.921	15.800

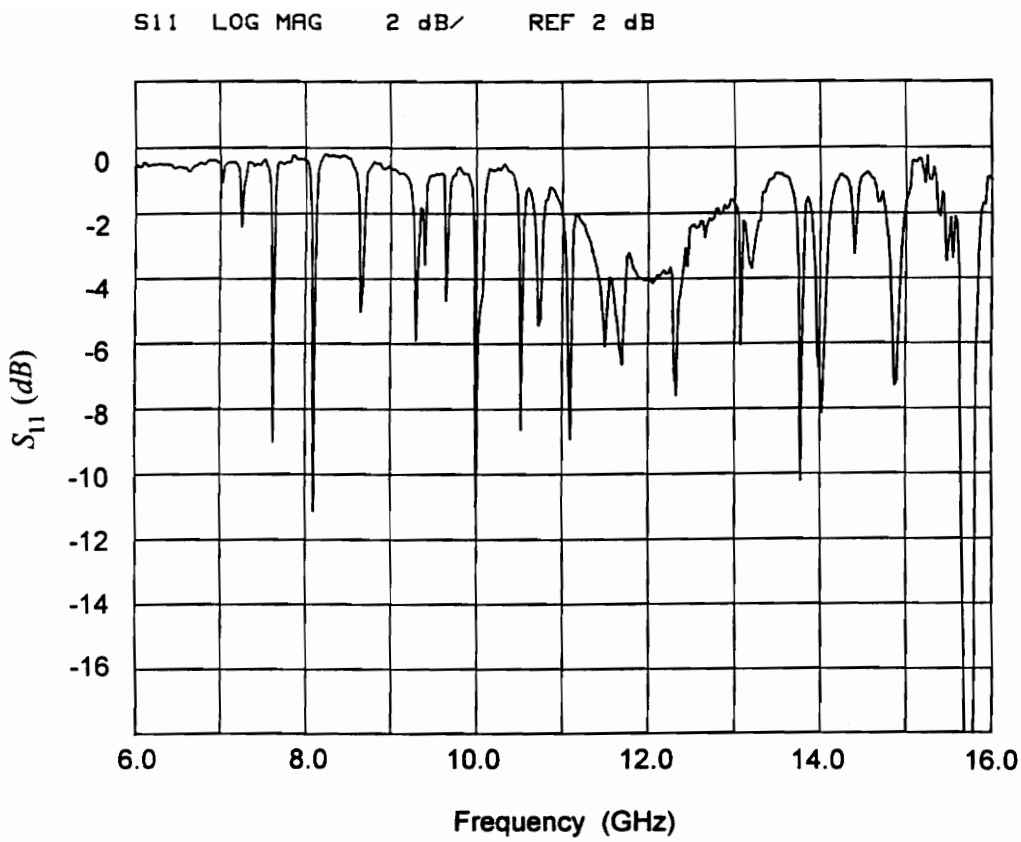

Figure 6-8. Measured $|S_{11}|$ vs. frequency for Test Case #2 without mode filters, using H_x-loop coupling.

10 GHz is the likely to be the TE_{11} mode however it is difficult to be certain, due to the proximity and obstruction by other modes. Although H_x loop coupling favors excitation of the dominant mode, clearly there are other resonances present over the frequency response indicating higher-order mode excitation. In order to determine the TM mode resonances, S_{11} measurements were performed using E_z-probe coupling, as is shown in Figure 6-9. The responses clearly indicate the excitation of both TM_{11} and TM_{12} resonances as summarized in Table 6-4b. Agreement between theory and experiment is very good.

In the experimental demonstration of mode filters and single-mode propagation, what is needed is a method to clearly identify the dominant mode at frequencies above the onset of the first higher-order modes. A method for achieving this can be found in the use of the Type-3 mode filter which was defined in Section 6.4.2. The Type 3 mode filter lies in the plane of the TE_{01}, TM_{11}, and TE_{11} mode electric fields and therefore will rapidly attenuate these modes. By inspection of the TE_{10} mode fields, one finds the electric field is normal to the plane of the Type 3 mode filter and therefore will not be attenuated. Although the Type-3 mode filter will *not* support a circular polarized wave, it is a valuable test tool in identifying the dominant mode resonances by removing the unwanted modal resonances. A plot of S_{11} measured with the Type-3 mode filter present is shown in Figure 6-10. A comparison between theory and experimentally observed dominant mode resonances are provided in Table 6-4a, and shows consistent agreement over the range of frequencies measured.

The next stage of the experimental program was to demonstrate a suitable mode filter over the intended frequency range bounded by the TE_{10} and TE_{20L} modes. It was experimentally found that Type-2 mode filters yielded better results over the intended frequency range, compared to Type-1 mode filters. Measured S_{11} data for the CSW with Type-2 mode filters are shown in Figure 6-11. Comparison of the data with the mode filters (Figure 6-11) to that data without the mode filters (Figure 6-8), shows that the presence of the mode filter indeed removes the unwanted resonance, leaving most of the energy propagating in the dominant mode. The modal resonances are provided in Table 6-4a and indicate excellent agreement when compared to the Type 3 mode filter data. However unlike the Type 3 mode filter, the Type 2 mode filter will support dual polarization which is one of the key requirements for the radiating element described in Chapters 2 and 3.

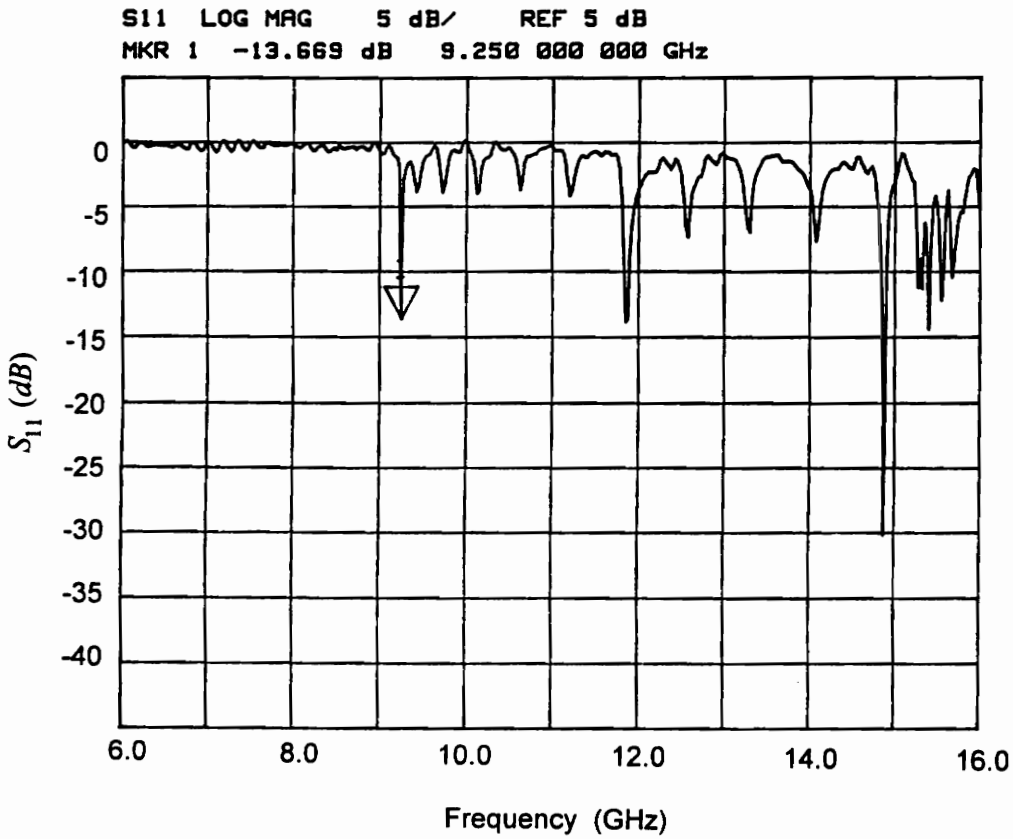

Figure 6-9. Measured $|S_{11}|$ vs. frequency for Test Case #2 without mode filters, using E_z-probe coupling.

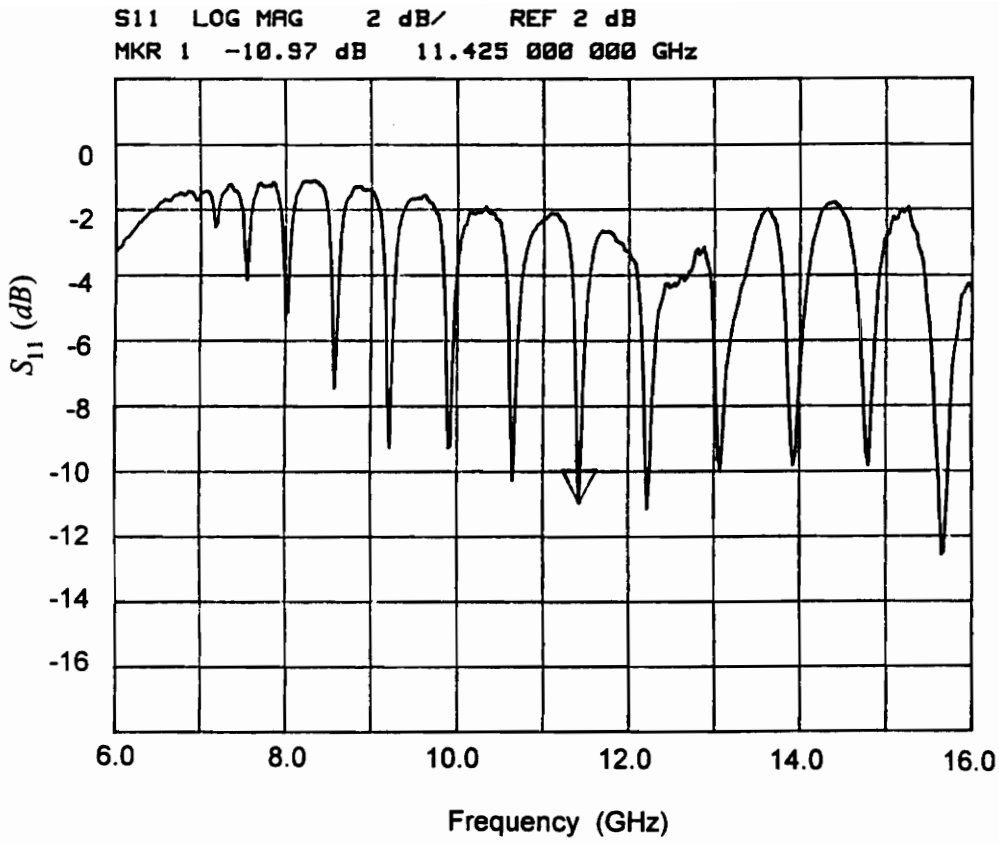

Figure 6-10. Measured $|S_{11}|$ vs. frequency for Test Case #2 with Type 3 mode filters, using H_x-loop coupling.

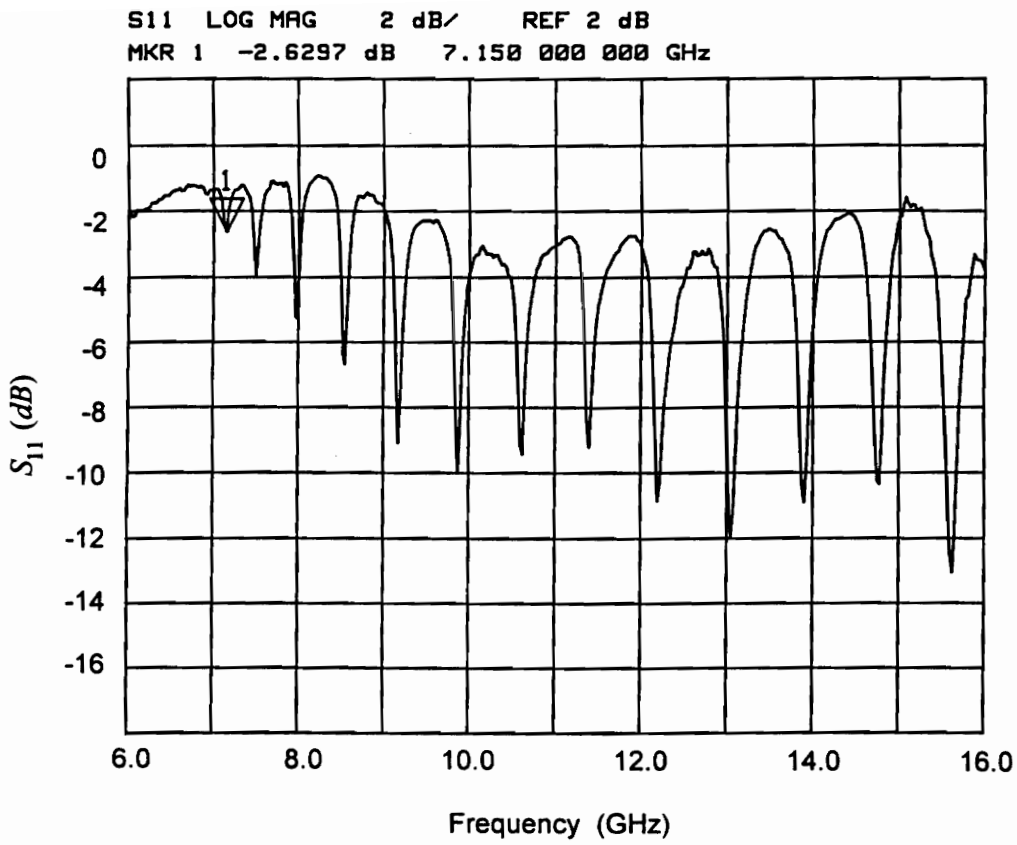

Figure 6-11. Measured $|S_{11}|$ vs. frequency for Test Case #2 with Type 2 mode filters, using H_x-loop coupling.

The theoretical bandwidth from Table 6-1 for Test Case #2 is 6.96-15.3 GHz, which is a bandwidth ratio $BW = f_c(\mathrm{TE}_{20\mathrm{L}})/f_c(\mathrm{TE}_{10}) = 2.20{:}1$. It has been demonstrated that one can excite both the dominant and higher-order modes above cutoff and 'remove' unwanted modal resonance with mode filters as described by the design example provided in this section. The following chapter provides further evidence to show that the propagating mode is the desired mode and is not an undesired mode. Furthermore, the work in the following chapter shows that the CSW element can be used as a radiating structure and the resulting patterns are sufficiently well behaved that it would be useful for some applications.

6.6 References for Chapter 6

[1] Edited by C.G. Montgomery, R.H. Dickey and E.M. Purcell., *Principles of Microwave Circuits*, MIT Rad. Lab. Series, 1948, McGraw Hill.

[2] R.E. Collin, *Foundations for Microwave Engineering*, McGraw Hill, New York, 1966.

[3] E.L. Ginzton, *Microwave Measurements*, McGraw Hill, NewYork, Chapters 8 and 9, 1957.

[4] L.Stark, C.V. Bell, R.A. Notvest, R.E. Griswold, D.A. Charlton and R.W. Howard, "Microwave components for wide-band phased arrays", *Proc. IEEE*, Vol. 56, NO.11, November 1968, pp.1908-1923.

[5] G.N. Tsandouglas, D.H. Temme, and F.G. Willwerthet, "Longitudinal Section Mode Analysis of Dielectrically loaded waveguides with application to phase shifter design", *IEEE Trans. on Microwave Theory and Techniques*, Vol. MTT-18, No. 2. Feb. 1970.

[6] C.A. Balanis, *Advanced Engineering Electromagnetics*, John Wiley and Sons, New York, Chapter 8, 1989.

CHAPTER 7

CSW RADIATION CHARACTERISTICS THEORY AND EXPERIMENT

7.1 Overview of CSW Radiation Characteristics

The results of an investigation into the far-field characteristics are presented in this chapter. The theoretical far-field radiation patterns of the CSW are analyzed and compared to measurements performed on an experimental CSW radiating element. For an application such as a phased array antenna, one needs "well behaved" patterns in the scan range of the antenna. The term "well behaved" is intended to imply a beam having a well defined main lobe and side lobes that do not contain an appreciable portion of the radiated energy. High cross-polarization is also undesirable since it is an indication of energy present in a higher-order mode as discussed in Sections 7.3 and 7.4.

The propagation characteristics of the CSW described in Chapter 6 were experimentally investigated by measurement of a resonant cavity both with and without mode filters. This chapter will further characterize the CSW properties by showing that when properly excited and with the use of mode filters, the energy can be largely confined to the dominant TE_{10} mode. Under these conditions, it is shown that resulting patterns are well behaved especially at the low frequency end and exhibit graceful degradation through the highest frequency of operation.

Aperture theory is used to compute the far-field patterns arising from the electric fields at the mouth of the open-ended CSW. Although the intent is to demonstrate radiation characteristics for a single mode of propagation in the CSW, the problem must be considered in a more general sense. A multimode analysis (see for example [5-7]) is performed in order to identify the salient features which could be present in the antenna patterns if the mode of propagation in the CSW were not the dominant mode. The far-

field patterns of the CSW are therefore computed for three cases accounting for secondary effects. First, it is assumed that the all energy is confined to the dominant TE_{10} mode and the resulting patterns are computed. Second, it is assumed that all propagating energy in the CSW is confined to a higher-order mode such as the TM_{11} and the resulting patterns are computed. Third, it is assumed that the energy propagating in the CSW is present in a multimode configuration, and the resulting patterns are computed. Next, the far-field patterns of a CSW are measured and compared to theory. Both E- and H-Plane patterns including the co- and cross-polarization patterns are considered. An investigation of the co- and cross-polarization performance is used to infer information about the type of modes propagating and radiating in the CSW.

Two prototype CSW units were experimentally investigated in Chapter 6. These two units were designated Test Case #1 and Test Case #2, where the dimensions and parameters are also defined in Table 6-1. Although measurements were performed on both test cases, this report presents the experimental results of Test Case #2 since it was demonstrated to have the largest usable bandwidth of the two test cases.

7.2 Theory and Analysis of the CSW Far-Field

The modal characteristics and fields of an infinitely long CSW were described in Chapters 4 and 5, where the solutions were obtained for the CSW using the mode matching technique. Figure 7-1 shows the CSW and the corresponding coordinate system used for the analysis. The transverse fields for a given mode at the mouth of an open ended waveguide CSW can be expressed in the form

$$\vec{E}_{an}(x',y') = \sum_{v=1}^{N} \left\{ E_{xnv}(x',y')\hat{x} + E_{ynv}(x',y')\hat{y} \right\} \tag{7.1}$$

$$\vec{H}_{an}(x',y') = \sum_{v=1}^{N} \left\{ H_{xnv}(x',y')\hat{x} + H_{ynv}(x',y')\hat{y} \right\} \tag{7.2}$$

where $E_{xnv}, E_{ynv}, H_{xnv}$ and H_{ynv} are the corresponding series field expansion coefficients, and n represents the nth propagating mode. Propagating modes are those modes excited above cutoff frequency including the higher-order modes attenuated at least partially by

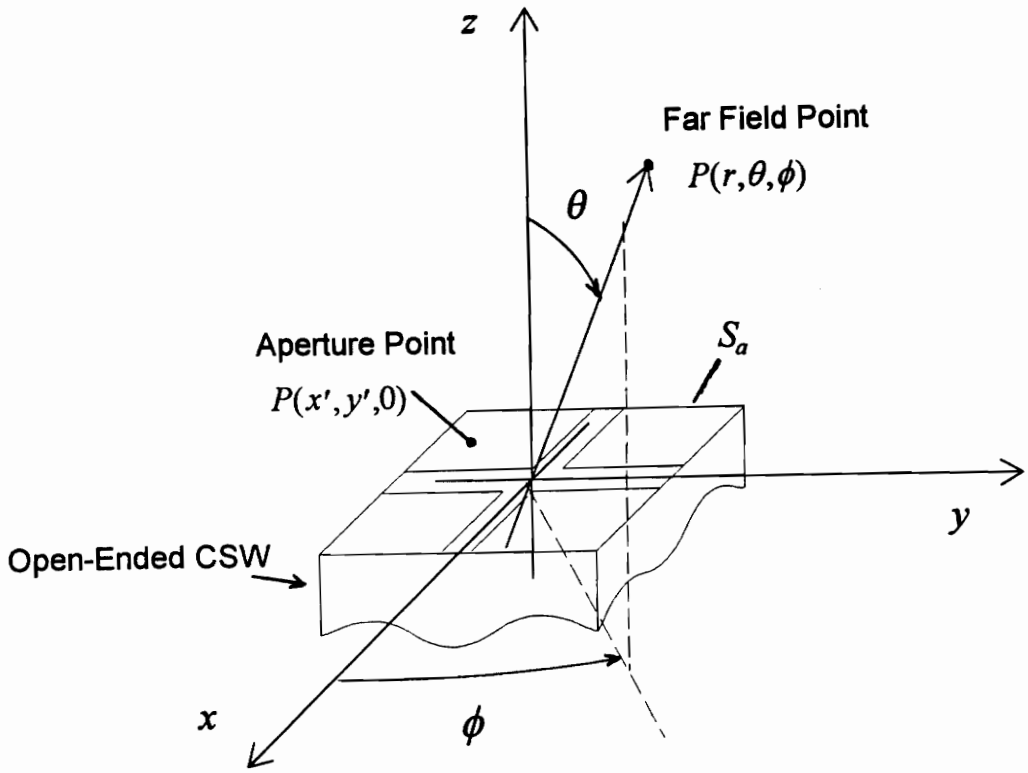

Figure 7-1. Open-ended CSW radiating element and coordinate system.

the mode filters as discussed in Chapter 6. Implicit in (7.1) and (7.2) is the assumption that reflections at the waveguide/air interface are neglected. For simplicity, we define n for each of the propagating modes under consideration as given in Table 7-1.

Table 7-1.
Mode Description and Designation for Pattern Analysis.

n	mode	description/comment
1	TE_{10}	dominant (desired) mode
2	TE_{01}	dominant (orthogonal) mode
3	TM_{11}	higher-order mode
4	TE_{11}	higher-order mode

Most generally it is assumed that the fields at the mouth (or aperture) of the guide are a linear combination of all propagating modes in the guide. Therefore, the aperture fields are written as

$$\vec{E}_a(x',y') = \sum_n \chi_n \vec{E}_{an}(x',y') \tag{7.3}$$

$$\vec{H}_a(x',y') = \sum_n \chi_n \vec{H}_{an}(x',y') \tag{7.4}$$

where χ_n is a complex scaling constant.

In expressing the fields $\vec{E}_{an}$ and $\vec{H}_{an}$ as in (7.1) and (7.2), it is further assumed that the fields for each of the n propagating modes have been normalized such that the energy passing a reference cross sectional plane of the guide is the same. The normalization is expressed by integrating the z-component of the Pointing vector over a cross section of the guide, given by

$$P_{en} = \frac{1}{2} \int_{-a/2}^{a/2} \int_{-a/2}^{a/2} \left(\vec{E}_{an} \times \vec{H}_{an}^{\,*} \right) \bullet \hat{z}\, dx\, dy. \tag{7.5}$$

Each mode is normalized relative to the emitted power P_e passing through a reference plane at the point $z = 0$ of a section of the guide. Therefore, in terms of the emitted power for each mode, one can write

$$P_{e1} = P_{e2} = P_{e3} = P_{e4} \tag{7.6}$$

Then by definitions in (7.3) through (7.6) the scaling constant χ_n is used to describe the amount of energy radiated by a given mode, relative to all modes carrying equal energy.

Aperture theory is used to compute the far-field patterns in the investigation of the CSW radiation properties. It is assumed that the fields in the mouth of the guide are the same as those computed in an infinitely long length of the guide subject to scaling of the energy radiated by each mode. The physical optics approximation is used, in which the fields on the surface S_a are generally non-zero and in the region outside the mouth of the guide in the *x-y* plane are assumed to be zero.

Since both $\vec{E}_a$ and $\vec{H}_a$ are known, one could use either one or both of these to compute the far-field patterns. For simplicity $\vec{E}_a$ is used here to compute the far-field patterns. From (7.1), let the electric field across the aperture be written in the general form

$$\vec{E}_a(x',y') = E_{ax}(x',y')\hat{x} + E_{ay}(x',y')\hat{y} \tag{7.7}$$

Then the radiated electric fields in the far-field are given by [1]

$$\vec{E}(r,\theta,\phi) = E_\theta(\theta,\phi)\hat{\theta} + E_\phi(\theta,\phi)\hat{\phi} \tag{7.8}$$

where:

$$E_\theta = jk_o \frac{e^{-jk_o r}}{2\pi r}\left[P_x \cos\phi + P_y \sin\phi\right] \tag{7.9}$$

$$E_\phi = jk_o \frac{e^{-jk_o r}}{2\pi r}\cos\theta\left[P_y \cos\phi - P_x \sin\phi\right] \tag{7.10}$$

and

$$P_{x,y}\left(\frac{u}{\lambda},\frac{v}{\lambda}\right)=\iint_{S_a} E_{ax,y}(x',y')e^{j2\pi\frac{u}{\lambda}x'}e^{j2\pi\frac{v}{\lambda}y'}dx'dy' \tag{7.11}$$

$$k_o = 2\pi/\lambda \tag{7.12}$$

$$u = \sin\theta\cos\phi \tag{7.13}$$

$$v = \sin\theta\sin\phi \tag{7.14}$$

In (7.11) λ is the free space wavelength. When computing far-field patterns one is primarily interested in the real (physically observable) space inside the unit circle of the *u-v* plane, given by

$$u^2 + v^2 \le 1. \tag{7.15}$$

The aperture surface S_a is the region defined by $|x'| \le a$ and $|y'| \le a$ and by the physical optics approximation, the fields are assumed to be zero for all points outside S_a. One can therefore replace S_a with $\pm\infty$ in equation (7.11) and obtain

$$P_{x,y}\left(\frac{u}{\lambda},\frac{v}{\lambda}\right)=\int_{-\infty}^{\infty}\int_{-\infty}^{\infty} E_{ax,y}(x',y')e^{j2\pi\frac{u}{\lambda}x'}e^{j2\pi\frac{v}{\lambda}y'}dx'dy' \tag{7.16}$$

The functions P_x and P_y are recognized as the familiar 2-dimensional Fourier transform of the aperture fields E_{ax} and E_{ay} respectively.

For simple canonical cases where the tangential aperture fields are expressed in closed form, (7.16) is often easily computed by direct evaluation of the Fourier transform integral. However the CSW has a relatively complex aperture field pattern that is non-separable and is not in closed form. Therefore, it is relatively difficult to obtain simple analytical expressions for the far-field patterns of the CSW. Appropriate Fourier transform theory [2,3] can be applied to efficiently evaluate (7.16) by sampling the aperture fields and obtaining a discrete sequence for evaluation on a digital computer. Let $\tilde{E}_{ax,y}$ be the aperture field sampled at spacings of $\Delta x' = \Delta y' = W/M$, where W is an

observation window larger than the dimension of the aperture and M is an integer power of 2. Furthermore, let $\widetilde{P}_{x,y}$ be sampled at spacings $\Delta u = \Delta v = 1/W$, then one obtains

$$\widetilde{P}_{x,y}(p_1\Delta u/\lambda, p_2\Delta v/\lambda) = \sum_{n_1=-M/2}^{M/2-1} \sum_{n_2=-M/2}^{M/2-1} \widetilde{E}_{ax,ay}(n_1\Delta x', n_2\Delta y') \exp\left\{ j\frac{2\pi}{M}(p_1 n_1 + p_2 n_2) \right\} \quad (7.17)$$

where p_1 and p_2 are integers. Equation (7.17) is in the form of the 2-dimensional discrete Fourier transform and is efficiently evaluated with the use of the fast Fourier transform (FFT) algorithm [2,3].

Once the radiated electric fields in (7.8) are obtained, the normalized far-field patterns can be calculated. In computing the far-field patterns the polarization characteristics of the CSW radiator must be preserved for comparison to the measured data. In this report the third definition of polarization given by Ludwig [4] is used, which relates measured, calculated or observed far-field pattern at an observation point (or probe) relative to a test antenna located at the origin. The corresponding relationship for a y-directed source (the CSW) and a probe (the measurement horn) is given by:

$$F_{co}(\theta,\phi) = \vec{E}(\theta,\phi) \bullet \left[\sin\phi\,\hat{\theta} + \cos\phi\,\hat{\phi}\right] \frac{r}{\max\left\{\left|\vec{E}(\theta,\phi)\right|\right\}} \quad (7.18)$$

$$F_{cr}(\theta,\phi) = \vec{E}(\theta,\phi) \bullet \left[\cos\phi\,\hat{\theta} - \sin\phi\,\hat{\phi}\right] \frac{r}{\max\left\{\left|\vec{E}(\theta,\phi)\right|\right\}} \quad (7.19)$$

where F_{co} and F_{cr} are the normalized co- and cross-polarized far-field patterns respectively. As stated, both the co- and cross-polarization patterns are normalized to the maximum of the electric field. The normalized far-field patterns are used to calculate the theoretical patterns for comparison to measured data in the following sections. In this report it is assumed that all calculations and measurements are relative to a y-directed source.

7.3 Computed Patterns for the CSW

In this section, Section 7.4, and Appendix B, the CSW far-field co-polarized patterns are computed using (7.18) and the cross-polarized patterns are calculated from (7.19). The patterns in this section are computed at a frequency of 11 GHz using the Test Case #2 CSW. The computed cases in this section allow one to form a general understanding of the CSW radiation characteristics, for comparison to the measured results in Section 7.4. The general case of both dominant and higher-order mode radiation is considered to identify key factors necessary to understand measurements of the CSW. To perform the multimode analysis presented in this section, the scaling constant χ_n defined by (7.3) through (7.6) is used to vary the relative energy contained in each of the propagating modes. Additional computed far-field pattern data for one octave frequency bandwidth are provided in Appendix B, for comparison to measured results discussed in Section 7.4.

7.3.1 Dominant Mode Radiation Characteristics

For measurement and analysis purposes the "ideal case" radiation condition occurs when all of the propagating energy in the CSW is confined to the dominant TE_{10} mode. Therefore no is energy propagating in the higher-order modes and the orthogonal TE_{01} mode[1] ($\chi_1 = 1$, and $\chi_2 = \chi_3 = \chi_4 = 0$). A plot of the computed radiation characteristics for the Test Case #2 CSW is shown in Figure 7-2. Co- and cross-polarization patterns for both the E- and H-planes of the CSW are provided in the figure. As shown in the co-polarization patterns of Figures 7-2a and 7-2b, the E-plane has a wide main beam compared to the H-plane. The wider beamwidth in the E-plane is due to the electric field taper across the aperture.

The cross-polarization for the E- and H-plane is determined by a relatively weak x-directed electric field present on the boundary of the dielectric septum and air. This x-directed field component is not present in an unloaded waveguide excited only by the TE_{10} mode. The cross-polarization due to this weak x-directed component was found to be about -60 dB and is relatively small compared to the cross-polarization levels calculated and measured in the non-ideal cases in following sections.

[1]This assumes we are transmitting or receiving pure linear polarization, for a y-directed source.

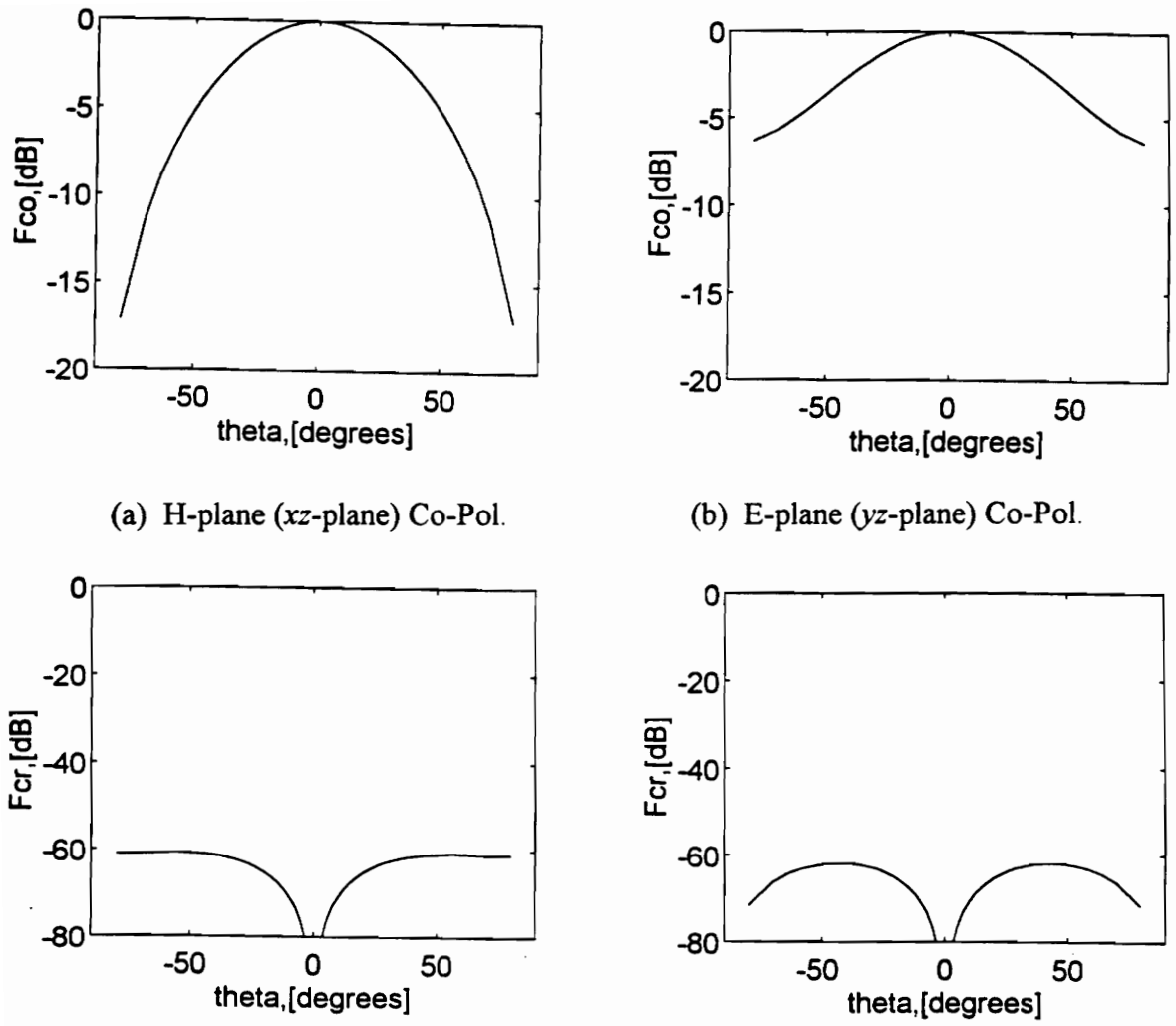

(a) H-plane (*xz*-plane) Co-Pol.

(b) E-plane (*yz*-plane) Co-Pol.

(c) H-plane (*xz*-plane) Cross-Pol.

(d) E-plane (*yz*-plane) Cross-Pol.

Figure 7-2. Computed far-field patterns for the CSW assuming pure TE_{10} mode radiation. The parameters are; Test Case #2, frequency = 11.0 GHz, $\chi_1 = 1$, and $\chi_2 = \chi_3 = \chi_4 = 0$.

7.3.2 Orthogonal Mode Radiation Characteristics

The method of coupling energy into the CSW may also result in exciting the dominant orthogonal (TE_{01}) mode, as well as the desired dominant (TE_{10}) mode. Once excited, the dominant orthogonal mode will propagate relatively unattenuated since the mode filters are intended to remove only energy from the higher-order modes. It is therefore necessary to include the dominant orthogonal mode in the multimode analysis of the CSW radiation properties. A plot of the CSW radiation patterns for $\chi_1 = 1$ and $\chi_2 = 0.1, 0.3, 0.5, 1.0$, and 10^{10} is shown in Figure 7-3. The patterns indicate that when χ_2 is small, there is little change in the main beam. However as χ_2 increases, power is shifted from the co-polarized beam to the cross-polarized beam as expected. When nearly all the energy is in the orthogonal mode ($\chi_2 \rightarrow 10^{10}$) the cross-polarization pattern of Figure 7-3 identically resembles the co-polarization pattern for the case of $\chi_2 = 0$ shown in Figure 7-2. The presence of the orthogonal mode results in a lobe at $\theta = 0$ rather than a null as will be seen in the next section.

7.3.3 Higher-Order Mode Radiation Characteristics

The case when all energy is contained in one of the higher-order modes is now considered. We will arbitrarily choose the TM_{11} mode as the propagating mode by letting $\chi_1 = \chi_2 = \chi_4 = 0$ and $\chi_3 = 1$ when computing the far-field patterns. The computed patterns for this case are shown in Figure 7-4. The patterns indicate that the H-plane cross polarization and the E-plane co-polarization patterns are identical, and have a deep null in the center. Likewise the H-plane cross-polarization and the E-plane co-polarization patterns are identical, however have a lobe in the center of about -18 dB. The observed symmetry in the calculated patterns for the TM_{11} mode is expected since the electric field pattern for this mode is identical when rotated by 90 degrees. A similar discussion also applies to the TE_{11} mode.

7.3.4 Multimode Radiation Characteristics

A more complete and realistic understanding of the CSW radiation characteristics can be obtained by considering energy distributed among multiple propagating modes in the CSW, referred to as multimode propagation. Propagating modes referred to here are modes that are above cutoff frequency, and the associated energy is that which may be coupled into the guide but not completely removed by the mode filters. This includes all

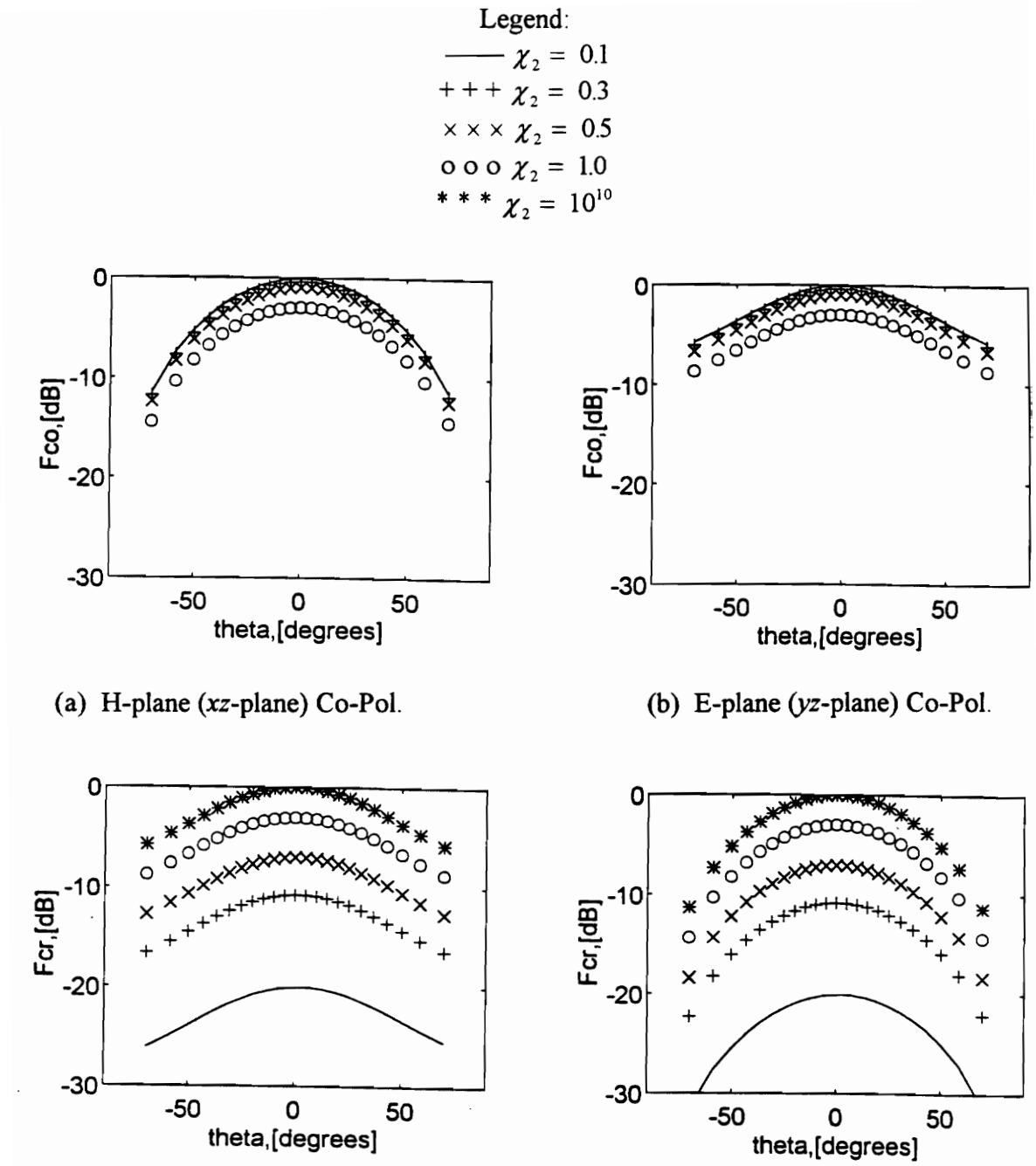

(a) H-plane (*xz*-plane) Co-Pol.

(b) E-plane (*yz*-plane) Co-Pol.

(c) H-plane (*xz*-plane) Cross-Pol.

(d) E-plane (*yz*-plane) Cross-Pol.

Figure 7-3. Computed far-field patterns for the CSW assuming both dominant TE_{10} and orthogonal TE_{01} mode radiation. The parameters are; Test Case #2, frequency = 11.0 GHz, $\chi_1 = 1$, $\chi_2 =$ 0.1, 0.3, 0.5, 1.0, 10^{10}, and $\chi_3 = \chi_4 = 0$.

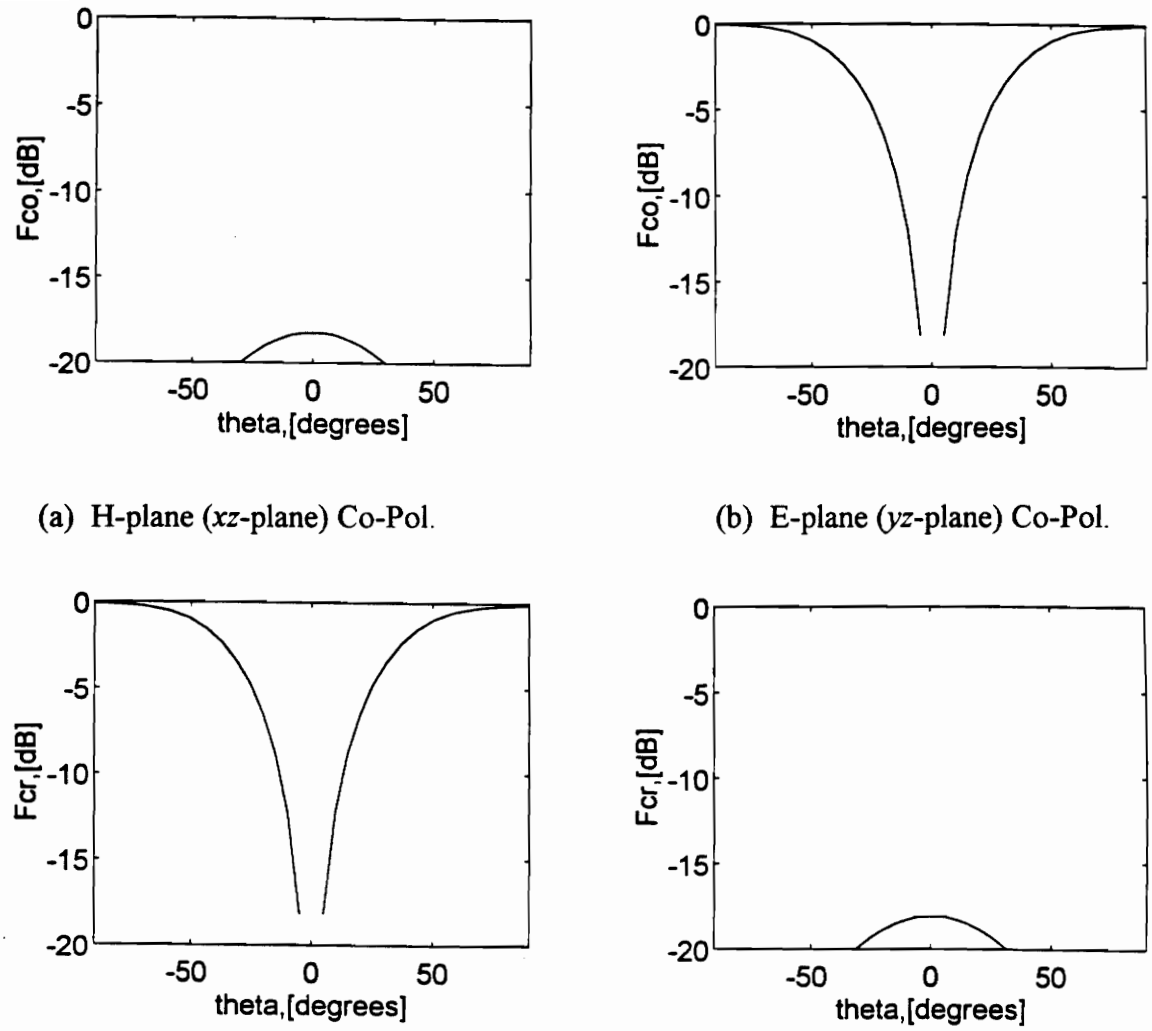

(a) H-plane (*xz*-plane) Co-Pol.

(b) E-plane (*yz*-plane) Co-Pol.

(c) H-plane (*xz*-plane) Cross-Pol.

(d) E-plane (*yz*-plane) Cross-Pol.

Figure 7-4. Computed far-field patterns for the CSW assuming pure TM_{11} higher-order mode radiation. The parameters are; Test Case #2, frequency = 11.0 GHz, $\chi_3 = 1$, and $\chi_1 = \chi_2 = \chi_4 = 0$.

modes given in Table 7-1, provided that the frequency of operation is at least above cutoff for the corresponding mode.

Energy content in each mode is controlled by adjusting the scaling constant χ_n in computed values. The first multimode case is computed by holding the dominant TE_{10} mode energy constant ($\chi_1 = 1$), and letting the energy in each of the other modes be equal, however varied for values of $\chi_2 = \chi_3 = \chi_4 = 0, 0.1, 0.3, 0.5, 1.0$ representing power levels of $-\infty, -20, -10, -6$ and 0 dB respectively relative to the TE_{10} mode. The computed radiation patterns in Figure 7-5 show that the shape of the main beam for the H-plane remains constant, however the peak of the main beam is reduced in amplitude, as energy is redistributed into the other modes. The E-plane in contrast to the H-plane shows the main beam becoming asymmetric as the beam tends to squint with increasing values of χ_2, χ_3 and χ_4. Also, as shown in the figure, the maximum cross polarization in the H-plane is higher than that of the E-plane for all cases of χ_2, χ_3 and χ_4. The introduction of energy in the higher-order modes results in an increase in cross-polarization.

The next computed multimode radiation case holds energy in the dominant TE_{10} mode constant, and energy associated with a single higher-order mode, specifically the TM_{11} mode is varied; this is expressed as $\chi_1 = 1$, $\chi_2 = \chi_4 = 0$, and $\chi_3 = 0, 0.1, 0.3, 0.5, 1$. The computed far-field patterns in Figure 7-6 are somewhat similar to those obtained in Figure 7-5. As χ_3 is increased, the H-plane pattern remains relatively constant. Also as in the prior case, the increase energy in the higher-order mode results in distortion of the E-plane pattern referred to as beam squinting. The patterns for the cross-polarization also indicate one can expect the peak cross-polarization in the H-plane to be affected more severely than the E-plane by about 15-20 dB, when χ_3 is increased.

7.3.5 Comments on Analysis Results

For a CSW radiator element, one would design the waveguide to minimize χ_2, χ_3 and χ_4 relative to χ_1 which is accomplished by the use of proper coupling methods and mode filters as discussed in Chapter 6. It must be emphasized that as a practical matter, one does not have knowledge or control of the amplitude and phase of the scaling constant χ_n for each mode under consideration. Considering both magnitude and phase of χ_2, χ_3 and χ_4, there are six unknowns which cannot be uniquely specified or inferred by measurements of the far-field patterns. Therefore, the calculated patterns obtained

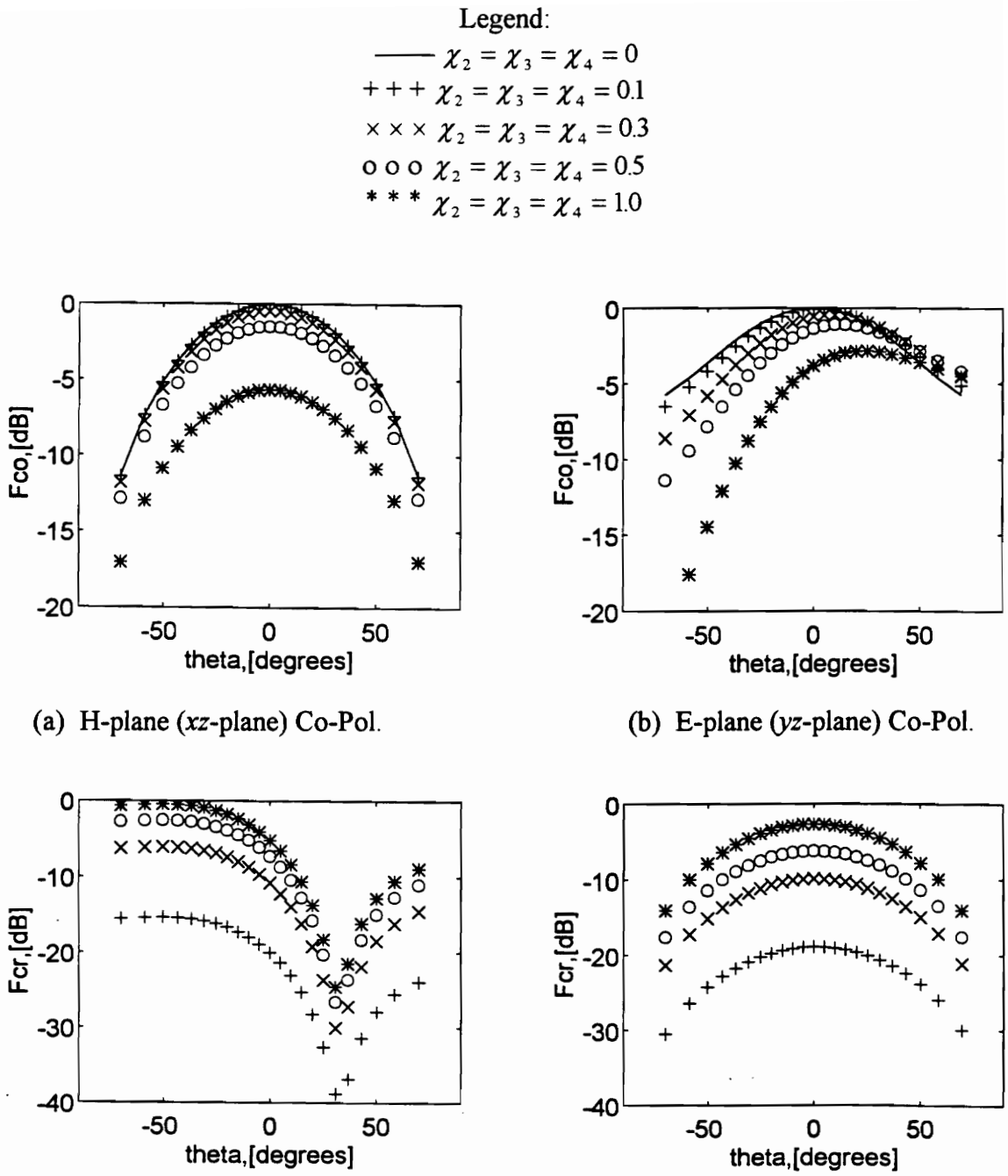

(a) H-plane (*xz*-plane) Co-Pol.

(b) E-plane (*yz*-plane) Co-Pol.

(c) H-plane (*xz*-plane) Cross-Pol.

(d) E-plane (*yz*-plane) Cross-Pol.

Figure 7-5. Computed far-field patterns for the CSW assuming TE_{10}, TE_{01}, TM_{11}, and TE_{11} multimode radiation. The parameters are; Test Case #2, frequency = 11.0 GHz, $\chi_1 = 1$ and $\chi_2 = \chi_3 = \chi_4 = 0, 0.1, 0.3, 0.5, 1.0$.

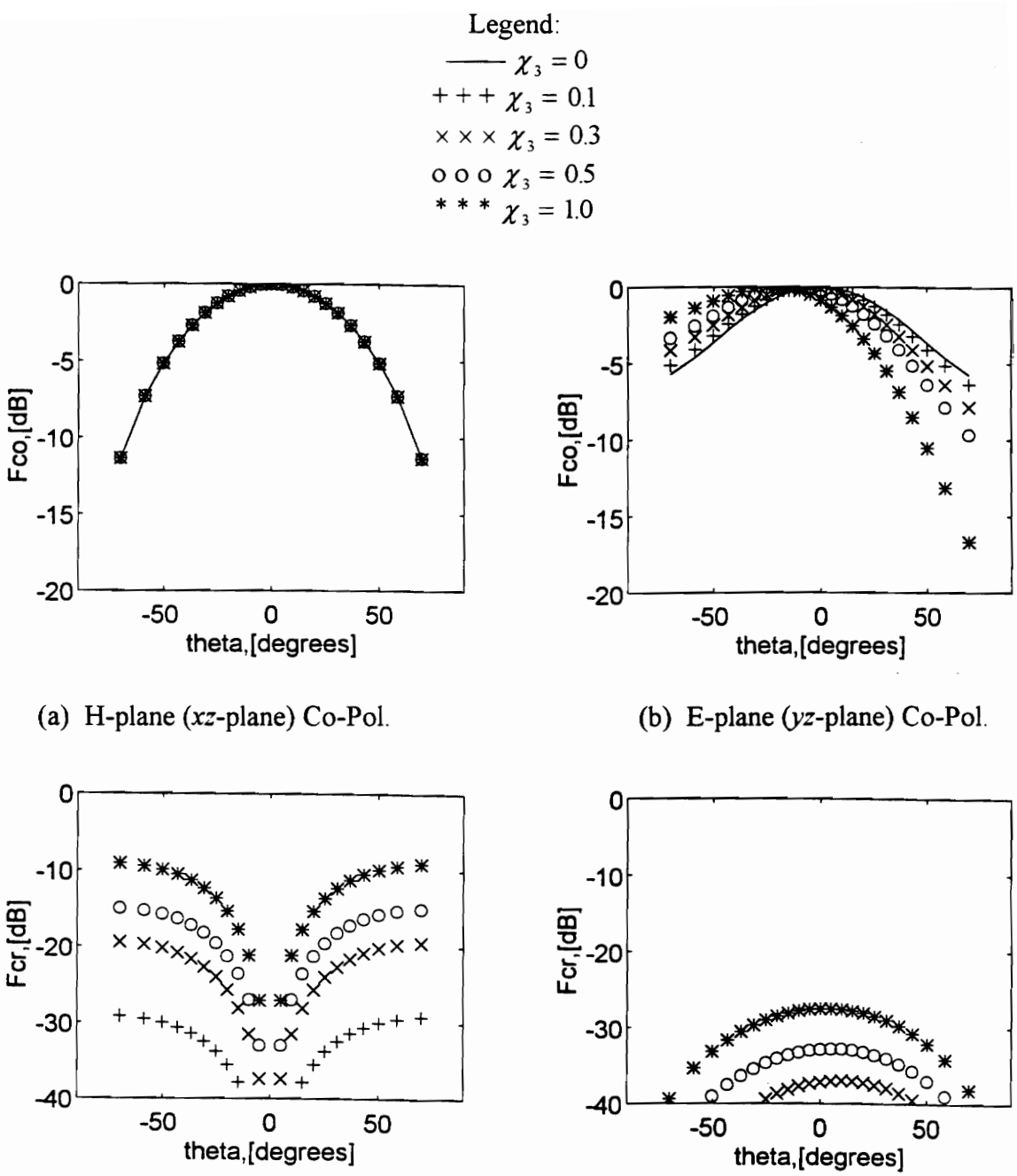

(a) H-plane (*xz*-plane) Co-Pol.

(b) E-plane (*yz*-plane) Co-Pol.

(c) H-plane (*xz*-plane) Cross-Pol.

(d) E-plane (*yz*-plane) Cross-Pol.

Figure 7-6. Computed far-field patterns for the CSW assuming TE_{10}, and TM_{11} multimode radiation. The parameters are; Test Case #2, frequency = 11.0 GHz, $\chi_1 = 1$, $\chi_3 =$ 0, 0.1, 0.3, 0.5, 1.0, and $\chi_2 = \chi_4 = 0$.

above are useful only in identifying effects of the dominant and higher-order modes. This however is quite valuable in identifying the important far-field measurement parameters necessary for characterizing the CSW far-field patterns. From the data computed in Sections 7.3.1 through 7.3.4 and from Figures 7-2 through 7-6, one can summarize the generally observed trends of the multimode analysis. These trends are referred to in Section 7.4 for comparison of theoretical to measured data:

- Co-polarization, H-Plane: As energy shifts from the dominant mode to the higher-order modes, little change in the shape of the main beam shape occurs. If all the energy were contained in one of the higher-order modes, then one would observe a decrease in the main beam strength. If all of the energy were contained in the dominant orthogonal mode, one would also observe a substantial decrease in the main beam strength.

- Co-polarization, E-Plane: A deformation in the shape of the main beam is observed as energy shifts from the dominant mode to the higher-order modes. This deformation can lead to an off axis peak referred to as beam squinting. If all of the energy were contained in a higher-order mode then a null would be measured on boresight. If all of the energy were contained in the dominant orthogonal mode, one would also observe a dramatic decrease in the main beam strength.

- Cross-polarization, H-Plane: An increase in the cross-polarization is observed as energy shifts from the dominant mode to the higher-order modes. In all of the multimode computations performed above, the maximum H-plane cross-polarization was found to be *larger* than that of the E-plane cross-polarization. If all of the energy were contained in a higher-order mode then a null would be measured on boresight and the cross polarization level would be relatively high. If all of the energy were contained in the dominant orthogonal mode, then a main beam with relatively high amplitude would be observed on boresight.

- Cross-polarization, E-Plane: The effects of multimode propagation on the E-plane cross-polarization are roughly the same as those of the H-plane, except that the peak amount of cross-polarization is less. If all of the energy is contained in one higher-order mode, then one would observe a main beam similar to that of the H-plane co-polarization

pattern. If all of the energy were contained in the dominant orthogonal mode, a main beam would be observed on boresight, and its amplitude would be relatively high.

7.4 Measured Results

Using the CSW referred to as Test Case #2, far-field pattern measurements were performed using the antenna measurement range at Va-Tech's Whittemore Hall. Both co- and cross-polarization of the H-and E-planes were measured at frequencies of 7.5, 9.0, 10.0, 11.0, 12.0, 13.0, 14.0 and 15.0 GHz. Therefore the measurements frequencies span one octave within the theoretical bandwidth ratio of 2.20:1, based on cutoff frequencies of the TE_{10} and TE_{20L} modes given in Table 7-2.

Table 7.2
Test Case #2 Modal Cutoff Frequencies.

Mode	Cutoff frequency (GHz)
TE_{10}	6.96
TE_{01}	6.96
TM_{11}	9.34
TE_{11}	10.10
TE_{20L}	15.30
TM_{12}	15.43

7.4.1 Co-Polarized Measured Results

Appendix B lists all of the Test Case # 2 measured data presented for each of the frequencies given above. Shown are the measured and theoretical patterns for the CSW. The theoretical patterns were computed assuming only the dominant TE_{10} mode present, i.e., $\chi_1 = 1$ and $\chi_2 = \chi_3 = \chi_4 = 0$. In interpreting the measured results, one can consider two subsets of measurement frequencies: a.) those below the TM_{11} (the first higher-order mode) cutoff frequency where only the dominant mode is propagating, and b.) those

above the TM_{11} mode cutoff frequency where we desire single mode propagation but there may also be energy contained in higher-order modes.

7.4.1.1 Co-Polarized Patterns Below Higher-Order Mode Cutoff

The first set of measured patterns includes those performed below the cutoff frequency of the TM_{11} mode, specifically the 7.5 and 9.0 GHz measurements. At these frequencies the aperture must contain only the dominant mode fields[2]. Therefore, in terms of aperture fields, the dominant mode theory should best predict the far-field patterns of the CSW since as in Section 7.3 above, the effects of multimode radiation will not apply. The H-plane co-polarized data shown in Figures B-1 and B-2 (Appendix B) indicate excellent agreement with theory, especially within the $\theta = \pm 45°$ region of the patterns. Beyond about $\theta = \pm 60°$, there is increased ripple in the measured patterns and there is less agreement between measurement and theory, likely due to surface currents on the edge of the guide which are not accounted for by the physical optics approximation. Cross-polarization patterns are discussed in Section 7.4.2.

In the measured E-plane patterns of Figures B-9 and B-10, two trends are obvious. First, the measured patterns are well behaved over about $\theta = \pm 30°$, but beyond that exhibit increased ripple. However, these patterns are likely to be sufficiently good for many phased array antenna applications. The second observation is that the computed patterns predict a broader pattern than was observed experimentally. There are several possible explanations for this discrepancy between theory and experiment. The CSW is an electrically small aperture with a width of about 0.375λ at the lowest measurement frequency. One possibility for the discrepancy between theory and measurement is in consideration of the electric field distribution of the TE_{10} mode. For the TE_{10} mode the field strength at $x = 0$, $y = \pm a/2$ (where a = width of guide) is a maximum compared to the field strength in the x-variation which is roughly cosine tapered and zero at $x = \pm a/2$. This could conceivable introduce edge currents that contribute to the E-plane patterns but leave the H-plane relatively unaffected, especially since the CSW is an electrically small aperture. There may also be perturbations in the fields at the aperture due to the mode filters which are not accounted for. These secondary effects are discussed in Section 7.5

[2] We will neglect evanescent modes which contain stored energy near the aperture.

7.4.1.2 Co-Polarized Patterns Above Higher-Order Mode Cutoff

The second set of measured patterns includes those performed above the cutoff frequency of the TM_{11} mode, including 10.0, 11.0, 12.0, 13.0 14.0 and 15.0 GHz. At these frequencies, the higher-order modes may have an effect on the far-field patterns, depending on the amount of energy coupled into the each of the modes and the performance of the mode filters at a given frequency. The H-plane patterns shown in Figures B-3 through B-8 are well behaved within about $\theta = \pm 45°$ and the comparison to theory is good at frequencies up to about 12.0 GHz. As the frequency increases (to 13.0 GHz or greater), there is increased ripple present in the patterns.

The E-plane patterns shown in Figures B-11 through B-16 are well behaved at frequencies through about 12.0 GHz. Above about 13.0 GHz, the beam squinting phenomena described by theory in Section 7.3 gradually appears as the frequency increases. This beam squinting is normally considered undesirable and is most likely due to energy associated with a higher-order mode such as the TM_{11} mode present at the CSW aperture. The appearance of energy in a higher-order mode is an indication of reduced performance of the mode filters at the high frequency end of operation.

7.4.2 Cross-Polarized Measured Results

Cross-polarization measurements in both the E- and H-planes were performed at the identical frequencies as described in Section 7.4.1. The data are shown along with the co-polarization measurements provided also in Appendix B. The measured cross-polarization data for both planes for the CSW are plotted in Figure 7-7 as a function of frequency. The plotted cross-polarization values are the maximum levels within a $\theta = \pm 45°$ region. It is reasonable to neglect cross-polarization levels outside $\theta = \pm 45°$ since this region is more likely to be dominated by effects of surface currents which are neglected in the physical optics analysis.

As in the co-polarization measurements, the cross-polarization measurements are best interpreted in two sets defined by those below and those above the cutoff frequency of the TM_{11} mode. Each of these cases are considered below.

7.4.2.1 Cross-Polarized Patterns Below Higher-Order Mode Cutoff

The measured cross-polarization of the CSW at frequencies below the cutoff of the first higher-order mode (7.5 and 9.0 GHz) provide very useful information about the Test

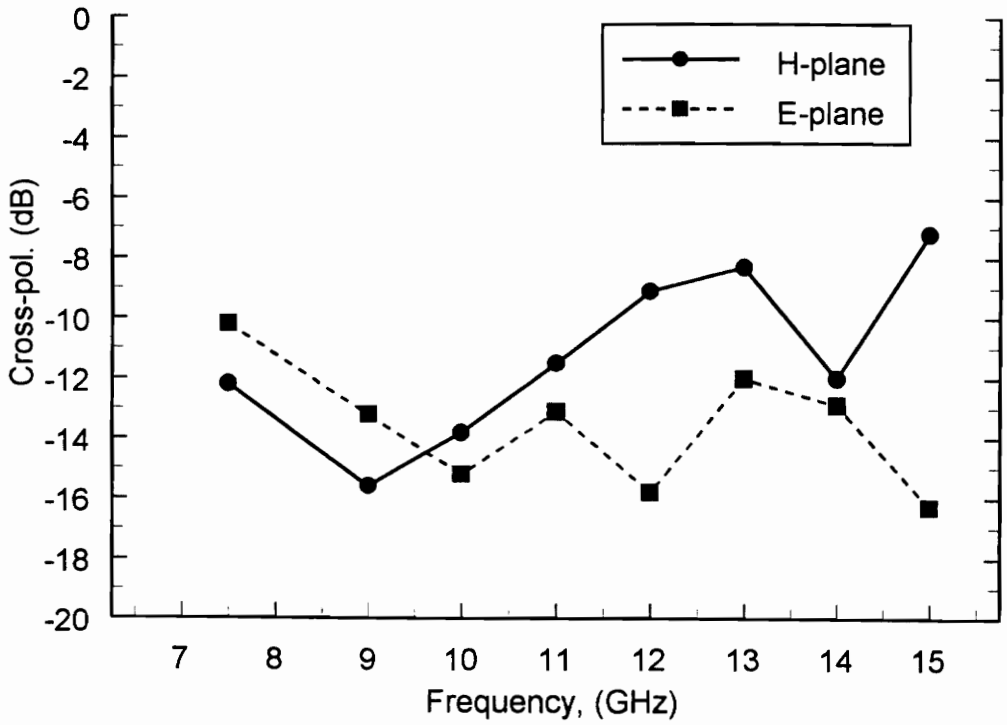

Figure 7-7. Measured cross-polarization vs. frequency for E- and H-planes. The values given are the maximum cross-polarized values within $\theta = \pm 45°$, from the CSW Test Case # 2 measured results in Appendix B.

Case #2 since the pattern contribution must come only from the dominant TE_{10} or the orthogonal TE_{01} modes. The levels of cross-polarization range between about 10-16 dB, and from Section 7.3.1, this is indicative of energy coupled into the TE_{01} mode at about 10-16 dB relative to the TE_{10} mode. We recall that the mode filters are intended to remove the TM_{11} and TE_{11} mode energy, and hence will not affect the TE_{01} mode relative to the TE_{10} mode. Although this cross-polarization is not excessively high, it is somewhat of a disappointment when compare to the -60 dB levels computed using only the TE_{10} mode. Several possible explanations for the observed cross-polarization levels include the coupling into the orthogonal mode and also imperfections in the construction of the CSW.

The calculations performed in Section 7.3.1 showed that for the case when energy is confined to only the dominant TE_{10} and TE_{01} modes, cross polarization levels in both planes should be the same. As shown in Figure 7-7, it was observed that the E-plane and H-plane cross-polarization levels are equal to within about 2-3 dB. This point is considered further in the following section.

7.4.2.2 Cross-Polarized Patterns Above Higher-Order Mode Cutoff

At frequencies above the TM_{11} mode cutoff frequency (i.e., 10.0 -15.0 GHz) the cross-polarization measurements must be evaluated in terms of the multimode radiation characteristics. In Section 7.3 it was shown that the peak cross-polarization of the H-plane is greater than the peak of the E-plane cross-polarization, when the higher-order modes are present. In Figure 7-7 we see that for all frequencies above the TM_{11} mode cutoff frequency, the H-plane cross-polarization is larger than the E-plane cross-polarization. For the cases where this difference is significant, it is likely that the high cross-polarization is due largely to the higher-order mode radiated energy, rather than to the orthogonal mode. The cross-polarization tends to gradually increase at the higher frequencies and is likely due to reduced performance of the mode filters at the higher frequency of operation.

7.5 Higher Order Effects on Far Field Patterns

The modal analysis of the CSW in the preceding Chapters was performed on a 2-dimensional cross section of an infinitely long waveguide. The assumption of an infinitely

long waveguide is a good approximation when the both ends of the waveguide are well matched. However, the open ended waveguide radiating element discussed in this chapter may not necessary be well matched. Both the aperture (open end of the waveguide) and the coaxial feed present discontinuities for waves traveling in the $\pm z$-directions. Therefore one must solve a 3-dimensional boundary value problem when performing an exact analysis of the CSW modal and radiation characteristics. Of particular interest for the radiation problem is the waveguide/air interface which forms the aperture. The waveguide/air interface represents a discontinuity for waves that are incident to the interface. According to Maxwell's equations, continuity of both the magnetic and electric fields must be maintained at the interface. A perturbation in the field structure at the aperture will occur and therefore produce higher order effects[3] on the radiation patterns that are neglected in the analysis provided in Sections 7-2 through 7-4. These higher order effects have been examined in relatively simple cases, such as unloaded rectangular waveguides [8-12]. A discussion of the higher order effects can be useful in explaining discrepancies between computed and measure patterns. The discrepancies referred to here include differences in computed and measured beamwidths, and the presence of ripple in the measured patterns.

There are two phenomena which occur due to the boundary conditions at the waveguide/air interface; reflections of z-directed waves [8-12] and surface currents on the edge of the guide walls due to fringing [10]. Each of these two phenomena are now discussed to identify and qualitatively explain likely higher order effects apparent when comparing the patterns computed using (7.3) through (7.19) (e.g., aperture theory) to the measured patterns.

7.5.1 Effects Due to Reflections at the Air/Waveguide Interface

First, we will discuss the likely effects of the reflections occurring at the air/waveguide interface. The exact representation of the fields at the interface can be written in terms of the sum of incident and reflected waves traveling in the $+z$ and $-z$ directions respectively. Gardoil [8] gives an expression for the fields in a waveguide for which a single propagating mode is incident the aperture and multiple (dominant and higher-order) modes are reflected. Gardiol's representation can be expanded to include

[3] The terms 'higher order effect' in this context is referring to a secondary effect, not higher-order modes.

multiple propagating modes which are incident the waveguide/air interface. Then the electric and magnetic fields at the $z = 0$ interface (see Figure 7-1) are given by

$$\vec{E}_a(x',y') = \sum_n^N \chi_n \vec{E}_{an}(x',y') + \sum_m^M \chi_m \Gamma_m \vec{E}_{am}(x',y') \tag{7.20}$$

and

$$\vec{H}_a(x',y') = \sum_n^N \chi_n \vec{H}_{an}(x',y') - \sum_m^M \chi_m \Gamma_m \vec{H}_{am}(x',y'). \tag{7.21}$$

As given in (7.3) and (7.4), χ_n is a complex scaling constant representing losses in the guide and the relative excitation of the nth mode. In (7.20) and (7.21) the summation over N represents modes traveling in the $+z$ direction that are incident the interface. The summation over M represent modes traveling in the $-z$ direction that are reflected from the interface having a reflection coefficient given by Γ_m. One can note that when $\Gamma_m = 0$, (7.20) and (7.21) reduce to (7.3) and (7.4) respectively. Incident modes in general include the unattenuated dominant mode and multiple higher order propagating modes which are desired to be suppressed by the mode filters. Reflected waves include both propagating and nonpropagating (evanescent) modes. The reflection coefficient was shown to have the effect of changing the beamwidth of an unloaded open-end waveguide radiator [9,11].

A rigorous solution of (7.20) and (7.21) for the CSW is somewhat of a protracted problem since it requires solving a 3-dimensional boundary value problem. One must accurately know the relative excitation and suppression of each of the modes, as well as the reflection coefficients at the interface boundary and the feed point. To solve (7.20) and (7.21) one would need a model for expressing the relative excitation of each of the modes (such as a Green's function) for the CSW. To obtain the relative level of modal suppression one would need an expression (or model) that includes losses and reflections due to the mode filters. To pursue this problem further would require the development of more detailed mathematical models and/or an experimental program to determine the magnitude and phase of the reflection coefficient, for all modes of interest. An experimental investigation of general case multimode reflection coefficients is a task requiring significantly more equipment than was at hand for the work performed during the course of the research project. This task will be left as a potential area for future work.

7.5.2 Effects Due to Edge Surface Currents

The second likely higher order effect to consider is that of surface currents on the edge of the guide (i.e., the flange). It is believed that these edge currents may be responsible for the tendency of the aperture theory (Sections 7.2-7.5) to predict too wide of a beamwidth in the E-plane at the lower frequencies, and also for the presence of ripple in the measured patterns.

The magnitude of currents present on the edge (or flange) of the guide depend on the modal field distribution present in the aperture. The transverse electric field distribution of the dominant mode of the infinitely long CSW shown in Figure 5-1a is a maximum at $x/b = 0$ (i.e., on the y-axis). In order to maintain continuity of the electric field, one would expect that surface currents must extended to the edge (flange) in the $\pm y$-direction of the $z = 0^+$ plane of the open-ended waveguide. The maximum edge currents must then occur near the y-axis. These edge surface currents effectively increase the size of the radiating structure in the y-direction which in turn narrows the beamwidth in the E-plane. Upon inspection of the measured and computed E-plane patterns shown in Figures B-9 through B-16, one can note at the lower frequencies, the measured patterns exhibit a more narrow beam in comparison to aperture theory. At the higher frequencies where the aperture is electrically larger, aperture theory is a better predictor of the radiation patterns. For an unloaded rectangular open-ended waveguide, Yaphjian [10] corrects for the currents on the edge of the guide by the use of superposition. An 'artificially' line source is placed along the z-axis, to account for the edge currents on the guide thus forcing the computed pattern to become more narrow, and thus more closely resembling the measured data.

Where the transverse electric field shown in Figure 5-1a is a minimum (i.e., $x/b = \pm 1$), no edge currents need to be introduced on the edge of the guide in the $z = 0^+$ plane in order to maintain continuity of the electric field since the electric field is zero. Therefore, one would expect that the x-dimension of the radiating structure will not significantly increase beyond the confines of the aperture; hence the H-plane beamwidth will not become narrower. Upon inspection of the H-plane data in Figures B-1 through B-8, one finds that there is generally very good agreement between aperture theory and experiment over the whole range of frequencies.

7.6 Summary of CSW Radiation Characteristics

The measured and calculated results of this chapter demonstrate several key points. These points can be summarized as follows:

- Aperture theory has been used to model the CSW radiation characteristics. The analysis included both single mode and multimode radiation in order to also model the secondary effects of the higher-order modes on the radiation patterns.

- The measured patterns clearly indicate that when the CSW (with mode filters present) is excited with a loop, the dominant mode will propagate and radiate producing patterns which may be sufficient for many applications. Typical observed cross-polarization levels were about -10 dB. The absence of a strong cross-polarization component indicates energy is largely confined to the dominant mode, rather than a higher-order mode.

- Patterns for the CSW Test Case #2 were measured and compared to theory over an octave of bandwidth. The patterns are well behaved and may be suitable for many phased array applications. Performance indicates graceful degradation, with reduced performance at the high frequency end of the bandwidth.

- The mode filters have no noticeable adverse effects at the low frequencies where only the dominant mode can propagate. Since cross-polarization levels of -10 dB were observed even at the low frequencies, this may be an indication of energy also coupled into the orthogonal mode.

- Several higher order effects apparent in the measured patterns have been identified and discussed. These effects include ripple present in the measured patterns and differing beamwidths in the E-plane which are not accounted for using the aperture theory presented here. Based on prior work, these secondary effects are likely attributable to factors including edge currents and reflection of waves at the air/waveguide interface.

7.7 References for Chapter 7

[1] W.L. Stutzman and G.A. Thiele, *Antenna Theory and Design*, New York: John Wiley and Sons, 1981, Chapter 8.

[2] A.B. Carlson, *Communications Systems*, Third edition, New York: McGraw Hill, 1986, Appendix B.

[3] N.S. Jayant and Peter Noll, *Digital Coding of Waveforms*, Englewood Cliffs, New Jersey: Prentice Hall, 1984, p.600.

[4] A.C. Ludwig, "The definition of cross polarization", *IEEE Trans on Ant and Prop*, Vol. AP-18, pp.116-119, January 1973.

[5] C.C. Han and A.N. Wickert, "A new multimode rectangular horn antenna generating a circular polarized elliptical pattern", *IEEE Trans on Ant and Prop*, Vol. AP-22, pp.764-751, Nov. 1974. See also *Electromagnetic Horn Antennas*, ed. A.W. Love, New York: IEEE Press, 1976.

[6] P.A. Jensen, "A low-noise multimode cassegrain monopulse feed with polarization diversity", *Northeast Electron. Res. and Eng. Meeting*, Nov. 1963, pp.94-95. See also *Electromagnetic Horn Antennas*, ed. A.W. Love, New York: IEEE Press, 1976.

[7] A.W. Love, "The diagonal horn antenna", *Microwave J.*, Vol. V., pp. 117-122, March 1962. See also *Electromagnetic Horn Antennas*, ed. A.W. Love, New York: IEEE Press, 1976.

[8] F.E. Gardiol, "Open-Ended Waveguides: Principals and Applications", *Advances in Electronics and Electron Physics*, Vol. 63, Academic Press, New York, 1985.

[9] S. Silver, editor, Microwave Antenna Theory and Design, MIT radiation lab series, Vol. 12, McGraw-Hill: NY, 1949, Chapter 10.

[10] A.D. Yaghjian, "Approximate formulas for the far field gain of open-ended rectangular waveguide", *IEEE Trans on Ant and Prop*, Vol. AP-32, No. 4, pp.378-384, April 1984.

[11] H. Baudrand, J.W. Tao and J. Atechian, "Study of radiating properties of open-ended rectangular waveguides", *IEEE Trans on Ant and Prop*, Vol. AP-36, No. 8, pp.1071-1077, August 1988.

[12] K. Yoshitomi and H.R. Sharobim, "Radiation from a rectangular waveguide with a lossy flange", *IEEE Trans on Ant and Prop*, Vol. AP-42, No. 10, pp.1398-1403, October 1994.

CHAPTER 8

PHASED ARRAY IMPLICATIONS AND LIMITATIONS

8.1 Overview of Phased Array Implications

In Chapters 4 through 7 it was shown that the CSW element can provide more than one octave of single-mode bandwidth with the dielectric insert and mode filters present. The emphasis of the research described in this report is to assess the performance of the CSW with the focus on the wideband phased array application using the criteria outlined in Section 2.4. This criteria is based on both prior studies of canonical case infinite arrays (Section 2.3) and the hypothetical phased array requirements (Section 1.2). In this chapter, the practical implications of the results of Chapters 4 through 7 are interpreted in the context of the original phased array problem.

8.2 Array Element Size and Lattice Considerations

The k-β diagram discussed in Section 2.3.2 is a useful method of presenting array scan performance for a given frequency range and element spacing. Figure 2-9 presented Knittel's graphical method [1] of bounding the usable scan range as a function of frequency, higher order modes and grating lobe loci. The vertical axis of the k-β diagram is given by $k_o d_x/\pi$ where $k_o = 2\pi/\lambda_o$, $\lambda_o = \left(f_o\sqrt{\mu_o\varepsilon_o}\right)^{-1}$, d_x is the element spacing and f_o is the frequency. The horizontal axis is given by $\bar{k}_x d_x/\pi$, where $\bar{k}_x = k_o \sin\theta_o$ and θ_o is the scan angle.

The k-β diagram of Figure 8-1 shows the performance of an array of CSW elements having parameters defined as Test Case #2 in Tables 6-1a and 6-1b (see also

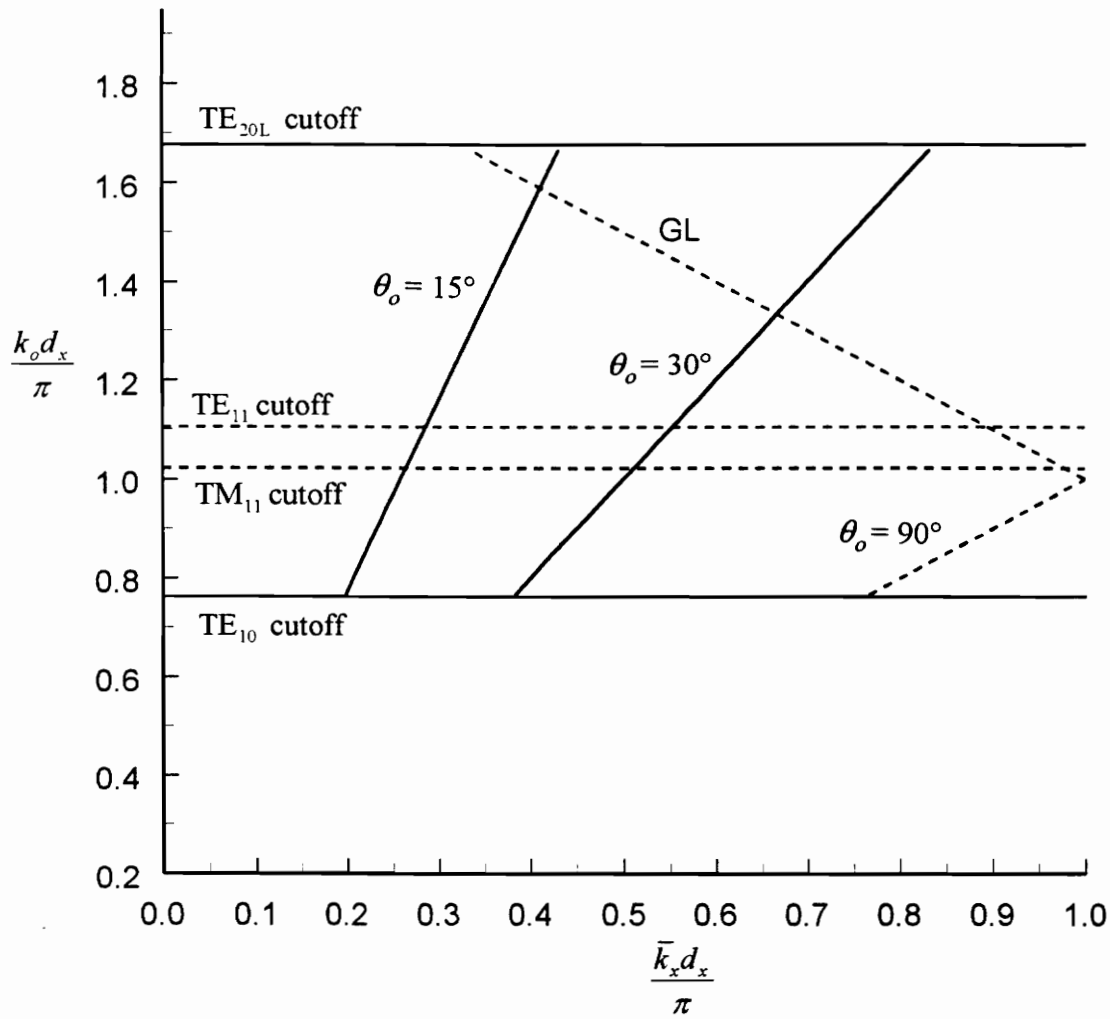

Figure 8-1. Bounds for scan angles using the k-β diagram, based on Knittel's graphical method [1]. An element spacing of $d_x = 1.1\,a$ is assumed, using the Test Case # 2 CSW. The grating lobe is denoted by 'GL'

Section 6.4.1). An element spacing of $d_x = 1.1a$ is assumed for the calculations of the k-β diagram. The spacing of $d_x = 1.1a$ is physically realizable for a closely packed rectangular lattice of elements, with a waveguide wall thickness of $0.05a$. The horizontal lines represent the theoretical modal cutoff frequencies given in Table 6-1b. The lower and upper frequency bounds are determined by the TE_{10} mode and TE_{20L} modal frequencies respectively. The upper bound frequency assumes that both the TE_{11} and TM_{11} modes are suppressed using the mode filters demonstrated in Chapter 6.

In Figure 8-1, the diagonal lines marked 15°, 30° and 90° represent lines of constant scan angle over the given range of frequencies. The diagonal line labeled GL represents the first grating lobe loci, computed using (2.7) as a function of frequency. Table 8-1 summarizes the maximum scan angle vs. bandwidth performance of the Test Case # 2 CSW based on Figure 8-1. The bandwidths given are ratios defined by (2.1) where the TE_{10} is the lower bound frequency. The upper bound is determined by either the higher-order TE_{20L} mode or the grating lobe. The size of the Test Case #2 CSW element is therefore sufficiently small that it can fit in an array lattice that satisfies the scan angle requirements given in Table 1-1 over an of octave bandwidth. Near the highest frequency of operation, the grating lobe and higher-order mode are the limiting factor for beam scanning the based on Knittel's graphical method [1]. The following section will further discuss the mutual coupling and matching considerations that must be addressed when designing a large scanning array.

Table 8-1. Maximum Scan Angle and Bandwidth Ratio.

Maximum Scan Angle for a Given Bandwidth	Bandwidth Ratio from Figure 8-1, using (2.1)	Upper Bound Limitation
11.2°	2.20:1	TE_{20L} mode
15°	2.08:1	grating lobe
30°	1.75:1	grating lobe

8.3 Mutual Coupling Considerations

As was discussed in Section 2.3.2 mutual coupling among array elements is a phenomena that can limit performance of the array when electronically scanned. In the analysis and design of large phased arrays, one often conducts infinite array studies which are then experimentally verified using a test array. Infinite array studies generally involve treatment of the array waveguide as a boundary value problem. A rigorous solution of the array boundary value problem is left as an area of future work.

Although one must be prudent when making claims of the performance of the CSW (without the rigorous array boundary value treatment), some inferences on the expected performance of the CSW can be made with respect to prior work. Again comparing the k-β diagram in Figures 2-9 and 8-1, one can speculate on the possible existence of blind spots. Recalling the discussion in Section 2.3, Figure 2-9 gives a graphical method [1] of predicting the bounds for blind spots. These bounds are due to the mutual coupling effects near a higher-order mode, based on the analytical work of Farrell and Kuhn [2]. The blind spots (in Figure 2-9) could possibly occur also for an array of CSW elements in Figure 8-1 just below the cutoff frequencies of the next higher-order mode, that is, the TE_{20L} mode. The extent of this must be further investigated to fully understand the phenomena in the context of the dominant TE_{10} mode and the suppressed TE_{11} and TM_{11} modes.

The scan dependent reflection coefficient in a array of waveguide elements is normally minimized to avoid unwanted reflections of energy. Therefore, one must use a suitable matching technique to match the element over some set of scan angles. Compared to an unloaded waveguide, the CSW has two additional parameters which may be varied to some extent to achieve a suitable match over the scan range. These parameters include the septum thickness and dielectric constant.

8.4 Cross-Polarization Considerations

In Section 7.4.2 cross-polarization levels for the Test Case #2 CSW were measured. Typical cross-polarization levels of about -12 *dB* were observed with a best case of -16 *dB* and worst case of -7.5 *dB*. Of interest to a phased array radar designer is

how these cross-polarization levels will impact system performance. For the radar threat simulator discussed in Section 1.2, several generalizations on cross-polarization can be made. If the phased array antenna is operated in an emitter only mode[1], then cross-polarization levels of this amount will have essentially no effect on the threat simulation performance [3],[4].

Cross-polarization rejection ratio is a measure of a radar system's ability to rejected an incoming wave orthogonal to the desired polarization state during the receive mode of the radar system. One must consider the cross-polarization rejection ratio of the antenna during tests of the jamming mode of operation and other electronic counter measures for a threat simulation application [4]. For active noise jamming methods (such as spot and barrage jamming [5]), the cross-polarization rejection ratio characteristics of the receiving antenna are typically not exploited [5]. Hence, typical cross-polarization levels of 12 *dB* are suitable for active noise jamming simulator applications. However for cross-polarization jamming, the cross-polarization rejection ratio of the phased array antenna is a significant factor in system performance [5]. The cross-polarization rejection ratio must then be evaluated on a case by case basis for a particular application using the simulator validation guidelines given in [4].

8.5 References for Chapter 8

[1] G.H. Knittel, "The relation of blindness to higher-order mode cutoff conditions," *IEEE G-AP Int. Symp. Digest*, pp. 69-72, September, 1971.

[2] G.F. Farrell and D.H. Kuhn, "Mutual coupling in infinite planar array of rectangular waveguide horns", *IEEE Trans. Antennas Propagat.*, vol. AP-16, no. 4, pp. 405-414, July 1968.

[3] "Electronic Combat Range User's Guide-Volume 1: an Overview," NAWCWPNS TM 7260, Vol. 1, May ,1993.

[4] "Threat Simulator Program Plan: Threat Definition Document Detailed Design Study -- Radar Parameters", Annex 1, Appendix A, Version 3, December 16, 1994. Prepared

[1] The 'emitter only mode' refers to an application where the antenna is operated only in the transmit mode, for the purposes of increasing signal density in space.

by the Defense Intelligence Agency, Missile and Space Intelligence Center, Redstone Arsenal, AL.

[5] A. Farina, "Chapter 9 - Electronic Counter-Counter Measures", *Radar Handbook*, Second Edition, edited by M.I. Skolnik, New York: McGraw-Hill, 1990.

CHAPTER 9

CONCLUSIONS

This report described the modal, bandwidth and radiation characteristics of a novel radiating element known as the crossed septum waveguide (CSW). The CSW consists of a square waveguide with crossed dielectric slab inserts placed so as to preserve the 90° rotational symmetry, which is a necessary condition for supporting dual polarization. The modal characteristics of the CSW were investigated using the mode matching technique. It was shown that the dominant TE_{10} and the TE_{20L} cutoff frequencies can be separated by the proper selection of dielectric thickness and permittivity. The modal separation for the dominant and first several higher-order modes depend on the symmetry properties of a given mode, and whether or not it is TE or TM. Another interesting observed phenomena is mode splitting, which was found to occur for the TE_{20} and TM_{13} modes. The mode splitting phenomena will split the designated modes into and upper 'U' and lower 'L' modes, each with significantly different field structures and phase constants.

The dielectric insert in the square waveguide increases the separation in the TE_{10} and the TE_{20L} cutoff, and one can achieve single-mode bandwidth extension if mode filters are used to 'remove' the TE_{11} and TM_{11} mode energy. A design procedure has been described for the necessary mode filters. A mode filter was constructed using a thin resistive film, and was demonstrated using the resonant cavity technique. A linear polarized mode filter was used to clearly identify dominant mode resonances, and then used to compared and corroborate the dual polarized mode filter measurements. The resonant cavity measurements performed both with and without mode filters present are shown in Figures 6-11 and 6-8 respectively. The dual polarized mode filter investigated and measured was successfully shown to suppress the TE_{11} and TM_{11} modal resonances that are excited when feeding the waveguide. Under these conditions, a theoretical bandwidth of 2.20:1 was demonstrated, limited by the TE_{10} and the TE_{20L} cutoff frequencies.

The open ended CSW was studied both theoretically and experimentally as a radiating element over an octave of bandwidth. A general single-/multi-mode analysis was performed to identify the higher-order mode contributions to the far-field patterns. The patterns for a prototype CSW were computed, and both co- and cross-polarization measured for comparison to theory, as shown in Figures B-1 through B-16. The results show several key points. First, the mode filters have no adverse effect at the low frequencies before the onset of the first higher-order mode cutoff frequency. Second, above the higher-order mode cutoff, the patterns indicate energy is confined mostly to the dominant mode. Performance is especially well behaved at the low frequencies, however at the high frequencies, performance rolls off and the E-plane beam squints slightly--a likely indication of higher-order mode energy radiation. The patterns are sufficiently well behaved for the radar simulator and hypothetical phase array application described in Chapters 1 and 2, since any pattern degradation occurs gradually as frequency is increased. Energy coupled into the TE_{11} and TM_{11} modes of the CSW by way of mutual coupling can be dampened by the mode filters and kept from resonating.

The novel components of the research which are contained in Chapters 4-7, include the theoretical and experimental study of the CSW and demonstration of a mode filter that supports dual polarization while achieving the bandwidth extension. Chapter 8 interpreted the results obtained in Chapters 4 through 7 in the context of the phased array antenna requirements. The CSW element will fit within a rectangular array lattice and support 15 degree scan over an octave of bandwdth, subject to matching the element in an array environment over the desired scan angle. Future work areas are suggested in Chapter 10 and include infinite array studies, CSW/phase shifter coupling, and mode filter refinements.

CHAPTER 10

FUTURE WORK

This dissertation reported on a study of the crossed-septum waveguide (CSW) in terms of obtaining single-mode bandwidth enhancement of a square waveguide. Although the work presented here has answered certain questions, there are additional remaining questions that are of interest and could potentially be addressed in the future. A few of the areas currently identified as potential future work include:

- The design of the broadband high power ferrite phase shifter using the CSW cross section, such that the radiating element and phase shifter can be integrated into a single device. This could conceivably require that the characterization of the CSW for a general μ and ε case where as the radiating element analysis is considered for the lossless dielectric case. The problem of an 'optimal phase shifter' is a separate issue and is beyond the scope of this work. As pointed out in Chapter 2, a broadband phase shifter already exists, but may not be the optimal design choice since it requires potentially complex coupling and matching networks.

- An investigation of optimal impedance matching and coupling networks is identified as an area of future work for the CSW radiating element. This problem may need to be addressed to provide the best possible match to a phase shifter. The difficulty inherent in this problem that of obtaining a wide band coupling match while retaining the dual polarization characteristics. The polarization switching scheme mentioned in Chapter 2 also requires further work to implement.

- In Chapter 6, it was clearly demonstrated that for Test Case #2, one could use mode filters to suppress unwanted TE_{11} and TM_{11} mode resonances. It was stated that it is believed that the Test Case #1 failed to achieve the octave bandwidth because of both mode filter and coupling considerations. Upon inspection of the TM_{12}, TM_{13L} and TM_{13U}

mode fields, one finds that there is a strong z-component of the electric field present in these modes. Furthermore, one can inspect the plot of S_{11} shown in Figures 6-8 and 6-11 and observe that the TM_{12} mode resonance at about 15.4 GHz is apparently dampened by the mode filters. One would speculate that if both the TM_{13L} and TM_{13U} modes could be suppressed also due to the strong z-component of the electric field present for these modes, then additional bandwidth might be obtained. Referring to the cutoff frequencies for the Test Case # 1 given in Table 6-1, it is observed that if the TM_{12}, TM_{13L} and TM_{13U} modes could also be suppressed, then one could obtain $BW = f_c(\mathrm{TE}_{20L})/f_c(\mathrm{TE}_{10})$ which is a ratio of about 2.93:1. It is possible that this would result in decreased efficiency since there are additional modes for which energy could couple into and hence more loss due to the mode filters. To investigate this would have required further machining and modifications to the Test Case #1 hardware to improve the probe coupling and the necessary perform measurements. Hence this was not further pursued within the allowed time frame of the research. An investigation of a mode filter to suppress these higher-order modes is left as an area of future work.

- From the onset of this investigation, the thrust was to obtain extended single-mode bandwidth of the square waveguide, which is needed (based on prior mutual coupling work) to support scanning the array without blind spots. Sound design practices including confinement energy to a single mode of propagation should minimize potential effects of mutual coupling. However, a rigorous analysis of the CSW array mutual coupling in terms of the infinite array problem discussed in Chapters 2 and 8 are a necessary area of future work required to show that the main beam can steer within the intended frequency/scan range without blind spots occurring. As discussed in Chapter 2, blindness is associated with a resonance condition of the higher-order modes. In this context, the problem is view in terms of achieving a suitable match over the desired scan and frequency range. One will need to model the higher-order suppressed modes to include mode filter loss rather than evanescent decay. It is believed by the author that a rigorous treatment of this problem does not currently exist in the open literature.

- Construction and testing of a fully populated 'test' array is an area of future work, and would conceivably follow the mutual coupling analysis discussed above. One would consider a small array of around 15×15 elements, and terminate all but one element as

discussed in Chapter 2. A single element would then be excited and the far field pattern measured and observed for the presence of nulls. This must be verified prior to building a complete array.

- A study of array architecture and element thinning for the hypothetical phased array discussed in Section 1.2 is recommended as an area of future work. For a space-fed array system using the CSW element, array architecture studies would be need to obtain a satisfactory design that operates over the frequency and scan range while minimizing the number of elements required.

- Section 7.5 stated that a reflection coefficient exists at the discontinuity of the open-ended waveguide and free space boundary. There are also secondary effects caused by the surface currents on the edge of the guide. It is believed that a rigorous analysis of these effects requires solving a 3-dimensional boundary value problem. An area of future work includes a rigorous treatment of the reflection coefficient and edge currents for an isolated CSW radiating element. This, however, may be of only limited interest for the phased array scanning application, compared to treatment of the element in an array environment.

APPENDIX A

ELECTRIC AND MAGNETIC FIELD COEFFICIENTS

A.1 Coefficient Definitions

In Chapter 4 the fields in the CSW are expanded in a series and solved using the mode-matching technique. The total electric and magnetic fields in each region are expressed in a summation of the following form:

$$\vec{E}^{(i)} = \sum_{n=1}^{N} \left\{ E_{xn}^{(i)}\hat{x} + E_{yn}^{(i)}\hat{y} + E_{zn}^{(i)}\hat{z} \right\} e^{-jk_z z} \tag{A.1}$$

$$\vec{H}^{(i)} = \sum_{n=1}^{N} \left\{ H_{xn}^{(i)}\hat{x} + H_{yn}^{(i)}\hat{y} + H_{zn}^{(i)}\hat{z} \right\} e^{-jk_z z} \tag{A.2}$$

where (i) = 1,2,3 for each region of the waveguide as defined in Chapter 4. The modal solutions are obtained using the numerical techniques given in Chapter 5, for a particular mode, phase constant k_z, and frequency. The following are a list of the field coefficients for each of the symmetry cases and regions. Since the regions are defined for a 1/4 section of the CSW per Figures 3-4 and 4-1, the symmetry properties of the solutions are used to reconstruct the fields in the whole waveguide cross-section.

A.2 Even / Odd Symmetry Case Coefficients

The field coefficients in region 1 for the even / odd symmetry case are given by:

$$E_{xn}^{(1)} = \frac{-j}{\omega\mu_1\varepsilon_1}(k_1^2 - k_{xn}^{(1)2})A_n^{(1)} \sin k_{xn}^{(1)} x \sin k_{yn}^{(1)}(y-b) \tag{A.3}$$

$$\begin{aligned} E_{yn}^{(1)} = & \frac{jk_z}{\varepsilon_1} F_n^{(1)} \cos \tilde{k}_{xn}^{(1)} x \cos \tilde{k}_{yn}^{(1)}(y-b) \\ & - \frac{j}{\omega\mu_1\varepsilon_1} k_{xn}^{(1)} k_{yn}^{(1)} A_n^{(1)} \cos k_{xn}^{(1)} x \cos k_{yn}^{(1)}(y-b) \end{aligned} \tag{A.4}$$

$$\begin{aligned} E_{zn}^{(1)} = & \frac{-1}{\varepsilon_1} \tilde{k}_{yn}^{(1)} F_n^{(1)} \cos \tilde{k}_{xn}^{(1)} x \sin \tilde{k}_{yn}^{(1)}(y-b) \\ & - \frac{k_z}{\omega\mu_1\varepsilon_1} k_{xn}^{(1)} A_n^{(1)} \cos k_{xn}^{(1)} x \sin k_{yn}^{(1)}(y-b) \end{aligned} \tag{A.5}$$

$$H_{xn}^{(1)} = \frac{-j}{\omega\mu_1\varepsilon_1}(k_1^2 - \tilde{k}_{xn}^{(1)2})F_n^{(1)} \cos \tilde{k}_{xn}^{(1)} x \cos \tilde{k}_{yn}^{(1)}(y-b) \tag{A.6}$$

$$\begin{aligned} H_{yn}^{(1)} = & \frac{-j}{\omega\mu_1\varepsilon_1} \tilde{k}_{xn}^{(1)} \tilde{k}_{yn}^{(1)} F_n^{(1)} \sin \tilde{k}_{xn}^{(1)} x \sin \tilde{k}_{yn}^{(1)}(y-b) \\ & - \frac{jk_z}{\mu_1} A_n^{(1)} \sin k_{xn}^{(1)} x \sin k_{yn}^{(1)}(y-b) \end{aligned} \tag{A.7}$$

$$\begin{aligned} H_{zn}^{(1)} = & \frac{k_z}{\omega\mu_1\varepsilon_1} \tilde{k}_{xn}^{(1)} F_n^{(1)} \sin \tilde{k}_{xn}^{(1)} x \cos \tilde{k}_{yn}^{(1)}(y-b) \\ & - \frac{1}{\mu_1} k_{yn}^{(1)} A_n^{(1)} \sin k_{xn}^{(1)} x \cos k_{yn}^{(1)}(y-b) \end{aligned} \tag{A.8}$$

The fields in region 2 are given by:

$$E_{xn}^{(2)} = \frac{-j}{\omega\mu_2\varepsilon_2}(k_2^2 - k_{xn}^{(2)2})A_n^{(2)} \cos k_{xn}^{(2)}(x-b) \sin k_{yn}^{(2)}(y-b) \tag{A.9}$$

$$\begin{aligned} E_{yn}^{(2)} = {} & \frac{jk_z}{\varepsilon_2} F_n^{(2)} \sin \tilde{k}_{xn}^{(2)}(x-b) \cos \tilde{k}_{yn}^{(2)}(y-b) \\ & + \frac{j}{\omega\mu_2\varepsilon_2} k_{xn}^{(2)} k_{yn}^{(2)} A_n^{(2)} \sin k_{xn}^{(2)}(x-b) \cos k_{yn}^{(2)}(y-b) \end{aligned} \tag{A.10}$$

$$\begin{aligned} E_{zn}^{(2)} = {} & \frac{-1}{\varepsilon_2} \tilde{k}_{yn}^{(2)} F_n^{(2)} \sin \tilde{k}_{xn}^{(2)}(x-b) \sin \tilde{k}_{yn}^{(2)}(y-b) \\ & + \frac{k_z}{\omega\mu_2\varepsilon_2} k_{xn}^{(2)} A_n^{(2)} \sin k_{xn}^{(2)}(x-b) \sin k_{yn}^{(2)}(y-b) \end{aligned} \tag{A.11}$$

$$H_{xn}^{(2)} = \frac{-j}{\omega\mu_2\varepsilon_2}(k_2^2 - \tilde{k}_{xn}^{(2)2})F_n^{(2)} \sin \tilde{k}_{xn}^{(2)}(x-b) \cos \tilde{k}_{yn}^{(2)}(y-b) \tag{A.12}$$

$$\begin{aligned} H_{yn}^{(2)} = {} & \frac{j}{\omega\mu_2\varepsilon_2} \tilde{k}_{xn}^{(2)} \tilde{k}_{yn}^{(2)} F_n^{(2)} \cos \tilde{k}_{xn}^{(2)}(x-b) \sin \tilde{k}_{yn}^{(2)}(y-b) \\ & - \frac{jk_z}{\mu_2} A_n^{(2)} \cos k_{xn}^{(2)}(x-b) \sin k_{yn}^{(2)}(y-b) \end{aligned} \tag{A.13}$$

$$\begin{aligned} H_{zn}^{(2)} = {} & \frac{-k_z}{\omega\mu_2\varepsilon_2} \tilde{k}_{xn}^{(2)} F_n^{(2)} \cos \tilde{k}_{xn}^{(2)}(x-b) \cos \tilde{k}_{yn}^{(2)}(y-b) \\ & - \frac{1}{\mu_2} k_{yn}^{(2)} A_n^{(2)} \cos k_{xn}^{(2)}(x-b) \cos k_{yn}^{(2)}(y-b) \end{aligned} \tag{A.14}$$

The fields in region 3 are given by:

$$E_{xn}^{(3)} = \frac{-j}{\omega\mu_1\varepsilon_1}(k_1^2 - k_{xn}^{(3)2})A_n^{(3)} \sin k_{xn}^{(3)} x \sin k_{yn}^{(3)} y \tag{A.15}$$

$$\begin{aligned} E_{yn}^{(3)} &= \frac{jk_z}{\varepsilon_1} F_n^{(3)} \cos \tilde{k}_{xn}^{(3)} x \cos \tilde{k}_{yn}^{(3)} y \\ &\quad - \frac{j}{\omega\mu_1\varepsilon_1} k_{xn}^{(3)} k_{yn}^{(3)} A_n^{(3)} \cos k_{xn}^{(3)} x \cos k_{yn}^{(3)} y \end{aligned} \tag{A.16}$$

$$\begin{aligned} E_{zn}^{(3)} &= \frac{-1}{\varepsilon_1} \tilde{k}_{yn}^{(3)} F_n^{(3)} \cos \tilde{k}_{xn}^{(3)} x \sin \tilde{k}_{yn}^{(3)} y \\ &\quad - \frac{k_z}{\omega\mu_1\varepsilon_1} k_{xn}^{(3)} A_n^{(3)} \cos k_{xn}^{(3)} x \sin k_{yn}^{(3)} y \end{aligned} \tag{A.17}$$

$$H_{xn}^{(3)} = \frac{-j}{\omega\mu_1\varepsilon_1}(k_1^2 - \tilde{k}_{xn}^{(3)2})F_n^{(3)} \cos \tilde{k}_{xn}^{(3)} x \cos \tilde{k}_{yn}^{(3)} y \tag{A.18}$$

$$\begin{aligned} H_{yn}^{(3)} &= \frac{-j}{\omega\mu_1\varepsilon_1} \tilde{k}_{xn}^{(3)} \tilde{k}_{yn}^{(3)} F_n^{(3)} \sin \tilde{k}_{xn}^{(3)} x \sin \tilde{k}_{yn}^{(3)} y \\ &\quad - \frac{jk_z}{\mu_1} A_n^{(3)} \sin k_{xn}^{(3)} x \sin k_{yn}^{(3)} y \end{aligned} \tag{A.19}$$

$$\begin{aligned} H_{zn}^{(3)} &= \frac{k_z}{\omega\mu_1\varepsilon_1} \tilde{k}_{xn}^{(3)} F_n^{(3)} \sin \tilde{k}_{xn}^{(3)} x \cos \tilde{k}_{yn}^{(3)} y \\ &\quad - \frac{1}{\mu_1} k_{yn}^{(3)} A_n^{(3)} \sin k_{xn}^{(3)} x \cos k_{yn}^{(3)} y \end{aligned} \tag{A.20}$$

A.3 Odd / Even Symmetry Case Coefficients

The field coefficients in region 1 for the odd/even symmetry case are given by:

$$E_{xn}^{(1)} = \frac{-j}{\omega\mu_1\varepsilon_1}(k_1^2 - k_{xn}^{(1)2})A_n^{(1)} \cos k_{xn}^{(1)} x \sin k_{yn}^{(1)}(y-b) \tag{A.21}$$

$$\begin{aligned} E_{yn}^{(1)} = {} & \frac{jk_z}{\varepsilon_1} F_n^{(1)} \sin \tilde{k}_{xn}^{(1)} x \cos \tilde{k}_{yn}^{(1)}(y-b)\ u(n-2) \\ & + \frac{j}{\omega\mu_1\varepsilon_1} k_{xn}^{(1)} k_{yn}^{(1)} A_n^{(1)} \sin k_{xn}^{(1)} x \cos k_{yn}^{(1)}(y-b) \end{aligned} \tag{A.22}$$

$$\begin{aligned} E_{zn}^{(1)} = {} & \frac{-1}{\varepsilon_1} \tilde{k}_{yn}^{(1)} F_n^{(1)} \sin \tilde{k}_{xn}^{(1)} x \sin \tilde{k}_{yn}^{(1)}(y-b)\ u(n-2) \\ & + \frac{k_z}{\omega\mu_1\varepsilon_1} k_{xn}^{(1)} A_n^{(1)} \sin k_{xn}^{(1)} x \sin k_{yn}^{(1)}(y-b) \end{aligned} \tag{A.23}$$

$$H_{xn}^{(1)} = \frac{-j}{\omega\mu_1\varepsilon_1}(k_1^2 - \tilde{k}_{xn}^{(1)2})F_n^{(1)} \sin \tilde{k}_{xn}^{(1)} x \cos \tilde{k}_{yn}^{(1)}(y-b)\ u(n-2) \tag{A.24}$$

$$\begin{aligned} H_{yn}^{(1)} = {} & \frac{j}{\omega\mu_1\varepsilon_1} \tilde{k}_{xn}^{(1)} \tilde{k}_{yn}^{(1)} F_n^{(1)} \cos \tilde{k}_{xn}^{(1)} x \sin \tilde{k}_{yn}^{(1)}(y-b)\ u(n-2) \\ & - \frac{jk_z}{\mu_1} A_n^{(1)} \cos k_{xn}^{(1)} x \sin k_{yn}^{(1)}(y-b) \end{aligned} \tag{A.25}$$

$$\begin{aligned} H_{zn}^{(1)} = {} & \frac{-k_z}{\omega\mu_1\varepsilon_1} \tilde{k}_{xn}^{(1)} F_n^{(1)} \cos \tilde{k}_{xn}^{(1)} x \cos \tilde{k}_{yn}^{(1)}(y-b)\ u(n-2) \\ & - \frac{1}{\mu_1} k_{yn}^{(1)} A_n^{(1)} \cos k_{xn}^{(1)} x \cos k_{yn}^{(1)}(y-b) \end{aligned} \tag{A.26}$$

The fields in region 2 for the odd/even symmetry case are identical to those of the even /odd symmetry case except that a $u(n-2)$ (unit step function) is inserted into the $TE^{(x)}$ modes. Therefore we obtain:

$$E_{xn}^{(2)} = \frac{-j}{\omega\mu_2\varepsilon_2}(k_2^2 - k_{xn}^{(2)2})A_n^{(2)} \cos k_{xn}^{(2)}(x-b)\sin k_{yn}^{(2)}(y-b) \tag{A.27}$$

$$\begin{aligned} E_{yn}^{(2)} = {} & \frac{jk_z}{\varepsilon_2}F_n^{(2)} \sin \tilde{k}_{xn}^{(2)}(x-b)\cos \tilde{k}_{yn}^{(2)}(y-b)\ u(n-2) \\ & + \frac{j}{\omega\mu_2\varepsilon_2}k_{xn}^{(2)}k_{yn}^{(2)}A_n^{(2)} \sin k_{xn}^{(2)}(x-b)\cos k_{yn}^{(2)}(y-b) \end{aligned} \tag{A.28}$$

$$\begin{aligned} E_{zn}^{(2)} = {} & \frac{-1}{\varepsilon_2}\tilde{k}_{yn}^{(2)}F_n^{(2)} \sin \tilde{k}_{xn}^{(2)}(x-b)\sin \tilde{k}_{yn}^{(2)}(y-b)\ u(n-2) \\ & + \frac{k_z}{\omega\mu_2\varepsilon_2}k_{xn}^{(2)}A_n^{(2)} \sin k_{xn}^{(2)}(x-b)\sin k_{yn}^{(2)}(y-b) \end{aligned} \tag{A.29}$$

$$H_{xn}^{(2)} = \frac{-j}{\omega\mu_2\varepsilon_2}(k_2^2 - \tilde{k}_{xn}^{(2)2})F_n^{(2)} \sin \tilde{k}_{xn}^{(2)}(x-b)\cos \tilde{k}_{yn}^{(2)}(y-b)\ u(n-2) \tag{A.30}$$

$$\begin{aligned} H_{yn}^{(2)} = {} & \frac{j}{\omega\mu_2\varepsilon_2}\tilde{k}_{xn}^{(2)}\tilde{k}_{yn}^{(2)}F_n^{(2)} \cos \tilde{k}_{xn}^{(2)}(x-b)\sin \tilde{k}_{yn}^{(2)}(y-b)\ u(n-2) \\ & - \frac{jk_z}{\mu_2}A_n^{(2)} \cos k_{xn}^{(2)}(x-b)\sin k_{yn}^{(2)}(y-b) \end{aligned} \tag{A.31}$$

$$\begin{aligned} H_{zn}^{(2)} = {} & \frac{-k_z}{\omega\mu_2\varepsilon_2}\tilde{k}_{xn}^{(2)}F_n^{(2)} \cos \tilde{k}_{xn}^{(2)}(x-b)\cos \tilde{k}_{yn}^{(2)}(y-b)\ u(n-2) \\ & - \frac{1}{\mu_2}k_{yn}^{(2)}A_n^{(2)} \cos k_{xn}^{(2)}(x-b)\cos k_{yn}^{(2)}(y-b) \end{aligned} \tag{A.32}$$

The fields in region 3 are given by:

$$E_{xn}^{(3)} = \frac{-j}{\omega\mu_1\varepsilon_1}(k_1^2 - k_{xn}^{(3)2})A_n^{(3)} \cos k_{xn}^{(3)} x \cos k_{yn}^{(3)} y \tag{A.33}$$

$$\begin{aligned} E_{yn}^{(3)} = {} & \frac{jk_z}{\varepsilon_1} F_n^{(3)} \sin \tilde{k}_{xn}^{(3)} x \sin \tilde{k}_{yn}^{(3)} y \, u(n-2) \\ & - \frac{j}{\omega\mu_1\varepsilon_1} k_{xn}^{(3)} k_{yn}^{(3)} A_n^{(3)} \sin k_{xn}^{(3)} x \sin k_{yn}^{(3)} y \end{aligned} \tag{A.34}$$

$$\begin{aligned} E_{zn}^{(3)} = {} & \frac{1}{\varepsilon_1} \tilde{k}_{yn}^{(3)} F_n^{(3)} \sin \tilde{k}_{xn}^{(3)} x \cos \tilde{k}_{yn}^{(3)} y \, u(n-2) \\ & + \frac{k_z}{\omega\mu_1\varepsilon_1} k_{xn}^{(3)} A_n^{(3)} \sin k_{xn}^{(3)} x \cos k_{yn}^{(3)} y \end{aligned} \tag{A.35}$$

$$H_{xn}^{(3)} = \frac{-j}{\omega\mu_1\varepsilon_1}(k_1^2 - \tilde{k}_{xn}^{(3)2})F_n^{(3)} \sin \tilde{k}_{xn}^{(3)} x \sin \tilde{k}_{yn}^{(3)} y \, u(n-2) \tag{A.36}$$

$$\begin{aligned} H_{yn}^{(3)} = {} & \frac{-j}{\omega\mu_1\varepsilon_1} \tilde{k}_{xn}^{(3)} \tilde{k}_{yn}^{(3)} F_n^{(3)} \cos \tilde{k}_{xn}^{(3)} x \cos \tilde{k}_{yn}^{(3)} y \, u(n-2) \\ & - \frac{jk_z}{\mu_1} A_n^{(3)} \cos k_{xn}^{(3)} x \cos k_{yn}^{(3)} y \end{aligned} \tag{A.37}$$

$$\begin{aligned} H_{zn}^{(3)} = {} & \frac{-k_z}{\omega\mu_1\varepsilon_1} \tilde{k}_{xn}^{(3)} F_n^{(3)} \cos \tilde{k}_{xn}^{(3)} x \sin \tilde{k}_{yn}^{(3)} y \, u(n-2) \\ & + \frac{1}{\mu_1} k_{yn}^{(3)} A_n^{(3)} \cos k_{xn}^{(3)} x \sin k_{yn}^{(3)} y \end{aligned} \tag{A.38}$$

A.4 Even / Even Symmetry Case Coefficients

From Chapter 4, the boundary conditions of regions 1 and 2 are the same for the even / even symmetry case as for the even / odd symmetry case. Therefore the coefficients for region 1 are given by equations (A.3) through (A.8), and the coefficients for region 2 are given by equations (A.9) through (A.14). The field coefficients in region 3 are given by:

$$E_{xn}^{(3)} = \frac{-j}{\omega\mu_1\varepsilon_1}(k_1^2 - k_{xn}^{(3)2})A_n^{(3)} \sin k_{xn}^{(3)}x \cos k_{yn}^{(3)}y \tag{A.39}$$

$$\begin{aligned} E_{yn}^{(3)} = & \frac{jk_z}{\varepsilon_1} F_n^{(3)} \cos \tilde{k}_{xn}^{(3)}x \sin \tilde{k}_{yn}^{(3)}y \\ & + \frac{j}{\omega\mu_1\varepsilon_1} k_{xn}^{(3)} k_{yn}^{(3)} A_n^{(3)} \cos k_{xn}^{(3)}x \sin k_{yn}^{(3)}y \end{aligned} \tag{A.40}$$

$$\begin{aligned} E_{zn}^{(3)} = & \frac{1}{\varepsilon_1} \tilde{k}_{yn}^{(3)} F_n^{(3)} \cos \tilde{k}_{xn}^{(3)}x \cos \tilde{k}_{yn}^{(3)}y \\ & - \frac{k_z}{\omega\mu_1\varepsilon_1} k_{xn}^{(3)} A_n^{(3)} \cos k_{xn}^{(3)}x \cos k_{yn}^{(3)}y \end{aligned} \tag{A.41}$$

$$H_{xn}^{(3)} = \frac{-j}{\omega\mu_1\varepsilon_1}(k_1^2 - \tilde{k}_{xn}^{(3)2})F_n^{(3)} \cos \tilde{k}_{xn}^{(3)}x \sin \tilde{k}_{yn}^{(3)}y \tag{A.42}$$

$$\begin{aligned} H_{yn}^{(3)} = & \frac{j}{\omega\mu_1\varepsilon_1} \tilde{k}_{xn}^{(3)} \tilde{k}_{yn}^{(3)} F_n^{(3)} \sin \tilde{k}_{xn}^{(3)}x \cos \tilde{k}_{yn}^{(3)}y \\ & - \frac{jk_z}{\mu_1} A_n^{(3)} \sin k_{xn}^{(3)}x \cos k_{yn}^{(3)}y \end{aligned} \tag{A.43}$$

$$H_{zn}^{(3)} = \frac{k_z}{\omega\mu_1\varepsilon_1}\tilde{k}_{xn}^{(3)}F_n^{(3)}\sin\tilde{k}_{xn}^{(3)}x\sin\tilde{k}_{yn}^{(3)}y + \frac{1}{\mu_1}k_{yn}^{(3)}A_n^{(3)}\sin k_{xn}^{(3)}x\sin k_{yn}^{(3)}y \tag{A.44}$$

A.5 Odd / Odd Symmetry Case Coefficients

From Chapter 4, the boundary conditions of regions 1 and 2 are the same for the odd / odd symmetry case as for the odd / even symmetry case. Therefore the coefficients for region 1 are given by equations (A.21) through (A.26), and the coefficients for region 2 are given by equations (A.27) through (A.32). The field coefficients in region 3 are given by:

$$E_{xn}^{(3)} = \frac{-j}{\omega\mu_1\varepsilon_1}(k_1^2 - k_{xn}^{(3)2})A_n^{(3)}\cos k_{xn}^{(3)}x\sin k_{yn}^{(3)}y \tag{A.45}$$

$$E_{yn}^{(3)} = \frac{jk_z}{\varepsilon_1}F_n^{(3)}\sin\tilde{k}_{xn}^{(3)}x\cos\tilde{k}_{yn}^{(3)}y\,u(n-2) + \frac{j}{\omega\mu_1\varepsilon_1}k_{xn}^{(3)}k_{yn}^{(3)}A_n^{(3)}\sin k_{xn}^{(3)}x\cos k_{yn}^{(3)}y \tag{A.46}$$

$$E_{zn}^{(3)} = \frac{-1}{\varepsilon_1}\tilde{k}_{yn}^{(3)}F_n^{(3)}\sin\tilde{k}_{xn}^{(3)}x\sin\tilde{k}_{yn}^{(3)}y\,u(n-2) - \frac{k_z}{\omega\mu_1\varepsilon_1}k_{xn}^{(3)}A_n^{(3)}\sin k_{xn}^{(3)}x\sin k_{yn}^{(3)}y \tag{A.47}$$

$$H_{xn}^{(3)} = \frac{-j}{\omega\mu_1\varepsilon_1}(k_1^2 - \tilde{k}_{xn}^{(3)2})F_n^{(3)}\sin\tilde{k}_{xn}^{(3)}x\cos\tilde{k}_{yn}^{(3)}y\,u(n-2) \tag{A.48}$$

$$H_{yn}^{(3)} = \frac{j}{\omega\mu_1\varepsilon_1}\tilde{k}_{xn}^{(3)}\tilde{k}_{yn}^{(3)}F_n^{(3)}\cos\tilde{k}_{xn}^{(3)}x\sin\tilde{k}_{yn}^{(3)}y\,u(n-2) - \frac{jk_z}{\mu_1}A_n^{(3)}\cos k_{xn}^{(3)}x\sin k_{yn}^{(3)}y \tag{A.49}$$

$$H_{zn}^{(3)} = \frac{-k_z}{\omega\mu_1\varepsilon_1}\tilde{k}_{xn}^{(3)}F_n^{(3)}\cos\tilde{k}_{xn}^{(3)}x\cos\tilde{k}_{yn}^{(3)}y\,u(n-2) - \frac{1}{\mu_1}k_{yn}^{(3)}A_n^{(3)}\cos k_{xn}^{(3)}x\cos k_{yn}^{(3)}y \tag{A.50}$$

APPENDIX B

MEASURED CSW FAR-FIELD PATTERN DATA

Provide in this appendix are the measure patterns for the Test Case #2 CSW. The measurements were performed using the Satellite Communication Group's Antenna measurement range at Whittemore Hall, Bradley Department of Electrical Engineering, Blacksburg VA. Both co- and cross-polarization of the H- and E-planes were measured at frequencies of 7.5, 9.0, 10.0, 11.0, 12.0, 13.0, 14.0 and 15.0 GHz. Figures B-1 through B-8 provide the H-plane patterns, and Figures B-9 through B-16 provide the results for E-plane patterns. All co-polarization patterns are computed using (7.18) and assuming only the dominant (i.e., single) mode of propagation and radiation, as defined by $\chi_1 = 1$ and $\chi_2 = \chi_3 = \chi_4 = 0$ (see Section 7.3.1 and Figure7-2). The computed cross-polarization levels (see also Section 7.3.1 and Figure 7-2) are found to be about -60 *dB* and lower; hence computed cross-polarization levels are omitted from Figure B-1 thorough B-16.

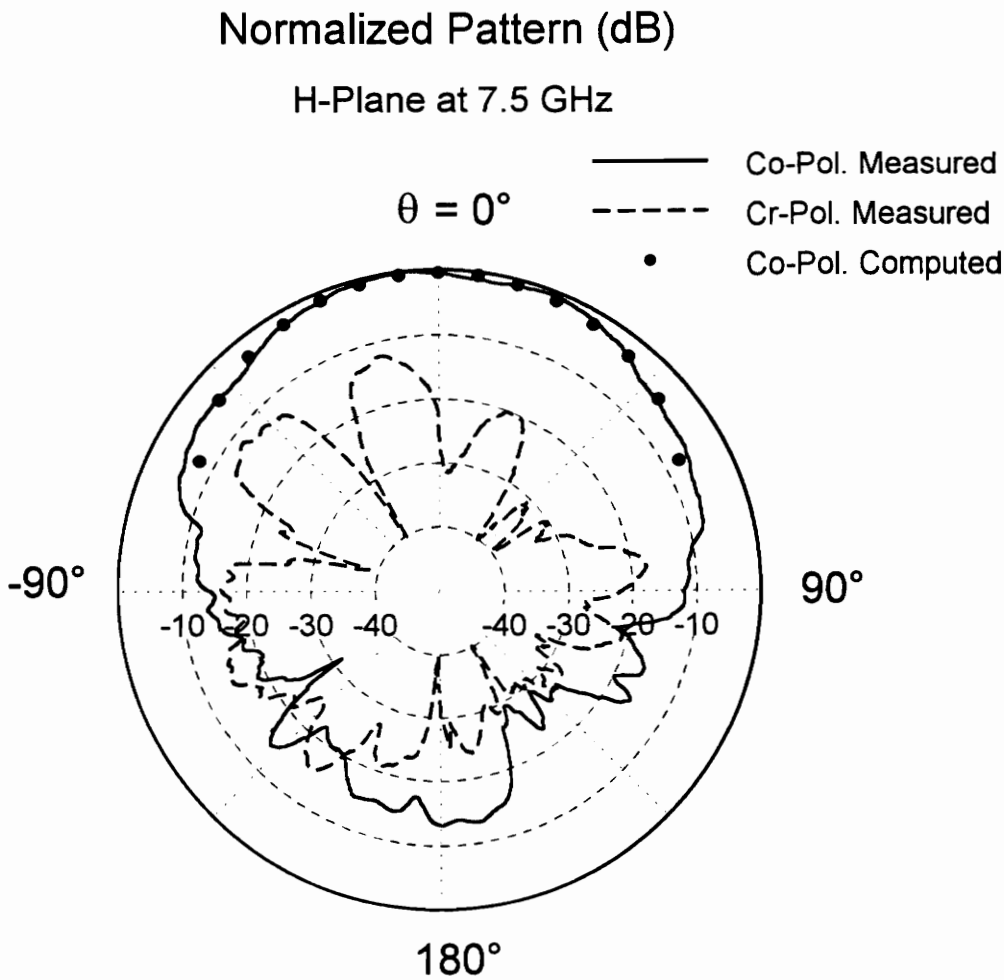

Figure B-1. Measured and computed H-plane far-field pattern at 7.5 GHz. Shown are the co-polarized (Co-Pol.) and cross-polarized (Cr-Pol.) cases. The computed pattern is found using (7.18) assuming single-mode propagation. The data are for the Test Case # 2 CSW.

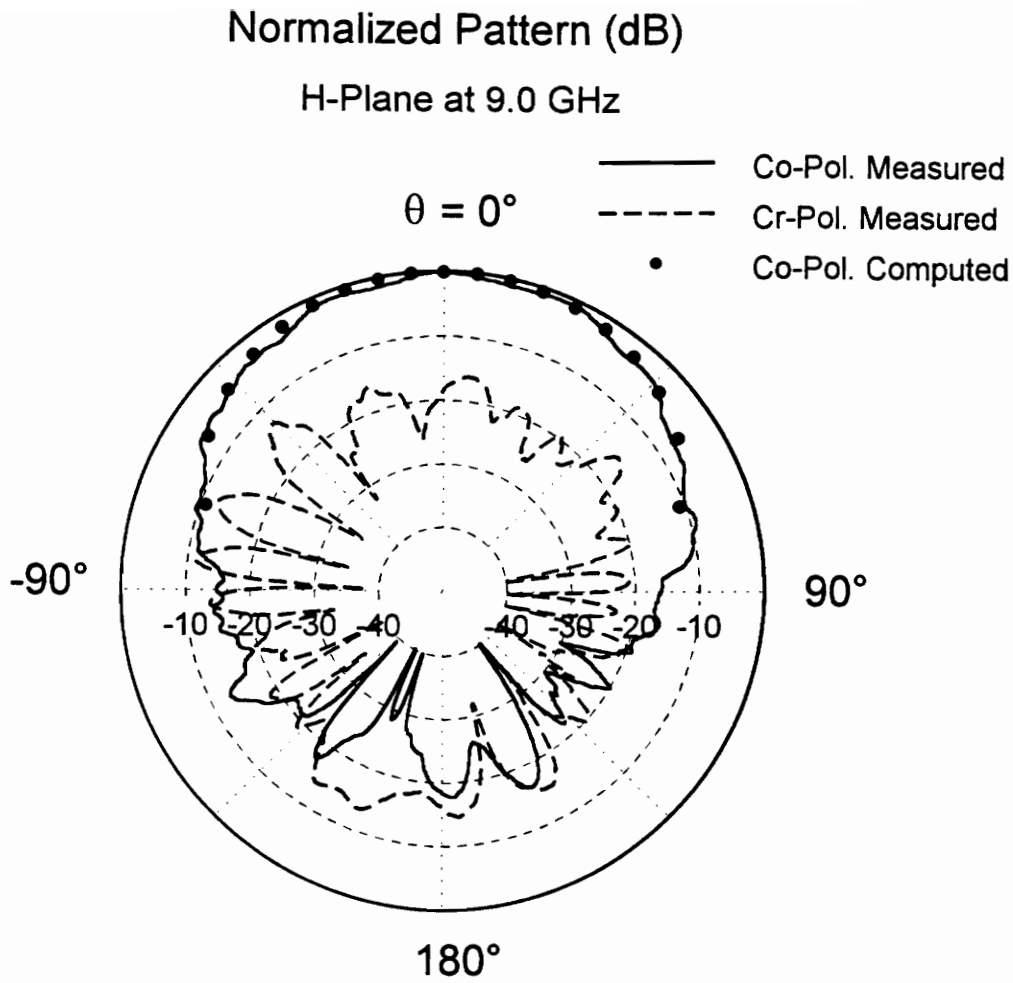

Figure B-2. Measured and computed H-plane far-field pattern at 9.0 GHz. Shown are the co-polarized (Co-Pol.) and cross-polarized (Cr-Pol.) cases. The computed pattern is found using (7.18) assuming single-mode propagation. The data are for the Test Case # 2 CSW.

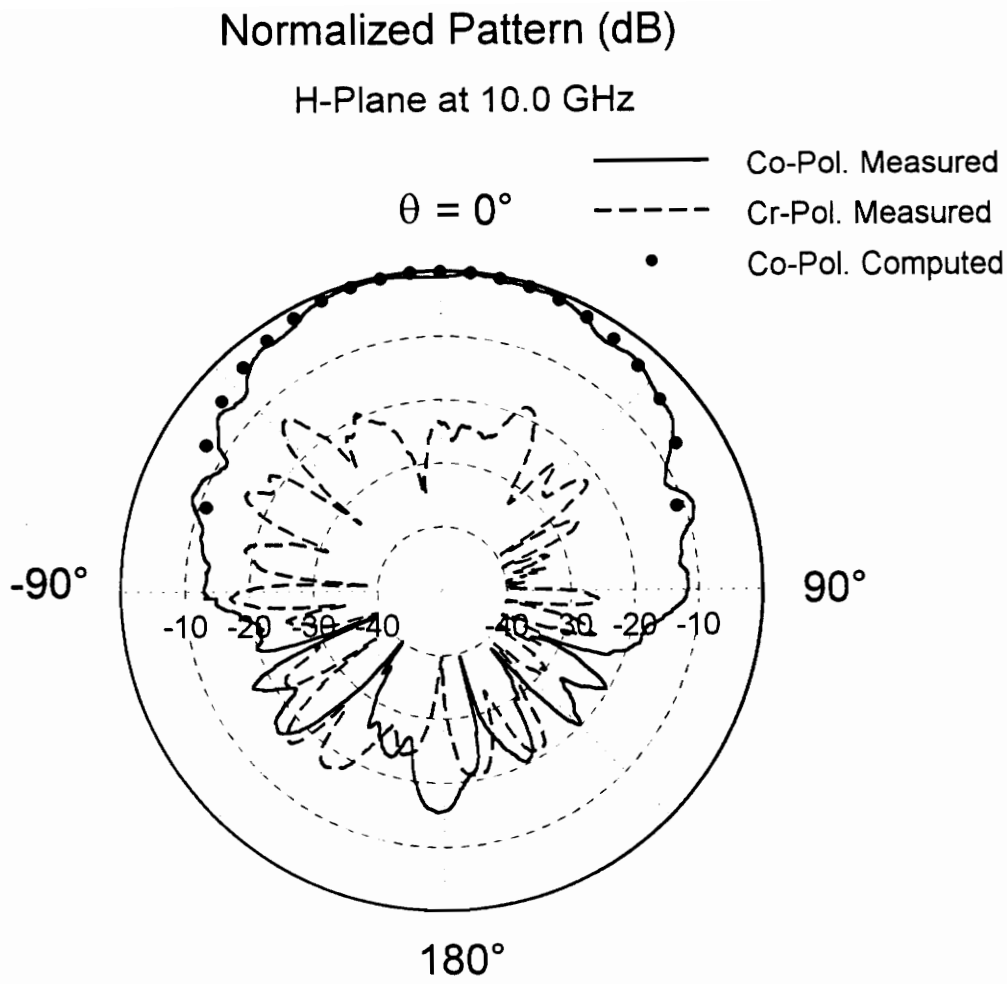

Figure B-3. Measured and computed H-plane far-field pattern at 10.0 GHz. Shown are the co-polarized (Co-Pol.) and cross-polarized (Cr-Pol.) cases. The computed pattern is found using (7.18) assuming single-mode propagation. The data are for the Test Case # 2 CSW.

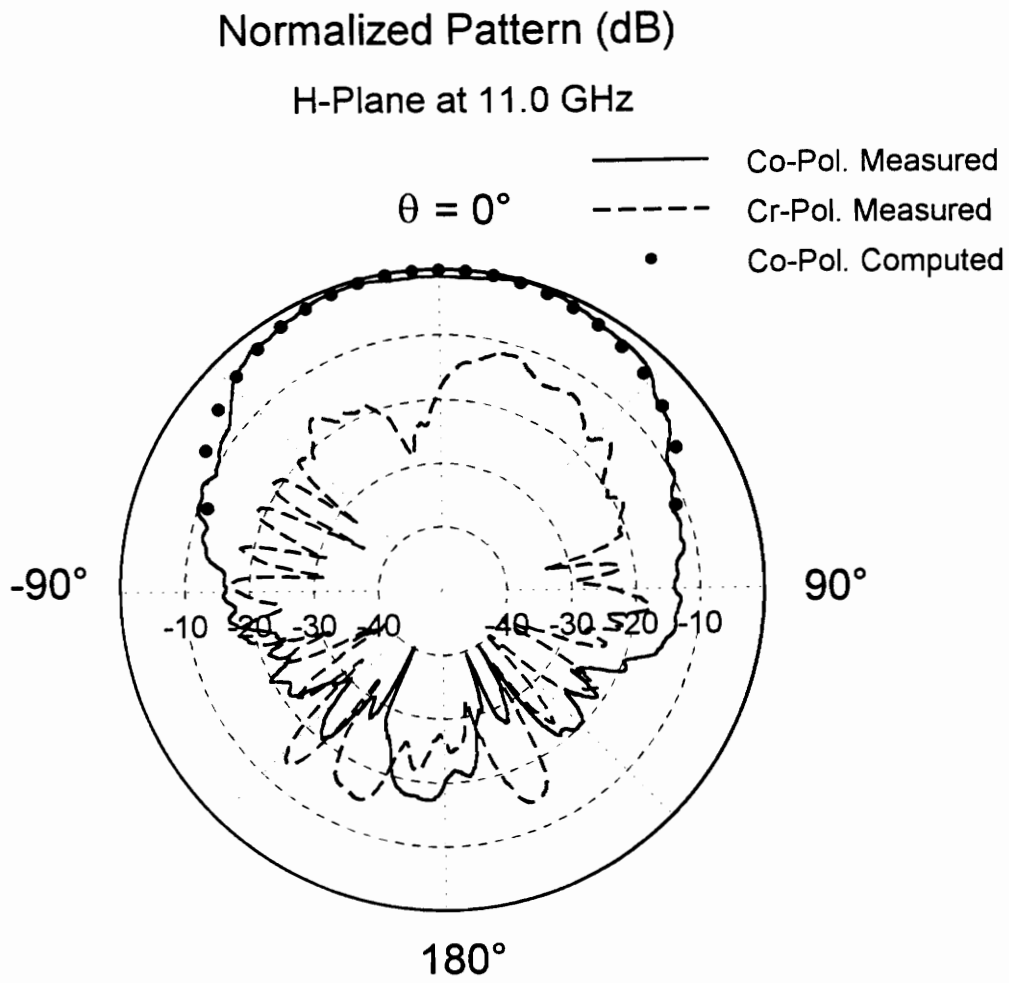

Figure B-4. Measured and computed H-plane far-field pattern at 11.0 GHz. Shown are the co-polarized (Co-Pol.) and cross-polarized (Cr-Pol.) cases. The computed pattern is found using (7.18) assuming single-mode propagation. The data are for the Test Case # 2 CSW.

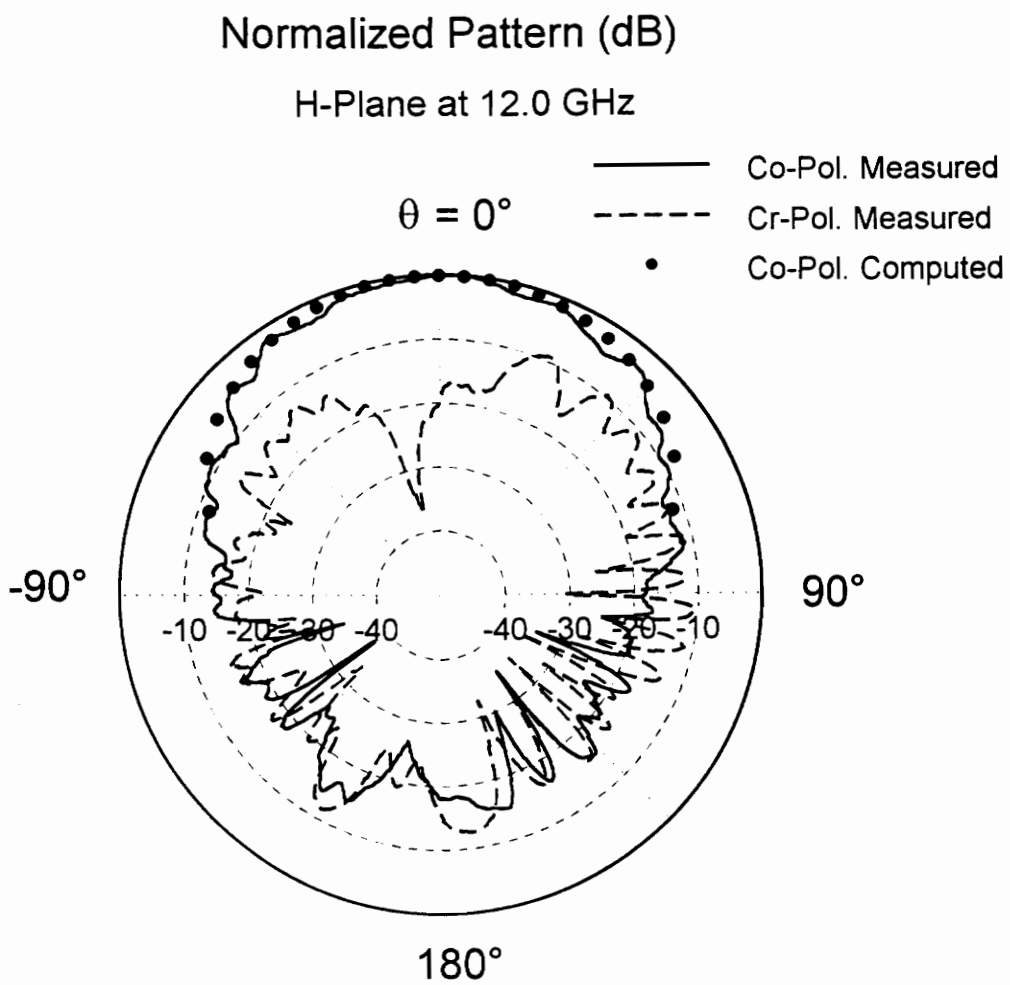

Figure B-5. Measured and computed H-plane far-field pattern at 12.0 GHz. Shown are the co-polarized (Co-Pol.) and cross-polarized (Cr-Pol.) cases. The computed pattern is found using (7.18) assuming single-mode propagation. The data are for the Test Case # 2 CSW.

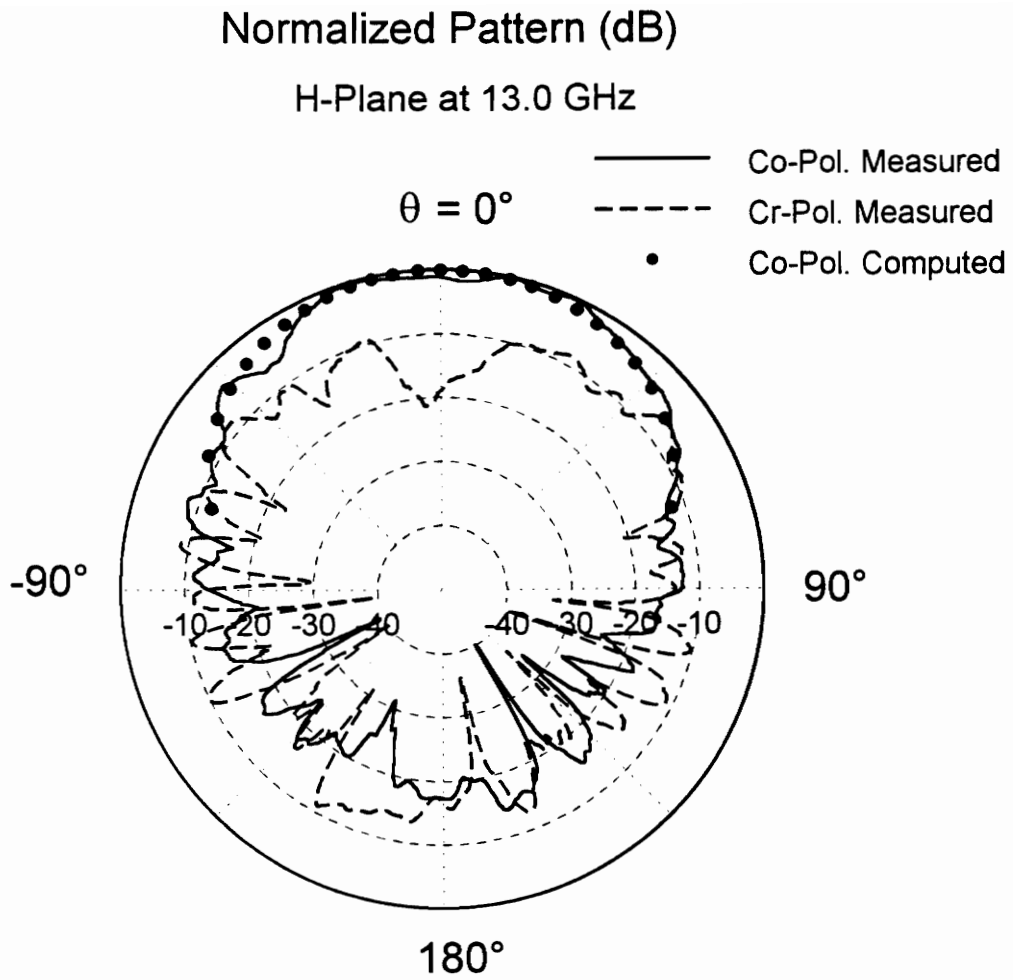

Figure B-6. Measured and computed H-plane far-field pattern at 13.0 GHz. Shown are the co-polarized (Co-Pol.) and cross-polarized (Cr-Pol.) cases. The computed pattern is found using (7.18) assuming single-mode propagation. The data are for the Test Case # 2 CSW.

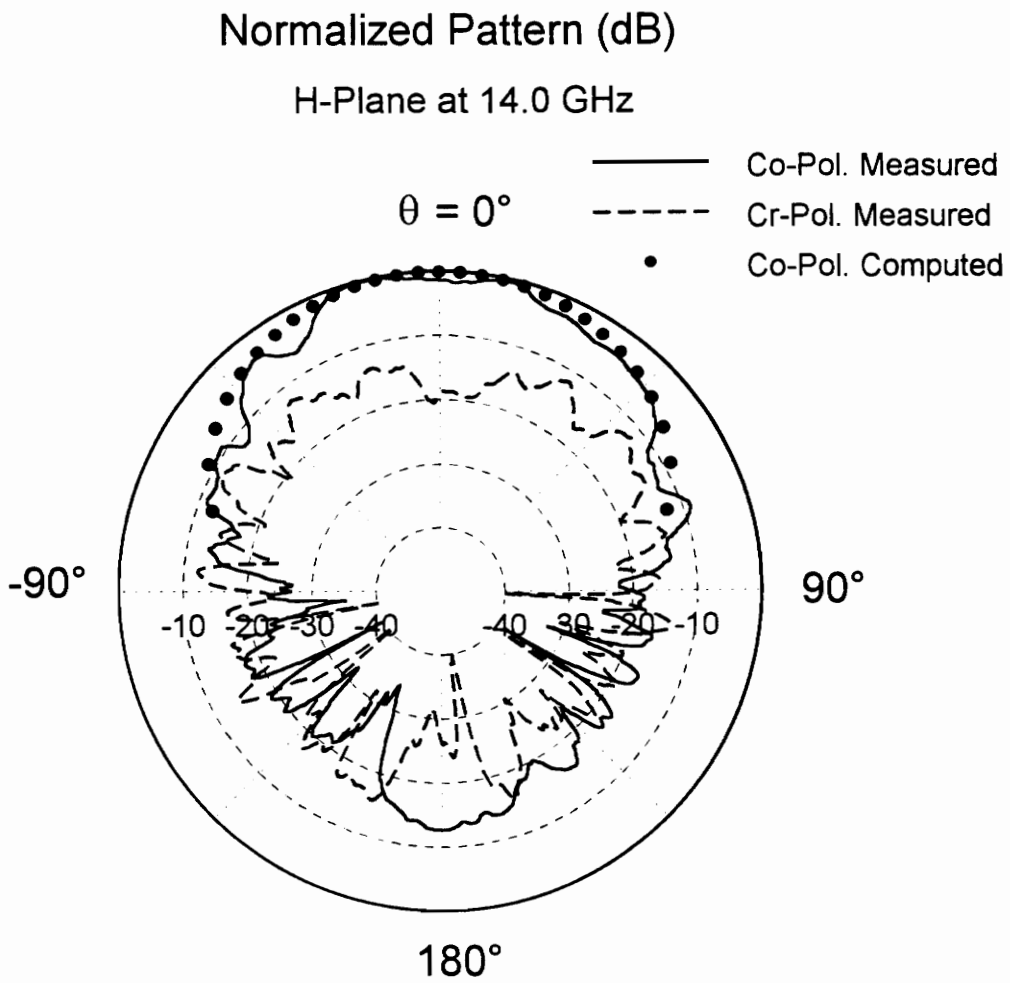

Figure B-7. Measured and computed H-plane far-field pattern at 14.0 GHz. Shown are the co-polarized (Co-Pol.) and cross-polarized (Cr-Pol.) cases. The computed pattern is found using (7.18) assuming single-mode propagation. The data are for the Test Case # 2 CSW.

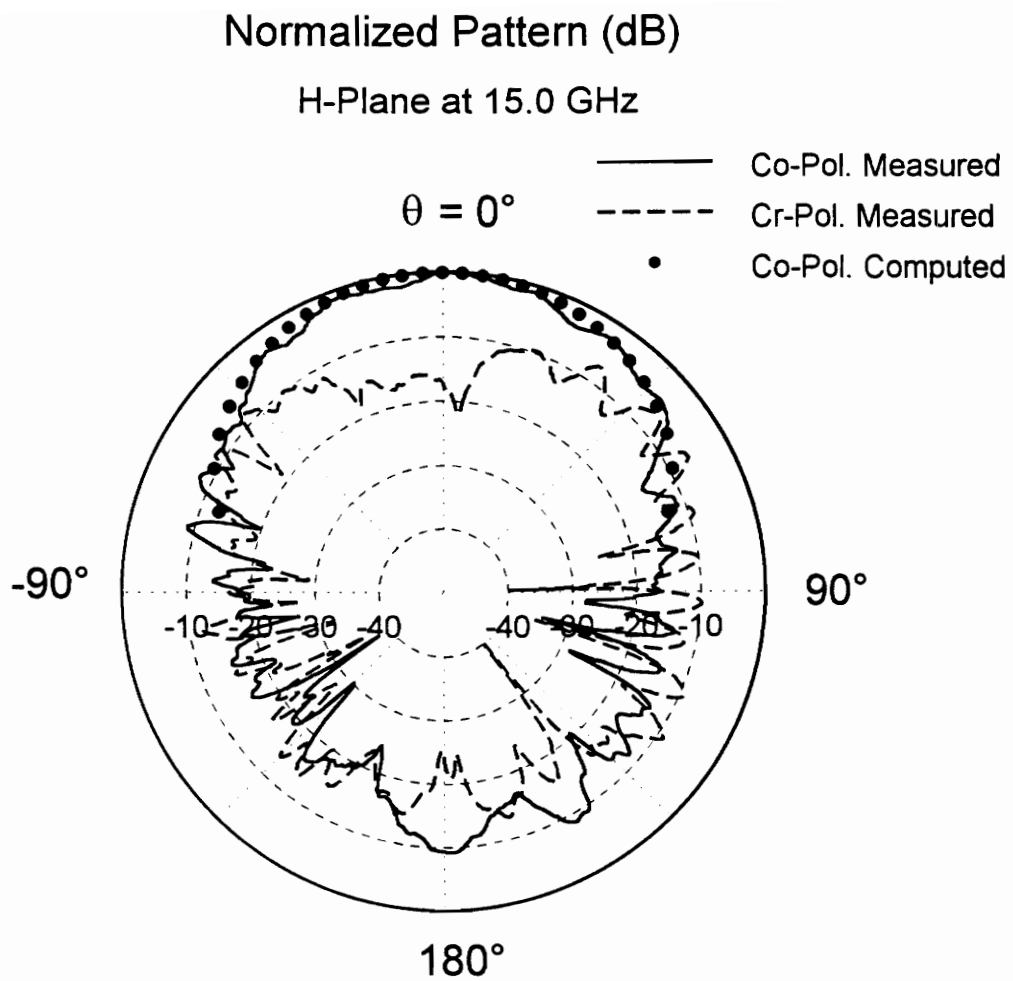

Figure B-8. Measured and computed H-plane far-field pattern at 15.0 GHz. Shown are the co-polarized (Co-Pol.) and cross-polarized (Cr-Pol.) cases. The computed pattern is found using (7.18) assuming single-mode propagation. The data are for the Test Case # 2 CSW.

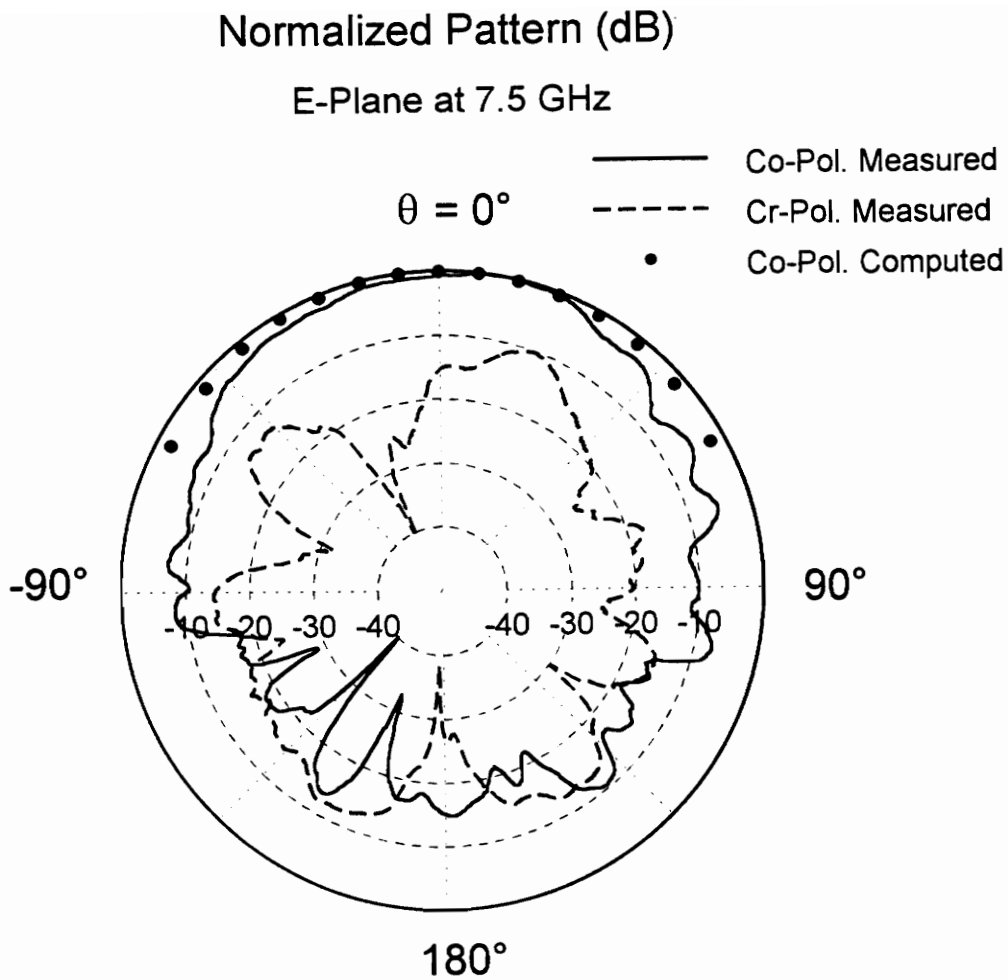

Figure B-9. Measured and computed E-plane far-field pattern at 7.5 GHz. Shown are the co-polarized (Co-Pol.) and cross-polarized (Cr-Pol.) cases. The computed pattern is found using (7.18) assuming single-mode propagation. The data are for the Test Case # 2 CSW.

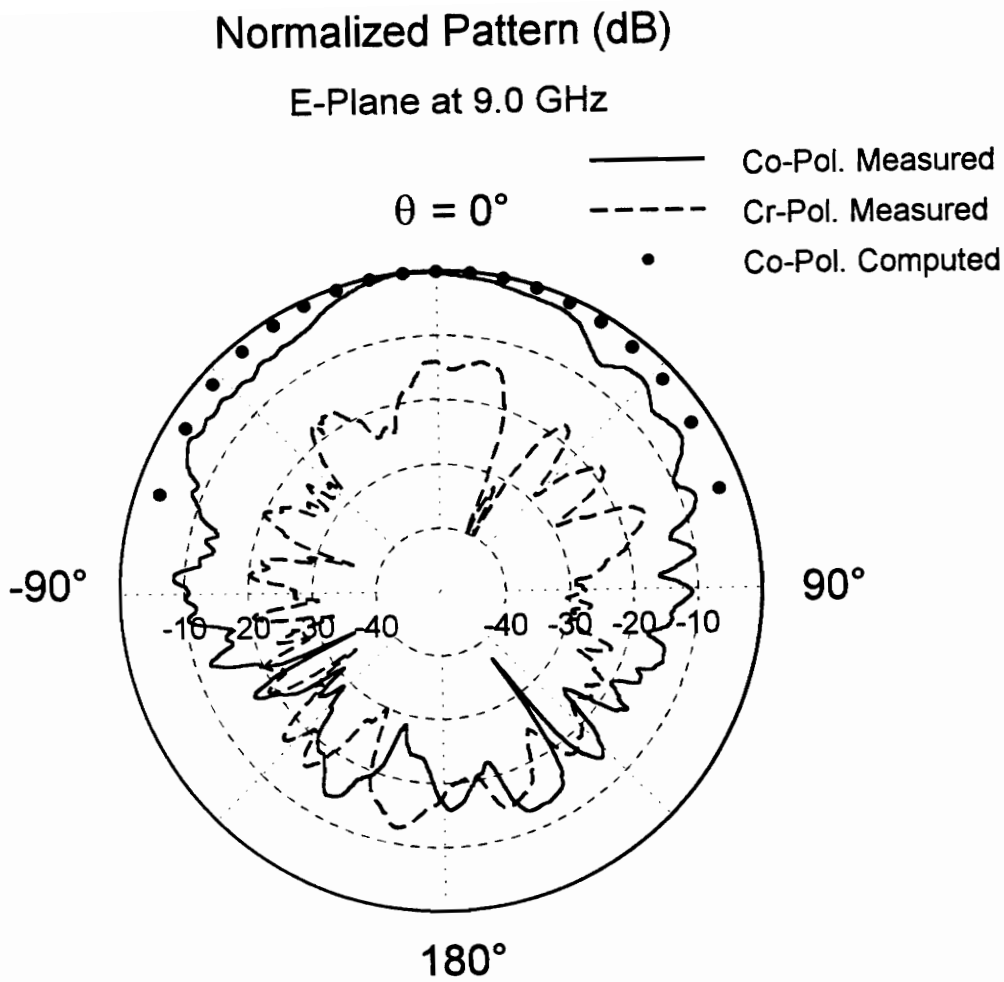

Figure B-10. Measured and computed E-plane far-field pattern at 9.0 GHz. Shown are the co-polarized (Co-Pol.) and cross-polarized (Cr-Pol.) cases. The computed pattern is found using (7.18) assuming single-mode propagation. The data are for the Test Case # 2 CSW.

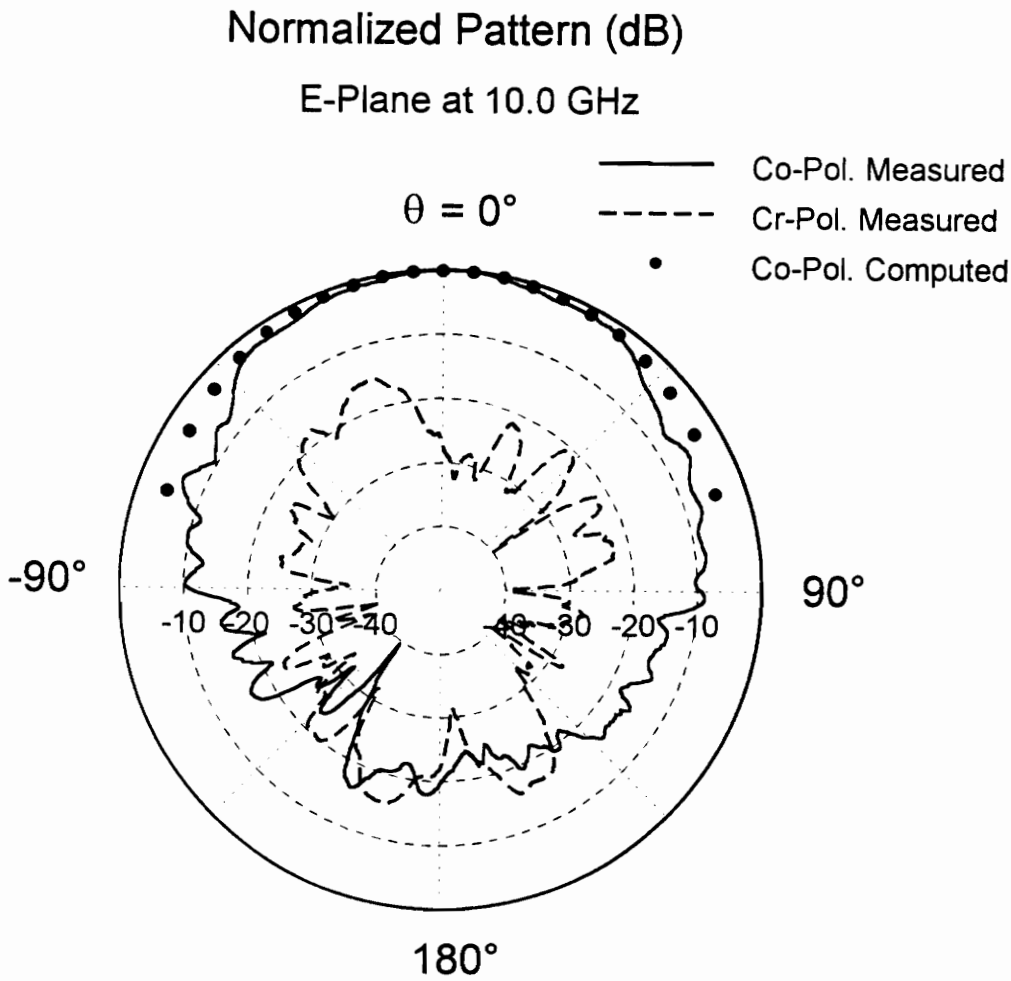

Figure B-11. Measured and computed E-plane far-field pattern at 10.0 GHz. Shown are the co-polarized (Co-Pol.) and cross-polarized (Cr-Pol.) cases. The computed pattern is found using (7.18) assuming single-mode propagation. The data are for the Test Case # 2 CSW.

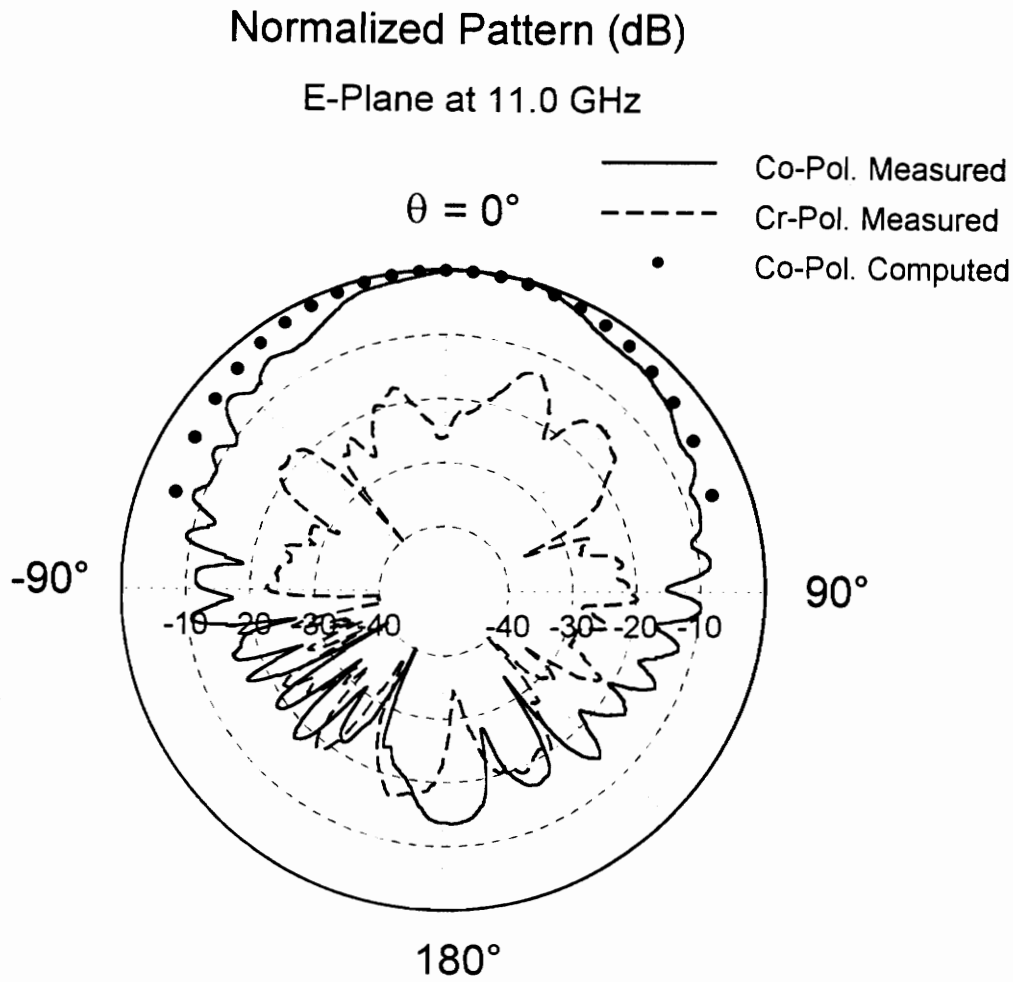

Figure B-12. Measured and computed E-plane far-field pattern at 11.0 GHz. Shown are the co-polarized (Co-Pol.) and cross-polarized (Cr-Pol.) cases. The computed pattern is found using (7.18) assuming single-mode propagation. The data are for the Test Case # 2 CSW.

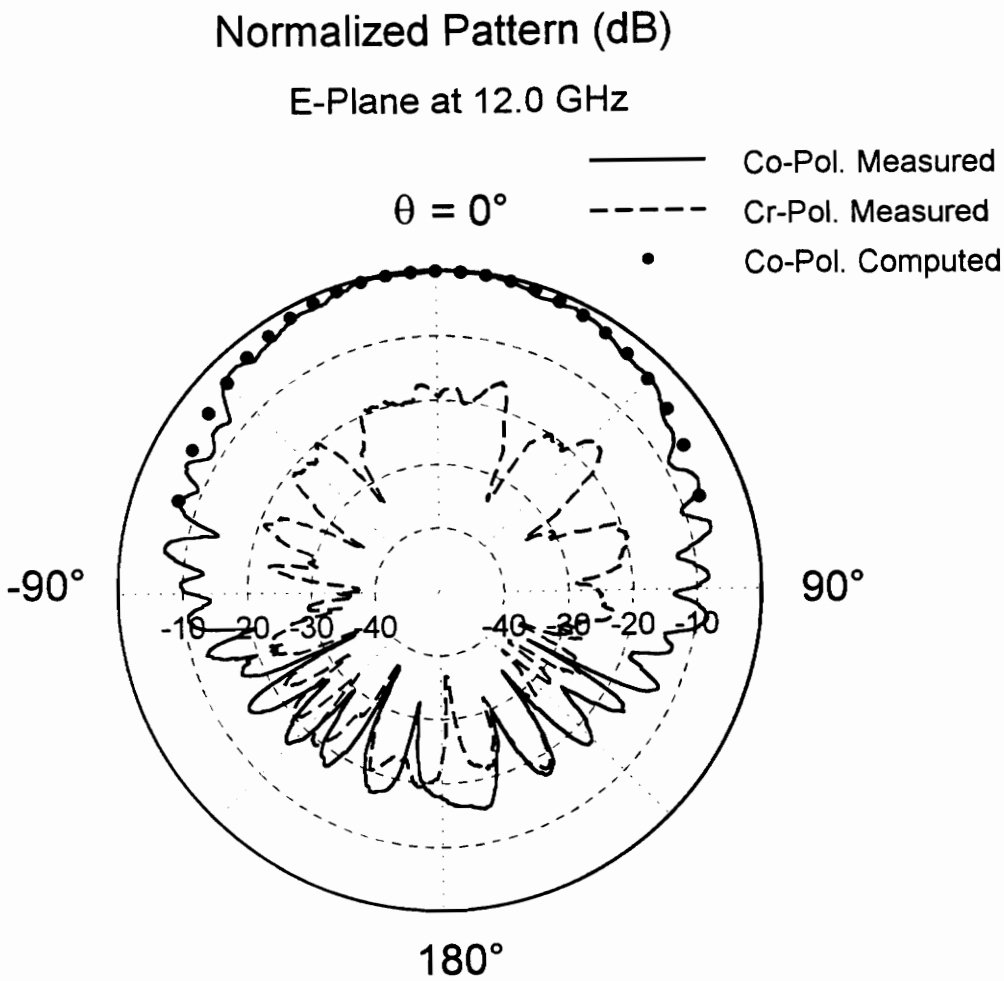

Figure B-13. Measured and computed E-plane far-field pattern at 12.0 GHz. Shown are the co-polarized (Co-Pol.) and cross-polarized (Cr-Pol.) cases. The computed pattern is found using (7.18) assuming single-mode propagation. The data are for the Test Case # 2 CSW.

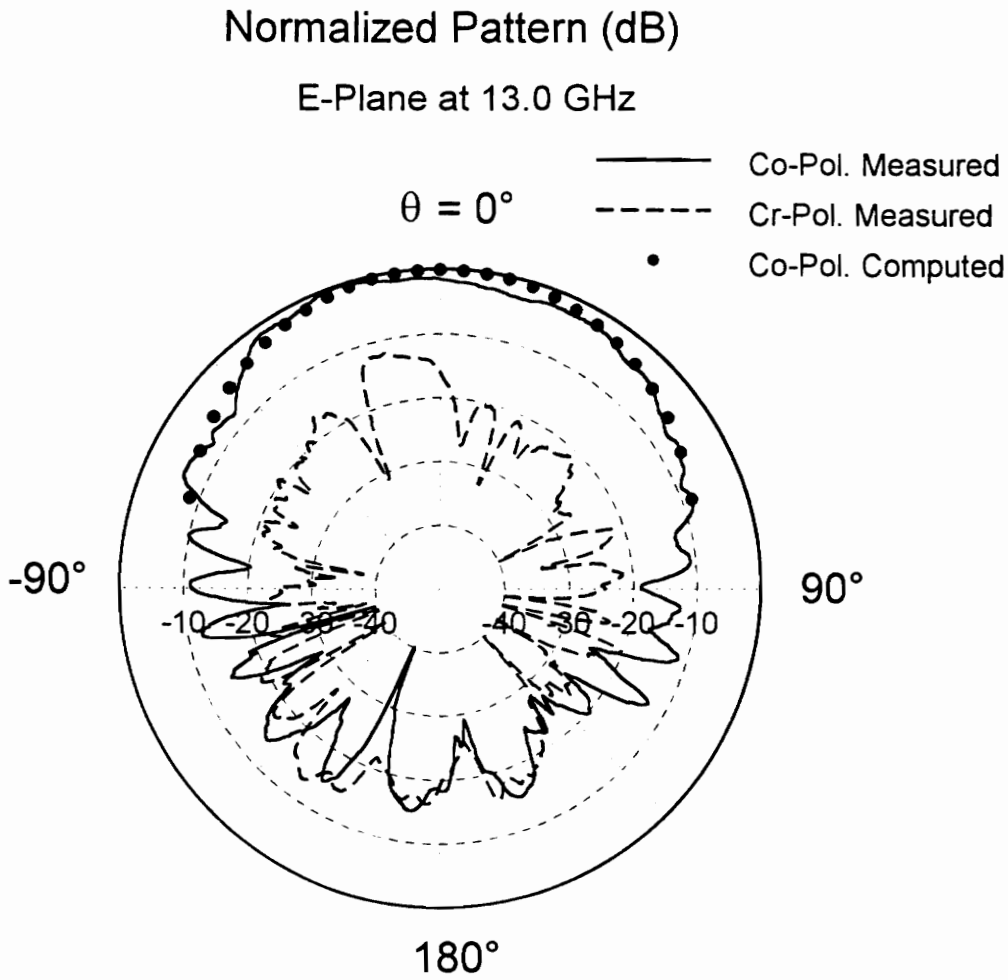

Figure B-14. Measured and computed E-plane far-field pattern at 13.0 GHz. Shown are the co-polarized (Co-Pol.) and cross-polarized (Cr-Pol.) cases. The computed pattern is found using (7.18) assuming single-mode propagation. The data are for the Test Case # 2 CSW.

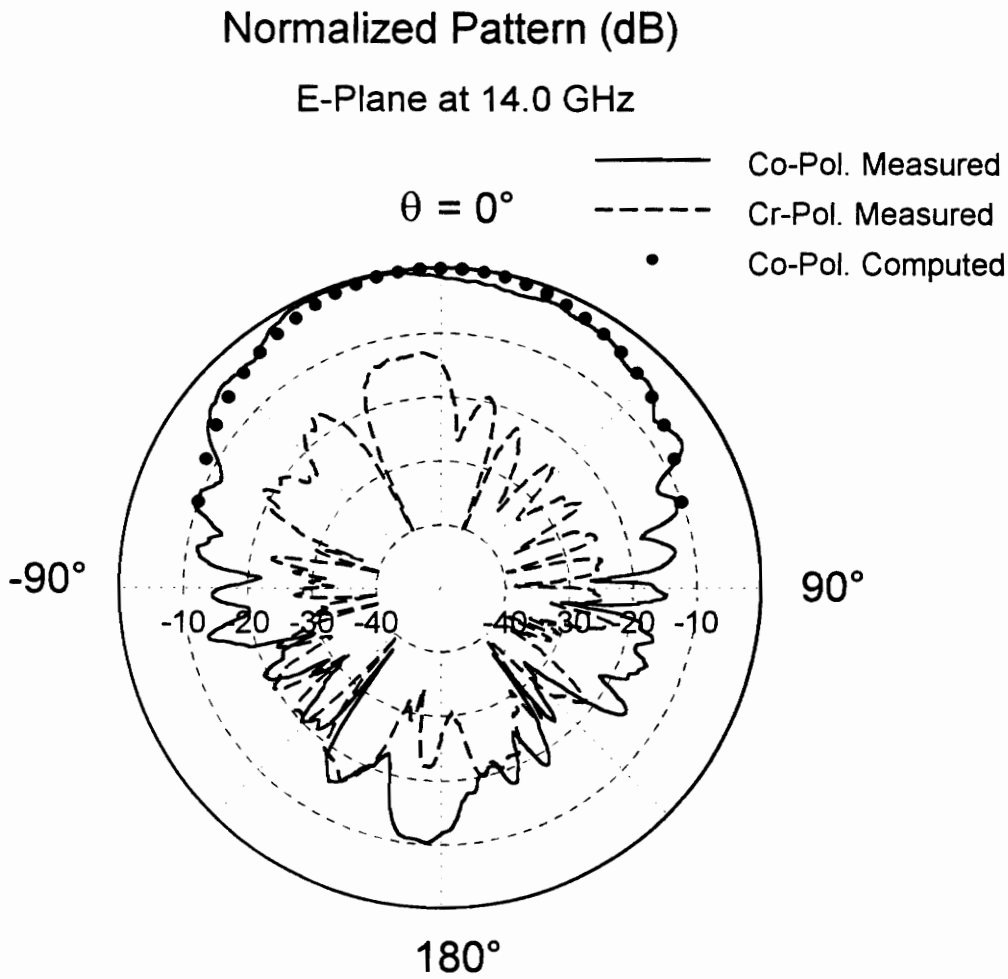

Figure B-15. Measured and computed E-plane far-field pattern at 14.0 GHz. Shown are the co-polarized (Co-Pol.) and cross-polarized (Cr-Pol.) cases. The computed pattern is found using (7.18) assuming single-mode propagation. The data are for the Test Case # 2 CSW.

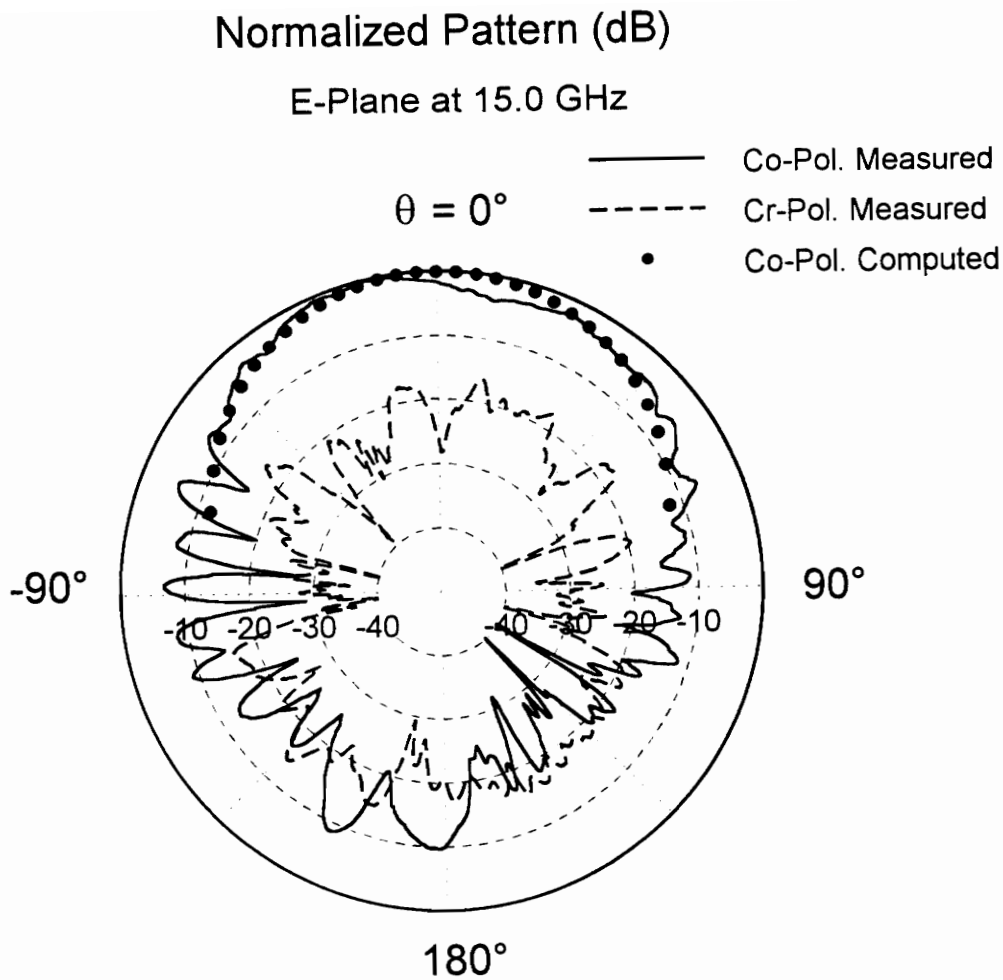

Figure B-16. Measured and computed E-plane far-field pattern at 15.0 GHz. Shown are the co-polarized (Co-Pol.) and cross-polarized (Cr-Pol.) cases. The computed pattern is found using (7.18) assuming single-mode propagation. The data are for the Test Case # 2 CSW.

APPENDIX C

ELECTROMAGNETIC FIELD PLOTS OF HIGHER-ORDER MODES

In Chapter 5, the electromagnetic field plots of the dominant TE_{10} mode and the TM_{11}, TE_{11}, TE_{20L}, and TE_{20U} higher-order modes were shown. In this Section, the field plots of the TM_{12}, TE_{12}, TM_{13L}, and the TM_{13U} higher-order modes are presented. Again as in Chapter 5, the plots shown are computed using the Test Case # 2 CSW parameters as defined in Chapter 6. The arrows represent the transverse field components and the contours give the magnitude of the normalized axial field at intervals of 0.2. The plots of these modes are given in Figures C-1 through C-4.

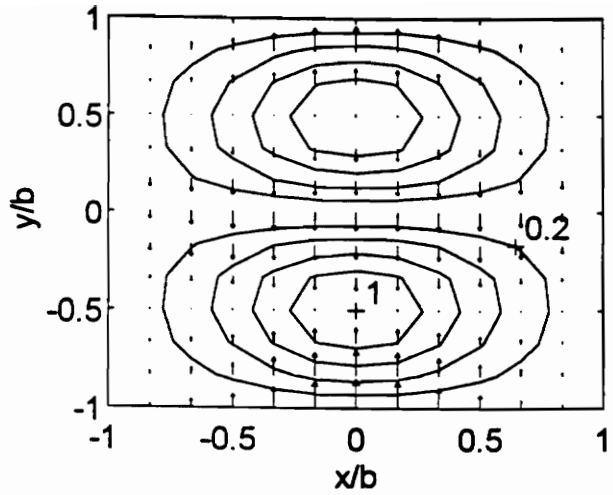

(a)

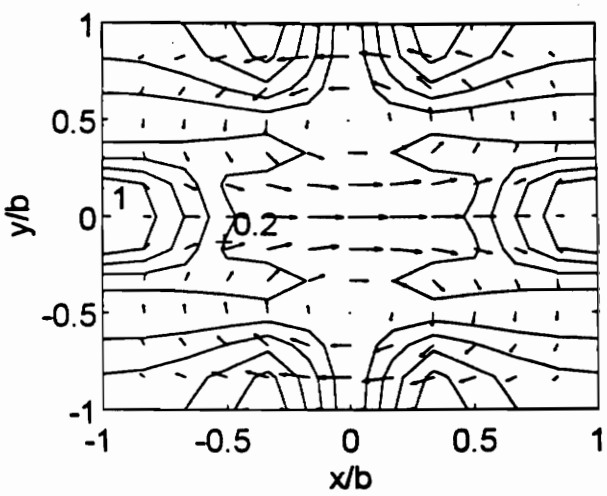

(b)

Figure C-1. Field distributions of the TM_{12} hybrid mode. (a) Electric field. (b) Magnetic field. Parameters are $\varepsilon_r = 2.56$, c/a = 0.319, cutoff frequency = 15.732 GHz, $k_z = 100$ (Test Case # 2). The arrows indicate the magnitude and direction of the transverse field component. Contours indicate the amplitude of the axial (or z-directed) field component in 0.2 increments, normalized to the maximum axial component.

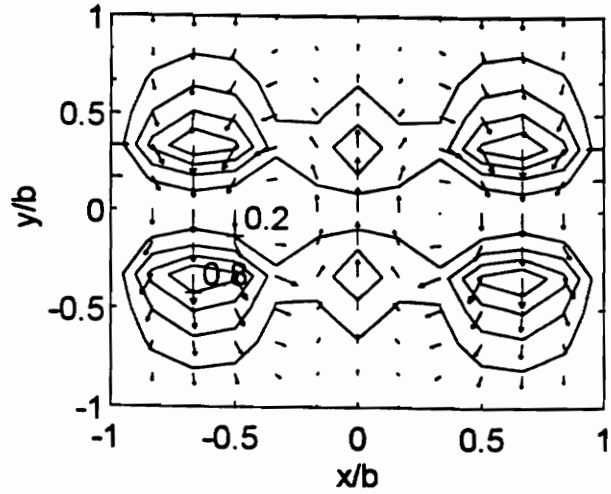

(a)

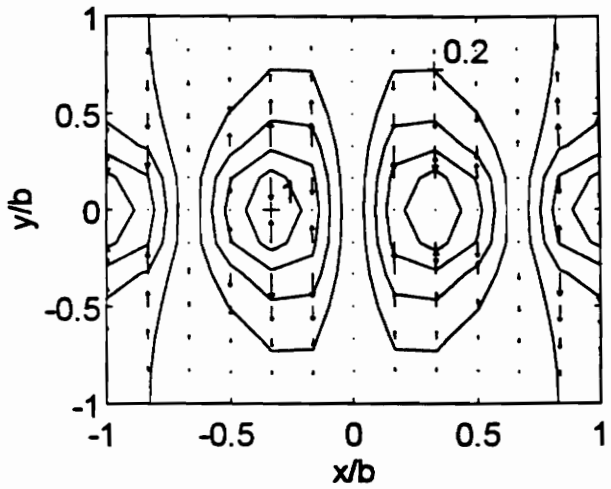

(b)

Figure C-2. Field distributions of the TE_{12} hybrid mode. (a) Electric field. (b) Magnetic field. Parameters are $\varepsilon_r = 2.56$, $c/a = 0.319$, cutoff frequency = 22.470 GHz, $k_z = 100$ (Test Case # 2). The arrows indicate the magnitude and direction of the transverse field component. Contours indicate the amplitude of the axial (or z-directed) field component in 0.2 increments, normalized to the maximum axial component.

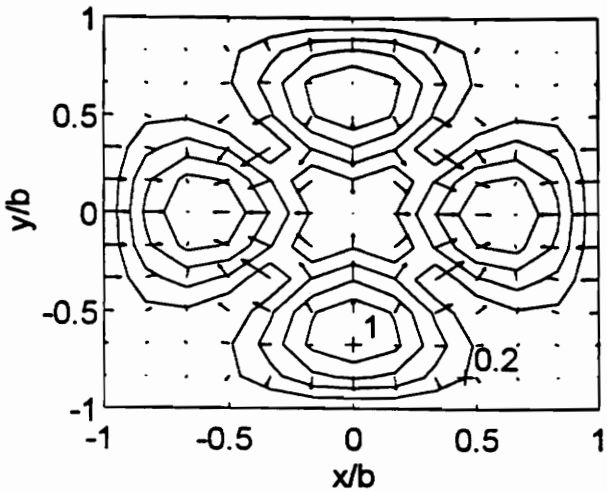

(a)

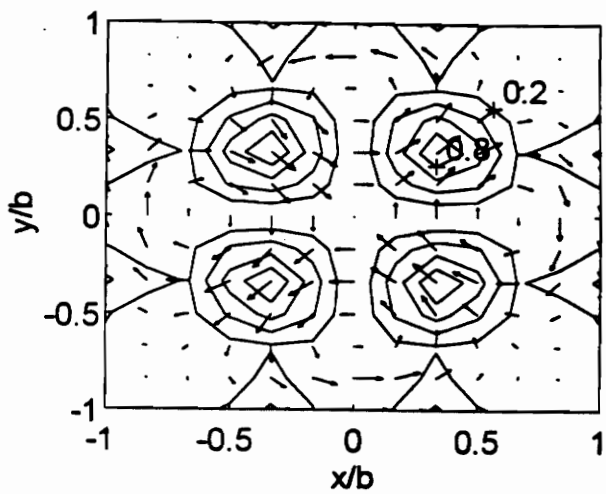

(b)

Figure C-3. Field distributions of the TM_{13L} hybrid mode. (a) Electric field. (b) Magnetic field. Parameters are $\varepsilon_r = 2.56$, $c/a = 0.319$, cutoff frequency = 20.650 GHz, $k_z = 100$ (Test Case # 2). The arrows indicate the magnitude and direction of the transverse field component. Contours indicate the amplitude of the axial (or z-directed) field component in 0.2 increments, normalized to the maximum axial component.

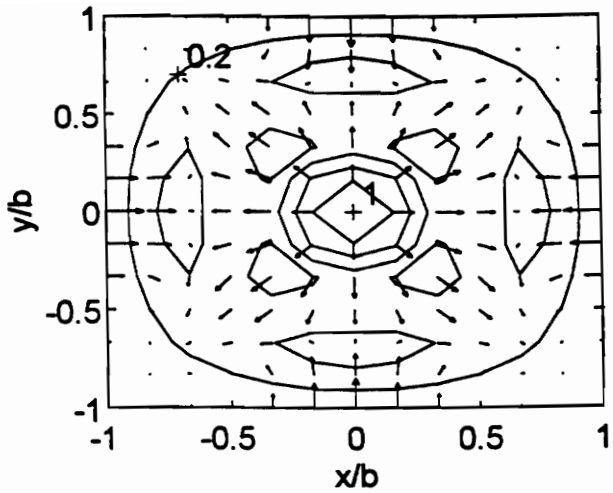

(a)

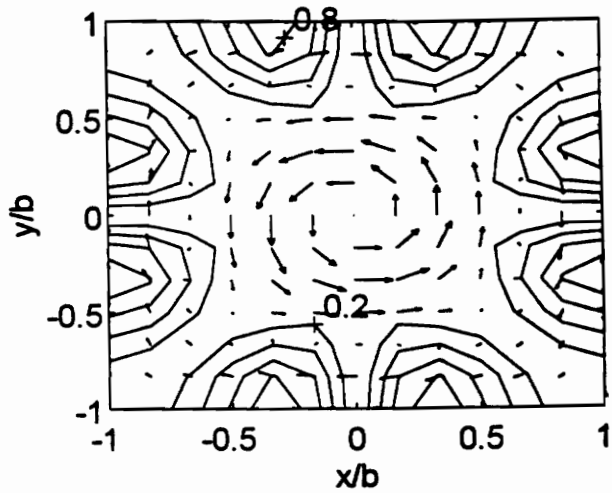

(b)

Figure C-4. Field distributions of the TM_{13U} hybrid mode. (a) Electric field. (b) Magnetic field. Parameters are $\varepsilon_r = 2.56$, $c/a = 0.319$, cutoff frequency = 22.454 GHz, $k_z = 100$ (Test Case # 2). The arrows indicate the magnitude and direction of the transverse field component. Contours indicate the amplitude of the axial (or z-directed) field component in 0.2 increments, normalized to the maximum axial component.

APPENDIX D

DISCUSSION OF A CANONICAL CASE IDEAL MODE FILTER

A mode filter that supports dual polarization and suppresses even/even symmetry modes and passes even/odd or odd/even modes is presented in Chapter 6. A canonical case 'ideal' mode filter is discussed in this appendix to provided an understanding of how mode filters can suppress unwanted modes and pass desired modes. This example will illustrate the basic principles and theory however will differ significantly compared to the geometry and modal suppression given in the dual polarized case of Chapter 6.

The canaonical case that will be considered is formed in a bifurcated square waveguide as shown in Figure D-1. Figure D-1a shows an incident wave containing an arbitrary spectrum of waves, having symmetry properties given by Table 3-2. It is assumed that the incident wave consists of even/even, even/odd, and odd/even modes. The section label 'mode filter' contains an infinitesimally thin perfect electric conductor (PEC) placed on the x-axis. The cross-section of the mode filter section is shown in Figure D-1b. To the right and left of the mode filter section is a square waveguide as shown in Figure D-1c.

Incident waves with an x-directed electric field having a maximum in the along the x-axis will not pass through the mode filter since the tangential electric field must vanish at the PEC boundary. Hence the modes with even/even and odd/even are filtered rather than passed by the filter. Modes with even/odd symmetry will have no x-directed electric field along the along the x-axis and therefore pass through the mode filter since the tangential electric field is zero on the PEC boundary. In consideration of the incident wave symmetry and the boundary conditions, only even/odd modes will exit the left side of the mode filter. Hence this mode filter ideally suppresses even/even and odd/even modes and passes even/odd modes.

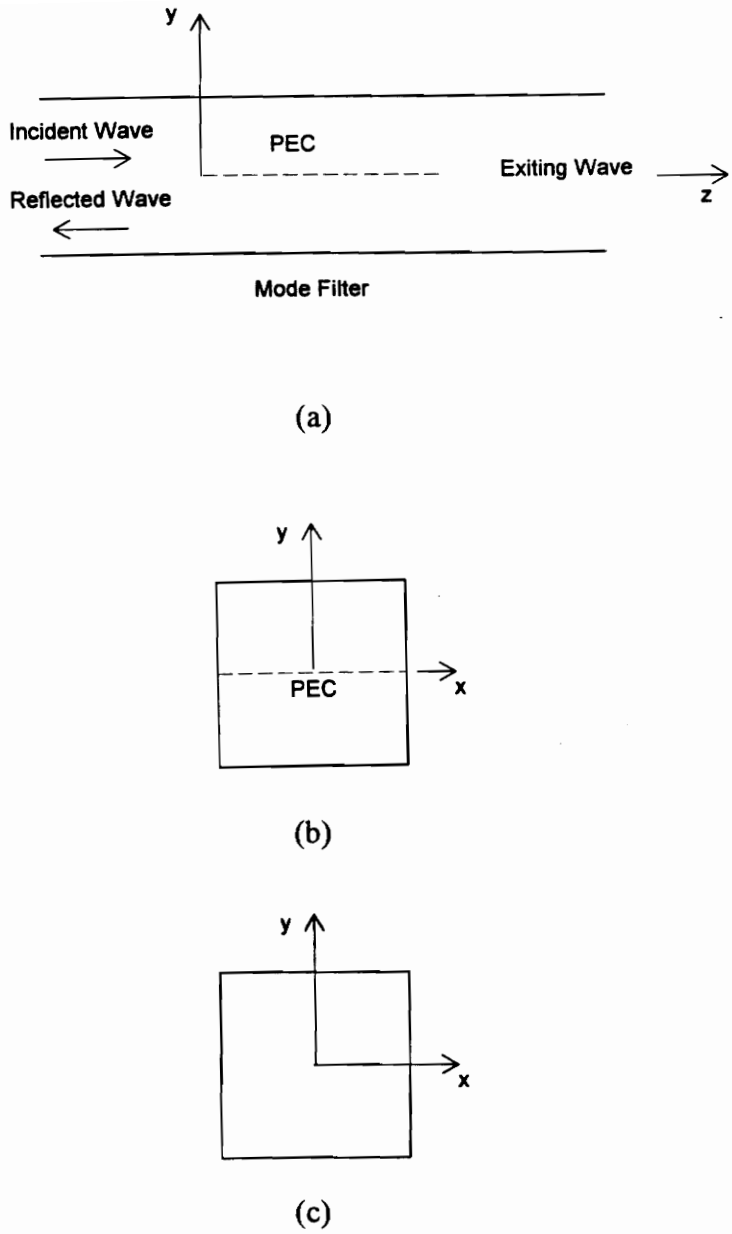

Figure D-1. Bifurcated square waveguide used to demonstrate ideal mode filter. (a) Bifurcated square waveguide. (b) Cross-section *with* mode filter. (c) Cross-section *without* mode filter.

This canaonical case mode filter supports only linear polarized waves and hence is insufficient for the CSW which requires dual polarization. An approximation of this ideal mode filter is found in [1] and [2] and consists if a thin resistive film placed on the x-axis of a rectangular waveguide. The Type-3 mode filter defined in Figure 6-5c is also an approximation of the ideal mode filter discussed above. The Type-3 mode filter will not support dual polarization, but will suppress odd/even modes and is useful in identifying resonances in the cavity measurements performed in Chapter 6.

The dual polarized mode filters discussed in Chapter 6 (Figures 6-5a and 6-5b) are based on the same principles and concept but vary in geometry, since the 90 degree rotational symmetry property must be satisfied.

References for Appendix D

[1] L.Stark, C.V. Bell, R.A. Notvest, R.E. Griswold, D.A. Charlton and R.W. Howard, "Microwave components for wide-band phased arrays", *Proc. IEEE*, Vol. 56, NO.11, November 1968, pp.1908-1923.

[2] G.N. Tsandouglas, D.H. Temme, and F.G. Willwerthet, "Longitudinal Section Mode Analysis of Dielectrically loaded waveguides with application to phase shifter design", *IEEE Trans. on Microwave Theory and Techniques*, Vol. MTT-18, No. 2. Feb. 1970.

VITA

Dan Purdy was born on December 13, 1960 in Chicago Illinois and was raised on a farm in the lovely Appalachia mountains of Western Pennsylvania. From 1981 to 1986 he attended George Mason University and Northern Virginia Community College part time while employed full-time as an Electronics Test Engineer. In 1986, Dan attended Virginia Tech and received his B.S. in Electrical Engineering in 1988. From 1988 through 1989 Dan conducted research in support of the Virginia Tech's Satellite Communications Group in the area of automated position location systems and completed his M.S. in Electrical Engineering in 1989. In 1989 Dan went to work for the U.S. Naval Air Warfare Center, China Lake, CA. where was employed in the areas of impulse radar, antenna design and development , signal processing, and measurement systems. In 1992, the China Lake Academic Fellowship Committee selected Dan to attend Virginia Tech for two years (1992-1994) of advanced studies on wide band phased array antennas, signal processing and radar. Dan is currently with Code C3931 (535200D) at the Naval Air Warfare Center, China Lake, CA. His current interests include antennas, microwaves, radar and signal processing. Dan is a member of the Institute of Electrical and Electronic Engineers (IEEE) including both the Antennas and Propagation Society and the Microwave Theory and Techniques Society. In his spare time Dan enjoys competitive distance running, backpacking, climbing and water activities.